Danmarks Tekniske Universitet

Graduate Schools Yearbook 2007

DTU Chemical Engineering
Department of Chemical and Biochemical Engineering

Department of Chemical
and Biochemical Engineering
Technical University of Denmark

Graduate Schools Yearbook 2007

Editors:
Kim Dam-Johansen
Martin Bøjer

Address: Department of Chemical and Biochemical Engineering
Søltofts Plads, Building 229
Technical University of Denmark
DK-2800 Kgs. Lyngby
Denmark

Telephone: +45 4525 2800
Fax: +45 4588 2258
E-mail: kt@kt.dtu.dk
Internet: http://www.kt.dtu.dk

Print: J&R Frydenberg A/S
København
Januar 2008

Cover: Anne Mette Dion

Cover photo: Klaus Holsting

ISBN: 978-87-91435-63-3

Contents

Contributions

Preface

Over the last five years we have succeeded in establishing a significant activity in the field of Bio Process Engineering and by January 1st 2008 the English name of the department was changed to "Department of Chemical and Biochemical Engineering" – in Danish "DTU Kemiteknik".

Since 2003 we have published a yearbook of our Graduate Schools. In this yearbook our newly matriculated graduate students present the background and the aims that motivate their studies while the graduate students matriculated for longer time present the progress and the status of their research projects. Readers of the yearbooks may thereby follow the progress of the individual graduate students and their studies.

2007 was a very productive year with more graduate students than ever before and the yearbook illustrates the broad spectrum of research activities performed by our graduate students within chemical and biochemical engineering disciplines: chemical kinetics and catalysis, process simulation and control, process integration and development, reaction engineering, thermodynamics and separation processes, oil and gas technology, combustion technology, enzyme technology, polymers science, aerosols physics, mathematical modeling, and quantitative product design.

It is with great pleasure that I present to you:

The Chemical and Biochemical Engineering Graduate Schools Yearbook 2007

Kim Dam-Johansen
Professor, Head of Department

Mohd. Kamaruddin bin Abd. Hamid
Phone: +45 4525 2912
Fax: +45 4593 2906
E-mail: mka@kt.dtu.dk
WWW: http://www.capec.kt.dtu.dk
Supervisors: Prof. Rafiqul Gani

PhD Study
Started: July 2007
To be completed: June 2010

Integration of Modeling, Design and Control for Efficient Operation of Chemical Processes

Abstract
The purpose of this study is to develop a model-based methodology for integration of process design and control (IPDC) problems. The new methodology is organized in four hierarchical stages based on a decomposition of the general optimization problem. The objective of each stage is to define the search space and enumerate/test a set of promising (feasible) candidates. In each subsequent stage, the search space is reduced until in the final stage only a small number of candidates need to be evaluated. Therefore, while the problem complexity increases with every subsequent stage, the dimension and size of the problem is reduced. The proposed methodology does not have difficulties in handling complex problem formulations with large number of variables and constraints, and its applicability is highlighted in relevant case studies.

Introduction
Traditionally, chemical process design and process control are two separate engineering problems that are performed independently, with little or no feedback between each other. Figure 1 shows a schematic representation of the two problems. That is, first the process is designed to achieve an optimum objective based on a fully specified nominal case. Only after the process has been designed the operability aspects are taken into account. These might include the control system design and the safety, reliability and the flexibility of the design. Chemical processes therefore tend to be highly constrained with few degrees of freedom left for process control purposes. This conventional sequential-forward approach has some inherent limitations such as dynamic constraint violations, process overdesign or under performance and does not guarantee robust performance [1]. In practice, process design is often tackled by chemical and process engineers, while process control is often done by control and instrumentation engineers.

To overcome the limitations encompassed by the conventional approach, a simultaneous approach for exploiting interactions between process design and process control that will include the process design variables as optimization variables whilst, at the same time, optimizing the controller tuning parameters, is needed. The potential economic benefits of such a simultaneous approach are also investigated.

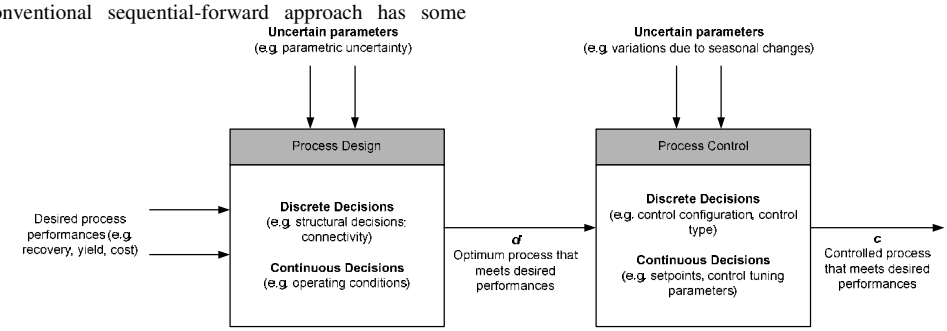

Figure 1: Conventional solution approach for process design and control problems.

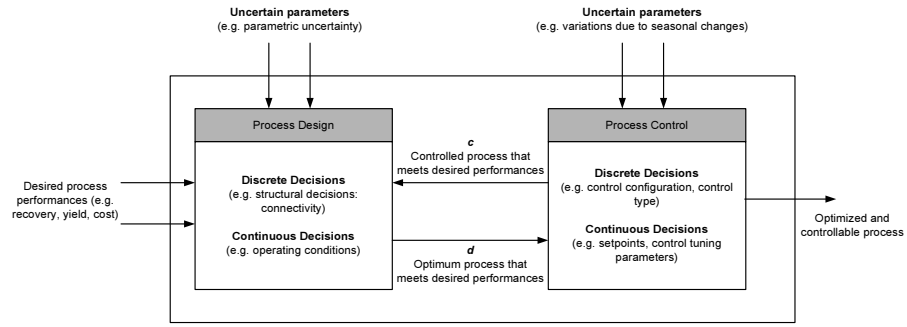

Figure 2: New approach for simultaneous solution of process design and control problems.

Figure 2 illustrates the simultaneous approach for process design and process control. Using this approach, both process design and control will share the same variable(s) in their decisions.

One important question needs to be answered here. Can we optimize the design and control decisions simultaneously to maximize the overall process performance in the presence of the operational and model uncertainty? Or, can chemical and process engineers sit down together with control and instrumentation engineers to make simultaneous decisions to guarantee robust performance of the new processes?

The challenges of the integration of process design and control (IPDC) were clearly identified and discussed by several group of researchers [2].

The subsequent section will explain the objective of the entire study. A new problem formulation based on decomposition methodology will be presented in *Methodology* section. *Conceptual Validation* section will highlight the applicability of the proposed methodology in solving simple optimization problem. This article closes with conclusions and suggestion for future work.

Specific Objective

The aim of this study is to develop a systematic model-based methodology that is capable of exploiting the interactions between process design and process control without having difficulties in handling complex problem formulations with large number of variables and constraints.

In general, the solution of this IPDC problem will require the determination of:

the optimal process design, in terms of structural decisions and connectivity (discrete decisions), and the operating parameters/conditions such as reactor volume, column length, etc. (continuous decisions); and

the optimal control scheme design, in terms of the control configuration, control type, etc. (discrete decisions), and the tuning parameters for the given control structure (continuous decisions).

Methodology

Figure 3 shows an overview of the new IPDC methodology. The new methodology is organized in four hierarchical stages based on a decomposition of the general IPDC problem into four subproblems: (1) pre-analysis stage, (2) steady-state analysis stage, (3) dynamic analysis stage, and (4) evaluation stage. The objective of each stage is to define the search space and enumerate (and/or generate) a set of promising candidates. In each subsequent stage, the search space is reduced until in the final stage only a small number of candidates need to be evaluated. Therefore, while the problem complexity increases with every subsequent stage, the dimension and size of the problem is reduced.

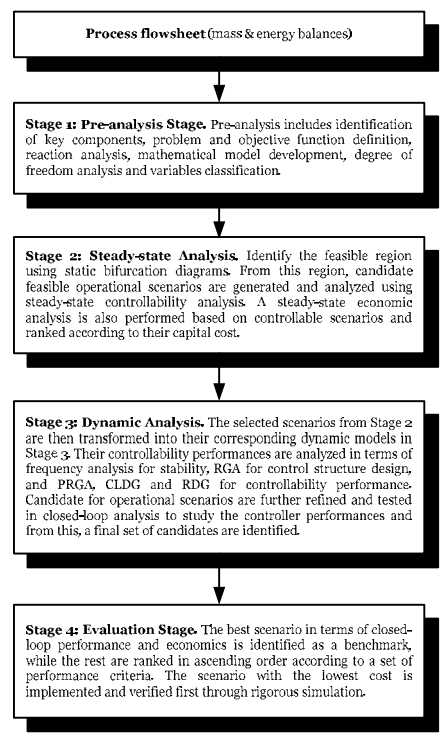

Figure 3: Overview of the new IPDC methodology.

Problem formulation

The general IPDC problem is treated as a mixed-integer dynamic optimization (MIDO) problem where control-related dynamic properties are considered simultaneously with *ESSE Index,* which is index of performance that may include weight on the **E**conomic, and/or **S**ustainability, and/or **S**afety, and/or **E**nvironmental Impact on the plant in order to design a cost effective, sustainable, and highly controllable process. It can be conceptually posed as follows:

Minimize	*ESSE Index* which may include weight on the **E**conomic, and/or **S**ustainability, and/or **S**afety, and/or **E**nvironmental Impact on the plant
Subject to	Differential-Algebraic Process Model, Inequality Path Constraints, Control Scheme Equations, Process Design Equations, Feasibility of Operation, Process Variability Constraints

A general formulation for IPDC problem can be presented as:

$$\min_{w.r.t.d,x^s,u^s,x(t),u(t)} I = \Phi(d, x(t), u(t)) \tag{1}$$

s.t.

Process control constraints

$$\dot{x} = f(x(t), u(t), d, \Theta(t), t) \tag{2}$$

$$x^d_{\min} \le x(t) \le x^d_{\max} \tag{3}$$

$$u^d_{\min} \le u(t) \le u^d_{\max} \tag{4}$$

$$h^d(d, x(t), u(t), \Theta(t), t) = 0 \tag{5}$$

$$g^d(d, x(t), u(t), \Theta(t), t) \le 0 \tag{6}$$

Process design constraints

$$f^s(d, x^s, u^s) = 0 \tag{7}$$

$$x^s_{\min} \le x^s \le x^s_{\max} \tag{8}$$

$$u^s_{\min} \le u^s \le u^s_{\max} \tag{9}$$

$$h^s(d, x^s, u^s, \Theta^s) = 0 \tag{10}$$

$$g^s(d, x^s, u^s, \Theta^s) \le 0 \tag{11}$$

Plantwide control constraints

$$y \in \{0,1\}^{NC} \tag{12}$$

where x is the vector of state variables, u the vector of control variables, Θ the vector of disturbances, and d is the vector of design variables. Superscripts d and s denote dynamic and steady-state of relevant variables, respectively.

In the objective function (Eq. 1), Φ, represents the *ESSE Index* which may include weight on the **E**conomic, and/or **S**ustainability, and/or **S**afety, and/or **E**nvironmental Impact on the plant related to dynamic properties. The system dynamics is described by a set of differential equations given in Eq. 2. Eqs. 3 - 4 are, respectively, the dynamic bounds on system and control variables. In Eqs. 5 - 6, signify possible dynamic equality and inequality constraints, respectively.

The steady-state system is described by the function given in Eq. 7. The steady-state bounds on system and control variables are represented in Eqs. 8 - 9, respectively. In Eqs. 10- 11, the possible steady-state equality and inequality constraints are expressed, respectively.

In Eq. 12, plantwide control structure selection is considered using binary numbers. *NC* represents the total number of possible plantwide control structure from controller superstructure.

The IPDC problem, which is combinatorial in nature, can be solved in many ways, but finding the optimal solution strategy is very important, especially when the constraints representing the process models are nonlinear or their number is large thereby causing difficulties in convergence and computational efficiency. Due to the large number of constraints involved, the feasible region can be very small compared to the search space. All of the feasible solutions to the problem may lie in that relatively small portion of the search space. The ability to solve such problems depends on the ability to identify and avoid the infeasible portion of the search space. One way to this is by decomposing the problem into subproblems, which are relatively easy to solve.

In Figure 4, we present a decomposition methodology of general IPDC problems into subproblems that correspond to their subsequent stages of the new model-based IPDC methodology. In this way, the solution of the decomposed set of subproblems is equivalent to that of the original general IPDC problem. The advantage is a more flexible solution approach together with relatively easy to solve subproblems and a solvable final optimization subproblem no matter how complex the problem formulations are.

Conceptual Validation

The solution through the proposed decomposition methodology is illustrated with the help of an analytical example. The objective here is to highlight the applicability of the decomposed methodology to solve a simple optimization problem. This is illustrated through a small MINLP problem [3], which is solved through the decomposition approach.

$$\min \quad 2x_1 + 3x_2 + 1.5y_1 + 2y_2 - 0.5y_3 \tag{v1}$$

subject to

$$x_1^2 \quad y_1 - 1.25 = 0 \tag{v2}$$

$$x_2^{1.5} \quad 1.5y_2 - 3 = 0 \tag{v3}$$

$$x_1 \quad y_1 - 1.6 \le 0 \tag{v4}$$

$$1.333x_2 \quad y_2 - 3 \le 0 \tag{v5}$$

$$x_1, x_2 \ge 0 \tag{v6}$$

$$y_1 y_2 - 1 = 0 \tag{v7}$$

$$-y_1 - y_2 + y_3 \le 0 \tag{v8}$$

$$y_1, y_2, y_3 = \{0,1\} \tag{v9}$$

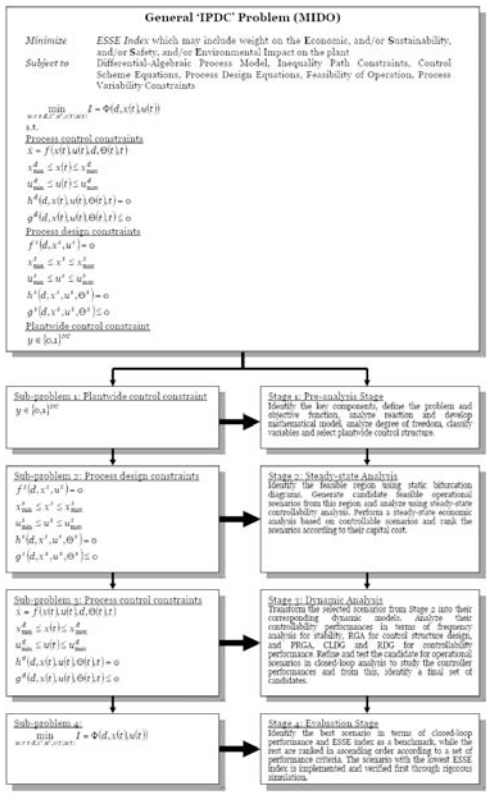

Figure 4: Decomposition methodology.

The above MINLP problem is decomposed using the proposed decomposition methodology as shown in the Figure 5. Since this is an MINLP problem, then it is only decomposed into 3 stages where the Stage 3 of dynamic analysis is skipped since there are no dynamic constraints involved.

The MINLP problem is reduced to an NLP problem for each set of candidates selected from Stage 2. For the selected feasible solutions, the NLP problems are solved using ICAS MoT, and the solution having the minimum objective function value is the optimal solution for the MINLP problem. The solutions are given in Table 1. The smallest objective function value is 7.9311, corresponding to (1,1,1). Therefore, the optimal solution for the MINLP problem using decomposed methodology, which could also have been obtained by other method in [3], is

$$(y_1, y_2, y_3, x_1, x_2, f_{obj}) = (1,1,1,0.5000,1.3103,7.9311)$$

Table 1: Solution of NLP Problems

candidate	x_1	x_2	f_{obj}
(1,1,1)	0.5000	1.3103	7.9311
(1,1,0)	0.5000	1.3103	8.4311

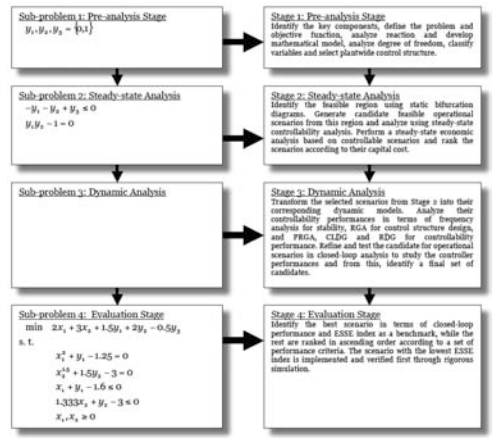

Figure 5: Decomposition methodology of small MINLP example problem.

Conclusions and Future Work

This article presents a new model-based methodology for solving simultaneous process design and process control problems. The methodology is organized in four hierarchical stages based on a decomposition of the general optimization problem into four sub-problems: (1) pre-analysis stage, (2) steady-state analysis stage, (3) dynamic analysis stage, and (4) evaluation stage. The objective of each stage is to define the search space and enumerate (and/or generate) a set of promising candidates. In each subsequent stage, the search space is reduced until in the final stage only a small number of candidates need to be evaluated. Therefore, while the problem complexity increases with every subsequent stage, the dimension and size of the problem is reduced. The applicability of this methodology was highlighted through a simple conceptual example. The result shows that the new methodology is able to find the same solution reported by others. Current and future work is involved with the further development of IPDC and illustrate its application through case studies involving reactor-separator-recycle systems.

Acknowledgement

The author acknowledges the financial support of the Ministry of Higher Education (MoHE) of Malaysia and Universiti Teknologi Malaysia (UTM).

References

1. A. Malcom, J. Polan, L. Zhang, B. A. Ogunnaike, A. A. Lingger. Integrating systems design and control using dynamic flexibility analysis. *AIChE Journal,* 53(8) (2007) 2048-2061.
2. P. Seferlis, M. C. Georgiadis. *The integration of process design and control.* Amsterdam: Elsevier B. V., 2004.
3. A. T. Karunanithi, L. E. K. Achenie, R. Gani. A new decomposition based CAMD methodology for the design of optimal solvents and solvent mixtures. *Industrial & Engineering Chemistry Research*, 44(13) (2005), 4785-4797

Jane Agger

Phone: +45 4525 2861
Fax: +45 4525 2906
E-mail: jag@kt.dtu.dk
WWW: http://www.kt.dtu.dk
Supervisors: Anne Meyer
Hanne Risbjerg Sørensen, Novozymes A/S

PhD Study
Started: March 2007
To be completed: April 2010

Enzymatic Opening of Diferulate Cross Linking in Plant Cell Walls

Abstract
Cereal residues such as e.g. wheat bran, brewers spent grain and corn fiber are rich in arabinoxylan and pose an important resource for the manufacturing of bioactive food ingredients and as raw material for bioethanol production. However, an improved utilization of these residues is highly dependent on efficient enzymatic hydrolysis. The hydrolysis is currently limited for some types of hemicellulose possibly due to the presence of diferulic acid cross linking in the primary cell wall structure. These cross linkings are believed to present a physical/chemical barrier preventing complete enzymatic hydrolysis of the polymers. The aim of this project is to open up diferulate cross linking of polysaccharides via enzymatic hydrolysis. Furthermore, it is the aim to obtain new knowledge regarding the occurrence and influence of diferulates on solubility and enzyme accessibility in plant cell walls.

Introduction
Cereal by-products from e.g. wheat, barley and corn are renewable resources with a potential of being an inexpensive raw material for production of bioethanol or bioactive food components. They are rich in non-starch structural polysaccharides with arabinoxylan being the major hemicellulose compound [1]. However, currently the utilization of these polysaccharides is limited due to inefficient conversion processes and enzymes pose a realistic opportunity for better exploitation. Polymers of arabinoxylan are known to be cross linked in certain plant cell wall materials with dehydrodimers of ferulic acid [1]. These cross linkings present a barrier currently preventing complete enzymatic hydrolysis of the polymers. Esterification of ferulic acid at 0-5-arabinofuranosyl moiety in arabinoxylan can cross link to form dehydrodimers with adjacent polymers and form rigid structures [2]. The extent of ferulic acid dimerization along with the degree of substitution with arabinose, glucuronic acid, acetic acid and monomeric ferulic acid are factors determining the solubility and the enzymatic accessibility of the polymer. Besides cross linking the arabinoxylan polymers, the dehydrodimers of ferulic acid are also believed to cross link to other polymeric structures in the cell wall, for instance lignin and structural proteins [3]. Figure 1 shows a schematic illustration of the proposed structure of cross linked arabinoxylan.

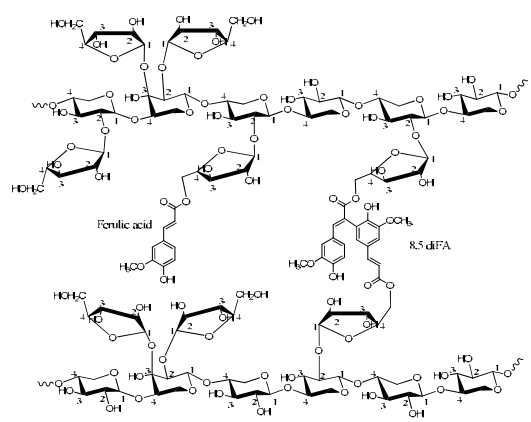

Figure 1: Schematic sketch of arabinoxylan cross linked by dehydrodimers of ferulic acid. The positional substitutions of arabinose are at this point uncertain.

Specific objectives
The project is based upon three major hypotheses, namely that the presence of diferulate cross linking in

the plant cell walls represents a physical/chemical barrier for enzymatic hydrolysis of the structural carbohydrates and in particular the arabinoxylan. Secondly it is believed that identification of enzymes and design of proper reaction conditions will accelerate the efficiency of the enzymatic opening of the cell wall matrix and thereby boost the degradation of structural polysaccharides. Finally, with such a process it will be possible to upgrade non-valuable cereal by-product streams to raw materials for biofuel production or for bioactive components in the food industry.

Results and discussion

Corn fiber is a cereal by-product with large industrial importance, because it is a by-product from the corn based starch production in the United States. It mainly consists of the pericarp cell wall of the corn kernel and the major chemical composition was investigated by acidic and alkaline hydrolysis and analysed by HPAEC and RP-HPLC methods.

Table 1: Monosaccharide composition of corn fiber (mg/g DM). Average of three samples ± standard deviation.

Component	Concentration (mg/g DM)
Glucose	393 ± 13
Galactose	46.7 ± 3.2
Xylose	233 ± 21
Arabinose	158 ± 10

Table 2: Chemical composition of corn fiber (mg/g DM). Average of three samples ± standard deviation.

Component	Concentration (mg/g DM)
Ash	7.91± 0.3
Polysaccharides[a]	831
Protein	89.9 ± 17
Lignin	76.6 ± 2.7
Acetic acid	42.4 ± 3.2
Total phenolics[a]	32.5
Ferulic acid	16.3 ± 0.2
Diferulic acid	14.6 ± 0.3
p-coumatic acid	1.63 ± 0.0
Total[a]	1080

[a]summarized from the individual components.

The content and composition of monosaccharides in corn fiber (Table 1) show that glucose is the major component. Glucose will mainly originate from starch and cellulose and starch determination (HCl hydrolysis) showed that the starch can be quantified to approx. 23% of the total dry matter (data not shown). The starch is most likely residual starch from the endosperm loosely attach to the cell wall surfaces and not an integrated part of the cell wall matrix. Accounting for this amount of starch the cellulose content can be estimated to 16%. The content of xylose, arabinose and galactose will represent the hemicellulosic polysaccharides with arabinoxylan as the major specimen. Using conventional assumptions the total amount of arabinoxylan can be estimated to 36% on a dry matter basis. Looking into other cell wall components (Table 2) protein and lignin comprises approx. 9% and 7.6% respectively, identifying a relatively complex cell wall matrix. The presence of phenolic compounds other than lignin summarises to approx. 3% of the total dry matter, of which the diferulic acids constitutes 45%. Assuming equal distribution of the diferulic acids on the arabinoxylan polymer every 25 arabinosyl-moiety of the arabinoxylan chain will be substituted with a dehydrodimer of ferulic acid. Furthermore, every 22 arabinosyl-moiety will be substituted with the monomeric ferulic acid. Analysis has revealed that the diferulic acids are mainly composed of the 8,5'-benz, 8-O-4', 5,5' and 8,5' form of the dehydrodimers, which is also consistent with previous findings [4]. p-coumaric acid is only found in minor amounts.

Conclusion

The polysaccharide composition of corn fiber reveals a large potential for use as a raw material for biofuel production or functional food ingredients due to a high content of residual starch, cellulose and a high content of arabinoxylan. However, the high degree of substitution especially with diferulic acids within the hemicellulose polymers complicates the chemical structure of the cell wall matrix and will most likely limit an efficient enzymatic hydrolysis. The presence of several types of compounds in the cell wall will add to the necessity of performing hydrolysis with a complex set of enzyme activities, which again will complicate the reaction condition optimization. However, the identification of key enzyme activities might expose the cell wall structure to already known and optimized enzymes and thereby create the basis for complete or controlled hydrolysis.

Acknowledgements

This project is co-financed by FOOD graduate school, Novozymes A/S and DTU. A special thanks to Novozymes A/S for providing substrate and comparable data.

References

1. L. Saulnier, C. Marot, E. Chanliaud, J-F. Thibault. Carbohydr. Polym. 26 (1995) 279-287
2. L. Saulnier, M-J. Crépeau, M. Lahaye, J-F. Thibault, M.T. Garcia-Conesa, P.A. Kroon, G. Williamson. Carbohydr. Research 320 (1999) 82-92
3. D.W.S. Wong. Appl. Biochem. Biotechn. 133 (2) (2006) 87-112
4. L. Saulnier, J-F. Thibault. J Sci Food Agric 79 (1999) 396-402

List of publications

No publications yet

Muhd Nazrul Hisham Zainal Alam

Address: Building 227, room 240
Phone: +45 4525 2993
Fax: +45 4593 2906
E-mail: mza@kt.dtu.dk
WWW: www.kt.dtu.dk
Supervisors: Krist V. Gernaey
Prof. Anne Meyer
Gunnar Jonson

Ph.D. Study
Started: July 2007
To be completed: June 2010

Continuous Membrane Micro-Bioreactors for Development of Integrated Pectin Modification and Separation Processes

Abstract
The project aims at designing continuous membrane microbioreactors for the development of integrated pectin modification and separation processes. This microbioreactor should encompass the requirements to perform a continuous enzymatic reaction with simultaneous product separation and integration of optical sensors for on-line monitoring of relevant process parameters. The project is linked to a new strategic research effort on enzymatic modification of pectins for producing pre-biotics initiated at the Department of Chemical Engineering at DTU.

Introduction
Pectin is a complex carbohydrate (heterosaccharide) mostly found in primary cell walls and intercellular regions of higher plants. Pectic substances are abundant in agro-industrial waste streams from sugar and potato starch production. At present, these low-value waste streams are dumped at large expense. Agro-industries are highly interested in converting these low-value waste streams into useful high-value products [1,2].

This conversion can be done by breaking down the pectin substance into oligosaccharides through the hydrolysis reaction catalyzed by combined action of pectinolytic enzymes, namely the pectinmethylesterase (PME) and polygalacturonase (PG). Enzymatic depolymerization of pectin to oligosaccharides is a very promising process. However; like any other enzymatic reaction, there is an abundance of factors dictating its reaction and kinetics. These include control of multiple enzymes action, broad molecular weight of oligomers product, low solubility of substrate, end-product inhibition and a highly viscous reaction mixture [2 - 4].

Presently, the concept of microbioreactors to accommodate specific enzymatic reactions has been successfully demonstrated. However, most of the currently existing micro-scale systems for studying enzyme reactions are systems where the enzyme is immobilized [5-6]. Despite of its advantages in enzyme reutilization and elimination of enzyme recovery processes (recycle stream channel), this system is not suitable for the enzymatic depolymerization of pectin to oligosaccharides. This is due to the presence of multiple enzymes (PME and PG) and end-product inhibition. Under these circumstances, a free-cell system (stirred tank reactor) is most favorable. Microbioreactors (free-cell system) with a working volume ranging from milliliters down to nanoliters in different operating modes (batch, fed-batch and continuous operation) have been established. These microbioreactors are integrated with optical sensors for on-line monitoring of relevant process parameters (OD, DO, pH) [7,8]. Nevertheless, currently existing microbioreactors were mainly designed to facilitate the fermentation processes of bacterial and animal culture strains.

The development of micro-systems for high throughput enzymatic reactions and on site production of expensive bioproducts at the point of demand is an on-going research activity. At this stage, a feasible continuous membrane microbioreactor for pectin modification processes has yet to be established. Therefore, development of a novel continuous membrane microbioreactor for pectin modification and separation processes will be a strong motivation and driving force of this research work.

Motivation
When evaluating new enzymes for novel enzyme-catalysed production processes, the costs and availability of the enzymes are often a limit, as the production of limited quantities of new enzymes is costly. In this respect, microbioreactors offer a number of cost-reducing advantages for assessing enzymatic processes (particularly screening of new enzymes). First, the microreactors operate with very small volumes, even when operated as a chemostat as

envisaged in this project, thus offering significant cost reduction for assays with expensive substrates (e.g. labeled substrates) or expensive enzymes. Second, by adapting technologies from polymeric bio-microsystems, microbioreactors can be made disposable to minimise reactor preparation efforts. Third, and maybe most important, due to the small size, the microbioreactors can mimic in a controlled fashion a wide range of environmental conditions, which can be related to conditions in full-scale bioprocesses. Moreover, the microbioreactors can be scaled out to platforms of multiple reactors, thus greatly increasing throughput for elucidating enzyme behaviour under various relevant bioprocessing conditions. [7,8].

Objectives

The first project goal is the establishment of continuous membrane microbioreactors for the systematic experimental evaluation of enzyme-catalysed production processes under precisely defined environmental conditions. Successful application of continuous membrane bioreactors for studying the enzymatic modification of polygalacturonic acid has been reported [3,4], which explains the selection of this reactor type in this project. The selection of the microscale for performing experiments is a direct consequence of the advantages offered by these systems as previously mentioned.

In a first project phase concepts for pH control need to be developed further to allow tight pH control of the microbioreactor contents during enzymatic reactions. The pH measurement can be achieved using an optical method [7,8]. For pH control, the addition of ammonia and carbon dioxide in a carrier gas stream will be investigated.

In a second phase of the project the continuous microbioreactor will be combined with an ultrafiltration membrane that is permeable for the targeted oligosaccharide products, thus establishing a continuous membrane microbioreactor. Besides allowing separation of target oligosaccharide products from the reaction mixture, the membrane also has the advantage of retaining the enzyme, thus leading to reduced operating costs when results obtained at the micro-scale are extrapolated to a full-scale process. Establishing a suitable separation method is a crucial issue in the search for efficient production processes.

In the third phase of the project, the focus will shift from microbioreactor technology development to demonstrating the usefulness of the micriobioreactors for investigation of enzymatic processes. First, optimal process conditions (pH, T, retention time, molecular weight cut-off of membranes) for the production of oligosaccharides will be targeted. Once these optimal process conditions are established, the remaining part of the project will aim at unraveling the kinetics of the conversion of pectins to oligosaccharides. The latter will be possible by performing experiments under well-controlled conditions in the continuous membrane microbioreactors.

Work Done

In the first 5 months, techniques for design and fabrication of the microsystems were practiced (3D drawings in SolidWorks, micromilling machine). The first prototype of the micro Ultrafiltration (UF) unit was designed and fabricated. This micro UF unit includes a micro flow valve at the outlet of the flow channel. This micro flow valve is used to regulate the flow rate in the micro UF unit in such a way that a sufficiently large trans-membrane pressure for the separation process can be created. The micro UF unit is illustrated in Figure 1.

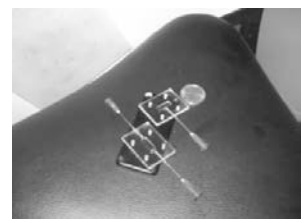

Figure 1. The micro Ultrafiltration (UF) unit

Next Steps

The next step of this research work will be on the establishment of a Labview based measurement (e.g. pH and pressure) and control system for the micro unit. Focus will also be directed to the development of the pH control concept for the micro system. Moreover, optical measurement techniques such as Raman spectroscopy will also be investigated and integrated into the micro system, if successful measurements with this measurement technique can be demonstrated. Once this is established, the first continuous membrane microbioreactor prototype will be designed and fabricated in accordance to the requirements for the pectin modification and separation processes.

Acknowledgements

I would like to express my gratitude to Universiti Teknologi Malaysia (UTM), Skudai, Johor, Malaysia and the Malaysia Ministry of Education for their financial support of this project.

References

1. Ridley B. L. *et al.* (2001). *PhytoChem*. 57: 929 – 967.
2. Todisco S. *et al.* (1994). *Mol. Cat.* . 92: 333 – 346.
3. Gallifuoco A. *et al.* (2003). *Ind. Eng. Chem. Res*. 42: 3937 – 3942.
4. Belafi-Bako K. *et al.* (2007). *Food. Eng*. 78: 438 – 442.
5. Miyazaki M. *et al.* (2006), *Trends. Biotechnol.*, 24 (10). 463-470.
6. Muller D. H. *et al.* (2005), *Chem. Eng. Technol.*, 28 (12). 1569-1571.
7. Szita N. *et al.* (2005), *Lab on Chip*, 5, 819-826.
8. Zanzotto A. *et al.* (2004), *Biotechnol & Bioeng*, 87 (2), 243-254.

Jimmy Andersen
Phone: +45 4525 2838
Fax: +45 4525 2258
E-mail: jia@kt.dtu.dk
WWW: http://www.kt.dtu.dk
Supervisors: Peter Glarborg
Peter Arendt Jensen
Søren Lovmand Hvid, DONG Energy

PhD Study
Started: April 2006
To be completed: April 2009

CFD Modeling and Validation by Bench Scale Measurements

Abstract
The project concerns development and validation of CFD models that can predict mixing as well as chemical reactions in combustion processes. The primary focus of the project is on NO formation and destruction in the freeboard of grate fired boilers. Therefore a model reactor setup has been constructed, that can reproduce the conditions present in the freeboard of grate fired boilers.

Introduction
Computational Fluid Dynamics (CFD) is a powerful tool to predict mixing and fluid motion, and it have gained increasing popularity in design and trouble shooting industrial combustion installations. It is however challenging to include detailed kinetic models in CFD codes.

The focus of this project is to combine knowledge of detailed kinetic mechanisms with the prediction of mixing and local combustion stoichiometry that commercial CFD codes can provide.

In particular the project focuses on modeling the formation and destruction of NO in the freeboard section of grate fired boilers. For this purpose a bench scale freeboard combustion chamber has been designed and constructed, that will make it possible to provide well controlled and detailed measurements for validation of a CFD freeboard model. At present only limited well controlled measuring data on combustion in non swirled flames that can be used as CFD validation is available in the literature.

Validation of CFD models is essential if the modeling approach is to be the basis of research and design work. The initial objective of this project is therefore to supply reliable and relevant test data for modeling the mixing and gas phase reactions taking place in the freeboard section of grate fired boilers.

Specific objective
The overall objectives of this PhD study are:

To provide detailed validation data for CFD models.

To develop and verify a CFD based model of freeboard processes in grate fired boilers.

To implement and verify a chemical kinetic model of the formation and destruction of NO in a CFD model.

Experimental setup
An experimental setup has been constructed to investigate the detailed chemical reactions taking place in the freeboard section of a grate fired power plant. The setup is designed so that the flue gas from a substoichiometric natural gas flame is mixed with additional natural gas. This gas mixture is supposed to simulate the pyrolysis and primary combustion gasses emerging from a straw layer at grate firing conditions.
The combustion gasses are led through a flow straightner, which can be thought of as the surface of the bed layer, and into the freeboard section, where secondary gas is added to complete the combustion process.
The setup is an almost 3 meter long cylindrical construction that consists of two major sections; a 1st stage and a freeboard section, the diameter in the freeboard section is 49 cm. (see figure 1).
Several ports give entrance to the reactor and thereby make it possible to perform temperature measurements and gas sampling at many different positions, as well as visual access is possible for optical measurements.
Ammonia addition to the reactor is done to simulate fuel nitrogen – a major precursor to NO_x [1].

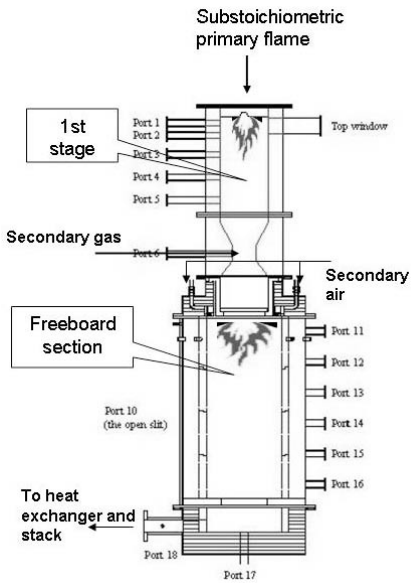

Figure 1: Sketch of the experimental setup – a natural gas fired freeboard simulator

Complete mapping of the freeboard combustion chamber is being done for important parameters:

Temperature – Shielded thermocouples provide detailed temperature mapping in the freeboard chamber.

Velocity – Laser Doppler Anemometry (LDA) measurements provide gas velocity measurements, using a non-intruding particle tracer technique

Figure 2: Picture from the LDA experiments.

Gas species concentrations - Extractive gas analysis using water cooled probes makes it possible to detect and quantify numerous gas phase (for instance O_2, CO, CO_2, NO and NO_x by means of standard analyzing techniques.

Experimental Results

Extractive gas analysis was done using a water-cooled probe to quench the sample gas before leading it to the gas analyzers.

The measurements were made by inserting the probe into various openings at port 10 and traversing, which results in 216 individual measurement positions covered. Measurement data in a point was collected after approximately 5 minutes of steady gas concentration measurement. In general the standard deviation on species O_2, CO_2 and NO/NOx is very low but the CO measurement could fluctuate several hundred ppm.

Figure 3 shows a contour map of the O_2 concentration in the freeboard area. It gives a good impression of how the secondary air enters and is consumed. Unfortunately there is a leak near the left wall, where high O_2 concentrations are detected. For security reasons the setup runs at sub pressure and a leak means that air is sucked into the reactor.

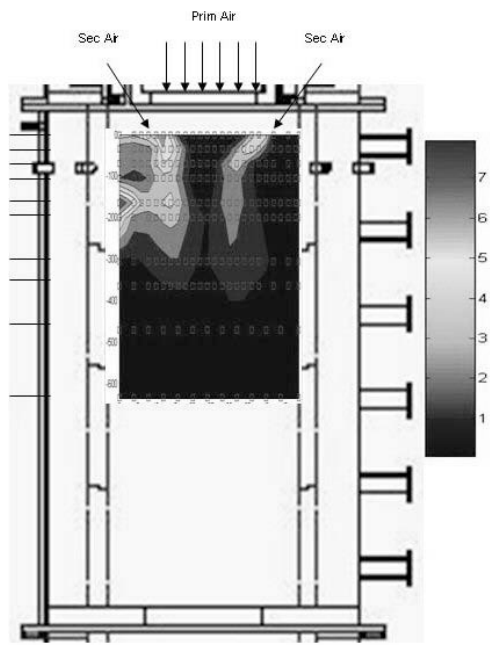

Figure 3: dry O_2 concentration mapping of the freeboard section of the reactor. Overall stoichiometry λ=1.03.

The leak detected by the O_2 measurements does not seem to influence the flame structure based on the CO contours in Figure 4. It has been a challenging task to obtain a symmetric flame zone in the freeboard area, but based on the CO measurements this seems to have been obtained now.

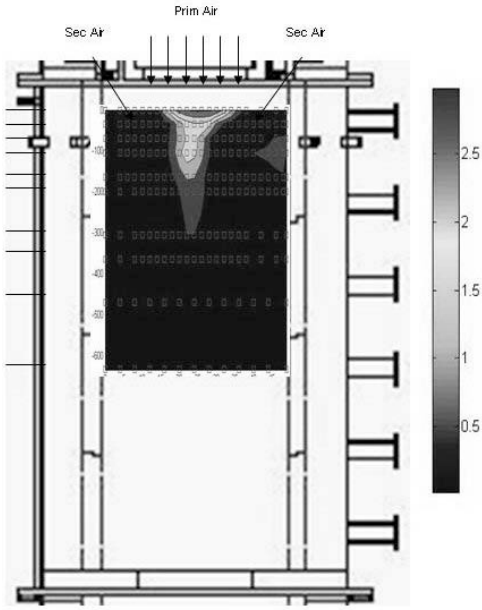

Figure 4: dry CO concentration mapping of the freeboard section of the reactor. Overall stoichiometry λ=1.03.

A parameter that is influenced dramatically by the air leak is the NO concentration, which is displayed in Figure 5.
NO is formed through oxidation of the ammonia added to the secondary gas stream (see Figure 1). The NO formation process from ammonia, is highly relevant since ammonia is the main intermediate N-compound formed during pyrolysis of solid fuels [1]. But the product from ammonia oxidation is very dependent on local conditions such as oxygen concentration and temperature. At the wrong conditions ammonia will react to form NO as shown in the global reaction (1).

(1) $2\ NH_3 + 2½\ O_2 \rightarrow 2\ NO + 3\ H_2O$

However ammonia is also used as a deNOx agent during Selective Non-Catalytic Reduction (SNCR) of NO from flue gases. This is done by adding ammonia at conditions (~950°C) that favors the reaction of NH_3 and NO to yield N_2 and H_2O. Figure 5 illustrates how the formation of NO is highly affected by the leak and thereby locally increased O_2 concentrations. When using the data from Figures 3-5 it will be necessary to discard the left side data set due to the leaking, and use the right side for model validation. Fortunately the CO contours confirm that the left side data is not affected by the leak.

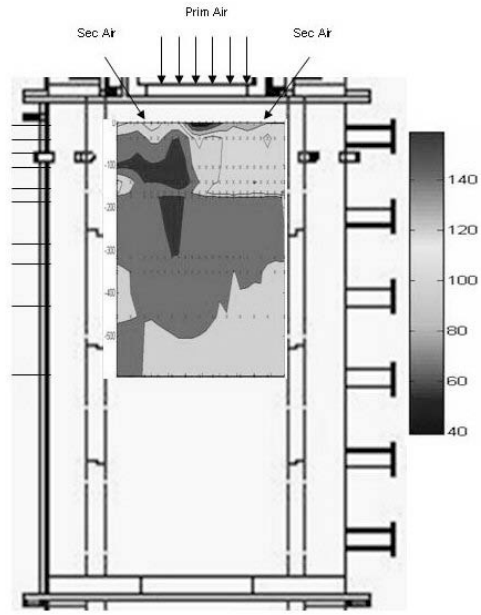

Figure 5: dry NO concentration mapping of the freeboard section of the reactor. Overall stoichiometry λ=1.03.

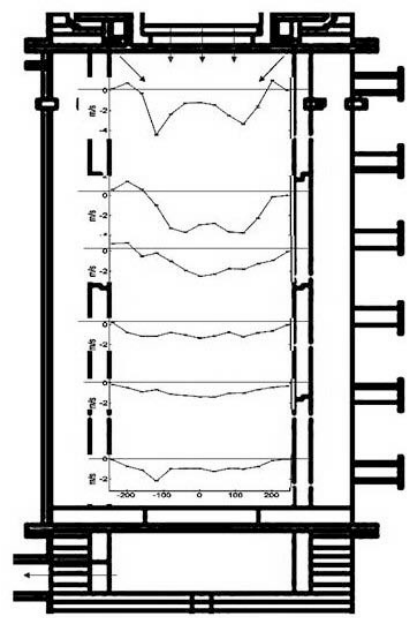

Figure 6: Axial velocities in the freeboard section. Max velocity recorded 4.3 m/s.

Another parameter that is being mapped in the experimental facility is the axial velocity in the reactor as displayed in figure 6. The velocity measurements reveal a flow pattern dominated by the secondary air jets entering with high velocity in the first optical measurement plane and slowly dissipating to a developed parabolic flow. The velocity measurements also reveal recirculation zones in the top corners all features that must be captured with a CFD model.

CFD modeling approach

What a CFD model basically does is to predict the flow of fluid and heat in a computational domain. This is done by solving the governing transport equations, the equation of continuity, momentum and Energy respectively:

$$\frac{\partial \rho}{\partial t} + \nabla \cdot (\rho \vec{v}) = 0 \quad (2)$$

$$\frac{\partial}{\partial t}(\rho \vec{v}) = -\nabla \cdot (\rho \vec{v}\vec{v}) - \nabla p + \nabla \bar{\bar{\tau}} \quad (3)$$

$$\frac{\partial}{\partial t}(\rho E) + \nabla \cdot (\vec{v}(\rho E + p)) = \nabla \cdot (k_{eff} \nabla T - \sum_j h_j F_j + (\bar{\bar{\tau}} \cdot \vec{v})) + S_h \quad (4)$$

The CFD code will then discretize, linearize and solve the governing transport equations including submodel input from radiation, turbulence and chemical reaction-turbulence interaction submodels.

For this project CFD modeling can be carried out in two steps, one that describes the general combustion based on a simplified reaction scheme – for instance the global reaction scheme from Jones and Lindstedt [3]:

(5) $H_2 + \frac{1}{2}O_2 \leftrightarrow H_2O$
(6) $CO + H_2O \leftrightarrow CO_2 + H_2$
(7) $CH_4 + H_2O \rightarrow CO + 3H_2$
(8) $CH_4 + O_2 \rightarrow CO + 2H_2$

The second step will take into consideration the advanced kinetic aspects of NO formation. These two steps can either be coupled directly (which will be computationally expensive), or post-processing the NO chemistry is possible, by assuming that the NO processes does not affect the global combustion or flow parameters significantly. This reasonable assumption makes post-process a detailed NO mechanism on an already validated general temperature and flow field a good option. Different approaches on how to model the combustion and NO formation processes will be compared in the future.

Conclusions and future work

Extensive experimental work has been performed in mapping local concentrations and velocity field in an experimental setup simulating the freeboard conditions of a grate fired boiler. In the future the work will be expanded to include reliable temperature measurements performed using a suction pyrometer to exclude radiation effects. Furthermore the reactor wall temperatures will be measured using a IR pyrometer and hopefully NH_3 concentration will be measured as well. The modeling work performed will consist of testing different turbulent interaction models with more less elaborate chemical kinetic models in order to find the most accurate approach to predict NO formation, but also to find the optimal way of locating computational resources when doing CFD analysis of combustion systems.

Acknowledgements

The project is funded by the Danish PSO program and from STVF (Danish Technical Research Council), DONG Energy, Vattenfall, Babcock & Wilcox Vølund, and B&W Energy.

References

1. P. Glarborg, A.D. Jensen, J.E. Johnsson, Progress in Energy and Combustion Science 29 (2003) 89-113.
2. Fluent inc. Fluent 6.2 users guide.
3. W.P. Jones, R.P. Lindstedt, Combustion and Flame 73 (1988) 233-249.

Pavle Andrić

Phone: +45 4525 2842
Fax: +45 4588 2258
E-mail: pan@kt.dtu.dk
WWW: http://chec.kt.dtu.dk
Supervisors: Prof. Kim Dam-Johansen
Prof. Anne Meyer
Associate Prof. Peter Arendt Jensen

Ph.D. Study
Started: October 2005
To be completed: September 2008

Reactor Design for Enzymatic Degradation of Cellulose from Pre-Treated Wheat Straw

Abstract
Large-scale application of enzymatic hydrolysis of ligno-cellulose is limited by lack of an effective reactor for the complex heterogeneous reaction and high cost of cellulases, due to their inefficient action on this substrate and loss of activity. One of the main problems related to reactor design is in inefficient mixing of highly viscous reaction mixture, while the activity of enzymes is lost due to the product inhibition, un-productive adsorption to lignin, temperature de-activation, etc.

Introduction
Ethanol produced from biomass is emerging as a promising transportation fuel, which can be used as an alternative to the fossil gasoline. Ethanol produced from any kind of biomass is termed as ''bio-ethanol''.

Bio-ethanol is today the world's most widely used transport bio-fuel, accounting for around 90% of total consumption, and it has a central place in a new EU target for total share of bio-fuels (25%) by year 2030. Furthermore, in the USA the bio-ethanol is one of the main bio-fuels, and the research focusing on further improving the technology for bio-fuels production will according to several speeches of US President Bush be intensified.

Production of ethanol from primary biomass, i.e. starch, which can be used as a food or feed, is a well established and known technology. However, this technology is significantly limited by the high price of this kind of biomass.

An alternative feed stock to produce ethanol is ligno-cellulose which has low or no value as food (Figure 1). Ligno-cellulosic biomass includes a variety of relatively cheap agricultural or forestry residues, dedicated crops and different kinds of waste, such as wheat straw, corn stover, wood chips, etc.

Ligno-cellulose is a generic term describing the main constituents in most of the plants, namely cellulose, hemi-cellulose and lignin. In the ligno-celulose, cellulose chains are aggregated together into elementary fibrils of crystalline structures, as it is in the cell wall of different kind of biomass. In the biomass, bunches of elementary fibrils are embedded in a matrix of hemi-cellulose with a thickness of 7-30nm, while lignin is located primarily on the exterior of such formed micro-fibril. The compounding of ligno-cellulose is almost perfect: linear cellulose chains contributing to tensile strength, while hydrophobic amorphous lignin brings chemical resistance and protection against water.

One of the possible process layouts for bio-ethanol production is shown on Figure 1.

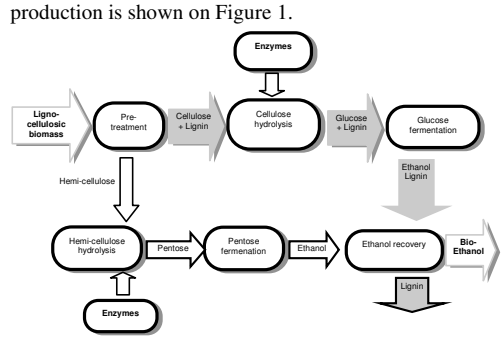

Figure 1: Bio-ethanol production from ligno-cellulosic biomass-simplified scheme of possible process

Bio-ethanol production from ligno-cellulosic is composed of several main steps: biomass transport and handling, biomass pre-treatment, cellulose and hemi-cellulose hydrolysis, fermentation of sugars and ethanol recovery.

Upon transport to the site of production, biomass is handled using various mechanical operations (separation from dirt and stones, cutting, shredding, milling, conveying, etc.) to facilitate satisfactory heat and mass transfer in the subsequent steps. In the pre-treatment, biomass is usually submitted to high temperature and/or use of chemical agents, in order to open the ligno-cellulosic structure and make cellulose and hemi-cellulose susceptible to the following hydrolysis step. In hydrolysis, cellulose and hemi-cellulose are converted to monosaccharide sugars using enzymes or different acids, while in fermentation these sugars are converted by microorganisms to ethanol which will be present in a mixture with water, other fermentation products and residual biomass etc. Ethanol can be further purified using stripping, distillation or pervaporation to obtain fuel grade.

Besides of ethanol, a variety of co-products are formed – some of these of value as animal feed or as fuels in thermal processes for heat and electricity production.

Enzymatic degradation of cellulose from ligno-cellulosic biomass

Sugars for fermentation to bio-ethanol can be produced from ligno-cellulose by using concentrated acid, dilute acid or enzymes.

The relatively recent process of enzymatic hydrolysis of cellulose seems to be the most promising method. Enzymatic hydrolysis is performed at mild conditions (40-50^{o}C, pH 4-5) and utility costs are lower than in acid hydrolysis. Furthermore, since the enzymes are catalysts that catalyze very specific reactions, minimum of the degradation products are formed as well as no corrosion problems are associated with this reaction. It is stated that enzymes have advantage in that they are naturally occurring compounds which are biodegradable and environmentally benign.

However, the use of cellulose degrading enzymes (cellulases) for the hydrolysis of pre-treated ligno-cellulosic biomass is a promising, but also a very difficult task. Bio-ethanol production from ligno-cellulose has not yet been demonstrated on a commercial scale, due to technical and economical obstacles. A key element underlying bio-ethanol processing cost reductions is improvement in the pre-treatment and enzymatic hydrolysis technology.

The large-scale application of enzymatic hydrolysis has in general been limited by lack of an effective reactor for the complex bio-catalysis, due to: a) the problems with the inefficient stirring of the highly viscous and heterogeneous feed mixture (pre-treated biomass and enzymes), b) ligno-cellulose structure (fibrous, porous, water retaining, partially crystalline and resistant to enzymes), c) enzymes de-activation (by heavy product inhibition, un-productive adsorption to lignin or shear stress) d) slow reaction rate.

On the other side, due to the overall economy of the process, it is desired to operate the process with high dry matter contents (DM%, high cellulose content), which posses a significant challenge due to the problematic mixing and pronounced product inhibition.

Specific Objectives

The main objective of this PhD work is to investigate the enzymatic hydrolysis of the pre-treated wheat straw and to develop an improved reactor concept for a more efficient cellulose conversion utilizing enzymes.

The specific aim of this phase of the project is to quantify the glucose product inhibition during enzymatic degradation of pre-treated wheat straw, at glucose levels corresponding to high dry matter contents.

Acknowledgements

This Ph.D study is sponsored by Technical University of Denmark.

List of publications

L. Rosgaard, P. Andric, K. Dam-Johansen, S. Pedersen, A.S. Meyer, Effects of substrate loading on enzymatic hydrolysis and viscosity of pretreated barley straw, Appl. Biochem. and Biotechn., 143 (2007) 27-40.

P. Andric, K. Dam-Johansen, A. S. Meyer, P. A. Jensen, Product inhibition of cellulases during enzymatic hydrolysis of the pre-treated ligno-cellulose, ECCE-6, Conference proceedings and poster presentation, Copenhagen, Denmark, 2007

P. Andric, A. S. Meyer, K. Dam-Johansen, P. A. Jensen, Quantification of glucose inhibition of enzymatic cellulose degradation in pre-treated wheat straw, NordForsk 3rd workshop, Book of abstracts and oral presentation, Lyngby, Denmark, 2007

L. Rosgaard, P. Andric, K. Dam-Johansen, S. Pedersen, A.S. Meyer, Effect of Fed-Batch Loading of Substrate on Enzymatic Hydrolysis and Viscosity of Pretreated Barley Straw, Conference proceedings and oral presentation, AIChE Annual Meeting, San Francisco, 2006

P. Andric, K. Dam-Johansen, R. Gani, P. A. Jensen, Retrol vision: Preliminary Techno-Economical Analysis, Conference proceedings and oral presentation, AIChE Annual Meeting, San Francisco, 2006

P. Andric, K. Dam-Johansen, P. A. Jensen, A. S. Meyer, Bio-ethanol process development: Application of enzymes during hydrolysis of the pre-treated wheat straw, Bio-process Engineering Course, Book of abstracts, poster and oral presentation, Brac-Croatia, (2006)

Pavle Andric, Kim Dam-Johansen, Peter Arendt Jensen, Lisa Rosgaard, Bio-Ethanol Process Development: Pre-Treatment and Enzymatic Hydrolysis of Ligno-Cellulose, Book of abstracts and poster, DK_2 conference, Lyngby, 2006.

Anis Arnous

Phone: +45 4525 2958
Fax: +45 4593 2906
e-mail: aar@kt.dtu.dk
www: www.bioeng.kt.dtu.dk
Supervisors: Prof. Anne S. Meyer

Ph.D. Study
Started: March 2004
To be completed: September 2008

Wine and Berry Fruit Juice with Improved Health Potential

Abstract
Fruits skins contribute a main part of produced fruits pomaces which are a rich source of phenolics phytochemicals compounds. Knowledge about fruits skins composition is needed to understand how phenolics phytochemicals are locked inside skin cell wall polysaccharides matrix. Such detailed compositional knowledge is a key issue to upgrades the press residues wine making or valorise the fruit skin for phenolics phytochemicals production as functional food additive. The overall objective is to provide more detailed knowledge on the use of enzymes in pre-press treatments of fruits used in juices and wines processing. This knowledge will be used to improve the release of the phenolics phytochemicals having potential health benefits.

Introduction:
It has been amply documented that phenolic phytochemicals from fruits and berries, including mixed extracts, juice samples, different individual flavonoids and phenolic acids exert antioxidant activity towards human low-density lipoprotein (LDL) oxidation *in* vitro [1-4]. Since oxidation of LDL is a key step in the pathogenicity of atherosclerosis and thus inducive to coronary heart disease, compounds exerting antioxidant activity on LDL may exert protective, disease preventing effects in humans. Enzyme assisted plant cell wall breakdown of press residues, i.e. mainly skins and seeds, from red wine production and black currant juice pressing results in improved release of phenolics that inhibit *in vitro* oxidation of human LDL [5- 7], Fig. 1.

The antioxidant potency of the released phenols varies depending on the enzyme treatment [5, 6], Fig. 2. This suggests that it may be possible to optimize the enzyme treatments to increase concentrations of certain potent antioxidant phenols. Enzymatic pre-press treatments are already widely employed in the berry juice and wine industries. A better understanding of the plant cell wall degrading enzymes action on fruit skin materials for release of potentially health beneficial compounds appear transferable to juice and wine processing operations. The knowledge gained can therefore pave the ground for production of wines and fruit juices with improved health properties.

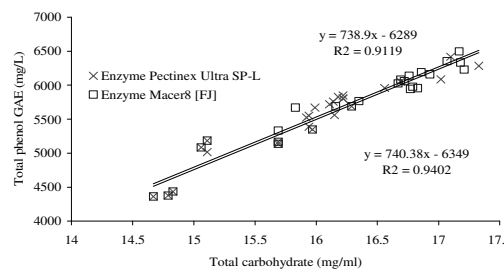

Figure 1: Phenolics determined as gallic acid equivalent (GAE) released when the polysaccharides in the cell wall, notably in the skin fraction, are degraded [7].

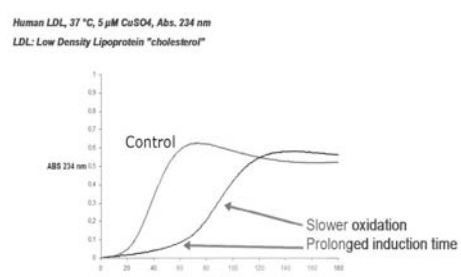

Figure 2: Enzyme gives different antioxidant activity.

Specific Objectives

The aim of the proposed Ph.D. project is to explore in detail the enzyme assisted extraction of phenolics from different berry and grape press residues resulting from juice and wine processing. As a part of this, the project will also provide knowledge on how the phenols are bound in the skin polysaccharide-lignin matrix.

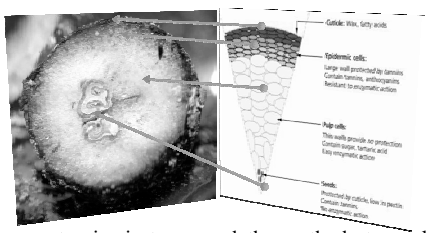

A separate aim is to expand the methods to evaluate possible health benefits to other effects than antioxidant activity on human LDL oxidation.

The main hypothesis to be tested during the PhD study are:

a) Whether it is possible to selectively extract and retain the most potent antioxidants by novel physical and enzymatic treatments of the press residues.
b) Whether it is possible to enzymatically modify the phenolics to optimize their health potential.

Results and Discussion

Practically there is sparse knowledge about the phenolics detailed locations, and how they are bound into the fruit skin polysaccharides matrix. Knowledge about skins composition is needed. As first attempt we used grapes and apples skins as model to understand the relation between skin cell walls polysaccharides and phenolics compounds. Such detailed compositional knowledge is a key issue to upgrades the press residues wine making or valorise the fruit skin for phenolics phytochemicals production as functional food additive. Polysaccharide composition of cell walls fruits skins are usually determined by measuring the monosaccharides released after hydrolysis with acid, alkaline, or enzyme. Chemical hydrolysis is simple, standardised, and an easily repeatable technique. By acid chemical hydrolysis, chromatographic data are simplified and interferences from undesired substances could be minimized. Trifluoroacetic (TFA) and hydrochloric acid (HCl) are commonly used as hydrolysing agents. The difference in monosaccharides and phenolics profiles between grape and apple skins was expected. And it is simply reflects the difference in polysaccharides cell structures between distant plants species [8].

During enzymatic extraction higher phenolics content was released from apples skin (Gold and Red delicious) relative to chemical extraction of phenolics by 60% methanol [8]. This supports the hypothesis: phenols are bound in the skin polysaccharide-lignin matrix and not only present in cell vacuoles. We also found a strong relation between antioxidant capacity (lag-phase) and the content flavan-3-ols in the different extracts, Fig. 3 suggesting the possibility of selecting and extracting certain antioxidants using specific enzymes treatments.

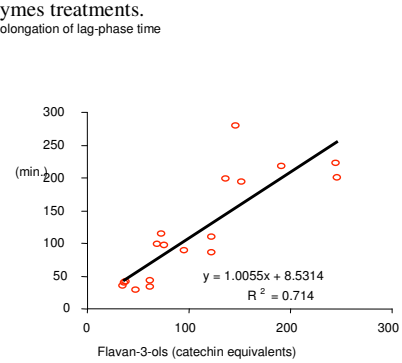

Figure 3: Correlation between antioxidant capacity to inhibit human LDL oxidation *in vitro* and flavan-3-ol content in Red delicious and Golden delicious peel extracts, [8].

Conclusions

A better understanding of the cell walls in fruit skins is needed. We need to know more about how enzymes influence the antioxidant potency of the phenolics. Exploring more specific and mono-active enzymes will help in building the right tailored enzymatic matrix to fit different propose.

References

1. Meyer, A. S.; Heinonen, M.; Frankel, E. N. Food Chemistry 1998, 61 (1-2), 71-75.
2. Meyer, A. S.; Donovan, J. L.; Pearson, D. A.; Waterhouse, A. L.; Frankel, E. N. Journal of Agricultural and Food Chemistry 1998, 46 (5), 1783-1787.
3. Frankel, E. N.; Bosanek, C. A.; Meyer, A. S.; Silliman, K.; Kirk, L. L. Journal of Agricultural and Food Chemistry 1998, 46 (3), 834-838.
4. Meyer, A. S.; Yi, O. S.; Pearson, D. A.; Waterhouse, A. L.; Frankel, E. N. Journal of Agricultural and Food Chemistry 1997, 45 (5), 1638-1643.
5. Meyer, A. S.; Jepsen, S. M.; Sorensen, N. S. Journal of Agricultural and Food Chemistry 1998, 46 (7), 2439-2446.
6. Landbo, A. K.; Meyer, A. S. Journal of Agricultural and Food Chemistry 2001, 49 (7), 3169-3177.
7. Bagger-Jorgensen, R.; Meyer, A. S. European Food Research and Technology 2004, 219 (6), 620-629.
8. Anis Arnous, Rikke A. Trinderup, Manuel Pinelo, and Anne S. Meyer. Journal of Agriculture and Food Chemistry; (in preparation).

List of Publications:

1. Pinelo, M.; Arnous, A.; Meyer, A. S. Trends in Food Science & Technology; 2006, 17 (11), 579-590.

Ane Søgaard Avlund
Phone: +45 4525 2983
Fax: +45 4588 2258
E-mail: asa@kt.dtu.dk
WWW: http://www.ivc-sep.kt.dtu.dk
Supervisors: Georgios M. Kontogeorgis
Michael L. Michelsen

PhD Study
Started: August 2007
To be completed: July 2010

Extension of the CPA Equation of State to Systems Containing Alkanolamines

Abstract
An association model, the CPA (Cubic-Plus-Association) equation of state is applied for the first time to a class of multifunctional compounds, alkanolamines. Three alkanolamines of practical and scientific significance are considered; MEA, DEA and MDEA. Vapor pressures and liquid densities, as well as parameter trends against the van der Waals volume, solvatochromic parameters and mixture LLE data with alkanes are used for estimating the five parameters for the three alkanolamines. VLE calculations for cross-associating mixtures especially with water are used in the validation of the parameters. The influence on the results of the association scheme, cross-association combining rule, interaction parameter and the data available is discussed also in connection to other aqueous cross-associating mixtures, previously studied with the model (alcohols, amines and glycols).

Introduction
Alkanolamines are widely used in many different industries e.g. the oil industry where aqueous solutions of alkanolamines are used for removal of CO_2 and H_2S from natural gas streams.

The CPA EoS [1] has previously been applied to both self- and cross-associating mixtures containing water, alcohols, amines, glycols and hydrocarbons [e.g. 2-4], but where the associating compounds listed here all only contain one type of functional group alkanolamines contain both hydroxyl- and amine-groups. That makes them somewhat more complex to model.

There are several studies available on modeling CO_2-alkanolamine-water systems with electrolyte models, but no independent studies of water-alkanolamines and alkanolamines-alkane using association models.

Three alkanolamines are considered in this work; monoethanolamine (MEA), diethanolamine (DEA) and methyldiethanolamine (MDEA). The structures are shown below.

MEA	$OH\text{-}CH_2\text{-}CH_2\text{-}NH_2$
DEA	$OH\text{-}CH_2\text{-}CH_2\text{-}NH\text{-}CH_2\text{-}CH_2\text{-}OH$
MDEA	$OH\text{-}CH_2\text{-}CH_2\text{-}N(CH_3)\text{-}CH_2\text{-}CH_2\text{-}OH$

Important available data in use for thermodynamic SAFT-type models are vapor pressures and liquid densities, but for the three alkanolamines the range of the typically used DIPPR correlations are much more extended than the actual experimental data from which the correlations were estimated. This is a limitation and care should be exercised in the regression.

The purpose of this work is to investigate the applicability of CPA to alkanolamines. The investigation is considered a first-step approach, i.e. how far can we reach under certain simplifying assumptions. No special treatment of polarity is used, only the association term of CPA/SAFT. Existing association schemes, like 2B and 4C will be used [5] without distinguishing the difference of N and O in MEA, while the N in DEA and MDEA will be ignored. No intramolecular association will be considered either.

Parameter Estimation
The parameters were at first estimated, in the usual way, from pure component vapor pressure and liquid density data (P^s and ρ_l). As DEA and MDEA both contain two OH groups (like MEG and other glycols), the 4C scheme is used in agreement to the use of this scheme for glycols. MEA has one OH and one NH_2 groups, and both the 2B and 4C scheme are considered.

For MEA and DEA different parameter sets were obtained from the pure component data and additional data is therefore needed in order to determine the optimal sets. As discussed in previous

work (with glycols; Derawi et al. [6]) one way is to use LLE for the compound of interest and an inert compound e.g. n-alkanes. Such LLE data are available for MEA with n-heptane and benzene and for DEA with hexadecane. Figures 1-4 show the model correlation with parameter sets solely from P^s and ρ_l (MEA sets 1 and 3 and DEA set 1) and when these LLE data are also used (MEA sets 2 and 4 and DEA set 2)).

Figures 1 and 2 show the mutual solubility of MEA and n-heptane, where MEA has been modeled with the 2B and 4C scheme respectively. In both cases it is not possible to match the experimental data satisfactorily with the parameters estimated from vapor pressure and liquid density only by fitting an interaction parameter. The association energy in parameter sets 2 and 4 were therefore fitted to this system simultaneously with the interaction parameter which resulted in a good match to the experimental data.

Figure 3 shows the results for MEA-benzene using the 4C parameter set for MEA obtained from the previous system. It is possible to match one of the solubilities when an interaction parameter is fitted, but it is necessary to also fit the cross-association volume (BETCR) in order to match both solubilities satisfactorily (modified CR-1 rule).

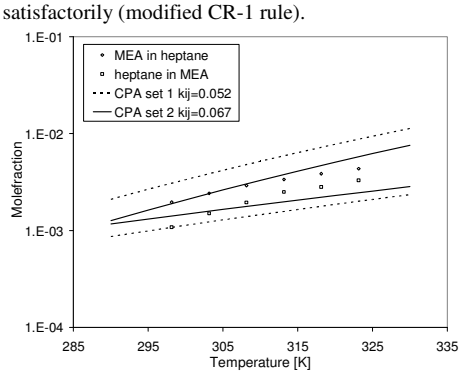

Figure 1: MEA – n-heptane LLE with the 2B scheme for MEA and a fitted $k_{ij.}$

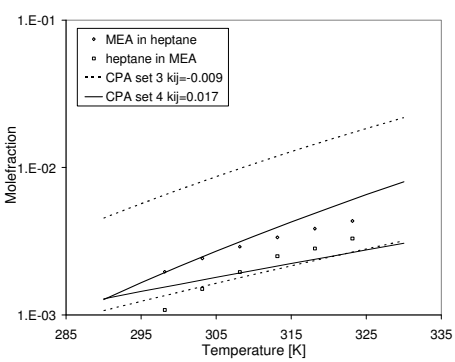

Figure 2: MEA – n-heptane LLE with the 4C scheme for MEA and a fitted k_{ij}.

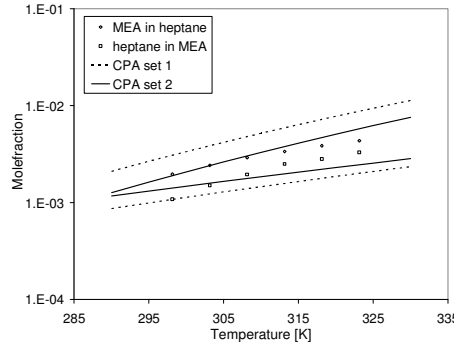

Figure 3: MEA – benzene LLE with set 4 (4C) for MEA.

Figure 4 shows the results for the DEA-hexadecane system. As for the MEA LLE it was necessary to fit the association energy to the system to obtain satisfactory results.

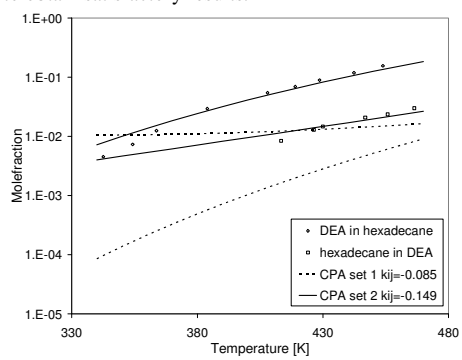

Figure 4: DEA – hexadecane LLE, with an optimal interaction parameter.

Based on the results for these systems the following was concluded:

- Use of LLE data is of imperative importance in the parameter selection
- The 4C scheme for MEA performs better than 2B and thus all three alkanolamines are treated as 4C molecules
- The MEA-benzene LLE is satisfactorily represented by accounting for the solvation in a way similar to glycols or water with aromatics using the modified CR-1 combining rule (Folas et al. [7]).

For MDEA it was not possible to estimate parameters from vapor pressure/liquid density data alone, and no LLE data for MDEA-alkanes is available. The Kamlet-Taft solvatochromic parameters (Table 1) indicate that the association should be similar to DEA, and thus using the association parameters of DEA, the three other parameters of MDEA could be estimated.

Table 1: Kamlet-Taft solvatochromic parameters for the three alkanolamines investigated in this work [8]. α indicates the acidity and β the basicity.

	MEA		DEA		MDEA	
T [K]	α	β	α	β	α	β
298.15	0.40	0.72	0.59	0.68	0.53	0.59
323.15	0.39	0.73	0.61	0.65	0.49	0.61
348.15	0.39	0.71	0.58	0.67	0.46	0.60

A single system with an inert compound for MDEA, MDEA-methane, was used for validation and very good results were obtained with a temperature-independent k_{ij} as can be seen in Figure 5.

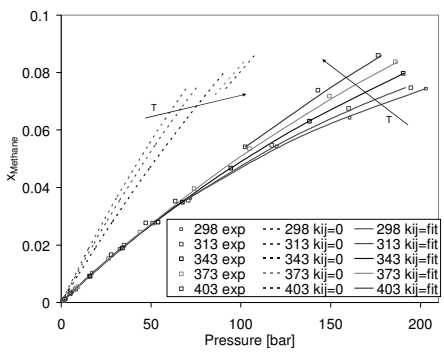

Figure 5: MDEA – methane VLE, with $k_{ij} = 0$ and a fitted $k_{ij} = 0.164$.

The figure shows that CPA predicts ($k_{ij} = 0$) a wrong temperature dependency for this system, and that this is corrected, when a temperature-independent interaction parameter fitted at T = 298.15 K is used

Cross-Associating mixtures VLE

CPA was then applied to binary VLE for cross-associating mixtures containing alkanolamines especially with water. Such systems are of importance, for practical purposes as intermediate stage in the application of the model to CO_2 or H_2S-water-alkanolamines, but also from a scientific point of view and for validating the model.

Figures 6-8 present some of the results obtained for each of the three alkanolamines.

Figure 6 shows MEA-water VLE at T = 298 K, with the 4C parameter set estimated using LLE data for MEA – n-heptane. The figure shows results for two different combining rules for the association parameters; CR-1 and ECR (Elliott rule).

It is evident from the figure that CR-1 performs better than ECR for this system, both for $k_{ij} = 0$ and with a fitted k_{ij}, and with a smaller absolute value of the interaction parameter. This was found to be the case for all the three alkanolamine-water systems, while the two combining rules perform similar for the other cross-associating system investigated, MEA-ethanol.

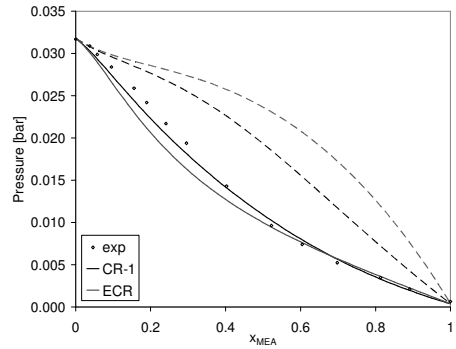

Figure 6: MEA – water VLE at T = 298.15 K, with set 4 for MEA. Dashed line: prediction ($k_{ij} = 0$), solid line: fitted k_{ij}; -0.165 for CR-1 and -0.249 for ECR.

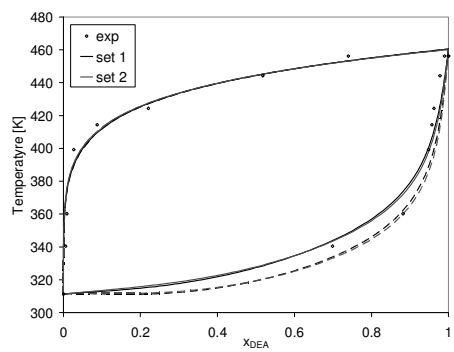

Figure 7: DEA – water VLE at P = 0.0667 bar. Dashed line: prediction ($k_{ij} = 0$), solid line: fitted k_{ij}; -0.15 for set 1 and -0.12 for set 2.

Figure 7 shows the results for DEA-water VLE with each of the two estimated parameter sets. The figure clearly shows that the two sets perform very similarly and with similar values of the interaction parameter. This confirms that several parameter sets satisfactorily can match VLE data, and that LLE data therefore is very important in the parameter estimation in order to determine the most correct parameter set.

The results for MDEA-water at P = 0.400 bar are shown in Figure 8, with the parameters for MDEA obtained using the association parameters for DEA.

The figure shows that CPA matches the experimental values very accurately, even with $k_{ij} = 0$.

Because of some computational problems it was not possible to do simulations at very small water concentrations for this system.

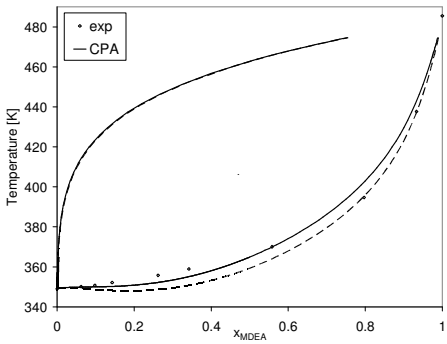

Figure 8: MDEA – water VLE at P = 0.400 bar. Dashed line: prediction (k_{ij}=0), solid line: fitted k_{ij}.

In general CPA performs satisfactorily for this type of systems using a temperature-independent interaction parameter. The predictive performance is however poor and large negative values of the interaction parameter are usually needed.

The conclusions for cross-associating systems, presented here, are in good agreement with results for similar systems previously obtained with CPA [2-4].

Conclusion

The CPA EoS has been applied to three alkanolamines (MEA, DEA, MDEA) as well as to cross-associating mixtures with water and ethanol. The investigation showed that vapor pressures and liquid densities were not sufficient for obtaining reliable parameters, but that at least one other type of information is needed. Moreover some problems in the parameter estimation were found to be caused by the uncertainty in some of the data.

The 4C association scheme proved to be the best choice for MEA, and was also used with success for DEA and MDEA.

A temperature independent interaction parameter gave satisfactory results for LLE and for alkanolamine-water VLE. Large negative values were, however, typically needed for the interaction parameter in the later case, which is in agreement with previous results for other aqueous cross-associating mixtures, e.g. water-alcohols and water-glycols

Future Work

The work presented here was carried out during my Master of Science project. Future work during my Ph.D. project will contain a more fundamental study of the theory used in this work, the association theory of Wertheim. The work will focus on the limitations of the theory, and on where the model can be improved.

Acknowledgements

The author wishes to thank the Technical University of Denmark for funding the Ph.D. project.

The author wishes furthermore to thank Georgios Kontogeorgis and Michael Michelsen for their supervision.

References

1. G.M. Kontogeorgis, E.C. Voutsas, I.V. Yakoumis, D.P. Tassios, Ind. Eng. Chem. Res. 35 (1996) 4310-4318.
2. G.K. Folas, J. Gabrielsen, M.L. Michelsen, E.H. Stenby, G.M. Kontogeorgis, Ind. Eng. Chem. Res, 44 (2005) 3823-3833
3. S.O. Derawi, G.M. Kontogeorgis, M.L. Michelsen, E.H. Stenby, Ind. Eng. Chem. Res, 42 (2003) 1470-1477
4. M. Kaarsholm, S.O. Derawi, M.L. Michelsen, G.M. Kontogeorgis, Ind. Eng. Chem. Res, 44 (2005) 4406-4413
5. S.H. Huang, M. Radosz, Ind. Eng. Chem. Res., 29 (1990) 2284-2294.
6. S.O. Derawi, M.L. Michelsen, G.M. Kontogeorgis, E.H. Stenby, Fluid Phase Equil., 209 (2003) 163-184.
7. G.K. Folas, G.M. Kontogeorgis, M.L. Michelsen, E.F. Stenby, Ind. Eng. Chem. Res., 45 (2006) 1516-1526.
8. A.F. Lagalante, M. Spadi, T.J. Bruno, J. Chem. Eng. Data, 45 (2000) 382-385.

Niels Bech
Phone: +45 4525 2851
Fax: +45 4588 2258
E-mail: nsb@kt.dtu.dk
WWW: http://www.chec.kt.dtu.dk
Supervisors: Kim Dam-Johansen
Peter A. Jensen

PhD Study
Started: September 2004
To be completed: February 2008

In-Situ Flash Pyrolysis of Straw

Abstract
Energy derived from straw remains a largely untapped energy resource offering a significant potential in the cereal-growing parts of the world. The main barrier for introducing straw to the energy market competitively is its higher cost relative to fossil fuels. The thermochemical process Flash Pyrolysis is capable of converting straw to an attractive liquid fuel. This project focuses on developing an ablative flash pyrolysis process specifically targeted for the production of heavy fuel substitute Bio-oil from straw.

Introduction
Bioenergy in the form of straw represents a significant energy source on a world-wide scale but is today largely unutilized. According to FAO [1], the aggregate world production of cereals including barley, mixed grains, oats, rye sorghum, triticale and wheat amounted to 814 million tons in 2003 of which wheat constituted close to 70%. Geographically, the most significant wheat production areas were Western Europe (17%), North America (16%), India (12%) and the former USSR (12%). Assuming a straw/grain ratio equivalent to the Danish average for 1994-1996 of 40% [2] and straw availability for energy to be 50%, these areas potentially have a virtually untapped energy reserve equivalent to 40 mill. tons (approx. 215 mill. barrels) of heavy fuel originating from wheat. For 2003, this amount of energy corresponded to 8 days of OPEC crude oil production (27 mill. barrels/day) [3] or a market value close to $13 bill. For the net energy importing areas (*i.e.* North America, Western Europe and India), utilization of straw for energy production is thus a CO_2 neutral prospect to gain more independence from the historically less stable oil exporting regions.

Unfortunately, straw does not posses the attractive properties that crude-oil products do such as a relatively high volumetric energy content, good transportability, standardized specifications and simplicity in use. The result is that utilization of straw is only practiced under primitive conditions where it is readily available or where massive public subsidies or regulation warrant it. Apart from the unresolved problems in handling combustion of raw straw, the expense associated with logistics (*e.g.* baling, storage and transport) is the single largest barrier for utilizing straw efficiently in competition with fossil fuels under free market conditions. Access to an uninterrupted supply of fuel is also of importance to energy consumers and accordingly, expenses arising from long-distance transport of straw-derived energy need to be insignificant compared to the value of the fuel itself in order to market the product successfully.

Specific Objectives
Flash pyrolysis is a thermochemical process which under conditions of medium temperature and short residence time converts organic materials to char, tar and gas. Tar, a homogeneous mixture of organics and water commonly referred to as Bio-oil, is a highly compressed energy carrier and may be used in the existing combustors and distribution systems for fossil heavy fuel, while gas can be utilized for process heat.

For straw, the yields of Bio-oil, char and gas are approximately 50, 30 and 20% on dry weight basis [4]. Straw is a relatively inexpensive material provided baling and transportation are not needed. This implies that capital cost is of higher importance for in situ conversion and the development of a high capacity compact reactor system for mobile operation (*c.f.* [5]) is a cardinal point. Accordingly, the main objective of the project is to identify a suitable reactor system and optimize its performance.

Reactor System

Fluid beds and ablative reactors are the two principal technologies available for flash pyrolysis. In the former, biomaterial is introduced into a bed of hot fluidized inert material, usually sand. Although a well-known technology, fluid beds do have several disadvantages including the requirement for a large flow of inert gas for heat transport and fluidization, a relatively poor capacity/volume ratio and the need for small particle size feed. Therefore, the project focuses on developing and optimizing an ablative process for straw flash pyrolysis.

Figure 1 depicts the reactor which has been specifically developed for this project. Straw in the form of rolled and sieved straw pellets are introduced by a screw feeder into a horizontal heated tube. Here, a three-blade rotor with close clearance to the reactor wall provides rotation to the gas phase and in turn the straw particles.

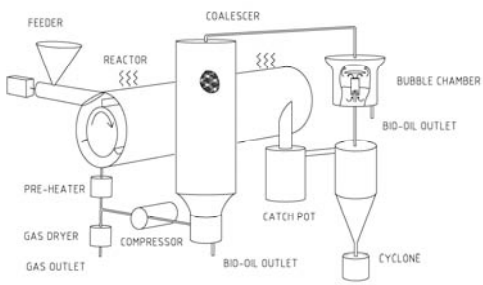

Figure 1: Schematic diagram of the developed ablative pyrolysis bench reactor system.

The residence time in the reactor for the evolved gasses is controlled by means of a recirculation compressor. Liquids are condensed by passing the gasses through a cool pool of Bio-oil after char particles have been removed in the catch pot and cyclone. Aerosols are collected to droplets in a coalescer and removed by gravity. Before the gas is metered, it is cooled to ambient temperature in order to remove water. Gas for recirculation is preheated in order to avoid condensation of liquid products within the reactor. Further details of the reactor are available elsewhere [6].

Modelling

When a particle undergoes pyrolysis in the ablative regime the degradation will take place as surface reaction. Under these conditions the energy transported to the surface will balance the requirement for heating the material to the reaction temperature. This phenomenon has been modelled in order to describe the reaction temperature of the particle as a function of reactor parameters (*e.g.* reactor temperature and rotor speed), material properties and particle conversion.

Degradation of the particle is treated as a pseudo-surface reaction even though, strictly speaking, the reaction may not exclusively proceed on the surface. For ablative pyrolysis, the steep temperature gradient observed experimentally (*e.g.* [7]) combined with a reaction rate which is strongly dependent on temperature suggest, that reaction is concentrated in a relatively thin shell near the surface. This approach is inspired by the study of Lédé [8] for slab geometry.

In order to predict the distribution of reaction products, the surface temperature of the reacting particle may be combined with an appropriate kinetic model. Figure 2 displays a common kinetic model employed in flash pyrolysis, a modified version of the Broido-Shafizadeh model [9-11], where the products have been lumped according to their physical properties at standard conditions. Detailed information on the model can be found elsewhere [12, 13].

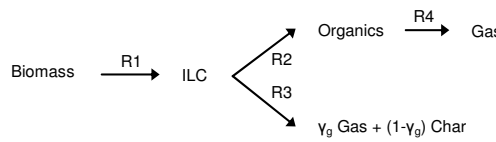

Figure 2: Broido-Shafizadeh model for prediction of yield distribution.

The modeling results reported with lines in figure 3 show the limits of a credible interval located centrally around the model prediction. This interval was established by measuring twice the standard deviation for five runs at 550 ºC and a centrifugal force of $1.7 \cdot 10^4$ g.

Table 1 – Physical and kinetic parameters used in the simulation.

Parameter	*Value*	*Unit*	*Ref.*
Particle shape	Sphere	-	[14]
Mean Diameter	$633 \cdot 10^{-6}$	m	[14]
Density	700	kg m^{-3}	[15]
Heat capacity	2446	J kg^{-1} K^{-1}	[15]
Conductivity	0.21	W m^{-1} K^{-1}	[15]
A_1	$2.8 \cdot 10^{19}$	s^{-1}	[16]
E_1	206	kJ mol^{-1}	Fitted
A_2	$6.79 \cdot 10^{9}$	s^{-1}	[16]
E_2	140	kJ mol^{-1}	[16]
A_3	$1.30 \cdot 10^{10}$	s^{-1}	[16]
E_3	143	kJ mol^{-1}	Fitted
A_4	$4.3 \cdot 10^{6}$	s^{-1}	[17]
E_4	108	kJ mol^{-1}	[17]
γ_g	0.65	-	[18]

Experimental

Crushed wheat straw pellets were treated in the reactor system depicted on figure 1. Table 2 displays the main properties of the feed material and the static conditions employed throughout the runs. It is noted that solid residence time depends on rotor speed as was established by direct measurement in a glass reactor operated without heat. Reactor wall temperature and centrifugal force (G, expressed in units of gravity) was

Table 2 – Experimental conditions.

Parameter	*Value*	*Unit*
Ash	6.8	% db.
Moisture	5.8	% wt.
Volatile matter	75	% db.
Solid feed rate	23	g min^{-1}
Feed Time	14	min
Gas recycle temperature	400	ºC
Gas residence time	0.6±0.3	s
Particle Residence time		
@ G=4.9·10³	2.8±0.3	s
@ G=1.0·10⁴	3.3±0.3	s
@ G=1.7·10⁴	6.0±0.3	s

varied between runs and the influence on the yield of principal products recorded and reported in Figure 3.

Results and Discussion

When fitting the model it was assumed that the higher ash content in the wheat straw has a pronounced catalytic effect on the pyrolytic reactions favoring the formation of char and gas [19] by reducing the activation energies of the affected reactions. Accordingly, the distribution between char and gas (γ_g) and the pre-exponential factors were left equal to those of the original cellulose kinetic model, whereas the gas phase cracking of tar was assumed to be unaffected by the ash content which largely stays in the solid state for the investigated temperature domain. Furthermore, as the distribution between gas/char and organics can be described by one parameter, the activation energy for R2 was kept unchanged for simplicity. Fitting the remaining two activation energies for R1 and R3 simultaneously to the three investigated rotor speeds visually, the result shown in figure 3 were obtained. Although the predictive power of the model was somewhat reduced compared to when applying the cellulose model to pine (not shown), reducing the activation energies by 14 % and 4.5 %, respectively, produced an acceptable fit but could likely be improved by investigating the kinetics for straw in more detail.

From the experimental results it is noted that the maximum yield of organics did not change significantly with increasing centrifugal acceleration which merely lowered the optimum temperature. From figure 4 it can be noted that increasing G above approximately $5 \cdot 10^3$ has only a moderate effect on organics yield and that 90 % of the yield at $G=3.0 \cdot 10^4$ is obtained at $G=1.0 \cdot 10^4$. However, assuming that the surface loading (or average particle-particle distance) is independent of rotor speed, the decreasing conversion time with rotor speed will result in a progressively higher area-specific throughput as demonstrated (full line) for particles of MMD. Consequently, increasing the centrifugal acceleration above the domain investigated is not expected to contribute significantly to the yield of organics but is predicted to increase throughput.

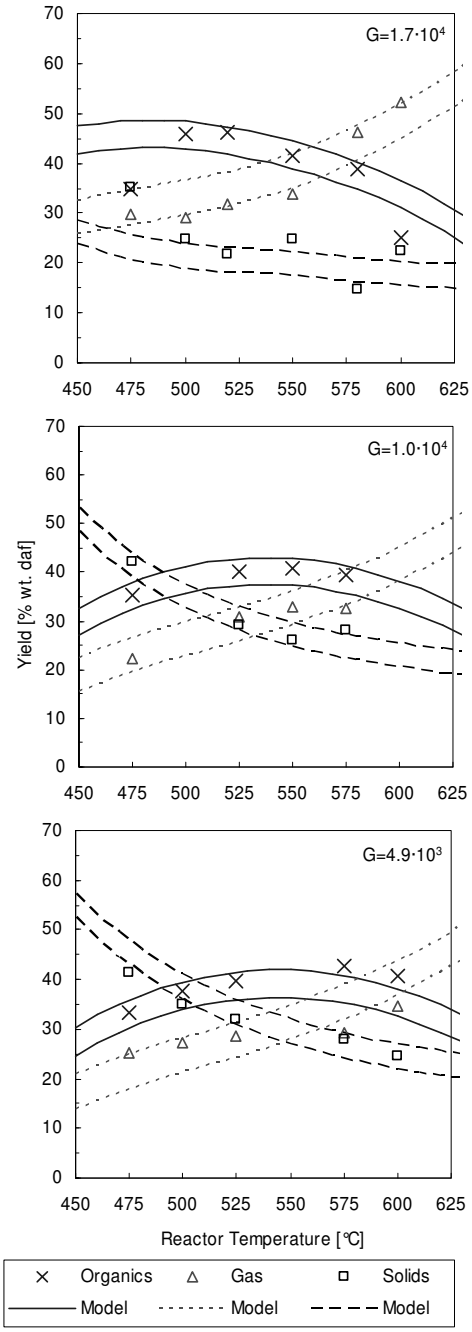

Figure 3: Experimental results (symbols) and model predictions for yield of main fraction with reactor temperature for wheat straw pyrolysis at three centrifugal accelerations. Only credible interval shown for model predictions.

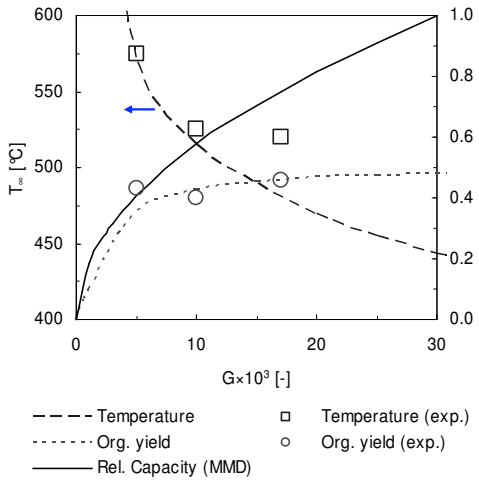

Figure 4: Simulated optimum reactor temperature (T_∞, broken line) needed to maximize organics yield (Y_o, dots) with centrifugal acceleration compared with experimental results (symbols). Full line shows simulated relative reactor capacity with centrifugal acceleration for straw particles of MMD.

Conclusions

A bench reactor system to study the ablative pyrolysis of straw has been constructed and a model to predict the fate of a particle submitted to the environment of the reactor has been developed. An acceptable fit to the straw experimental results was obtained with the model by employing modified cellulose data with the Broido-Shafizadeh kinetic scheme. Experimental results backed by modeling showed that increasing centrifugal acceleration above $5.0 \cdot 10^3$ g had only a moderate effect on organics yield but did lower the optimum reactor temperature. However, the model predicted that increasing the applied centrifugal acceleration will increase reactor throughput.

Acknowledgements

CHEC is financially supported by the Technical University of Denmark, DONG Energy A/S, Vattenfall A/S, FLSmidth A/S, Hempel A/S, Energinet.dk, the Danish Research Council for Technology and Production Sciences, the Danish Energy Research Program, Nordic Energy Research, EU and many industrial partners. This particular project is financed by the DTU Innovation Program and the Nordic Energy Research Program.

References

1. FAOSTAT data, last accessed December 2004.
2. Handbook for Farm Management (in Danish), Landbrugsforlaget, Aarhus, 2003.
3. OPEC Annual Statistical Bulletin 2003, OPEC, Vienna, 2004.
4. Bech, N. In-Situ Flash Pyrolysis of Straw. In: Dam-Johansen, K., Skjøth-Rasmussen M.S. (eds.), Graduate Schools Yearbook 2004, Dept. of Chemical Engineering, DTU, Kgs. Lyngby, 2004, 13-14.
5. Bech, N., Dam-Johansen, K. PCT Application WO 2006/117006. Geneva: World Intellectual Property Organization, 2006.
6. Bech, N., Jensen, P.A., Dam-Johansen, K. PCT Application WO 2006/117005. Geneva: World Intellectual Property Organization, 2006.
7. Lédé, J., Panagopoulos, J. Li, H.Z., Villermaux, J. Fuel, 64, 1985, 1514-1520.
8. Lédé, J. Biomass Bioenerg., 7, 1994, 49-60.
9. Bradbury, A.G.W., Sakai, Y., Shafizadeh, F. J. Appl. Polym. Sci., 23, 1979, 3271-3280.
10. Di Blasi, C. Biomass Bioenerg., 7, 1994, 87-98.
11. Lédé, J. Ind. Eng. Chem. Res., 39, 2000, 893-903.
12. Bech, N. In-Situ Flash Pyrolysis of Straw. In: Dam-Johansen, K., Bøjer, M. (eds.), Graduate Schools Yearbook 2006, Dept. of Chemical Engineering, DTU, Kgs. Lyngby, 2006, 15-20.
13. Bech, N., Larsen, M.B., Jensen, P.A., Dam-Johansen, K. Modeling Ablative Flash Pyrolysis of Straw and Wood in the Pyrolysis Centrifuge Reactor. Submitted for publication, 2007.
14. Bech, N., Jensen, P.A., Dam-Johansen, K. Proc 15th European Biomass Conference and Exhibition, Berlin, 7-11 May, 2007 (in press).
15. Jensen, P.A., Sander, B., Dam-Johansen, K. Biomass Bioenerg., 20, 2001, 431-446.
16. Diebold, J.P. Bioenerg, 7, 1994, 75-85.
17. Liden, A.G., Berruti, F., Scott, D.S. Chem Eng Comm, 65, 1988, 207-21.
18. Di Blasi, C. Biomass Bioenerg, 7, 1994, 87-98.
19. Fahmi R, Bridgwater AV, Darvell LI, Jones JM, Yates N, Thain S et al. Fuel 86, 2007, 1560-69.

Søren Prip Beier

Phone: +45 4525 2955
Fax: +45 4525 2258
E-mail: spb@kt.dtu.dk
WWW: http://www.kt.dtu.dk
Supervisor: Gunnar Jonsson
gj@kt.dtu.dk

PhD Study:
Started: September 2005
To be completed: August 2008

Vibrating Dynamic Microfiltration

Abstract
The work in this Ph.D. project is focused on testing alternative ways of saving energy in microfiltration and enhancing transmission of macromolecules through microfiltration membranes. The majority of the experimental work is conducted with a vibrating microfiltration set-up with a hollow fiber membrane module. Till now it is clearly shown that the extent of membrane fouling is reduced by vibrations. Furthermore, the necessary transmembrane pressure is very low and the transmission of macromolecules is almost complete when the system is operated below a certain critical flux level. This could be useful in the recovery of macromolecules directly from fermentation broth.

Introduction
A huge problem when processing solute containing chemical, biochemical, pharmaceutical and waste water suspensions using microfiltration is the fouling of the membrane surface and pores. I) The fouling increases the hydraulic resistance of the membrane module leading to an increase of transmembrane pressure necessary for maintaining a certain flux level. The extent of surface fouling can be reduced by increasing the cross-flow velocity tangentially to the membrane surface. However, this approach is quite expensive due to a high power consumption of the feed suspension pump. II) Furthermore, the fouling layer on the membrane surface and inside the pores can change the pore size distribution of the membrane resulting in a dramatic change in the possibility of transmitting for example macromolecules through the membrane.

Our microfiltration set-up (Figure 1) is constructed to deal with both problems. I) The necessary pumping energy is eliminated because the shear on the membrane surface is disconnected from the feed suspension velocity by vibrating the membrane module. II) The reduction of fouling on the membrane surface and inside the pores by the vibrations more or less maintains the pore size distribution of the membranes, compared to that of the beginning of the filtration. Thus, an initial high transmission of for example macromolecules can be sustained as long as the flux is kept below a certain critical flux level.

Experimental:
A sketch of our vibrating microfiltration apparatus is shown in Figure 1.

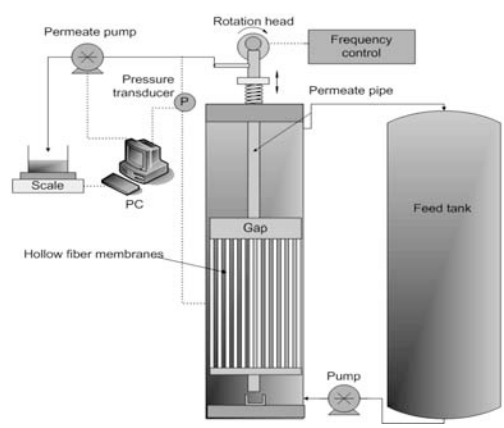

Figure 1: Sketch of the vibrating dynamic microfiltration set-up.

The core of the system is the membrane module itself. The module consists of asymmetric microfiltration hollow fibers with the skin layer on the outside, as seen in Figure 2. The permeate peristaltic pump creates a lowered pressure inside the module (permeate pipe, gap

and inside fibers). Thus, permeate is sucked through the fibers to a beaker on a scale, connected to the PC, measuring the flux. This means that the flux is logged and kept constant and the corresponding transmembrane pressure is monitored and logged as well.

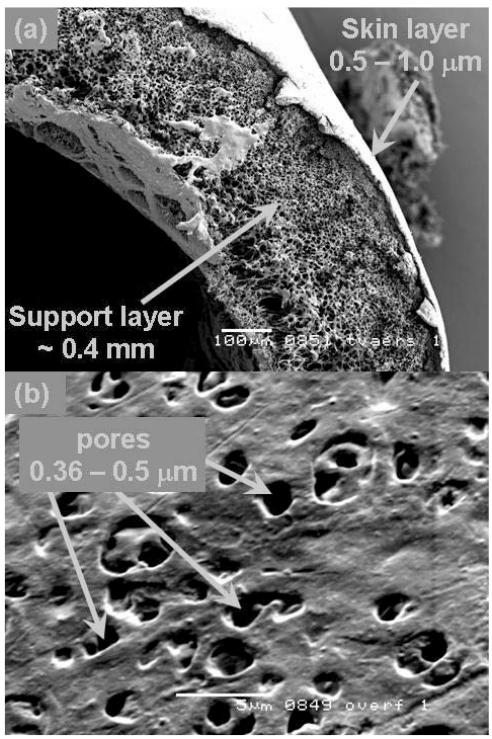

Figure 2: SEM pictures of a hollow fiber microfiltration membrane. (a) Cross sectional cut of a single fiber. (b) Surface of a fiber.

The whole membrane module is vibrated up and down at variable frequency and amplitude by the "rotation head". The feed suspension is circulated between the feed tank and the module cylinder at a very low pumping rate corresponding to a velocity below 1 cm/s in the module cylinder.

Results

When operating a microfiltration device it is advantageous to keep the flux below a certain critical flux level. Above this level membrane fouling becomes severe. Below, the fouling and fouling rate is more of less controlled and the flux and transmembrane pressure is thus sustainable.

We have shown that the critical flux is very dependent on the hydrodynamics. The difference between the fouling rate of a vibrating and a non-vibrating membrane module is quite marked [1]. The critical flux varies with the average surface shear rate as a power function for bakers yeast suspensions [2,3] and for suspensions containing macromolecules [4]. Thus, higher degree of module vibrations yields higher critical fluxes. When operating below the critical flux we have achieved almost 100 % transmission of macromolecules from a bakers yeast suspension which is almost a complete separation of cellular material and macromolecules [4]. Furthermore, we have shown that the level of extracellular polymeric substances from the yeast cells in the bulk suspension differs below and above the critical flux [5]. Finally we have investigated the effect of static adsorption of macromolecules on membrane surfaces [6]. The relatively tight chemical static adsorption is not avoided by vibrations. However, it is the more loosely bounded membrane fouling onto the adsorbed monolayer that is markedly reduced by module vibrations.

Conclusions

Enhancing the surface shear rate is a known way of minimizing and controlling membrane fouling. We have shown that we are able to decouple the normal connection between enhanced surface shear rate and feed suspension velocity by vibrations. Thus, the feed velocity can be kept very low and fouling of the membrane module is reduced by vibrations. Furthermore, we have shown that we are able to separate cellular material and macromolecules with almost 100 % transmission of macromolecules so that the system actually operates as microfiltration. This could be advantageous in the recovery of macromolecules directly from fermentation broth.

References/List of publications

1. S.P. Beier, G. Jonsson, En rystende filterforklaring, Dansk Kemi 10 (2007) 12-15.
2. S.P. Beier, G. Jonsson, M. Guerra, A. Garde, Dynamic Microfiltration with a Vibrating Hollow Fiber Membrane Module; Filtration of Yeast Suspensions, J. Membr. Sci. 281 (2006) 281-287.
3. S.P. Beier, G. Jonsson, Dynamic Microfiltration with a Vibrating Hollow Fiber Membrane Module, Desalination 199 (2006) 499-500, Presented at EUROMEMBRANE 2006, 24-28 September 2006, Giardini Naxos, Italy.
4. S.P. Beier, G. Jonsson, Separation of Yeast Cells and Enzymes with a Vibrating Hollow Fiber Membrane Module, Sep. Purif. Technol. 53 (2007) 111-118.
5. S.P. Beier, G. Jonsson, A Vibrating Membrane Bioreactor Operated at Supra- and Sub-critical Flux: Influence of Extracellular Polymeric Substances From Yeast Cells, Proceedings of European Congress of Chemical Engineering (ECCE-6) Copenhagen, 16-20 September 2007.
6. S.P. Beier, A.D. Enevoldsen, G.M. Kontogeorgis, E.B. Hansen, G. Jonsson, Adsorption of Amylase Enzyme on Ultrafiltration Membranes, Langmuir 23 (2007) 9341-9451.

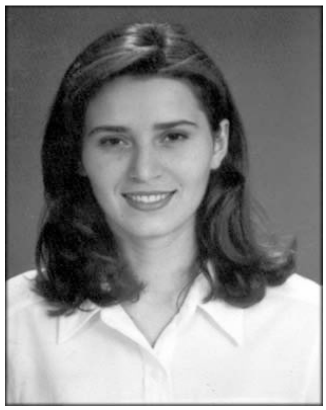

Suzan Biran

Phone: +45 4525 2920
Fax: +45 4588 2258
e-mail: sb@kt.dtu.dk
www: http://www.chec.kt.dtu.dk
Supervisors: Anker Jensen
Søren Kiil
Poul Bach, Novozymes A/S
Ole Simonsen, Novozymes A/S

Ph.D. Study
Started: September 2003
To be completed: January 2008

Stability of Enzymes in Granular Enzyme Products for Laundry Detergents

Abstract
Enzymes are important constituents in laundry detergents due to their contribution to a more effective and milder washing process (lower energy and water consumption, less wear of fabric). Storage stability of detergent enzymes is a significant quality parameter considered in the development of a new product. The complexity of the detergent matrix implies the presence of a complicated mechanism involved in the inactivation. It is believed that a combination of factors such as humidity, released H_2O_2, autolysis of enzymes, high local pH in the granule, oxygen, defects in granulate structure and other detergent components plays a role in the activity loss. The aim of this project is to investigate the factors responsible for the inactivation of enzymes and propose new formulations and protective components for improved stability.

Introduction
Enzymes are used today in a wide range of industrial processes and in consumer products. The largest application of industrial enzymes is in detergents. The detergent industry absorbs about 45% of enzyme sales in western Europe and more than 25% of the total worldwide enzyme production [1]. After being produced by submerged microbial fermentation, enzymes are recovered and sold as either powder or liquid products for industrial use. In powdered laundry detergents, they are granulated and covered with a protective coating to prevent dust allergies and increase the stability of enzymes.

The main enzyme activity in biological laundry detergents is protease, which acts on organic stains such as grass, blood, egg and human sweat. However, it has become more common in recent years to include a "cocktail" of enzyme activities including lipases and amylases. Lipases are effective on stains resulting from fatty products such as oils and fats, while amylases help remove starchy food deposits. More recently, color enhancing and "anti-bobbling" washing powders have been developed which contain cellulases. The mode of action of such cellulases is to remove detached cellulose fibrils, which cause a progressive dulling of the color as dirt is trapped on the rough surface of the fabric.

Laundry detergents typically consist of a mixture of separate granular materials including surfactants, buil ders, bleaching agents and enzymes. The surfactants are the main cleaning agent, while the builders provide alkalinity and ionic strength to the wash liquor. Bleaching agents are added to provide a white shine and remove stains on the fabric. A modern bleaching agent is Sodium Percarbonate (SPC), which decomposes in water and releases hydrogen peroxide, being the actual bleaching chemical. In addition to these, powdered laundry detergents contain soil anti-deposition polymers, anti-corrosion agents, perfumes etc.

Enzymes are fragile biomolecules. They can loose their activity in environments, like detergents, where harsh chemicals are present. In practice the enzymes loose a significant part of their activity over a time period of several weeks. To overcome this problem, manufacturers prefer to add more enzyme granules in their products to have satisfactory wash performance. However, this results in an increase in the production cost of the laundry detergent. Partly to obtain a better stability during storage, the enzyme containing particles are typically coated by layers of salts, polymers and/or waxes. This reduces the rate of diffusion of aggressive species into the particles where reaction with the enzymes may cause deactivation. Furthermore, the particles are often formulated with anti-oxidants, such as thiosulfates, to minimize deactivation reactions. For the enzymes in laundry detergents, the deactivation is mainly related to the release of hydrogen peroxide from the bleaching chemicals in a moisture-containing atmosphere. Moreover, humidity, autolysis of enzymes,

high local pH in granule, oxygen, defects in granulate structure and other detergent components are some of the factors affecting the granulate stability during storage.

The present understanding of inactivation mechanism of detergent enzymes during storage [2] involves diffusion of water vapor through bleaching particles, where SPC is "activated" and hydrogen peroxide is released. The subsequent diffusion of hydrogen peroxide vapor in the enzyme granule results in oxidation of the enzyme. The fact that enzyme activity is reduced significantly even in non-bleach containing detergents implies that other mechanism(s) are also involved in deactivation of granulates.

Specific Objectives

The objective of this project is to understand the inactivation mechanism of detergent enzymes during storage. It is also aimed to investigate the effect of different detergent ingredients on the granulate stability. According to the new findings, the previously proposed mechanism can be confirmed or modified. In light of the results, new stability-enhancing components or coatings will be proposed and tested for their efficiency in reducing enzyme deactivation in powdered detergents.

Experimental Setup

The set up (Figure 1) provides controlled conditions of H_2O_2 (g) concentration, humidity and temperature. H_2O_2 (g) is generated by bubbling N_2 through a concentrated solution of H_2O_2. Relative humidity (RH) of the gas stream is adjusted by bubbling N_2 through distilled H_2O at appropriate temperature. Further tuning of the H_2O_2 level and moisture is done by a third stream of N_2. Enzyme sample is placed in a column where quartz wool serves as a support material. A gas stream is passed through the column, where freeze-dried Savinase is in direct contact with the flowing gas.

Selected Results and Discussion

Adsorption

Exposure of the enzyme powder to H_2O_2 vapor and humidity resulted in simultaneous adsorption of moisture and H_2O_2, water being physically and H_2O_2 being chemically adsorbed.

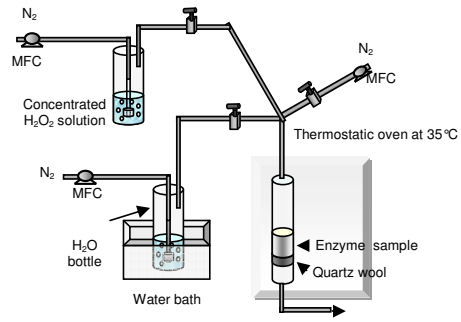

Figure 1: Sketch of the enzyme exposure setup

The effect of RH in the gas stream on the H_2O_2 adsorption was investigates. Figure 2 clearly illustrates that amount of H_2O_2 adsorbed by the sample was independent of the moisture in the system. Therefore, water and H_2O_2 were not competing for the same adsorption sites.

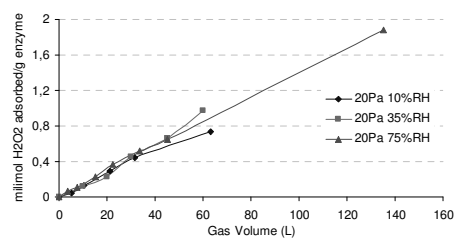

Figure 2: Effect of relative humidity on H_2O_2 adsorption at 35°C. Equal amounts of H_2O_2 were up taken independently of the moisture in the gas stream.

The variation of adsorbed H_2O_2 amount with respect to varying H_2O_2 partial pressures at constant humidity was also determined (Figure 3). As the concentration of H_2O_2 in the gas was increased, the adsorbed H_2O_2 by the enzyme sample also increased. Equilibrium was attained and limit adsorption value was reached provided enough exposure time.

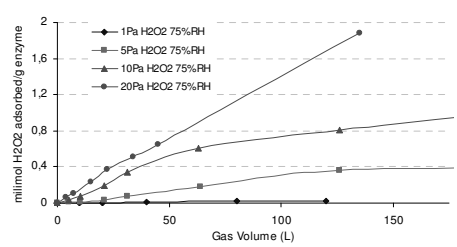

Figure 3: Effect of H_2O_2 (g) concentration on the adsorbed H_2O_2 by the enzyme at 35°C.

Enzyme inactivation

The inactivation kinetics of the freeze-dried Savinase was investigated as a function of H_2O_2 (g) concentration and relative humidity. The effect of H_2O_2 (g) on Savinase stability was studied at 10% and 75%RH. On Figure 4, the decrease in % residual activity is illustrated. At 10%RH conditions, the gradual increase in the extent of enzyme inactivation as H_2O_2 (g) concentration went from 0 to 20Pa could be noticed (Figure 4-a). At 75%RH, on the other hand, no matter the concentration, presence of H_2O_2 was enough to cause a drastic reduction in the Savinase activity (Figure 4-b). This implies that at high humidity conditions, enzymes became more susceptible to oxidation.

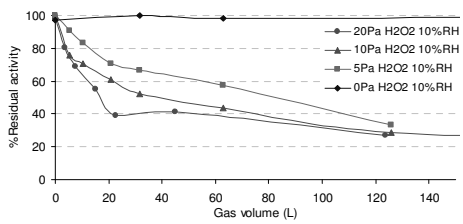

a)

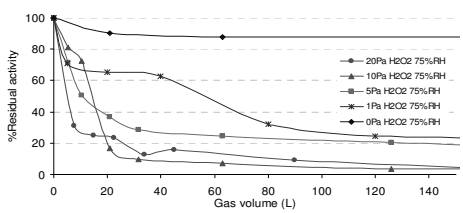

b)

Figure 4: Effect of increasing H_2O_2 (g) concentration on Savinase stability; a) 10%RH; b) 75%RH. At high humidity, presence of H_2O_2 has more detrimental impact on enzyme stability.

Effect of humidity

Dry proteinous products adsorb significant moisture when exposed to humid conditions. Experimental evidence shows that increased residual moisture results in a noticeable reduction in the stability of the product. The detrimental effect of moisture on storage stability is often interpreted in terms of mobility in the solid and reactivity of the protein. Above monolayer levels of water, protein's conformational flexibility is increased and the additional water has ability to mobilize the potential reactants in the amorphous phase. Both effects increase the rate of protein degradation [3]. The negative effect of increasing humidity on enzyme activity was illustrated by exposing the enzymes in the presence of H_2O_2 (g) with constant concentration (20Pa) (Figure 5). The high moisture content in the sample increased the mobility of the enzyme molecules and enhanced the oxidative effect of H_2O_2.

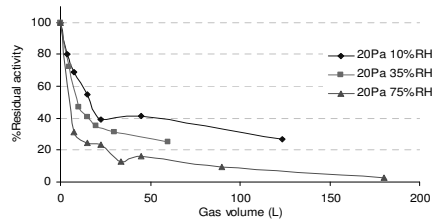

Figure 5: Effect of relative humidity on inactivation extent of the enzyme exposed to 20Pa H_2O_2. As the moisture in the sample increases, the loss of activity becomes more drastic

Moreover, residual activity results of samples exposed to high (75%) and low (10%) relative humidity showed that Savinase may loose part of its initial activity even in the absence of oxidizing agent (Figure 5 a- and b- 0Pa H_2O_2 samples). This was further studied by exposing the freeze-dried Savinase to extreme conditions, i.e. 100%RH and 80% of activity loss was measured. Samples were analyzed by sodium dodecylsulfate polyacrylamide gel electrophoresis (SDS-PAGE), where the proteins were unfolded and separated according to their molecular weight. No proteolytic activity was observed in the gel. The dehydration-rehydration studies of subtilisin conducted by De Paz *et al*. [4] also resulted in absence of proteolysis. In fact, Towns [5] stated that self-proteolysis is of minimal concern in solid-state protease formulations, because the inter-molecular reactions require a significant mobility to the segmental portions of the protein backbone. The exposure result of solid-state Savinase to an extreme humidity undoubtedly confirmed this statement.

Enzyme oxidation on molecular level

Stauffer and Etson [6] revealed the oxidation mechanism of a commonly studied protease, subtilisin, by H_2O_2. The enzyme was inactivated by the formation of methionine sulfoxide at position 222. Oxidized enzyme activity towards synthetic substrates decreased relative to native enzyme activity due to the proximity of Met 222 to the active site. Experimental evidence showed that activity decrease of the enzyme was accompanied by the oxidation of just 1 Met residue. Met-sulfoxide formation did not inactivate subtilisin completely but, depending on the substrate, the activity was reduced by 57 to 92%. The authors suggested the following mechanisms responsible for activity loss: a) oxidative modification of Met 222 might result in a conformational change in the protein structure; b) the alteration from a hydrophobic sulfide to a hydrophilic sulfoxide might alter the electronic environment around the active site sufficiently to affect the rate at which

individual reaction steps occur; c) the presence of 1 additional oxygen atom might have a conformational interference to the optimum interaction between substrate and enzyme molecules. Other oxidation studies described in the literature also involve utilization of H_2O_2 in a solution [6,7,8,9]. However, they do not reveal the impact of gaseous hydrogen peroxide released in the detergent box on enzyme stability during storage.

Alterations in the Savinase® structure (Figure 6) upon oxidation were studied with electrospray ionization mass spectroscopy. The results showed that as the exposure time increased the single oxidation product of the enzyme emerges and after 13h exposure time all native forms of the enzyme were completely oxidised. The position of oxidised residue was located by peptide mapping, where the mass of CNBr-cleaved fragments was determined by MALDI TOF mass spectroscopy. Solid evidence of Met 222 oxidation was obtained. The other two methionine residues present in Savinase® structure remained mainly unchanged. The result was further confirmed by examination of carbonyl group formation in H_2O_2-exposed samples, indicating that other residues in the protein backbone are not oxidized.

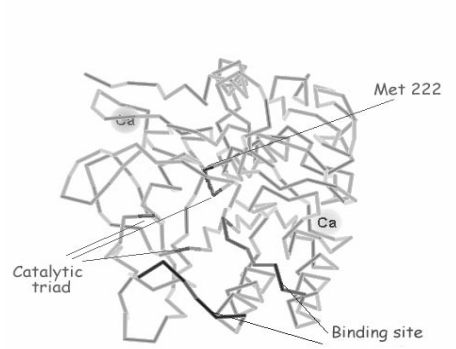

Figure 6: Structure of Savinase: the substrate binding site (blue), the catalytic triad (red), oxidation-sensitive residue Met 222 (purple)

Conclusions

An accurate method for the generation and measurement of low concentrations of hydrogen peroxide vapor was established. The experimental setup provides controlled conditions for the exposure of freeze-dried enzymes to different concentrations of H_2O_2 vapor and %RH. The effect of these factors is being studied for the determination of the inactivation kinetics of Savinase. The results showed that a combined action of moisture and H_2O_2 (g) is responsible for the inactivation of solid-state Savinase®. The noticeable decrease in enzyme activity at high humidity implied that moisture provoked the oxidizing effect of H_2O_2. In other words, adsorbed water increased the mobility and molecular volume of the protein chain and facilitated the diffusion of H_2O_2 (g) to the amino acid residues susceptible to oxidation. Peptide mapping studies revealed that oxidation of Met 222 is the primary cause for activity loss.

Acknowledgements

The Novozymes Bioprocess Academy is acknowledged for the financial support of this project.

References

1. Broze G. (Edr.), Handbook of Detergents, Part A: Properties, Surfactant Science Series Vol. 82, Marcel Dekker, Inc. New York, 1999, p.639.
2. Simonsen O. and Lagnemo H., 2001, Mechanism of Deactivation of Enzymes and Sodium Percarbonate (SPC) in HDP, *40th International Detergency Conference Proceedings*, 228-231.
3. Pikal M.J., 1994, Freeze-Drying of Proteins: Process, Formulation, and Stability , H*ACS Symposium Series* H, Vol. 567, 120-133.
4. DePaz, R.A., Dale, D.A., Barnett, C.C., Carpenter, J.F., Gaertner, A.L., Randolph, T.W., 2002, Effects of drying methods and additives on the structure, function, and storage stability of subtilisin: role of protein conformation and molecular mobility, *Enzyme and Microbial Technology*, 31, 765-774.
5. Towns J.K., 1995, Moisture content in proteins: its effects and measurement, *Journal of Chromatography A*, 705, 115-127.
6. Stauffer C.E. and Etson D., 1969, The effect on subtilisin activity of oxidizing a methionine residue, *The Journal of Biological Chemistry*, Vol. 244, Iss. 10, 5333- 5338.
7. DePaz R.A., Dale D.A., Barnett C.C., Carpenter J.F., Gaertner A.L., Randolph T.W., 2000, The excluding effects of sucrose on a protein chemical degradation pathway: methionine oxidation in subtilisin, *Archives in Biochemistry and Biophysics*, Vol. 384, No.1, 123-132.
8. Nguyen T.H., Burnier J., Meng W., 1993, The kinetics of relaxin oxidation by hydrogen peroxide, *Pharmaceutical Research*, Vol. 10, No. 11, 1563-1571.
9. Levine R.L., Mosoni L., Berlett B. S., Stadtman E.R., 1996, Methionine residues as endogeneous antioxidants in proteins, *Biochemistry*, Vol. 93, 15036-15040.

Rasmus Risum Boesen

Phone: +45 4525 2983
Fax: +45 4588 2258
E-mail: rrb@kt.dtu.dk
WWW: http://www.ivc-sep.dtu.dk
Supervisors: Nicolas von Solms
Michael L. Michelsen
Kim G. Knudsen, Haldor Topsøe A/S

PhD Study
Started: March 2007
To be completed: March 2010

Development of a Component-Based Reactor Model for a Distillate Hydrotreater

Abstract
Due to tightened specifications regarding the sulfur content of diesel, the hydrotreating process is getting increased attention. A better understanding of the kinetics of hydrodesulfurization of refractive sulfur compounds will be helpful in the development of new and more active catalysts, and in predicting the reactivity of different feedstocks. It is the purpose of this project to develop a reactor model based on the kinetics of individual components that can describe hydrodesulfurization kinetics at all conversions.

Introduction
All over the world the environmental legislations regarding the sulfur content of diesel has been tightened and are moving towards an ultra low sulfur diesel (ULSD) specification as low as 10 wt ppm S [1]. Sulfur is removed through hydrotreating, a catalytic reaction with hydrogen in which hydrogen sulfide is formed. Typical hydrotreating catalysts are sulfided $CoMo/Al_2O_3$ and $NiMo/Al_2O_3$.
Tools for predicting the reactivity of a given feed stock at high HDS conversions are in demand for estimating the performance of industrial hydrotreating units.
In order to meet ULSD specifications it is necessary to remove some of the most refractive sulfur com-pounds, such as methylsubstituted dibenzothiophenes.
A key component in the understanding of HDS kinetics at high conversions is 4,6-dimethyldibenzothiophene, which due to sterical hindrance is among the most refractive sulfur compounds. Dibenzothiophenes can react through two parallel reaction routes, a direct desulfurization route and a pre-hydrogenation route, as illustrated in figure 1 [2].
During hydrotreating, two other important reactions take place: Hydrodenitrogenation (HDN) and hydro-dearomatization (HDA). The general HDA reaction of an aromatic (*A*) to a naphthene (*AH*) can be written as:

$$A + nH_2 \; f \quad AH$$

Hydrogenation of poly- and di-aromatics is in general quite fast compared to the hydrogenation of mono-aromatics. These reactions are important since certain large aromatics can inhibit the HDS reactions, and the aromatics content has a significant influence of physical properties of the product such as density and cetane number [3].

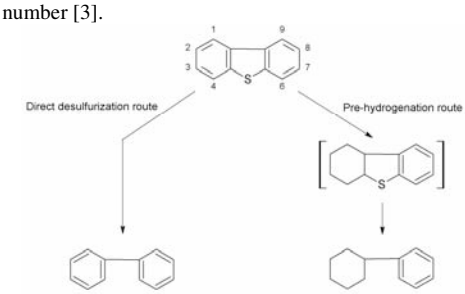

Figure 1 Reaction pathways for HDS of dibenzothiophene [2].

Specific Objectives
The purpose of this project is to develop a component-based kinetic model for the hydrodesulfurization reaction, which is applicable at all sulfur conversions. The model should account for the inhibition by certain nitrogen components and large aromatics. Furthermore it is the intension to develop a model for the hydrogenation of aromatic compounds, which accounts for the kinetics and the equilibrium between aromatic and naphthenic structures.
A hydrotreating reactor is a fixed bed catalytic reactor in which gas and liquid flow co-currently down. It is best described as a trickle-bed reactor in which the liquid trickles from pellet to pellet and the gas forms a continuous phase.

It is the purpose to develop a reactor model that accounts for the thermodynamic equilibrium between the diesel oil components, hydrogen, and the hydrogen sulfide and ammonia formed through reaction. The reactions occur in the liquid phase inside the pores of the catalyst, and the model should be able to describe the diffusion limitations inside the catalyst pellets and any external mass transfer limitations.

Experimental work

Experiments are done in a lab-scale reactor at Haldor Topsøe A/S. The reactor is illustrated in figure 2.

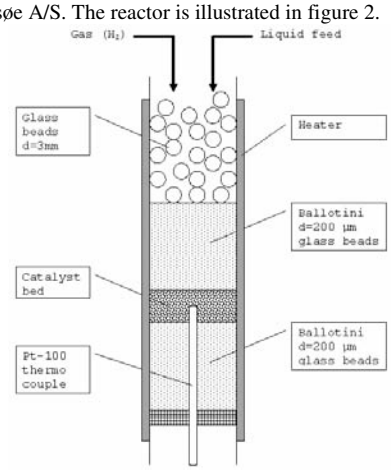

Figure 2 Illustration of lab-scale reactor used for kinetic experiments with model compounds.

Hydrogen gas and liquid feed enters at the top of the reactor, and the product stream is analyzed in a gas chromatograph.

Initially the hydrogenation of naphthalene to tetralin on a commercial CoMo catalyst has been studied. The reaction pathways of naphthalene are shown in figure 3.

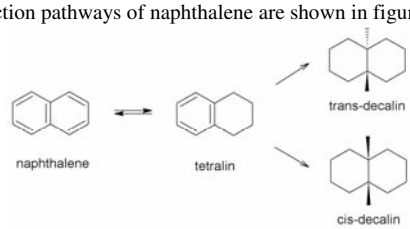

Figure 3 Reaction pathways of naphthalene hydrogenation [4].

It is the purpose of these experiments to get kinetic data for the reaction of naphthalene to tetralin that can be used to develop a kinetic model for this hydrogenation reaction. Furthermore the effect of diffusion limitations is also being investigated by doing experiments with different particle size fractions.

Reactor model

With some assumptions a trickle-bed reactor can be described by Eq. 1 to 4.

Concentration, c_k^L, in the bulk liquid phase:

$$u_L \frac{dc_k^L}{dl} = k_{k,LG} \cdot a_{LG} \left(c_k^{eq} - c_k^L \right) - k_{k,LS} \cdot a_{LS} \left(c_k^L - c_k^S \right) \quad (1)$$

Concentration, c_k^G, in the gas-phase:

$$u_G \frac{dc_k^G}{dl} = -k_{k,LG} \cdot a_{LG} \left(c_k^{eq} - c_k^L \right) \quad (2)$$

Mass balance at the catalyst pellet surface:

$$0 = k_{k,LS} \cdot a_{LS} \left(c_k^L - c_k^S \right) - R_{k,app} \cdot \left(1 - \varepsilon_{bed} \right) \quad (3)$$

The apparent reaction rate, $R_{k,app}$, is calculated by solving the diffusion reaction problem:

$$D_{e,k} \frac{d}{dr} \left(r^2 \frac{dc_k}{dr} \right) - r^2 R_k = 0 \quad (4)$$

$$BC: \frac{dc_k}{dr}(r=0) = 0 \qquad c_k \left(r=R_p \right) = c_k^S$$

Mass transfer coefficients, diffusion coefficients and other parameters are calculated from correlations, found in literature, or based on experimental data

Conclusions

Experimental work has begun on HDA of naphthalene. The experiments are done to investigate the kinetics, and the degree of diffusion limitations. Equations to describe a trickle-bed reactor have been set up, but more experimental data is needed in order to validate the model.

Future Work

Future work on this project involves further studies of HDS and HDA of model compounds.

The effect of different nitrogen compounds such as acridine, carbazoles and indoles on the HDS of dibenzothiophenes and real diesel oil will be studied.

Hydrogenation of naphthalene will be studied to get a better understanding of the reaction at normal hydrotreating conditions.

Based on the experimental studies and data from literature, it is the plan to include more compounds in the reactor model and investigate if hydrotreating of more complicated mixtures can be simulated.

Acknowledgements

This project is funded by Haldor Topsøe A/S, the MP_2T Graduate School in Chemical Engineering and the Technical University of Denmark.

References

1. T. Song, Z. Zhang,J. Chen, Z. Ring, H. Yang, Y. Zheng, Energy Fuels, 20, (2006), 2344-2349
2. K. G. Knudsen, B. H. Cooper, H. Topsøe, Applied Catalysis A: General, 189 (1999), 205-215.
3. B.H. Cooper, B.B.L. Donnis, Applied Catalysis A: General, 137 (1996) 203-223
4. M.J. Girgis, B.C. Gates, Ind. Eng. Chem, Res. 30 (1991), 2021-2058.

Jacob Brix
Phone: +45 4525 2922
Fax:
E-mail: jac@kt.dtu.dk
WWW: http://www.chec.kt.dtu.dk
Supervisors: Anker Degn Jensen
Peter Arendt Jensen

PhD Study
Started: October 2007
To be completed: September 2010

Oxy-Fuel Combustion of Coal and the Evolution of NO_x

Abstract
The focus on the environmental role of CO_2 and the thereby following legal legislations and international reduction programs, has increased the interest for a CO_2-friendly use of coal for heat and power generation. A method that can be used both for new and retrofitted plants are Oxy-Fuel combustion. In Oxy-Fuel combustion coal is burned in a mixture of oxygen and recirculated flue gas (RFG), which gives an exit gas consisting mainly of CO_2 and H_2O along with some impurities such as NO_x and SO_x. The high content of CO_2 makes this exit gas suitable for sequestration. The purpose of this project is to investigate differences between Oxy-Fuel and air combustion with respect to char combustion kinetics and NO_x evolution.

Introduction
The recent years there has been an increased focus on the environmental role of CO_2 and this focus has initiated stricter environmental legislations both globally and within the EU [1]. To overcome these legislations and to solve the problems related to CO_2 emission, the energy industry relaying on coal will need to find technological alternatives to the present combustion processes that will utilize coal in a more environmentally friendly way, seeing how the dependence on coal as an energy source can be expected to be present for many years to come [1], [2].

One solution that seems to be promising in the nearby to midterm future is Oxy-Fuel combustion [2].

Oxy-Fuel combustion is a combustion technique, which has been shown considerable research attention in resent years. There are several reasons for this continuously increasing interest, among which the following should be emphasized:

- Existing plants can be retrofitted to function under Oxy-Fuel conditions relatively easy [2].
- Oxy-Fuel combustion produces an exit stream with a very high CO_2 content (~90-95 %) [2], [3], [4], which are ready for sequestration. The CO_2 purity of the exit gas on industrial scale mainly depends on the efficiency of the Air Separation Unit (ASU).
- Combustion in an Oxy-Fuel environment has the potential to reduce NO_x emissions, when compared to traditional air-blown plants [2].

As a further benefit all of the Oxy-Fuel combustion unit operations, except the boiler, are in some sense relaying on existing and known equipment [5].

A scheme of the Oxy-Fuel combustion process can be seen in figure 1.

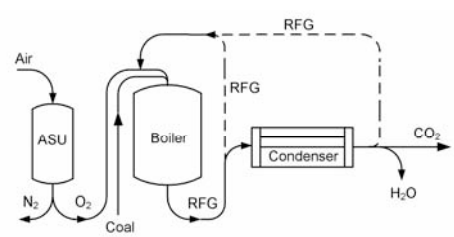

Figure 1: The overall thought behind the Oxy-Fuel combustion process is shown. Units such as desulphurization units and compressors are omitted. The need for desulphurization will depend on the feedstock.

Specific Objectives
This project is devoted to the kinetic investigation of char burnout and the evolution of NO_x under Oxy-Fuel combustion.

Combustion of char in oxygen enriched CO_2 atmospheres, such as those prevailing in oxy-fuel combustion, is not fully understood, and the influence of gasification at higher temperatures has been observed [6].

The differences between the combustion behavior in conventional air-blown furnaces and Oxy-Fuel furnaces make a detailed study of the Oxy-Fuel fuel combustion kinetics necessary along with accurate model predictions and interpretations of test results before large scale construction can be initiated [7].

The NO_x evolution changes between air-blown combustion and Oxy-Fuel combustion [1]. This is mostly due to the recirculation of the flue gas into the flame and the reduction of NO over char. These effects are functions of O_2 concentration, temperature and fuel feed rate [8].

These dependences on NO_x evolution are important to understand in detail in order to benefit fully from the possibilities Oxy-Fuel combustion gives for reducing the NO_x emission [9].

Methodology
The work will involve a literature survey on the subjects discussed in the section above.

The experimental investigation will mainly be carried out in an Entrained Flow Reactor (EFR) located at the department. Here reference experiments will be performed using conventional air-blown combustion and these will afterwards serve as the basis of comparison, when experiments with Oxy-Fuel combustion has been performed under similar conditions.

Conclusion
The kinetics of air-blown combustion has been thoroughly investigated over many years but it may not directly apply for Oxy-Fuel conditions. Works is therefore needed on the subject before industrial scale Oxy-Fuel plant construction can begin.

References

1. R. Tan, G. Corragio, S. Santos, Oxy-Coal Combustion with Flue Gas Recycle for the Power Generation Industri, Report No. G 23/y/1, International Flame Research Foundation, 2005.
2. B. J. P. Buhre, L. K. Elliott, C. D. Sheng, R. P. Gupta, T. F. Wall, Prog. Energy Combust. Sci. (31) (2005) 283-307.
3. H. Liu, K. Okazaki, Fuel (82) (2003) 1427-1436.
4. K. Okazaki, T. Ando, Energy (22) (1997) 207-215.
5. L. Strömberg, Combustion in a CO_2/O_2 Mixture for a CO_2 Emission Free Process, Second Nordic Minisymposium on Carbon Dioxide Capture and Storage, 2001, 58-63.
6. T. F. Wall, Proc. Combust. Inst. (31) (2007) 31.47.
7. J. J. Murphy, C. R. Shaddix, Combust. Flame (144) (2006) 710-729.
8. Y. Q. Hu, N. Kobayashi, M. Hasatani, Energy Convers. Manage. (44) (2003) 2331-2340.
9. Y. Tan, E. Croiset, M. A. Douglas, K. V. Thambimuthu, Fuel (85) (2006) 507-512.

Francesco Castellino
Phone: +45 4525 2829
Fax: +45 4525 2251
E-mail: frc@kt.dtu.dk
WWW: http://kt.dtu.dk
Supervisors: Anker Degn Jensen
Jan Erik Johnsson
Rasmus Fehrmann

PhD Study
Started: December, 2004
To be completed: April, 2007

Deactivation of SCR Catalysts by Additives

Abstract
The Danish power companies are obliged to burn biomass at the central power stations. The alkali fraction introduced by biomass into the combustion system is responsible for high rates of deposition and corrosion at the surface of the super-heat exchangers. To minimize these undesired effects, the power companies are considering to mix the biomass burned in their plants with some additives, which are able to fix the alkali fraction in harmless compounds. The objective of this Ph.D. project is to evaluate the effect of the selected additives on the commercial catalysts employed in the SCR process.

Introduction
Nitrogen oxides (NO_x) emitted from stationary sources can be effectively reduced by using the so-called Selective Catalytic Reduction (SCR) process [1]. Ammonia is injected into the flue gas and reacts with the NO fraction according to the following reaction:

$$4\ NH_3 + 4\ NO + O_2 \rightarrow 4\ N_2 + 6\ H_2O$$

The reactor operates at atmospheric pressure and temperature ranging between 300 and 400ºC. The catalysts employed are vanadia-based catalysts. This technology was first developed in Japan during the 1970s and is still nowadays the best-developed and worldwide used for fossil fuel combustion processes.

However, the application of this technology to the treatment of flue gas from (co)-combustion of biomass or secondary fuels such as sewage sludge or meat and bone meal (MBM) is problematic. This is mainly due to the high rates of catalyst deactivation observed and related to different compounds (*e.g.* alkali and alkaline earth metals, chlorides, etc.) introduced into the system by these alternative fuels [2,3]. The alkali fraction of the biomass is also responsible for a higher deposition rate on the superheater surfaces in the boiler. In fact, the fly ash produced during biomass combustion, due to the high content of alkali, has relative low melting point temperatures. At the temperatures of the superheaters, they thus present a melted fraction which makes them particularly sticky [4].

Deposition on the heat exchanger surfaces is a highly undesired process since it decreases the heat transport through the heat exchangers and causes corrosion, thus affecting the overall efficiency in steam production. The use of additives to the fuel is considered by the Danish power companies as a way to minimize this undesired effect, rending the combustion of biomass more efficient. Preliminary tests have mainly involved compounds rich in phosphorus like phosphoric acid, mono- and di-calcium phosphate [4]. Due to the presence of the phosphorus during combustion, ashes mainly constituted by K, P and Ca with higher melting point temperatures (>1300ºC) were formed. Accordingly, the deposition rate measured during addition of P-compounds was found to decrease up to 90%.

However phosphorus is known to be by itself a moderate poison for the vanadia-based catalysts normally employed in the SCR process [5,6]. Studies about poisoning by phosphorus have been conducted in the laboratory mainly by wet impregnation with phosphoric acid solutions. The activity of the powdered doped catalysts still showed up to 80-85% of the original activity at P/V ratio greater than 2. Commercial vanadia-based catalysts exposed at full-scale during (co)-combustion of sewage sludge and MBM has shown enrichment in phosphorus on the surface and the bulk of the catalysts [3]. The samples presented a decreased total pore volume and a shift of the average pore diameter towards smaller values. Formation of surface layers and pore condensation by phosphorus was thus indicated as the main mechanism of deactivation by phosphorus. However, since the catalysts were enriched also by other known poisons like potassium and arsenic,

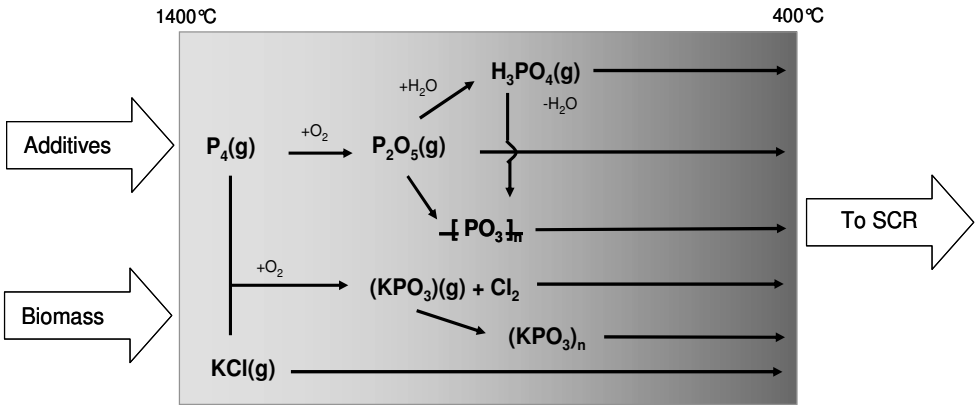

Figure 1: Examples of reactions given by gaseous molecular phosphorus, introduced into the system by the additives, and the KCl released during biomass combustion. Both the products of combustion of the additives, and the reaction between the additives and the alkali fraction of the flue gas could reach the SCR reactor and deactivate it. The different mechanisms of deactivation due to each of these species will be studied in this project.

it was not possible to directly correlate the influence of the phosphorus alone on the overall deactivation.

The purpose of this project is to investigate whether the P-additives may cause accelerated deactivation, what the mechanisms of the deactivation are and whether the deactivation can be inhibited or slowed down to an acceptable rate. Investigations will include both tests involving the additives, and the possible products of the addition process as shown in.

In the present contribution the main results about deactivation by potassium phosphate tribasic, K_3PO_4, at a pilot plant are presented.

Experimental

The catalysts employed were commercial Haldor Topsøe A/S DNX 3%V_2O_5-WO_3-TiO_2 full-length monoliths. The pilot-scale setup mainly consists of a 50 kW natural gas burner, a lance for injection of solutions into the flue gas, ammonia storage and addition line, and a reactor hosting the SCR monolith. The activity measurements have been performed at 350°C, in the presence of about 500 ppmv NO and 600 ppmv of NH_3 in the pilot scale reactor. Two different monoliths have been exposed during addition of 10 and 20 mg/Nm^3 K_3PO_4 respectively by spraying directly into the hot flue gas (T>800°C) different aqueous solutions of K_3PO_4. In this work they will be referred to as KP10 and KP20 respectively.

Since ammonia in our measurements is in excess with respect to NO, the reaction rate can be regarded as pseudo-first order with respect to NO and zero order with respect to NH_3. Therefore, directly from the fractional NO conversion, X, it is possible to calculate an observed catalyst activity constant, k' (ml/g/s), which includes both the influence of external and internal mass transfer:

$$k' = -\frac{F_{gas}}{m_{cat}} \ln(1-X) \qquad (1)$$

where F_{gas} is the gas flow rate (ml/s), m_{cat} is the weight of catalyst (g). The degree of deactivation have been then calculated as the ratio k/k_0 between the activity constant of the catalyst during exposure, k, and the one measured for the fresh element, k_0, right before starting the poison addition.

In the laboratory, powder samples have been tested for activity in a packed bed quartz micro-reactor. Around 0.07 g of powder have been used during activity measurement with a total flow equal to 2.8 NL/min constituted by 500 ppm NO, 600 ppm NH_3, 5% O_2 and 1.4% H_2O in N_2. Activity measurements have been performed in the temperature range 250-400°C. The catalyst activity has been again calculated according to Eq. 1 and the deactivation as the ratio between the activity constant of the spent catalyst and the one measured for the fresh one. At 350°C, the observed activity constant for the fresh catalyst was found only 10% less that the one calculated by Ahrrenius interpolation of the data at lower temperatures, mainly due to mass transfer limitations. No NH_3 oxidation has been measured up to 350°C during an empty reactor test.

The fresh and the spent catalysts have been characterized by Hg-porosimetry, SEM analysis and chemical composition.

Results and Discussion

Figure 2 shows the activity decrease measured at the pilot plant for the two elements exposed to 10 and 20 mg/Nm^3 for 190 and 720 h respectively. In both cases, the catalysts lost up to 10% of their original activity in only about 1 day of exposure. However, after this short period of time the deactivation proceeded at a slower

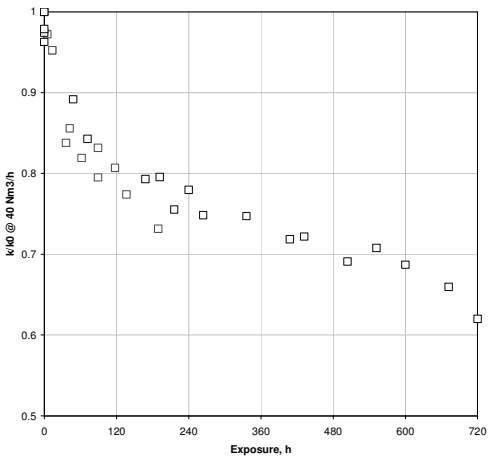

Figure 2: Relative activity for KP10 (blue) and KP20 (red) as a function of exposure time.

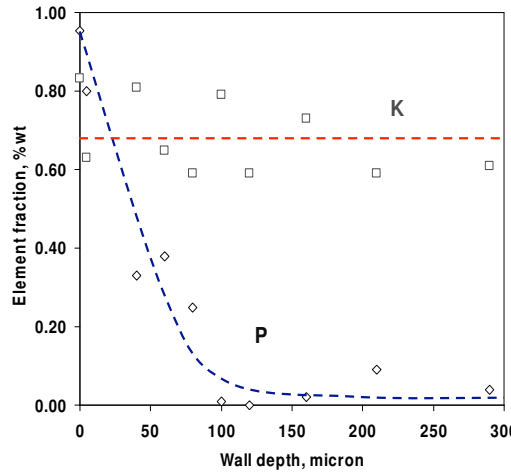

Figure 3: EDX analysis of the KP10 cross section.

but constant rate. At the end of the exposure, KP10 and KP20 lost 38 and 23% of their original activity respectively.

Table 1: Elemental bulk analysis of KP10.

KP10 Element	Top wt%	Bottom wt%
K	2.45	1.44
P	0.77	0.46
V	2.46	1.61
K/P	3.17	3.10

Table 1 shows the results of the chemical analysis made with samples cut at the end of the exposure from both the top and the bottom of the element KP10, together with the calculated K/P ratios (wt/wt). From the results it is possible to see that high levels of K were found in the catalyst walls, especially at the top of the element. This fact can be explained by the high mass transfer at the monolith inlet due to the developing flow. Moreover, it can be seen that the measured K/P ratio was lower than the one present in the K_3PO_4 molecule, which is equal to 3.8 on mass basis. The reasons for this result are not clear, but they would point to condensation reaction between the K_3PO_4 molecules in the gas phase with release of KOH.

Analysis of the samples by SEM-EDX showed a different penetration degree for K and P. Figure 3 shows the K- and P-content in the wall of sample cut from the bottom part of KP10. Here it can be seen that the K-concentration was found to be constant along the wall at a value of around 0.7 wt%. Contrarily, the P-concentration was found to be higher at the catalyst surface and almost zero at the inner points into the wall.

In order to explain the different penetration of K and P, mainly two explanations are possible. The first one assumes i) transport of K_3PO_4 particles inside the wall; and ii) reaction with the catalyst surface with release of H_3PO_4 in the gas phase. The second explanation would instead assume i) deposition of K_3PO_4 on the outer wall; ii) reaction on the catalyst surface forming KOH and iii) transport of KOH inside the wall. The first mechanism does not seem likely. According to its Tamman and Hütting temperatures, K_3PO_4 is not mobile at the SCR temperatures and therefore its penetration in the form of K_3PO_4 is unlikely. On the other hand, KOH melts at 360℃ and is likely to be very mobile at the SCR temperature. It could also be imagined that the transport of K could have been due to surface diffusion of K-atoms caused by K-gradients in the wall. This mechanism cannot be excluded. However, in this case, the profile in the K-concentration showed in Figure 3 would suggest a diffusion rate faster than the deposition rate.

The two exposed monoliths have been further investigated in the laboratory in order to correlate the local values of the intrinsic activities with the specific bulk K- and P-content for the samples. Figure 4 shows the results of the activity measurements carried out with powderized samples cut from the top and the bottom of KP10, together with the test made using powderized fresh catalyst. As expected, the relative activities measured with the powderized catalysts were lower than the one measured on the monoliths due to the hiding effect of mass transfer limitations. The sample cut from the top of the KP10 element only conserved 9% of the original activity, whereas the sample cut from the bottom of the same element retained 30%. Considering the different K/V ratios measured by EDX (K/V=0.2 for KP10 bottom), these results are in good agreement with previous investigation about deactivation by K carried out by wet impregnation with aqueous solution of K-salts. This fact indicates that the deactivation seen is mainly caused by K. The mechanism of deactivation will therefore include reaction between K and the

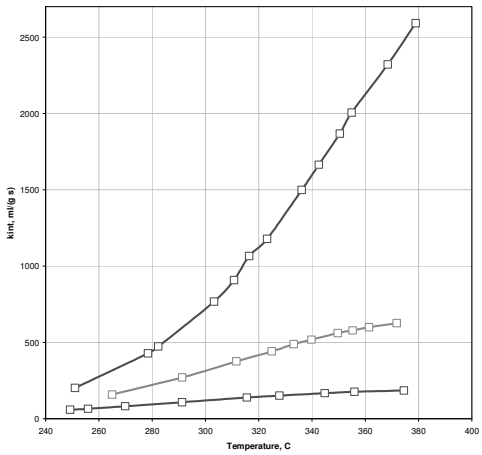

Figure 4: Activity of powderized fresh and KP10 samples. F=2.8 Nl/min, NO=500 ppm, NH_3=600 ppm, O_2=5%, H_2O=1.4%, N_2 balance. Catalyst mass m_{cat}=0.07 g. Fresh: green; KP10 top: brown; KP10 bottom: orange.

Brønsted V-OH sites present on the surface as already described elsewhere [2,7].

Conclusions

The main objective of this Ph.D. project is to study the effects of the proposed "anti-deposition" additives on the SCR catalysts. K-P salts might be the results of the addition process. Their effects on the SCR catalysts have then been studied.

K is known to be a dangerous poison when present in the flue gas in KCl and K_2SO_4 aerosols [2]. The results obtained in this work show that no beneficial effect is obtained by bounding K in K-P particles. The formed salts will not be mobile on the catalyst surface due to their higher melting temperature. However, they are not stable at the SCR temperature and in the presence of H_2O in the flue gas. Therefore, they tend to free some K and/or KOH that can penetrate the walls and *efficiently* deactivate the catalysts.

Acknowledgements

This project is supported by the PSO system. Supply of the catalyst samples by Haldor Topsøe A/S is gratefully acknowledged.

References

1. V.I. Parvulescu, P. Grange, B. Delmon, Catalysis Today 46 (1998) 233-316.
2. Y. Zheng, A.D. Jensen, J.E. Johnsson, Ind. Eng. Chem. Res. 43 (2004) 941-947.
3. J. Beck, R. Muller, J. Brandenstein, B. Matschenko, J. Matschke, S. Unterberger, K.R.G. Hein, Fuel 84 (2005) 1911-1919.
4. P.A. Jensen, L.H. Sørensen, G. Hu, J.K. Holm, F. Frandsen and U.B. Henriksen. Technical University of Denmark (2005). KT-Report No. 0504.
5. J.P. Chen, M.A. Buzanowski, R.T. Yang, J. Air Waste Manage. Assoc. 40, (1990) 1403-1409.
6. H. Kamata, K. Takahashi, C.U.I. Odenbrand, Catalysis Letters 53, (1998) 65-71.
7. R. Khodayari, C.U.I. Odenbrand, Applied Catalysis B: Enviromental 30 (2001) 87-99.

Jakob Munkholt Christensen
Phone: +45 4525 2927
Fax: +45 4525 2258
E-mail: jmc@kt.dtu.dk
WWW: http://www.kt.dtu.dk
Supervisors: Anker Jensen
Peter Arendt Jensen

PhD Study
Started: September 2007
To be completed: September 2010

Catalytic Conversion of Syngas to Mixed Long Chain Alcohols

Abstract
The catalytic synthesis of higher alcohols from syngas is a promising route to synthetic transportation fuels from biomass/coal via gasification. This project deals with an optimization of the alcohol synthesis process and catalyst. The experimental facilities and the results of preliminary investigations of the reaction kinetics are presented. The alcohol synthesis has a significant potential, but further improvements of catalyst productivity and selectivity are still needed for a commercially viable project.

Introduction
The campaigns in connection with the recently held election in Denmark unequivocally revealed the existence of a broad political consensus to reduce the environmental impact of the transportation sector and to avoid unnecessary dependence upon the often politically unstable oil-exporting countries. A method for generating synthetic transportation fuels is a gasification of coal and/or biomass by reaction with steam at high temperature. This generates a H_2/CO containing gas called synthesis gas or syngas. The generated syngas can then be converted to liquid transportation fuels in a catalytic reaction. An important benefit of the gasification route to liquid transportation fuels compared to for example fermentation of biomass is the ability to co-process various feedstocks like biomass, coal and residential wastes. This provides the process with an excellent flexibility towards for instance seasonal variations in biomass availability. Methanol has a high octane number and is today produced from syngas (derived from natural gas) in a very effective synthesis. Methanol would thus appear to be a very suitable synthetic fuel, but methanol is corrosive and methanol/gasoline mixtures have a tendency to separate into two phases in cold weather and in the presence of water[1,2]. A synthetic fuel more suited for blending with gasoline is a mixture of methanol and higher alcohols (primarily ethanol). As the higher alcohols act as co-solvents to methanol, this mixture does not have the same phase separation issues[1,2].

The mixture of methanol and higher alcohols can be produced over a wide variety of modified methanol or Fischer Tropsch synthesis catalysts[3-5]. A very promising catalytic system appears to be alkali-promoted sulfides of molybdenum or cobalt-molybdenum, which, at high pressure and low temperature, primarily produces linear alcohols with short hydrocarbons as the main by-product[5].

Specific Objectives
The specific objective of the present Ph.D. project is to improve the activity and selectivity of the molybdenum sulfide catalysts in order to minimize bi-product (primarily methane) formation. This will be achieved through an optimization of the catalyst formulation and potentially through the inclusion of novel additives to the formulation. Furthermore the practical use of the alcohol synthesis catalyst will be examined. This will include an investigation of the possibility for work-up of smaller components of lower value (e.g. methanol) to higher alcohols as well as an investigation of catalyst poisoning phenomena. Finally it is an objective of the present studies to further elucidate the reaction mechanism and achieve a theoretical description of the reaction kinetics. This will aid in the assessment of the potential of the process and be of practical use in for example reactor design.

Experimental work
The experimental investigations conducted with the catalyst are carried out using a high pressure reactor setup at the department of chemical engineering. The setup was originally constructed to study the direct gas phase conversion of natural gas to methanol[6].

A diagram of the experimental setup is depicted in figure 1.

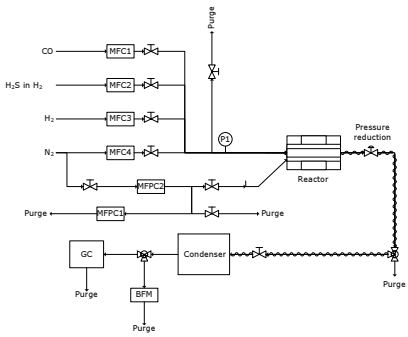

Figure 1: Diagram showing the experimental setup. BFM: Bubble flow meter; GC: Gas Chromatograph; MF(P)C: Mass flow (pressure) controller; Heat tracing is indicated by sinusoidal curves.

The examinations have hereto been conducted with a carbon supported K_2CO_3/Co/MoS_2 catalyst (2.9 (w/w)% Co; 14.8 (w/w)% Mo) provided by Haldor Topsøe A/S. A bed of catalyst is placed in a quartz tube contained inside a stainless steel pressure shell. The pressure shell itself is placed inside an oven, which provides the relevant reaction temperature. Nitrogen is dosed to the pressure shell to ensure equal pressure on both sides of the quartz tube wall. Characterisation of gaseous reaction products is conducted using a GC-FID/TCD detection system, but the setup also has the possibility to condense a liquid alcohol product.

Results and Discussion

Figure 2 illustrates the development of alcohol selectivity and space time yield (productivity per mass of catalyst) with temperature for the catalyst.

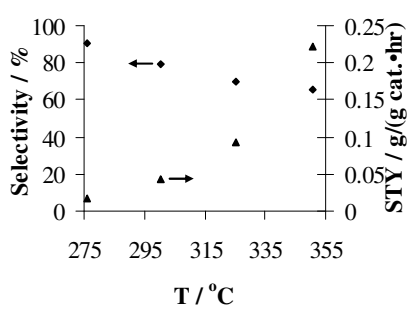

Figure 2: Alcohol selectivity and space time yield (STY) over a K_2CO_3/Co/MoS_2/C catalyst. Conditions: P = 100 bar, Feed: H_2/CO = 1/1, GHSV = 5238 hr^{-1} (based on total bed volume).

As the alcohol productivity becomes reasonable at higher temperatures the selectivity has decreased substantially, and methods for improving alcohol selectivity should have a high priority in future research. The presence of hydrogen sulphide in the syngas feed shifts the selectivity from alcohols to hydrocarbons, but appears to improve the long-term (+100 hrs) stability of the catalyst. Additionally the reaction kinetics have been investigated and expressed as a series of n'th order rate equations:

$$r_n = A_n e^{-\frac{E_a}{RT}} p_{H_2}{}^{a_n} p_{CO}{}^{b_n} p_{H_2S}{}^{c_n} \quad (1)$$

Table 1 summarizes the kinetic parameters for alcohol formation over the K_2CO_3/Co/MoS_2/C catalyst.

Table 1: Activation energy and reaction orders for alcohol formation over a K_2CO_3/Co/MoS_2/C catalyst.

Component	E_a / $\frac{kJ}{mol}$	Reaction orders		
		$H_2(a)$	CO(b)	$H_2S(c)$
Methanol	55	1.58	-0.16	-0.33
Ethanol	91	1.48	0.22	-0.27
1-Propanol	122	1.00	0.32	-0.10
1-Butanol	142	0.69	0.44	0.12

Conclusions

The synthesis of mixed higher alcohols from syngas derived from coal/biomass is a promising route to synthetic liquid fuels. The alcohol selectivity does however need to be improved to achieve a commercially viable product. The preliminary kinetic investigations reveal high H_2 reaction orders and low CO reaction orders, which indicates a high CO surface coverage at reaction conditions.

Acknowledgements

This work is part of the CHEC (Combustion and Harmful Emission Control) Research Center funded a.o. by the Technical University of Denmark, the Danish Technical Research Council, the European Union, the Nordic Energy Research, Dong Energy A/S, Vattenfall A.B, F L Smith A/S, and Public Service Obligation funds from Energinet.dk and the Danish Energy Research program. This particular project is financed by Haldor Topsøe A/S and the Technical University of Denmark.

References

1. J.F. Knifton, J. J. Lin, D. A. Storm, S. F. Wong, Catal. Today 18 (1993) 355-384.
2. I. Wender, Fuel. Proc. Tech. 48 (1996) 189-297.
3. P. Courty, D. Durand, E. Freund, A. Sugier, J. Mol. Catal. 17 (1982) 241-254.
4. J.G. Nunan, C. E. Bogdan, K. Klier, K. J. Smith, C.W. Young, R. G. Herman, J. Catal. 116 (1989) 195-221.
5. C.B. Murchison, M.M. Conway, R.R. Stevens, G.J. Quarderer, in: M. J. Phillips, M. Ternan (Eds.), Proceedings of the 9th international congress of catalysis, Calgary, Chemical Institute of Canada, 1988, p. 626.
6. C.L. Rasmussen, PhD thesis, Technical University of Denmark, 2007.

Elisa Conte
Phone: +45 4525 2959
Fax: +45 4525 2906
E-mail: elc@kt.dtu.dk
WWW: http://www.capec.dtu.dk
Supervisors: Rafiqul Gani
Jens Abildskov

PhD Study
Started: July 2007
To be completed: July 2010

Innovation in Integrated Chemical Product-Process Design - Development through a Model-Based Systems Approach

Abstract
The chemical industry has recently started to focus attention on 'consumer-oriented' chemical products; for these complex kinds of products, it is important to have the right properties in order to meet the consumer needs. To satisfy these needs, the aim of chemical product and process design is to find a candidate product that exhibits the targeted behaviour and to find a process that can manufacture it for the specified qualities. A systematic design methodology is being developed for this purpose using a framework for model-based design supplemented by experimental data: the framework allows the generation and use of process-product models for various design related calculations.

Introduction
The 'consumer-oriented' products are a new generation of products; they are mainly structured products and formulations [1]. In the structured products the micro structural properties are related to the desired product functions; they can be small and simple molecules such as solvents, or large and complex molecules such as drugs, cosmetics, detergents, agrochemicals, and so on. In formulations, the functional properties are further enhanced with the addition of other products, as ingredients to flavors, solvent blends, coatings and so on. These complex products need to have the right properties in order to meet the consumer needs, which are actually the target properties required.
This project aims to develop a systematic framework for the model-based design of chemical products and the process to manufacture them, employing computer aided methods.

Objectives
The main purpose of the project is to develop a library of models, collecting models already developed by CAPEC co-workers and developing new models, then to organize the models in a systematic framework through which product and process design problems can be solved more easily, quickly and efficiently.
The modeling effort deals with developing three different kinds of models:
- *properties models*, for the properties which affect the performance and the manufacturing processes;
- *performance process models*, for the process in which the product will be employed/used;
- *manufacturing process models*, for the process through which the product will be manufactured/produced.

All these models have to be organized in a *systematic framework* [2], which has to be divided in different sections: a section for the problem definition and target settings, a section for the calculation of the properties, one in which the performance model is solved, one in which the manufacturing model is solved, and finally a section for the verification/evaluation of the solution/solutions obtained. In such a framework the points of innovation are numerous: the product and the process are designed *simultaneously* (integrated product and process design [2]) in order to find at the same time a product that matches the target criteria and that can be reliably and economically manufactured, avoiding failures in designing products that can not be produced because of high costs or infeasibilities in the production. In addition, the design is based on the *reverse approach* which has different advantages over the more conventional forward approach: it is computationally inexpensive, it has the potential to find all the products that match the desired criteria in only one-flow of the algorithm, it gives the opportunity of combining models that are multidisciplinary and multiscale.
At least three case studies will be considered in this project, all coming from industry; they will be able to prove the validity of the models developed and the validity of the framework for the product and process

design. The products that could be considered are pharmaceuticals, pesticides/agrochemicals and personal care products.

Description

While in the past chemical product and process design focused mainly on the process (how-to-make), this new generation of 'consumer-oriented' products requires this perspective to be changed: the design has to be product based (what-to-make). In addition, to avoid wastes in time and resources, it is important product and process are designed simultaneously.

In this project, both these necessities are satisfied: first, with the *reverse approach* the product and process design becomes a product based design; second, the *systematic framework* gives the possibility of the integration between the product design and the process design. In addition, multiscale and multidisciplinary models can be combined in such a framework, and with this methodology not only one but all the products that match the desired targets are found as solution to the design problem.

The project has elements of innovation which contribute to the state of art in chemical process design and development. Currently, the product and the process to manufacture it are designed separately; in addition, the design is based mainly on experiments, spending a lot of time and resources in trial-and-error procedures. Besides, also the current computer-aided research has some disadvantages, since the approach employed (the forward approach) is computationally expensive, requires iterations and proceeds testing one product per time. Innovation is needed. In this project, the search for innovation will be carried out through the following options:

- product and process are designed simultaneously;
- the design is computer based and the models used are truly predictive;
- the approach is the reverse approach: all products that match the criteria are identified and analyzed with respect to a performance index.

The framework represents a goal in product and process design both for the research and the industry; the design can be completely computer-aided, and the experimental part can be conducted as the final step of the design, in order to test a small number of candidate products. The systematic framework is a powerful instrument, where numerous models are collected in order to be able to design a large range of products, where multiscale and multidisciplinary models are implemented, where the product, the performance process and the manufacturing process can be designed together, and, finally, where the products can also be verified. From an industrial point of view this instrument leads to a drastic decrease in the experimental effort, and, as a consequence, a drastic reduction in time and resources employed in the research.

The method

In a product and process design problem for consumer oriented products, the target criteria for the product have to meet consumer's needs; so, in the case of an insect repellent lotion for example, the targets are: the efficiency of the repellent has to be high, the lotion does not have to be sticky and toxic, the lotion has preferably to be spray. These preferences have to be translated into chemical properties for example a lotion can be sprayed only if the viscosity is under a certain value, and the lotion should not be toxic (if the NFPA index of the mixture is low).

The conventional way to solve a product and process design problem which involves a process model and properties models is using the *forward approach*: once the target criteria for the product are set, the design problem is started by guessing a product, then an algorithm which combines the process model and the properties models is solved, in order to obtain the performance of the product; finally the behavior obtained is compared with the target. If they match, one product that satisfies the target criteria has been found, if they do not, another product has to be guessed and the procedure described above has to be repeated until at least a product that matches is found. First, from a computational point of view it is expensive to implement the properties models in the same algorithm where the process model is implemented; second, with this approach an iterative solution method is needed and, third, in this way only one product that matches is found iterating several times.

In the *reverse approach* [1], the algorithm is based on the idea that all processes depend on some properties of the products. Based on this assumption, the algorithm splits the solution of the whole model into two stages. In the first stage the targets for properties are set, and this is done by setting the performance criteria of the process; then the process model is solved with property parameters as the unknown variables. In the second stage, properties model are used to obtain all the products that match the target properties calculated in the first stage. With this approach, properties models and process model are solved separately (computationally inexpensive), iterations are not needed and in only one-flow of the algorithm all products that match are found.

Current and future work involves the development of the framework for model-based product-process design.

References

1. R. Gani, Computers and Chemical Engineering 28, 2441-2457, (2004).
2. R. Gani, Chemical Engineering Research and Design, 82(A11), 1494-1504 (2004).

Michelangelo Dall'Ora

Phone: +45 4525 2839
Fax: +45 4588 2258
E-mail: mid@kt.dtu.dk
WWW: http://www.chec.kt.dtu.dk
Supervisors: Anker Degn Jensen
Peter Arendt Jensen

PhD Study
Started: December 2004
To be completed: May 2008

Reactivity and Burnout of Wood

Abstract
Wood is increasingly used as a CO_2-neutral and renewable fuel for the production of heat and power in highly efficient suspension fired power plants. In suspension fired boilers wood char oxidation is the slowest step and determines the degree of burnout of the fuel, thus affecting the efficiency of the plant. In order to enable prediction of the burnout and main heat release profile, wood char needs to be characterized, its reactivity to oxygen has to be assessed and kinetic data must be coupled with suitable models accounting for transport processes and char transformation during combustion. This project addresses these issues by means of experimental work at laboratory- pilot- and full-scale as well as modeling.

Introduction

The large availability of wood, neutrality with respect to CO_2 emissions and the fact that it is a renewable source make it a very attractive solid fuel for combined heat and power plants. Nowadays a variety of wood species are burned in power plants, depending on the location of the plant, the wood-related activities in the area (pulp and paper industry, sawmills, etc.) and other economical reasons; wood from conventional forestry, residues from manufacturing of wood-based products such as bark, sawdust and off-cuts from sawmills are some of the sources of wood fuel.

The most common techniques for the combustion of wood in combined heat and power plants are grate and suspension firing; this project deals with the latter. Suspension firing has been used for decades to burn pulverized coal; environmental concern and legislation have contributed to the conversion of some of those plants to wood combustion and to the building of new pulverized wood power plants. Today, the world's largest pulverized wood fired power plant in operation is in Denmark.

Wood is usually delivered to the plant as wood pellets (Figure 1) that are opened by milling prior to entering the boiler; what is fed to the boiler is thus pulverized wood, as is seen in Fig.1.

As they enter the furnace, the wood particles are heated up very quickly to high temperatures and thereby release volatiles (this process in known as pyrolysis), leaving a solid residue called char. The subsequent oxidation of the char is the slowest step in the conversion of wood and thus determines the degree of burnout of the fuel as well as the heat release profile in the boiler, affecting the operation and efficiency of the plant.

It is well known that pyrolysis conditions influence both the yield of char and its properties, including size, morphology, composition and reactivity. On the other hand, few studies are available in the literature about characterization of char produced at boiler-like conditions [1-3].

a b

Figure 1: a) wood pellets, b) pulverized wood.

In suspension boilers wood pyrolysis occurs in a time interval of the order of ms, whereas the subsequent oxidation of the char takes up to several seconds [4]. It is therefore evident that the process of char oxidation is the most relevant when the degree of burnout (conversion) of the fuel is to be calculated. In this

perspective, it is vital to assess the reactivity of the char to oxygen.

There is a well established awareness that the reactivity of chars from wood is far higher than the reactivity of chars from coal [5]; nevertheless, the dependence of char properties on pyrolysis conditions together with the heterogeneity of wood, result in a relatively poor agreement among published kinetic data for the oxidation of wood char.

It is not reactivity alone that determines the degree of char conversion in a suspension boiler. In fact, heat and mass transport play an important role; therefore a model is needed to combine char oxidation reactivity with transport phenomena during combustion. Several single char particle combustion models are available in the literature [6-8]; most of them were developed for char from coal and need therefore to be modified to apply to wood char combustion.

Specific Objectives

The overall objective of the project is to develop tools that can be applied to predict wood fuel burnout in suspension fired boilers.

This goal is approached by:

- Investigation of the relation between wood char properties and pyrolysis conditions;
- Assessment of wood char oxidation reactivity;
- Modeling of wood char particle combustion.

Experimental

Experimental work was carried out to investigate the influence of high temperature pyrolysis on wood char properties. Chars from different wood fuels (pine wood and beech swadust) were produced in a pilot-scale entrained flow reactor (EFR). The pyrolysis tests were carried out at different pyrolysis temperatures in the range 1073 K to 1573 K and with different fuel size fractions. With this reactor the wood particles experienced rapid heating and high temperatures, which reproduces the conditions in a real suspension boiler. For comparison, char was also produced in a thermogravimetric analyzer (TGA) at much lower heating rate (10-20 K/min).

The produced chars were analyzed by SEM microscopy to relate pyrolysis conditions to char morphology and size. Moreover the chars were oxidized in TGA in 4% O_2 – 96% N_2 atmosphere, during non-isothermal runs; the applied heating rate was as low as 2 K/min, so that transport limitations could be avoided. The TGA mass loss curves were used to derive the char oxidation kinetics (assuming a single first order reaction) whereas the residual ash content in char was used to calculate the yield of char during pyrolysis.

Results and discussion

Figure 2 shows a SEM picture of a pine particle in which the typical fibrous structure of wood is easily recognized. Figure 3 to Figure 5 show chars from pine wood produced at different conditions. Pine pyrolysis at 1373K and heating rate 10K/min in the TGA yielded a char that retained completely the fibrous structure, as seen in Figure 3.

The influence of pyrolysis conditions on pine char morphology is evident when char in Figure 3 is compared to the one in Figure 4 and Figure 5, produced in the EFR at boiler-like conditions: during pyrolysis in EFR pine wood particles went through a molten phase and completely lost the typical fiber-like structure of wood. The char appears as porous spheres. This agrees with results of previous studies by Cetin et al. [1] and Zolin [2]; they both found that biomass particles pyrolyzed at high temperatures and high heating rate undergo plastic deformation to different extents depending on parent fuel and pyrolysis conditions.

Figure 2: SEM picture of a pine particle.

Figure 3: SEM picture of a pine char particle produced in a TGA. The original pine was heated in N_2 at 10K/min to 1373K and was held at this temperature for 30 minutes.

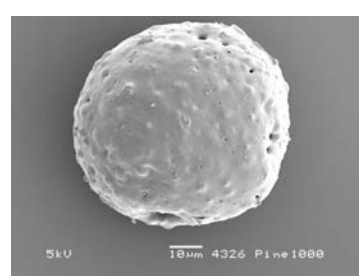

Figure 4: SEM picture of a char particle produced by fast pyrolysis of pine wood in the EFR. Pyrolysis temperature 1273K.

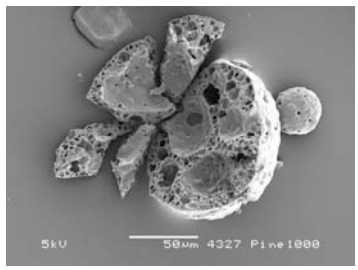

Figure 5: SEM picture of char produced by fast pyrolysis of pine wood in the EFR. Pyrolysis temperature 1273K.

Pine char morphology was similar for all the conditions and sizes applied; almost all the particles had the same spherical shape. Yet there was an effect of pyrolysis temperature on char: char particle size and char yield decreased as pyrolysis temperature increased.

Char from beech sawdust had a different morphology from that of pine char, as seen in Figure 6. The parent particles didn't seem to have melted completely during pyrolysis, although the char particle surface was smooth, indicating that some plasticity was attained.

Beech char morphology changed with pyrolysis temperature, in that higher temperature char particles were smoother and their structure was less similar to that of the original particles. Moreover, some of the beech char particles had a more round shape than others; the fraction of these round particles was higher when pyrolysis had occurred at higher temperature.

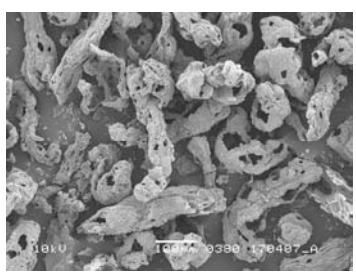

Figure 6: SEM picture of char produced by fast pyrolysis of beech sawdust in the EFR. Pyrolysis temperature 1273K.

The different ash content in pine wood and beech sawdust probably plays a very important role in determining char morphology. Jones et al. [9] have shown that mineral matter in wood affects the extent and the kind of structural changes of wood during pyrolysis. The higher ash and potassium content of beech sawdust, as reported in Table 1, may thus be responsible for beech particles not to have melted like pine particles during pyrolysis in EFR.

Table 1: Ash content and ash composition of the fuels.

	Pine	Beech sawdust
Ash (wt %, dry basis d.b.)	0.5	0.9
Ca (wt%, d.b.)	0.125	0.190
K (wt%, d.b.)	0.033	0.095
Mg (wt%, d.b.)	0.027	0.029
Si (wt%, d.b.)	0.065	0.063

It is important to stress that the ash forming matter in wood has a very strong influence on many aspects of wood pyrolysis and combustion. This study confirms previous observations that the mineral matter content, and in particular the potassium content, influences char yield [9,10].

In Figure 7 the char yields from the pyrolysis tests are shown. As the pyrolysis temperature increases, char yield decreases. At any temperature in the applied interval pyrolysis in TGA had much higher char yield than fast pyrolysis in EFR, which was as low as 1% to 2.6% for pine wood and 4.7% to 6.1% for beech sawdust on a dry ash free basis.

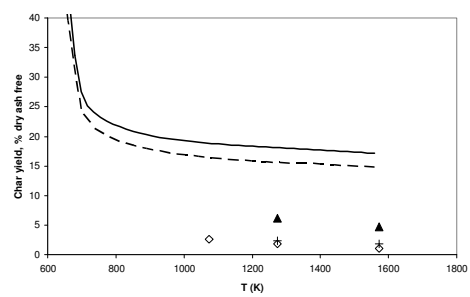

Figure 7: Wood char yield as a function of pyrolysis temperature. Lines correspond to pyrolysis in TGA at a heating rate of 40 K/min, symbols to fast pyrolysis in EFR. Continuous line: pine wood of nominal size 90-125 µm; dotted line: beech sawdust of nominal size 250-355 µm; ◊: pine wood 90-125 µm; +: pine wood 250-355 µm; ▲ beech sawdust 250-355 µm.

As far as char reactivity is concerned, a volumetric reaction model was used to analyze the mass loss curves from TGA experiments to determine the oxidation kinetics. The model assumes a single first order reaction (SFOR).

In order to make comparison of char reactivity easier the activation energy Ea was fixed at 166 kJ/mol and the pre-exponential factor was thus the only parameter to be derived. This method had been used previously by Zolin

[2]. Good agreement was generally found between experimental data and mass loss curves generated with the derived SFOR kinetic parameters.
Some of the kinetic results are illustrated in Figure 8, which shows the calculated pre-exponential factor as a function of the temperature of formation (pyrolysis temperature) of the chars.

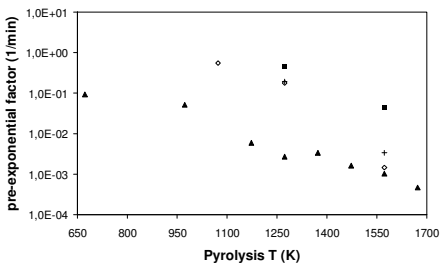

Figure 8: Oxidation reactivity (pre-exponential factor) of char. Activation energy was set to 166 kJ/mol. ▲: chars produced in STA, pine particles of nominal size 90-125 µm ; ◊: EFR pine chars, parent particles of nominal size 90-125 µm; +: EFR pine chars, parent particles of nominal size 250-355 µm; ; ■: EFR beech chars, parent particles of nominal size 250-355 µm.

As can be seen in Figure 8, chars produced in EFR under boiler-like conditions had higher reactivity than those produced at much milder conditions in the TGA analyzer. This is probably due to the major transformation of the particle structure during fast pyrolysis. Mineral matter also affects char reactivity; potassium and calcium, for instance, are known to catalyze the oxidation reaction [9,10]. This agrees with the observation, from Figure 8, that beech char was more reactive than pine char.

Conclusions

Pyrolysis experiments were carried out in an Entrained Flow Reactor (EFR) and in a thermogravimetric analyzer (TGA), to investigate how char properties depend on pyrolysis conditions. Pine wood and beech sawdust were used as fuels. The produced char was analyzed by SEM microscopy and its reactivity to oxygen was assessed by thermogravimetry.

Wood particles subjected to rapid heating to high temperatures in the EFR did not retain the typical wood fibrous structure: pine char particles were spherical and highly porous, beech char particles were less spherical but still porous with a smooth surface, indicating some plasticity during pyrolysis.

The char yield of pyrolysis in EFR was far lower than that of slow pyrolysis in TGA. EFR chars had a higher reactivity than TGA chars.

The mineral matter content of the fuel has been shown to be very important in determining char characteristics during fast pyrolysis, including char morphology and char reactivity. The fuel with the lowest ash content (pine) attained a greater structural modification of the particles during pyrolysis. Moreover, the catalytic action of mineral matter could explain the fact that the char from the more ash containing fuel (beech) had higher oxidation reactivity.

References

1. E. Cetin, B. Moghtaderi, R. Gupta, T.F. Wall, Fuel 83 (2004) 2139-2150
2. A. Zolin, Reactivity of solid fuels, Ph.D. Thesis, 2001, DTU
3. E. Biagini, C. Fantozzi, L. Tognotti, Combust. Sci. and Tech. 176 (2004) 685-703
4. T.F. Wall in: C.J. Lawn (Ed), Principles of Combustion Engineering for Boilers, Academic Press, UK, 1987
5. M.J. Wornat, R.H. Hurt, K.A. Davis, N.Y.C. Yang, 26th Symp. on Comb., The Comb. Inst. (1996) 3075-3083
6. R. Hurt, J. Sun, M. Lunden, Combust. Flame 113 (1998) 181-197
7. C. Branca, C. Di Blasi, Energy & Fuels 17 (2003) 1609-1615
8. S.V. Sotirchos, V.N. Burganos, Chem. Eng. Science 41 (6) (1986), 1599-1609
9. J.M. Jones, L.I. Darvell, T.G. Bridgeman, M. Pourkashanian, A. Williams, Proceed. Comb. Inst. 31 (2007) 1955-1963
10. Jensen A., Dam-Johansen K., Wójtowicz M.A., Serio M.A. Energy & Fuels 12 (1998), 929-938.

Florin Paul Davidescu

Phone: +45 4525 2811
Fax: +45 4525 2906
E-mail: xfpd@fpd.dtu.dk
WWW: http://capec.kt.dtu.dk
Supervisors: Sten Bay Jørgensen
Henrik Madsen

PhD Study
Started: January 2005
To be completed: December 2007

Quantitative Experimental Design for Stochastic Differential Equations

Abstract
An important and necessary step during dynamic model development is to design experiments. The aim of quantitative experimental design is to maximize the information required for parameter estimation to minimize their uncertainty by manipulating various control variables such as the initial values of the system states, the sampling times the input profile values and their switching times between the values. An algorithm for design of experiments for stochastic differential equations based on an iterated extended Kalman Filter for solving a system of stochastic differential equations is presented. An optimal experimental design for a fed-batch bioreactor is used as benchmark.

Introduction

In different applications such as design, control, optimization, in (bio)chemical engineering and especially in developing (enzymatic) reaction networks it is desirable to develop quantitative mechanistic dynamic process models to describe and understand the process under investigation.

It is therefore necessary to perform parameter estimation and validation of the model against experimental data. Generating and collecting experimental data is an expensive operation and in order to reduce the amount of data required, experimental design is a prerequisite step. Performing model based experimental design means to maximize the information content for parameters estimation while minimizing the number of experiments. Experimental design consists in principle of two phases: qualitative and quantitative experimental design [1]. Qualitative experimental design concerns determining which input variables should be varied and which outputs should be measured in the experiments in order to be able to render unknown model parameters identifiable [1]. Quantitative experimental design, which represents the main topic of this paper, concerns determining the optimal sampling time of the measurements, the input values, the times to switch between the values and the initial values of the states.

Several investigators have addressed quantitative experimental design for dynamic models. Koerkel, [2], was among the first to develop the concepts and algorithms for quantitative experimental design for nonlinear dynamic models in forms of systems of ordinary differential equations or differential-algebraic equations. However for processes described by stochastic nonlinear differential equations this topic has received limited attention this far, at least based on the authors' knowledge. Stochastic differential equations provide an opportunity for investigating experimental design for different relations between model and measurement uncertainty. Thereby attention may be focused upon development of more robust experimental designs than possible with deterministic models.

The main contribution of this paper is the development of a procedure and its algorithmic implementation as a software tool for performing quantitative experimental design for parameter estimation for stochastic differential equation models. The classical D-optimal design criterion is employed here. The algorithm is applied to a bioengineering example, which is used for benchmarking the methodology.

Specific Objectives

The objectives of the work are:

To develop a methodology and an algorithm addressing the problem of quantitative experimental design for stochastic differential equations

To illustrate the methodology though a case study

Methodology

Two approaches are usually taken when incorporating prior available knowledge about the

model parameters. The first approach takes into account the a-priori uncertainty of the model parameters (θ). The parameters are assumed to belong to a population with a known distribution p(θ). In this fashion, an ED-optimal experiment is one for which the choice of experiment decision variables maximizes the expected value over the population of possible parameter values [3]. Experiments designed in this way are good on average but can be poor for some values of the parameters [3].

The second approach aims to determine experimental designs φ_{WC}, that optimize the worst possible performance for any value of θ parameters in the parameter space. Using this approach the only prior information needed about θ is the admissible domain. In this way the design tries to ensure acceptable performance for all possible values of θ.

The problem of quantitative experimental design for stochastic differential equations is going to be solved as a dynamic optimization problem similar to the case of DAE proposed by [3] where the design variables to be optimized are the initial values of the stochastic states, the input profile values and their switching time and the sampling times. The objective function is to maximize the information content.

The optimization algorithm selected for this problem is a differential-evolution based algorithm with a small adaptation. The motivation for selecting a differential-evolution based algorithm is this is a global type of optimization algorithm, which can handle constraints and where the objective function can be noisy. Moreover, a differential-evolution based algorithm is one of the fastest algorithms for global search in terms of number of function evaluations needed to achieve an acceptable convergence. Various reviews on global optimization algorithms have demonstrated these properties in comparison with other algorithms [4].

Differential evolution (DE), in principle, works with a population P_G, of candidate solutions. These candidate solutions are G individuals of the population. A constant population during the optimization process, consisting of NP, real-valued vectors Φ_{iG} is used. The "i" indexes the population NP and G is the generation to which the population belongs. The population $P_{G=0}$ is initialized with random values chosen from within given boundaries. The vectors in the current population, P_G, are randomly sampled and combined to create candidate vectors for the next generation, P_{G+1}. Several operations have been proposed in literature for obtaining the trial population P_{G+1}. A simple algorithm is used to drive the population into the feasible domain as described below:

If both compared solutions are feasible, the one improving the objective function value is selected.

If one solution is feasible and the second is infeasible then the feasible one is selected.

If the compared solutions are infeasible, the sum of the constraints function violation is computed and the one for which the total violation is smallest will be selected.

The objective function is a standard scalar measure of the Fisher Information Matrix (FIM) e.g. the determinant of the matrix (D criterion). Since the data sets are to be collected for parameter estimation, initially the focus will be on all unknown parameters, thus the D-optimal experimental design will be considered in this work. The Fisher Information Matrix expresses the informational content. In a general formulation, the FIM is computed as the negative of the expectation of the second derivative of the log-likelihood function. In this framework the FIM will be computed using a Monte Carlo type of method as proposed by Spall [5]. The main idea is to generate a large number N of Hessian matrices in a Monte Carlo fashion and then to average them and obtain a FIM estimate. The algorithm used for calculating the design objective is illustrated in Figure 1.

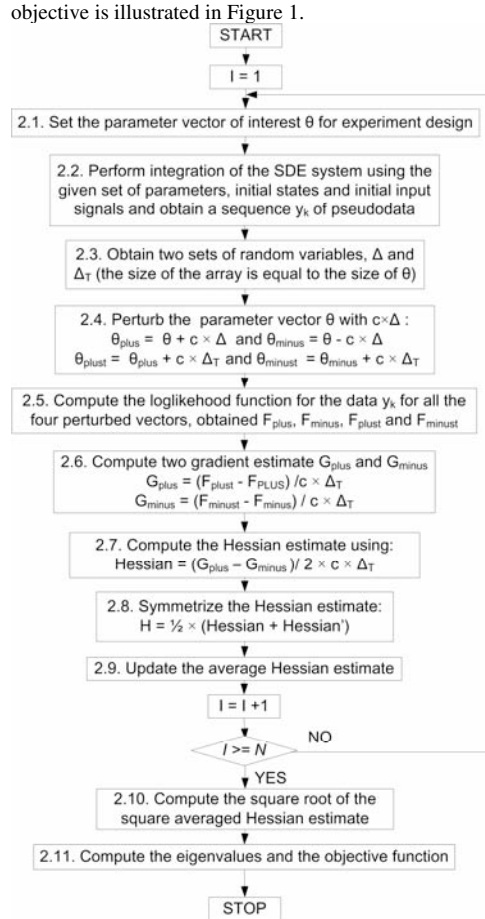

Figure 1: The algorithm used for computing the Fisher Information Matrix

It should be mentioned that the objective function is evaluated just for the case where both parameter vectors are feasible. For the case of an infeasible solution, the selection rule does not compare the objective function

values but only the evaluation of the constraints functions is required. Because of that, for finding the first feasible solution an effective selection pressure will be applied. This results in a fast convergence to the feasible regions of the search space [6].

Case study

This section presents the application of the algorithm to a model described by 2 stochastic differential equations. The model represents a fed-batch bio-reactor Asprey[3]. The system of ordinary differential equations has been modified to a system of stochastic differential equations. The diffusion terms are considered to be independent of the states. The model equations are reproduced below and the modifications included.

$$dx_1 = (r - u_1 - \theta_4) \cdot x_1 \cdot dt + \sigma_1 \cdot d\omega$$

$$dx_2 = -\frac{r \cdot x_1}{\theta_3} + u_1 \cdot (u_2 - x_2) + \sigma_2 \cdot d\omega$$

$$r = \frac{\theta_1 \cdot x_2}{\theta_2 + x_2}$$

In the equations above eq. (1-2), x_1 represents the biomass concentration [g/l], x_2 represents the substrate concentration [g/l], u_1 is the dilution rate [h^{-1}] and u_2 is the substrate concentration in the feed [g/l], the σ_1 and σ_2 represents the diffusion terms. The experimental conditions are:

The initial concentration, x_2^0, is always 0.1 [g/l] and cannot be manipulated for experimental design purposes.

Both x_1 and x_2 can be measured during the experiments. The objective is to design an experiment that will maximize the information for estimation of the four-model parameters θ_1- θ_4.

Results

The experimental design performed and reported here is equivalent to the first step of the robust optimal design proposed by [3]. In the original paper the authors also consider a known interval for each of the parameters. However, the goal of this comparison is testing the algorithm and the developed program rather than a full comparison of results/performance. The set of initial conditions is given below, in Table 1.

Table 1: Initial design as in [2].

Variable	Values
x_1^0	5.5
$t_{sp\,l}; l = 1,\text{K}, n_{sp}$	2.0,4.0,6.0,8.0,10.0, 12.0,14.0,16.0,18.0,20.0
$t_{sw1,i}; i = 1,\text{K}, n_{sw1}$	4.0, 8.0, 12.0, 16.0, 20.0
$t_{sw2,i}; i = 1,\text{K}, n_{sw2}$	4.0, 8.0, 12.0, 16.0, 20.0
$z_{1,i}; i = 1,\text{K}, n_{sw1}$	0.12,0.12,0.12,0.12,0.12
$z_{2,i}; i = 1,\text{K}, n_{sw2}$	15.0,15.0,15.0,15.0,15.0

The objective function has been evaluated for different values of diffusion terms and measurement variances. In [3], there is no mention of the measurements variance. Here, a screening of different values for the diffusion terms and for the variance was performed and is given below in Table 2.

Table 2: Variance influence on FIM

Variance, Σ=0.01	Det(FIM)
0.1	4.8704E-030
0.01	4270.3900
0.001	Singular matrix
1.0-06	147391.8855
1.0e-10	197272.5580
1.0e-16	132185.6403

The value reported by Asprey, [3] for this initial design obtained using the approach presented in the same paper was det(FIM)=$2.410*10^8$. The simulation data using this initial design and the parameters Σ= 0.01 and S=1.0e-8 are plotted in figures 2-3. By Σ it is denoted the diagonal matrix containing all the diffusion terms σ_i.

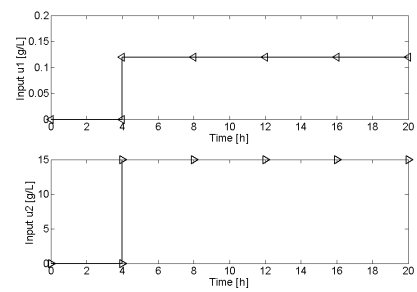

Figure 2: Intial input profiles, before performing experimental design.

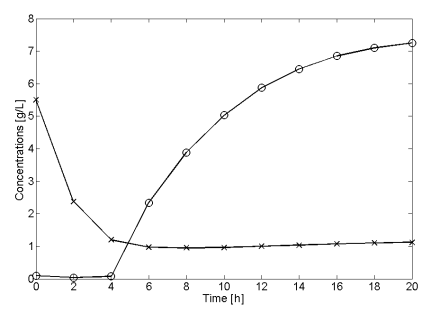

Figure 3: The output profiles for the initial design

The results obtained after optimization with the following values for Σ= 0.01, S=1.0e-10 and the optimization parameters G=5800, NP = 15, N = 100 are given in Table 3.

The design criteria has been improved significantly to a value of -log(det(FIM)) = -20.01 or det(FIM) = $4.9*10^8$

. Thus, by applying optimal experimental design the information content of the data for parameter estimation much larger.

Table 3: Optimized experimental design

Variable	Values
x_1^0	9.85E+00
$t_{sp_l}\ l=1,\mathrm{K}\ ,n_{sp}$	1.01,2.466,4.56,6.84,8.82,2.85,3.29,3.47,3.61,3.99
$t_{sw1,i}\ i=1,\mathrm{K}\ ,n_{sw1}$	0.21,3.61,13.45,27.59,36.66
$t_{sw2,i}\ i=1,\mathrm{K}\ ,n_{sw2}$	0.15,12.56,25.34,29.85,38.85
$z_{1,i}\ \ i=1,\mathrm{K}\ ,n_{sw1}$	0.168,0.06,0.15,0.06,0.08
$z_{2,i}\ \ i=1,\mathrm{K}\ ,n_{sw2}$	33.73,6.68,16.51,10.71,5.70

The simulated profiles of the obtained experimental design as well as the values of the inputs and their switching time are given below in figures 4-5.

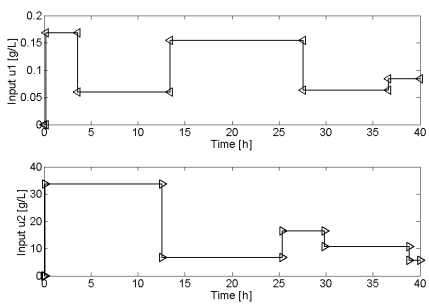

Figure 4: Input profile, after performing experimental design.

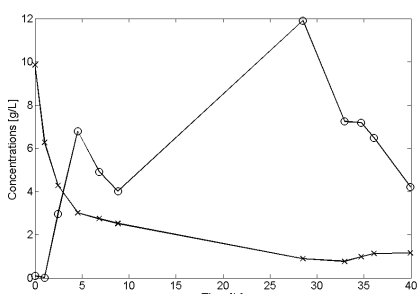

Figure 5: The output profiles for the optimal design

Even though the results presented in Table 2 and Figures 4-5 represents the output of a D optimal experimental design, when comparing with the Asprey [2] paper the results are different. The differences appears both from the difference in the objective value criterion and from the nature of the stochastic differential equations.

References

1. Walter, E. and Pronzato, L. 1990, Qualitative and quantitative experiment design for phenomenological models-a survey, Automatica 26(2), 195–213.
2. Korkel, S., Bauer, I., Bock, H. G. and Schloder, J. P. 1999, A sequential approach for nonlinear optimum experimental design in dae systems, Proc. of Int. Workshop on Scientific Computing in Chemical Engineering
3. S.P. Asprey and S. Macchietto, Designing robust optimal dynamic experiments, Journal of Process Control, 2002, 12, 545-556
4. Storn, R. 1997, Differential evolution simple and efficient heuristic for global optimization over continuous spaces, Journal of Global Optimization 11, 341–359.
5. Kukkonen, S. and Lampinen, J. 2006, Constrained real-parameter optimization with generalized differential evolution, 2006 IEEE Congress on Evolutionary Computation, IEEE, pp. 207–214
6. Spall, J. C.: 2005, Monte carlo of the fisher information matrix in nonstandard settings, Journal of omputational and Graphical Statistics 14(4), 889–909.

List of Publications

1. F.P. Davidescu, M. Henrik, S.B. Jørgensen, "Systematic qualitative experimental design based upon identifiability analysis", Computer-Aided chemical engineering ESCAPE17 volume, Elsevier 2007
2. F.P.Davidescu and S.B. Jørgensen, “Parameters identifiability analysis of nonlinear dynamic models”, submitted to Elsevier, 2007

Joanna Maria Drews

Phone: +45 4677 5490
Fax: +45 4677 4791
E-mail: jmd@polymers.dk
Supervisors: Søren Hvilsted, DTU
Kristoffer Almdal, Risø-DTU
Keld West, NanoGeoScience, Copenhagen University
Pater Kingshott, iNANO, Aarhus University

PhD Study
Started: February 2005
To be completed: January 2008

Surface Polymerisation Methods for Optimized Adhesion

Abstract
This Ph.D. project, which focuses on surface modification and surface characterisation, is part of an integrated framework programme on "Interface design of composite materials". As the project draws to an end, this paper summarises some of the main findings.

Introduction
Plasma polymerisation is widely used as a surface modification technique, e.g. for modifying carbon fibres in order to achieve an improvement in the strength of the fibre/matrix interface. In the present study glassy carbon was used as a planar model of carbon fibres. This model system has been confirmed by Launay et al. [1]. Glassy carbon and PE substrates were modified using a low-power AC 2-phase plasma system as described by Winther-Jensen et al [2]. The plasma modification technique allows for using a wide range of (organic and/or inorganic) monomers as well as for varying the coating thickness. The plasma modification time can vary from seconds to several minutes. The drawback of plasma polymerisation is that the resulting structure of the created layers is complicated and thus difficult to characterise, requiring detailed surface characterisation techniques.

The main goal of this Ph.D. study is to investigate the influence of functional groups and their density on the interfacial strength of adhesion between modified glassy carbon and epoxy resin. Different densities of functional groups on the surface were obtained by introducing different plasma power levels during the plasma modification. Furthermore, changes in the surface chemistry and topography of the modified surfaces were examined.

Results
Previously, Friedrich et al. [4] have studied the influence of different functional groups on the interfacial strength, i.e. between plasma modified layers and aluminium. Friedrich found carboxylic acid groups to yield promising results, and hence it was decided to investigate carboxylic acid groups as means of optimizing adhesion. Since maleic anhydride is well studied and widely used in industry, this monomer was chosen for the surface modification.

By using maleic anhydride one obtains surfaces having a high density of carboxylic acid (after hydrolysis of anhydride groups). To study the influence of carboxylic acid groups on the interfacial adhesion strength between the modified layer/matrix, i.e. for a low density of carboxylic acid groups, the 1,2-methylenedioxy benzene monomer was therefore investigated for comparison. This monomer has previously been examined by Winther-Jensen et al. [5], who has demonstrated that carboxylic acid groups are produced on the surface under the plasma conditions. Lastly, both of the monomers mentioned above were mixed together in order to obtain surfaces with an "intermediate" concentration of carboxylic acid groups.

The surfaces modified with maleic anhydride and 1,2-methylenedioxy benzene were polymerised with a range of plasma energies from 0.3 to 0.8 W/L (up to 1.2 W/L for maleic anhydride), holding the polymerisation time constant. No significant changes were found in the surface chemistry from XPS and ATR-FTIR analysis, while measurements of the thicknesses of the coatings showed significant changes. Since the surfaces were modified with different plasma powers and constant polymerisation time, the thickness changes can be attributed to different rates of deposition/polymerisation.

The deposition rate was found to increase with the plasma power. The influence of the plasma power is

clearly seen in the interfacial adhesion, where the maximum strength is achieved for glassy carbon surfaces modified with maleic anhydride, cf. Figure 1. At first glance the differences in the strength of the interface might be attributed to the thicknesses of the layers. The influence of the thickness was therefore further investigated by creating thinner layers of the modification yielding the strongest values for the fracture toughness (maleic anhydride), i.e. by reducing the polymerisation time to 3 minutes. The interface strength proved to be unchanged compared to that of the longer polymerisation, and hence we conclude that the thickness of the polymerised layer does not play an important role. A detailed discussion of the surface chemistry and the interfacial adhesion between the modified layer and the matrix can be found in Drews et al. [6].

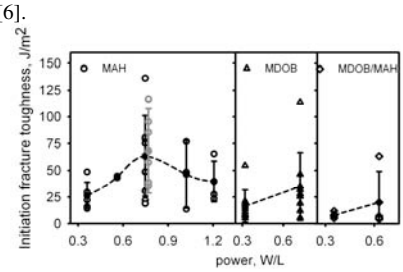

Figure 1: Initiation of the crack propagation of different plasma surface treatments, the plasma treatments in black is 10 min; in grey 3 min. The initiation fracture toughness for untreated glassy carbon is 5-7 J/m^2.

As seen on Figure 1, the plasma modification using 1,2-methylenedioxy benzene yield a significant and measurable improvement of the interfacial strength. This was not the case for the co-polymer made of 1,2-methylenedioxy benzene and maleic anhydride, where specimens would often break during processing to indicate a very weak interface.

The stability of the coatings of plasma modified maleic anhydride has been studied in details. The hydrolysis of the coatings is examined by the toluidine blue staining method in a number of different solutions, from low to high pH, and for varying temperature. The speed of the hydrolysis in water and in acid was found to be comparable and the plasma films stable. As for base solutions, coatings made with different plasma power (to keep the thickness constant) exhibited different temporal behaviour as shown on Figure 2. The different trends of the hydrolysis have been assigned to different levels of cross-linking of the plasma polymerised layer. For a detailed discussion, please see Drews et al. [7].

Similar base hydrolysis studies was subsequently carried out for the plasma coatings of 1,2-methylenedioxy benzene and the co-polymer. The coatings of 1,2-methylenedioxy benzene proved to be stable in 10 mM NaOH in the plasma range 0.3 – 1.2 W/L, while the co-polymer is completely unstable in the base solution.

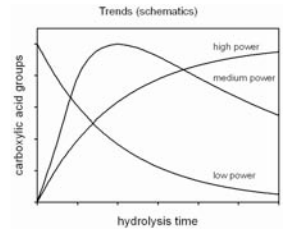

Figure 2: Schematics of the hydrolysis of anhydride groups and the dissolution of maleic anhydride coatings as a function of plasma power/constant thickness (based on hydrolysis in 10 mM NaOH).

The results of the hydrolysis seem largely consistent with the differences in the interfacial strength. Clearly, the co-polymer coatings are weak and unstable, while the plasma polymerised layers of 1,2-methylenedioxy benzene on the other hand exhibit remarkable stability. For the maleic anhydride, the layers created at low power evidently hydrolyse easily, i.e. exhibiting almost no degree of cross-linking, and thus the corresponding adhesion is also weak. The differences in the interfacial strength at intermediate and high polymerisation energy may likewise be explained by varying degrees of cross-linking: at high plasma energy, a high level of cross-linking affects the flexibility of the layer, reducing the fracture toughness (see also Drews et al. [8]).

Acknowledgement
This Ph.D study is part of a STVF project on “Interface design of composite materials” (26-03-0160). The project is coordinated by the Materials Research Department, Risø National Laboratory/DTU, and carried out at the Graduate School of Polymer Science, DTU.

References

1. H. Launay, C.M. Hansen, K. Almdal, Carbon *in press*
2. B. Winther-Jensen, K. Glejboel, US patent No. 6,628,084 B1 (30 Sep 2003); B. Winther-Jensen, S.F. Christensen, S.G. Petersen, US patent No. 0086660 A1 (6 May 2004).
3. B. Winther-Jensen, K. Norrman, P. Kingshott, K. West, Plasma Process. Polym. 2 (2005) 319;
4. J. Friedrich, G. Kuhn, R. Mix, and W. Unger, Plasma Processes Polym. **1** (2004) 28;
5. B. Winther-Jensen, K. Norrman, P. Kingshott, and K. West, Plasma Processes Polym. **2** (2005) 319;
6. J. Drews, S. Goutianos, P. Kingshott, S. Hvilsted, N. Rozlosnik, K. Almdal, B.F. Soerensen, J. Vacuum Sci. Techn. A **25** (2007) 1108.
7. J. Drews, H. Launay, C.M. Hansen, K. West, S. Hvilsted, P. Kingshott, K. Almdal, to appear in Appl. Surf. Sci.
8. J. Drews, S. Goutianos, K. West, S. Hvilsted, K. Almdal, Proceedings of the 28th Risø International Symposium on Materials Science.

Corinne Eenschooten
Phone: +45 4525 2886
Fax: +45 4588 2258
E-mail: cre@kt.dtu.dk
www: http://www.ivc-sep.kt.dtu.dk
Supervisors: G. Kontogeorgis (IVC-SEP)
E. Stenby (IVC-SEP)
F. Longin (Novozymes Biopolymer)
K. Schwach (Novozymes Biopolymer)
R. Gurny (University of Geneva)

Industrial PhD Study
Started: May 2005
To be completed: May 2008

Development of Hyaluronic Acid-Based Nanocarriers towards the Topical Delivery of Cosmetic Active Ingredients or Pharmaceutical Drugs

Abstract
The objective of this Industrial PhD research project is the development of hyaluronic acid (HA)-based nanocarriers towards the topical delivery of cosmetic active ingredients or pharmaceutical drugs. The physico-chemical properties of native HA were modified by the introduction of alkenyl chains onto HA backbone. This new amphiphilic HA was shown to spontaneously form polymeric micelles which were characterized in aqueous media for their shape, surface charge and size. A putative molecular structure of the micelles was suggested to explain how this amphiphilic HA self-associates. We believe that the nanostructures provided by HA-based polymeric micelles could constitute a potential valuable and versatile multi-functional biocompatible and resorbable delivery system which could be used to encapsulate and transport poorly soluble compounds in aqueous media.

Introduction
HA is a natural linear polymer consisting of alternating 1,4-linked units of 1,3-linked glucuronic acid and *N*-acetylglucosamine (Figure 1).

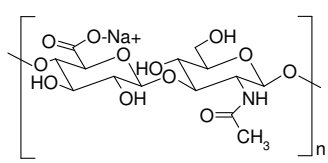

Figure 1: Repeating unit of hyaluronic acid (sodium salt).

HA is found in all mammalian tissues and is particularly abundant in the vitreous humor of the eye, the synovial fluid and the skin [1].

Due to its biocompatibility and resorbability, HA constitutes an interesting building block for applications in drug delivery [2]. However, the development of HA carriers is impeded by the high hydrophilicity and the poor biomechanical properties of the native molecule [3]. A variety of chemical modifications have therefore been devised to provide HA with new improved physico-chemical properties [3]. In particular, introduction of alkyl chains onto the HA backbone has shown that the resulting HA derivatives exhibit significantly different physico-chemical properties compared to the native polymer and that new associative systems based on these HA derivatives can be created [4-5].

In the present research project, HA was alkenylated with octenyl succinic anhydride (OSA). The physico-chemical properties of the resulting OSA-HA derivatives were studied by fluorescence spectroscopy (FS), transmission electron microscopy (TEM), zetapotentiometry (ZP) and light scattering (LS).

Specific Objective
Colloidal carriers such as HA-based microparticles have been devised for the encapsulation of hydrocortisone [6], nerve growth factor [7] and calcitonin [8]. However, due to their dimensions, these microdevices are unsuitable for (trans)dermal applications given the dimensions of the intercellular space between skin corneocytes [9].

The objective of this research project is to develop HA-based nanocarriers towards (trans)dermal drug delivery using an innovative technology resulting in entirely biocompatible and resorbable devices conveying all HA beneficial properties in addition to the cosmetic or therapeutic efficacy of encapsulated compound(s).

Methods

OSA-HA was prepared by reacting HA with OSA under mild alkaline conditions using the method described by Tømmeraas and Eenschooten [10].

The structure of OSA-HA was confirmed by Proton Nuclear Magnetic Resonance (^{1}H NMR) (Mercury VX, Varian, Palo Alto, CA, USA).

The degree of substitution (DS) of OSA-HA, which corresponds to the number of OSA chains covalently bound per one hundred HA disaccharide units, i.e. to the ratio y/(x + y) (cf.) was determined by ^{1}H NMR by comparing the intensity of the methyl protons on HA to that of the methyl protons on the covalently bound OSA chains.

The critical aggregation concentration (CAC) of OSA-HA was determined by FS using a thermostated spectrofluorometer (FluoroMax, HORIBA Jobin Yvon Inc, Edison, NJ, USA) and Nile Red as fluorophore.

The morphology of the OSA-HA polymeric micelles was studied by TEM (EM 410, Philips Electronic Instruments, Eindhoven, the Netherlands).

The surface charge of the OSA-HA polymeric micelles was measured by zetapotentiometry (Zetasizer 3000HS, Malvern, Worcestershire, United Kingdom).

The size distribution of the OSA-HA polymeric micelles was evaluated by LS (AVL-CGS-8, AVL, Langen, Germany).

Results and Discussion

Chemical modification of HA

HA was modified by reaction with OSA under mild alkaline conditions.

The molecular structure of the resulting OSA-HA can be described as a comb copolymer consisting of a hydrophilic HA backbone and covalently bound hydrophobic OSA chains.

By varying experimental conditions such as HA and buffer concentrations, OSA/HA molar ratio and reaction time, OSA-HA derivatives with a degree of substitution of 6, 18 and 44 % (OSA-HA6, OSA-HA18, OSA-HA44) were prepared.

Study of the physico-chemical properties of OSA-HA

Fluorescence study

The introduction of OSA chains onto HA is expected to change the physico-chemical properties of the native HA and more specifically the intra and/or intermacromolecular interactions between HA chains. The CAC of OSA-HA was determined in a phosphate buffer saline (PBS, pH = 7.4) at 25 °C by fluorescence spectroscopy using Nile Red as fluorophore.

The maximum fluorescence emission wavelength of Nile Red was followed as a function of the OSA-HA concentration as shown in .

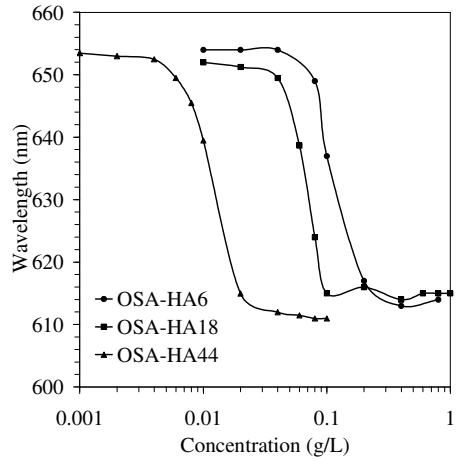

Figure 2: Evolution of the maximum fluorescence emission wavelength of Nile Red as a function of the OSA-HA concentration.

The latter decreases from approximately 650 to 610 nm when the OSA-HA concentration increases. Furthermore, the concentration at which this change is observed depends on the DS. Such a substantial decrease indicates that the immediate environment of Nile Red changes from polar to less polar. This is due to the increasing interactions between Nile Red and the OSA chains when OSA-HA polymeric micelles are formed.

A plot of the CAC as a function of the DS of OSA-HA indicates that the CAC linearly decreases with the DS. The increased attraction between the OSA chains at high DS indeed results in the earlier formation of the OSA-HA polymeric micelles which explains the lower CAC values found on the plot.

Microscopy study

The morphology of the OSA-HA polymeric micelles was studied in PBS (pH = 7.4), at room temperature, by TEM using a uranyl acetate negative staining. The TEM micrograph on Figure 3 illustrates that the OSA-HA polymeric micelles are relatively polydisperse spherical assemblies with diameters between 10 and 120 nm.

The difference in size between the micelles is most likely owing to the difference in the number of OSA-HA molecules involved in each micelle which can be due to the potential non-homogenous substitution of OSA chains on HA.

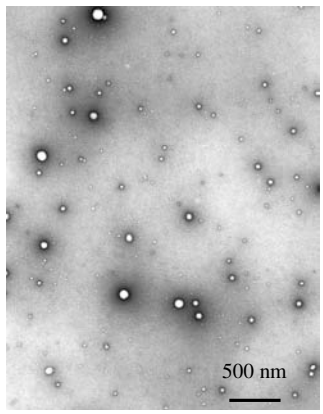

Figure 3: TEM micrograph of OSA-HA polymeric micelles (OSA-HA44, 1 mg/mL)

Electrophoretic mobility study

The zeta potential of the OSA-HA polymeric micelles was determined in PBS (pH = 7.4), at 25 °C, by zetapotentiometry. The surface of the OSA-HA polymeric micelles is negatively charged with a mean zeta potential of -28 mV. This negative charge is due to the presence, at neutral pH, of carboxylate groups on OSA-HA, arising from both the native HA backbone and the hemiesters generated during the reaction between HA and OSA

Light scattering study

In order to get a more detailed picture of the dimensions of the OSA-HA polymeric micelles, a statistical analysis of the micelle diameters on TEM micrographs was conducted in parallel to DLS measurements.

The hydrodynamic diameter of the OSA-HA polymeric micelles was determined in PBS (pH = 7.4), at room temperature, by DLS and was simulated from the micelle size distribution obtained by TEM by applying the Rayleigh-Gans-Debye (RGD) theory of dynamic light scattering [11].

Figure 4 represents the variation of the hydrodynamic diameter as a function of the scattering angle as measured by DLS and as simulated from the micelle size distribution obtained by TEM for two different values of the hydration coefficient α (α = 0 for dehydrated micelles and α = 12 for hydrated micelles). The diameter values of the micelle classes on the size distribution obtained by TEM were indeed adjusted so as to take into account micelle hydration. Micelle hydration was characterized by means of a coefficient α which was defined as the ratio between the volume of water and the volume of OSA-HA making up the fully hydrated micelles. Diameter values of the micelle classes on the size distribution obtained by TEM were accordingly multiplied by the constant $(\alpha + 1)^{1/3}$.

Values of the hydrodynamic diameter measured by DLS are considerably higher than those simulated from the crude microscopy data, i.e. when α = 0. Indeed the OSA-HA polymeric micelles are in a hydrated form during DLS measurements, whereas they lose their water content during TEM studies.

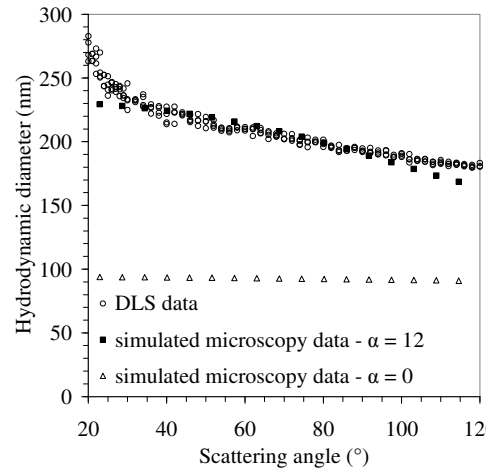

Figure 4: Hydrodynamic diameter of OSA-HA polymeric micelles (OSA-HA44) as a function of the scattering angle.

Taking micelle hydration into account in the simulation (α = 12) allows a better fit between the values of the hydrodynamic diameter obtained by DLS and those obtained by microscopy and over most of the scattering angles. The fairly large deviation of the hydrodynamic diameter measured by DLS from that simulated by microscopy (with α = 12) at low scattering angle indicates that few structures with dimensions superior to the detection range of the DLS instrument are present in solution. These few structures might be micelle aggregates although micelle aggregation could not clearly be identified on TEM micrographs. The comparison between the microscopy and LS evaluations shows that the OSA-HA polymeric micelles are highly hydrated structures in solution with a mean hydrodynamic diameter falling between 170 and 230 nm.

Molecular structure considerations

Chen et al. [12] have described the structure of the polymeric micelles based on HA modified with polycaprolactone (2300 Da) chains as a spherical HA hydrophilic corona surrounding a polycaprolactone hydrophobic core. Given the relatively short length of the OSA chains on HA, the aggregation of OSA-HA is unlikely to occur this way.

Substituted disaccharide units on OSA-HA were assumed to behave like monomeric surfactant molecules capable of self-associating into conventional spherical monomeric micellar domains. The OSA-HA polymeric micelles were therefore assumed to consist of a dispersion of hydrophobic domains formed by the substituted HA units in a hydrophilic matrix formed by

the remaining unmodified HA units. This structure represents the most probable molecular arrangement for the OSA-HA molecules in the polymeric micelles given the molecular structure of OSA-HA and the necessity for the OSA chains to interact in segregated hydrophobic domains.

Conclusions

Hyaluronic acid was modified with octenyl succinic anhydride so as to provide HA with new physico-chemical properties. We have shown that the hydrophobic character of the OSA-HA derivatives can be controlled by varying the experimental conditions such as the HA and buffer concentration, the OSA/HA molar ratio and the reaction time.

Association of OSA-HA in aqueous media and solubilisation of Nile Red into the hydrophobic domains formed by the OSA chains is a linear decreasing function of the degree of substitution of the derivative between 6 and 44 % and can be predicted for OSA-HA derivatives with a DS in this range.

OSA-HA polymeric micelles are negatively charged polydisperse spherical assemblies characterized by a high degree of hydration and a hydrodynamic diameter between 170 and 230 nm.

The molecular structure of the OSA-HA polymeric micelles is most probably a dispersion of OSA-rich hydrophobic monomeric micellar nanodomains into a HA-rich hydrophilic matrix.

The nanostructures provided by the OSA-HA polymeric micelles constitute a potential biocompatible and resorbable multi-functional system that could be used to solubilise and carry poorly hydrosoluble compounds. We believe that the presence of multiple hydrophobic nanodomains in the OSA-HA polymeric micelles could be useful for the controlled release of hydrophobic actives ingredients or drugs to their targeted site of action. Encapsulation of model hydrophobic compounds in stabilized OSA-HA nanocarriers and their release *in vitro* and *in vivo* will be the subject of future investigations.

Acknowledgements

We express our gratitude to the Danish Ministry of Science, Technology and Innovation and Novozymes Biopolymer A/S for co-funding this Industrial PhD research (Grant no.: 07-001687).

We are obliged to Professor R. Gurny and Assistant Professor F. Delie, Laboratory of Pharmaceutics and Biopharmaceutics, School of Pharmaceutical Sciences, University of Geneva, Switzerland, for hosting experimental work in the periods July-August 2006 and March-June 2007.

We would also like to thank Doctor C. Bauer, National Centre of Competence in Research, Frontiers in Genetics, Bioimaging Platform, University of Geneva, Switzerland, and Doctor A. Vaccaro, Laboratory of Colloid and Surface Chemistry, Department of Inorganic, Analytical and Applied Chemistry, School of Chemistry, University of Geneva, Switzerland for their proficient help in acquiring transmission electron microscopy micrographs and analysing the light scattering data, respectively.

References

1. J. Baier Leach, C.E. Schmidt, in: G.E. Wnek, G.L. Bowlin (Eds), Encyclopedia of Biomaterials and Biomedical Engineering, Marcel Dekker, New York, United States, 2004, p. 779.
2. S. Gustafson, in T.C. Laurent (Ed), The Chemistry, Biology and Medical Applications of Hyaluronan and its Derivatives, Portland Press Ltd, London, United Kingdom, 1998, p. 291.
3. G.P. Prestwich, D.M. Marecek, J.F. Marecek, K.P. Vercruysse, M.R. Ziebell, in T.C. Laurent (Ed), The Chemistry, Biology and Medical Applications of Hyaluronan and its Derivatives, Portland Press Ltd, London, United Kingdom, 1998, p. 43.
4. S. Pelletier, P. Hubert, F. Lapicque, E. Payan, E. Dellacherie**,** Carbohydr. Polym., 43 (2000) 343-349.
5. C. Creuzet, S. Kadi, M. Rinaudo, R. Auzley-Velty, Polymer 47 (2006) 2706-2713.
6. L.M. Benedetti, E.M. Topp, V.J. Stella, J. Controlled Release 13 (1990) 33-41.
7. E. Ghezzo, L.M. Benedetti, M. Rochira, F. Biviano, L. Callegaro, Int. J. Pharm. 87 (1992) 21-29.
8. M. Rochira, M.R. Miglietta, J.L. Richardson, L. Ferrari, M. Beccaro, L.M. Benedetti, Int. J. Pharm. 144 (1996) 19-26.
9. J. Bouwstra, G. Gooris, M. Ponec, J. Biol. Phys. 28 (2002) 211-223.
10. Tømmeraas K., Eenschooten C., WO2007033677-A1
11. B.J Berne, R. Pecora, Dynamic Light Scattering, John Wiley, New York, United States, 1981.
12. Y.H. Chen, S.H. Jan, M.J. Liu, US20050123505A1.

List of Publications

1. Eenschooten C., Vaccaro A., Delie F., Guillaumie-Longin F., Kontogeorgis G.M., Stenby E.H., Schwach-Abdellaoui K., Borkovec M., Gurny R., Development of Colloidal Carriers from a Novel Amphiphilic Hyaluronic Acid; poster presented at the 21st Conference of the European Colloid and Interface Society, 10-14 September 2007, Geneva, Switzerland.
2. Eenschooten C., Deli F., Guillaumie-Longin F., Kontogeorgis G.M., Stenby E.H., Schwach-Abdellaoui K., Gurny R., Development of Colloidal Carriers from Modified Hyaluronic Acid, poster presented at the 7th International Conference on Hyaluronan, 22-27 April 2007, Charleston, South Carolina, United State.
3. Eenschooten C., Deli F., Guillaumie-Longin F., Kontogeorgis G.M., Stenby E.H., Schwach-Abdellaoui K., Gurny R., Development of Colloidal Carriers from Modified Hyaluronic Acid; poster presented at the 8th Annual Meeting of Skin Forum, 3-4 March 2007, London, United Kingdom.

Tobias Dokkedal Elmøe
Phone: +45 4525 2976
Fax: +45 4525 2399
E-mail: tde@kt.dtu.dk
WWW: http://chec.kt.dtu.dk
Supervisors: Kim Dam-Johansen, KT, DTU, DK
Jan-Dierk Grunwaldt, ETHZ, CH
Sotiris E. Pratsinis, ETHZ, CH

PhD Study
Started: March 2005
To be completed: February 2008

Production of Porous Ceramic Membranes: Modelling of Particle Deposition in Porous Structures

Abstract
The deposition of flame-made nanoparticles in porous structures has been studied using Langevin dynamics. The model suggested poor pore-penetration under experimental conditions, which agrees well with SEM imagery. The simulations reveal that the deposits grow near the pore entrance (termed “pore mouth”) rather than from within the pore, as it was initially expected. Porosities ranging from 96%-98% have been calculated for the grown films, which also agree well with experimental findings (95%-98% typically)

1. Introduction

During the formation of porous ceramic membranes by filtration of flame-made nanoparticles, particles initially deposit inside the porous substrate [1]. The process of initial deposition is extremely important, as it defines the interface between deposited nanoparticles and the substrate at which they are to adhere. As a result of this, poor contact at the interface will undoubtedly lead to poor adhesion, with peeling off and cracking of the layer as a result. The deposition inside porous structures with subsequent plugging are until now very poorly understood. Several researchers [2,3,4] studied the deposition of nanoparticles on flat substrates, however only a few studies on the deposition inside porous structures exists. Reis [5] studied the deposition of coke particles inside a porous catalysts, but assumed that deposition only occurred inside the porous structure, without the ability to grow outside. This leads to artificially thin clogs at the entrance to the pore, which will most likely never occur in a real system. A detailed study therefore seems justified.

2. Particle deposition model

In order to properly investigate the effects of changing deposition parameters, a computational model has been set up. The deposition model uses Langevin dynamics to track particle motion, which has been used by several other researchers in past studies [3,6,5,7,8]. What separates this model from previous works is that the deposition initially takes place inside the porous structure (termed "pore-plugging"). The Pe (or Peclét) number, is a dimensionless number, which specifies the ratio of convective transport to diffusional transport:

$$Pe = \frac{v_z r_p}{D} \quad (1)$$

where v_z is the fluid velocity, r_p the particle radius and D is the particle diffusion coefficient. The smaller the Pe number, the the more the deposition mechanism will be dominated by brownian diffusion. Similarly, the larger the Pe number the more the deposition mechanism will be dominated by ballistic motions. For validation purposes, the model has been compared with literature in the limits of purely brownian motion ($Pe \to 0$) and purely ballistic deposition ($Pe \to \infty$). Structures grown for intermediate Pe number are also compared, but the difference is expected to be larger, due to differences in the integration of the Langevin equation of motion (see section 2.2). All depositions are carried out at 298 K and 1 bar.

2.1. Model description and assumptions

Particles are deposited due to the filtration through the substrate pores. Consider a porous surface as a number of cylindrical capillaries all in parallel. Particles are assumed to deposit one at a time, an approach used for dilute systems in previous film-deposition model studies [4,7]. In order to obtain true random motion before deposition, the particle is released into the

system at a certain distance from the pore-mouth ($\delta_{film} + \delta_{drop}$). The particle moves into the capillary, due to brownian motion and convective transport. It moves toward the wall of the capillary, where it is assumed to deposit irreversibly once it hits. If a particle escapes the domain on its way to the pore it is reintroduced with an opposite velocity vector similar to the approach by Heine and Pratsinis [8]. Particles only deposit by touching other particles or by touching the pore-wall. The deposits are allowed to grow out of the pore (for a maximum height of δ_{film}), which models properly the change from pore-plugging to film-deposition. Particles that escape through the outlet without depositing are counted, but not considered to contribute to the changing structure as they are deposited too far down. The model domain can be seen on figure 1.

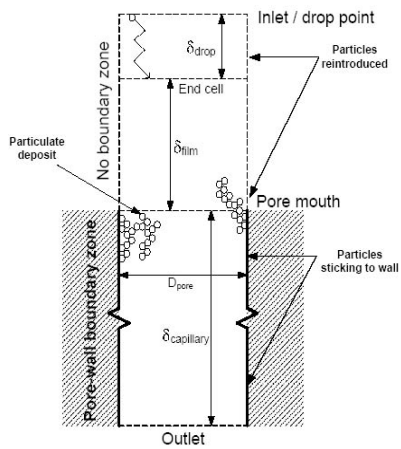

Figure 1: Schematic showing the model domain. Particles are entered at the inlet/drop point and allowed to move down through an initial cell, in which no particle deposition can take place, in order to obtain true random motion. Particles deposit on the pore-walls initially, until they build up a layer that eventually grows out of the capillary. The film is allowed to grow until it reaches the drop-cell, at which point calculations are halted.

2.2. Langevin equation of motion

The ordinary Langevin equation of motion is given as [6,8],

$$m\dot{\mathbf{v}} = -f(\mathbf{v}-\mathbf{w}) + \mathbf{F} + \mathbf{X} \qquad (2)$$

where m is the mass of the particle, $\mathbf{v}$ is the velocity (vector) of the particle, f is the friction factor (slip-correction included), $\mathbf{w}$ is the fluid velocity, $\mathbf{F}$ is the external force and $\mathbf{X}$ is a random force (due to brownian motions). Assuming no external forces are acting on the particles, partial integration of equation 2 yields [9],

$$\begin{aligned}\mathbf{v}(t+\Delta t) &= \mathbf{V} + \mathbf{v}(t)e^{-\beta\Delta t} + \mathbf{w}(1-e^{-\beta\Delta t}) \\ \mathbf{r}(t+\Delta t) &= \mathbf{R} + \mathbf{r}(t) + \frac{\mathbf{v}(t)}{\beta}(1-e^{-\beta\Delta t}) + \mathbf{w}\left(\Delta t - \frac{1}{\beta}(1-e^{-\beta\Delta t})\right)\end{aligned} \qquad (3)$$

where $\mathbf{r}$ is the particle position vector and β is equal to $\frac{f}{m}$. The capital $\mathbf{V}$ and $\mathbf{R}$ are the components of the respective velocity and particle displacement, due to the random force.

3. Model validation

3.1. Perfect sink validation

The model is first validated against the case where the capillary walls act as perfect sinks. That means, once particles deposit, they disappear, thereby not changing the geometry of the system. In this validation, the capillary was used for the entire domain ($\delta_{drop} = 0$ and $\delta_{film} = 0$). The diffusion-convection equation for large Pe numbers (> 100) is shown as equation 5.

$$v_z \frac{\partial C}{\partial z} = \frac{D}{r}\frac{\partial}{\partial r}\left(r\frac{\partial C}{\partial r}\right) \qquad (5)$$

where v_z is the fluid velocity (assumed to be plug-flow), C is the number concentration of the aerosol, z is the axial position, r is the radial position and D is the diffusion coefficient of the particles. The boundary conditions are,

$$\begin{aligned} C(r = R_p) &= 0 \\ \frac{\partial C}{\partial r}(r = 0) &= 0 \\ C(z = 0) &= C_0 \end{aligned} \qquad (6)$$

Equation 5 with boundary conditions 6 has an analytical solution which is,

$$C(r,z) = \sum_{n=1}^{\infty} \frac{2C_0}{\lambda_n R_p J_1(\lambda_n R_p)} J_0(\lambda_n r) e^{-\frac{\lambda_n^2 z D}{v_z}} \qquad (7)$$

where λ_n is the zeroes of the Bessel function of the first kind of order 0 scaled by the pore radius, R_p, and J_1 and J_0 are the Bessel functions of the first kind of order 1 and 0 respectively. The penetration, i.e. the ratio of particles entering at a given depth z to the inlet concentration, can be used to compare with the one calculated from langevin dynamics model. This is defined as,

$$P = \frac{\overline{C}(z)}{C_0} = \frac{2\int_{r=0}^{r=R_p} C(r,z) r \mathrm{d}r}{C_0 R_p^2} \qquad (8)$$

where $\overline{C}(z)$ is the average concentration of particles at a given depth (evaluated over the cross-section of the capillary). It is common to use the dimensionless parameter $\propto = \frac{zD}{\pi R_p^2 v_z}$ when plotting penetration

curves. On figure 2 the results of the analytical model has been compared to the langevin dynamics model for two runs at varying values of $\propto$. Good comparison between the results can be observed.

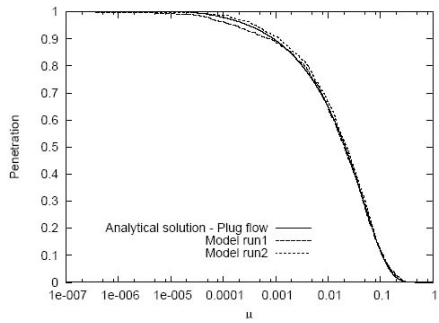

Figure 2: Analytical solution 7 compared to model runs.

3.2. Film-deposition validation

The second validation takes into account particle deposition and sticking and the changing geometry caused by this. The geometry of the model domain has been modified, so that sticking now only takes place initially at the bottom of the capillary and if the particle escapes the domain on its way down, they are reintroduced with an opposite velocity vector, like the "no boundary zone" shown on figure 1. The standard conditions for film-deposition can be seen in table 1.

Table 1: Deposition parameters and chosen domain dimensions for the film-deposition validation

Particle diameter(s) (d_p)	25,50,100 nm
Domain radius (R_p)	$40\,d_p$
δ_{film}	$80\,d_p$
Drop cell height	$20\,d_p$

In order to compare with existing models, the fractal dimension (D_f) of the deposit has been calculated. This quantity is found by first calculating the surface density [7,10],

$$\rho(z) = \frac{A_s(z)}{\pi R_p^2} \tag{9}$$

where $A_s(z)$ is the total cross-sectional area of the nanoparticles at a given depth z. The surface density is proportional to the deposition depth by,

$$\rho(z) \propto z^{D_f - 3} \tag{10}$$

which means a log-log plot of $\rho(z)$ vs. z yields the slope $D_f - 3$, from which D_f can then be evaluated. The results of the simulations at various Pe numbers can be can be seen on figure 3. The results have been compared to the ones obtained by Kulkarni and Biswas [7] and also the fractal dimension obtained by Meakin [11] for pure diffusionally grown deposits.

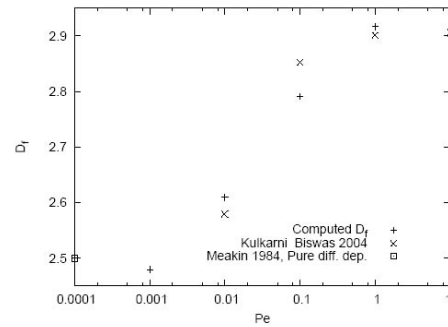

Figure 3: Fractal dimension of film deposits for varying Pe numbers. The results have been compared to the ones obtained by Kulkarni and Biswas [7] and Meakin [11].

As for the perfect sink model of section 3.1 good correlation between literature data and the model results can be observed.

4. Deposition in porous materials – Preliminary results

Now that the model has been fully validated, the deposition of particles inside the porous material has been simulated for the exact geometry shown in figure 1. The conditions for deposition can be seen in table 2. As this is still work-in-progress, only particle deposition for 50 nm particles has been shown.

Table 2: Deposition parameters and chosen domain dimensions for the capillary deposition simulations

Particle diameter (d_p)	50 nm
Domain radius (R_p)	2 ∝m
δ_{film}	10 ∝m
$\delta_{\text{capillary}}$	10 ∝m
Drop cell height	$20\,d_p$

Simulations have been carried out for $Pe = 0.01$ and $Pe = 0.1$. They have been characterized by calculation of the surface density (cf. equation 9) and the average porosity, calculated for the grown film (by grown film, one refers to the outside film from pore-mouth to the film-surface). Figure 4 shows a plot of the actual structure of the deposits for $Pe = 0.01$ and $Pe = 0.1$ respectively. The calculated average porosity was 96%-98% (highest for lower Pe numbers). This agrees well with typical experimental values (95%-98%).

From figure 4 it can be seen, that only a low degree of pore penetration takes place and the structure mainly grows from the pore-mouth and out, which has been

quantified by a plot of the surface-density for Pe = 0.1 seen on figure 5.

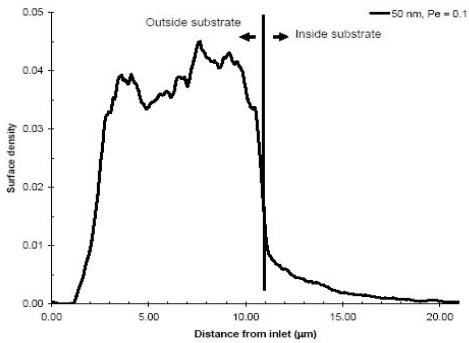

Figure 5: Surface density of a deposit in a porous material for Pe = 0.1. The density inside the pore is very low and increases rapidly near the pore mouth. This indicates a low penetration and that the deposit starts to grow from the pore mouth rather than further down into the pore

5. Preliminary conclusions

A code based on Langevin dynamics has been built. Excellent match was found for the perfect sink model. Fractal dimensions for the film-deposition model was found to range from 2.5 for purely diffusional deposition to 2.9 for balistically dominated deposition. Changing the Pe number from low values to high values showed the characteristic S-shaped curve and asymptotic behaviour, which was expected from literature. The deposition of nanoparticles within a porous substrate was afterwards simulated. It is observed visually as well as from plots of the surface densities, that the penetration of particles into the pore is quite low, and that pore plugging takes place very close to the pore mouth, rather than from within the pore. This agrees well with SEM imagery and can help explain the poor adhesion observed experimentally. It is the hope, that an increased adhesion can be obtained by an increased pore penetration. With the help of the model in the suggestion of deposition parameters, for instance changing fluid velocity and changing particle size, this may be easierly realized than by experimental trial and error. At the time of writing several simulations are currently ongoing and these will be documented soon in a planned paper.

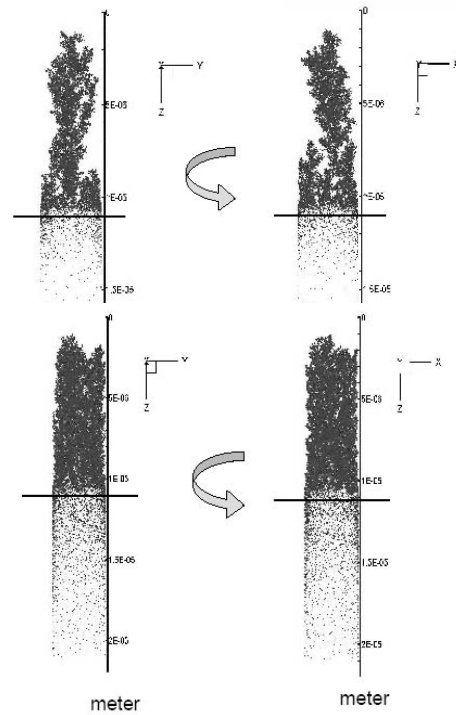

Figure 4: Structure of a deposit in a porous material for Pe = 0.01 (top) and Pe = 0.1. The latter value corresponds well to ones found during typical deposition conditions. The structure has been turned to show the YZ and XZ planes. The black line indicates the position of the pore mouth

References

1. S.K. Andersen, T. Johannssen, M. Mosleh, S. Wedel, J. Tranto, H. Livbjerg, J. Nanoparticle Res. 4 (5) (2002) 405-416
2. S. Veerapaneni, M.R. Wiesner, J. Col. Interface Sci. 162 (1) (1994) 110-122
3. P. Kulkarni, P. Biswas, J. Nanoparticle Res. 5 (3-4) (2003) 259-268
4. L. Mädler, A.A. Lall, S.K. Friedlander, Nanotec. 17 (2006) 4783-4795
5. F.D.A.A. Reis, Physica A. 350 (2005) 407-417
6. D.L. Ermak, H. Buckholz, J. Comp. Phys. 35 (2) (1980) 169-182
7. P. Kulkarni, P. Biswas, Aerosol Sci. Techn. 38 (6) (2004) 541-554
8. M.C. Heine, S.E. Pratsinis, Langmuir 23 (19) (2007) 9882-9890
9. A. Gutsch, S.E. Pratsinis, F. Löffler, J. Aerosol Sci. 26 (2) (1995) 187-199
10. P. Meakin, Physical Rev. Let. 51 (13) (1983) 1119-1122
11. P. Meakin, Physical Rev. B. 30 (8) (1984) 4207-4214

Leila Faramarzi

Phone: +45 4525 2892
Fax: +45 4525 2258
E-mail: lef@kt.dtu.dk
WWW: http://www.ivc-sep.dtu.dk
Supervisors: Georgios M. Kontogeorgis
Kaj Thomsen
Erling H. Stenby

PhD Study
Started: March 2007
To be completed: April 2010

Post-combustion Capture of Carbon Dioxide from Fossil Fueled Power Plants

Abstract

The purpose of this project is to contribute to the development of efficient CO_2 capture technology useful for coal fired power plants. This is done through modeling, theoretical and experimental work. In the first phase of the project, the extended UNIQUAC model as proposed by Thomsen and Rasmussen [1] for vapor liquid equilibrium calculations has been applied to thermodynamic representation of carbon dioxide, water and methyl-di-ethanolamine (MDEA) system. There are five temperature independent and four temperature dependent adjustable interaction parameters. The parameters of the model are regressed to the solid liquid and vapor liquid equilibrium data, as well as the excess enthalpy in a wide range of temperature (-14-200°C). The application of the model to a large number of experimental data for representation of total pressure over MDEA solution has been successful for the temperature range of (25-200° C) and the CO_2 partial pressure in the range of (0.10-7567 kPa). Considering the poor quality of experimental data, the model has also fitted the excess enthalpy data of binary MDEA and water solutions quite satisfactory at the temperatures of 25, 40 and 65°C. Experimental solid-liquid equilibrium data are also represented very well by the model.

Introduction

Post-combustion capture of CO_2 from power plant flue gases is now included in many countries energy policies as a method for mitigating the emission of greenhouse gases. A mature method of purification of acid gases from gaseous streams is chemical absorption into aqueous alkanolamine solutions.

In order to properly simulate the absorption-desorption process, a rate model is needed. It is necessary to integrate a good thermodynamic model with the rate model in order to get the driving forces for mass transfer well defined. The problem with thermodynamic modeling of gas treating plants is that the vapor-liquid equilibrium (VLE) data reported for these systems are not usually very consistent, therefore quite different partial pressures of CO_2 are reported in literature for the same exact temperature and acid gas loading. Also, some other essential data such as binary VLE on amine-water system, excess enthalpy data and enthalpy of formation of alkanolamines for both gas and liquid phases are scarce and those available from a few sources show disagreements.

In this work, extended UNIQUAC model as described by Thomsen et al. [1] for VLE calculations is applied for estimation of CO_2 solubility in aqueous alkanolamines, enthalpies of absorption, and the loss of amine through vaporization. The model was previously used by Addicks [2] for representation of VLE data in MDEA, methane, water and CO_2 system and by Thomsen and Rasmussen [1] for VLE calculation in H_2O, NH_3 and CO_2 system.

Chemical Equilibrium

The absorption of CO_2 in aqueous methyl-di-ethanolamine is along with a series of chemical reactions which greatly favor the solubility of the acid gas. Therefore, thorough understanding of the chemical reactions in the system is of great importance for the sake of accurate chemical modeling.

The presence of the following reactions in the solution has to be accounted for,

$$2H_2O \xleftrightarrow{K_1} H^+ \quad OH^- \tag{1}$$

$$CO_2 + 2H_2O \xleftrightarrow{K_2} H^+ \quad HCO_3^- \tag{2}$$

$$HCO_3^- + H_2O \xleftrightarrow{K_3} H^+ \quad CO_3^{2-} \tag{3}$$

The final reaction in the system is the dissociation of protonated MDEA,

$$MDEAH^+ + H_2O \xleftrightarrow{K_4} H^+ \quad MDEA \tag{4}$$

There is no direct N-H bond in MDEA molecule; hence, no carbamate ion is formed in the solution due to absorption of CO_2. Kamps and Maurer [3] have conducted electro-motive force (EMF) experiments at temperatures from 278 to 368 K and at different molalities of MDEA in order to determine the equilibrium constant of dissociation of $MDEAH^+$. Here the equilibrium constants from the noted work are being used for calculation of chemical equilibrium.

The Parameters of Extended UNIQUAC Model

The parameters of the model are the UNIQUAC volume and surface area parameters r and q respectively, and the binary interaction parameters u_{ji} accounting for the interaction energy between the components i and j.

In this work, the r and q parameters for MDEA and $MDEAH^+$ are considered as adjustable parameters of the extended UNIQUAC equation and the noted parameters for the rest of the species present in the solution are taken from Thomsen and Rasmussen (1999).

In this work, the interaction energy parameters for the water-water pair and the same cation pairs ($MDEAH^+$-$MDEAH^+$ and H^+-H^+) are set to zero and those of MDEA-$MDEAH^+$, $MDEAH^+$-water, $MDEAH^+$-CO_2, MDEA-water and MDEA-MDEA are fitted to all type of experimental data available in the parameter regression database in order to get a well-rounded model. The rest of the binary interaction parameters needed for model calculations are again taken from the work of Thomsen and Rasmussen [1].

There is no parameter in the Debye-Hückel term to be adjusted to experimental data and the A parameter in that term is based on the density and dielectric constant of pure water (water is considered to be the only solvent).

Results and Discussion

The parameter regression database contains 658 data-points on the vapor-liquid equilibrium for the ternary system of MDEA+water+CO_2. The databank also includes 102 binary VLE, SLE and excess enthalpy data-points in binary MDEA and water systems. A least-square minimization is performed in order to estimate the model parameters. The parameters are fitted to all types of experimental data i.e. ternary and binary VLE data, the excess enthalpy and SLE data. The estimated UNIQUAC volume and surface area parameters for MDEA and $MDEAH^+$ are presented table 1. The binary interaction energy parameters for the UNIQUAC residual term are reported in Table 2.

The results for the total pressure calculation for the ternary system of MDEA+ water+ CO_2 are illustrated in Figures 1, 2 and 3. Figure 4 represents excess enthalpy calculations together with the experimental data-points.

Figure 1 shows CO_2 solubility in MDEA solutions with varied concentrations from dilute (1.9 molal) to very concentrated (7.62 molal), all at the single temperature of 40°C. As it can be seen, there is good agreement between the experimental and calculated data at all amine strengths. Figure 2 and 3 show how the model represents CO_2 solubility in 2 and 8.4 molal MDEA. The experimental and calculated data agree well in the wide temperature range of 313-473K.

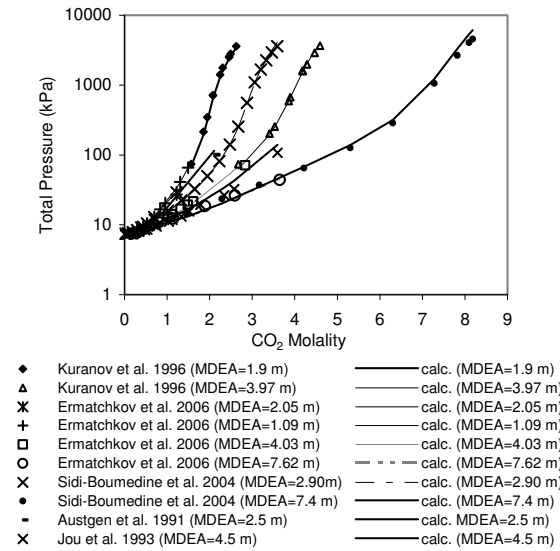

Figure 1: CO_2 solubility in aqueous MDEA with varied strength at 313 K.

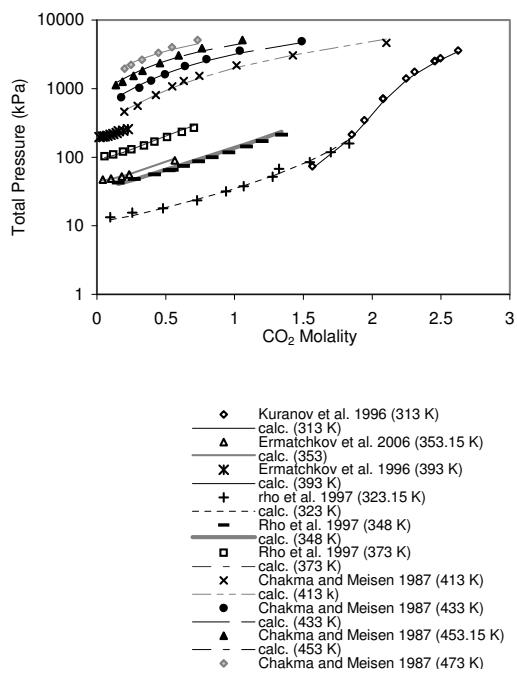

Figure 2: CO_2 solubility in 2molal aqueous MDEA at varied temperatures.

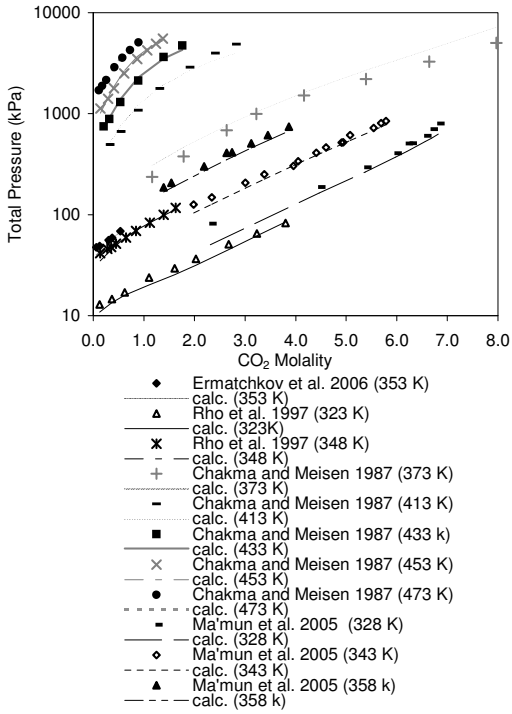

Figure 3. CO_2 solubility in 8.4molal aqueous MDEA at varied temperatures.

Table1. UNIQUAC volume parameters *(r)* and surface area parameters *(q)*.

Species	r	q
MDEA	2.919	5.888
$MDEAH^+$	2.741	3.710

Table2: UNIQUAC binary interaction parameters $u_{ji}^0(K),\ u_{ji}^t(K)$

Pair	u^0	u^t
MDEA-$MDEAH^+$	0.8391755E+03	-0.22199E+01
$MDEAH^+$-water	0.4177455E+03	0.10726E+01
$MDEAH^+$-CO_2	0.1702395E+03	0.00000E+0
MDEA-water	0.8419482E+03	-0.10606E+01
MDEA-MDEA	0.1199829E+04	-0.11651E+01

From Figures 2 and 3, it can be observed that for both dilute and highly concentrated MDEA solutions, the model represents the experimental data very well.
The results for excess enthalpy correlation are reported in Table 3. Provided that the experimental data are of good quality, fitting the parameters of an excess Gibbs energy model like extended UNIQUAC to excess enthalpy data could result in getting better temperature dependence of the parameters of the model as, there is a direct relationship between the temperature dependence of the excess Gibbs energy and excess enthalpy. Unfortunately there are not enough experimental data on the excess enthalpy of the MDEA +water system, and the available data show disagreement at the same exact conditions.

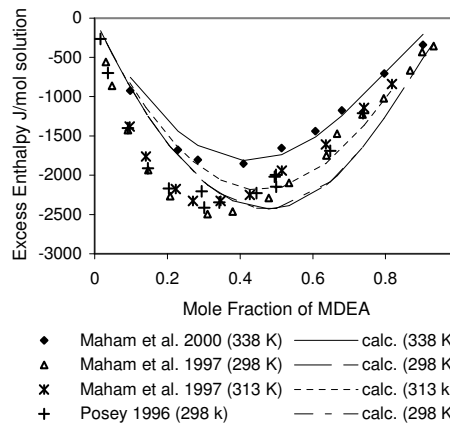

Figure 4: The calculated excess enthalpies of MDEA+ water system (the lines) together with the experimental data-points at different temperatures.

Table 3: The results of total excess enthalpy calculation, the mean absolute deviation between the calculated and experimental data are reported.

T(C)	Data-points	Mean absolute deviation (Jmole-1)	Reference
65	9	111.58	Maham et al. 2000
25, 40	26	332.75	Maham et al. 1997
25	19	325.32	Posey 1996

Conclusions

Extended UNIQUAC represents CO_2 solubility in MDEA solution generally very satisfactory in a wide range of temperature 25-200°C, a wide range of loading, 0.005-1.83 mole CO_2/mole MDEA, and varied amine strength from dilute, 0.44 mole MDEA/mole water to highly concentrated, 8.4 mole MDEA/mole water. The excess enthalpy data are very rare and quite erratic; having said that, the model has performed considerably well in representing the experimental data. More experimental data on the binary VLE of MDEA + water system are needed so that the model can give a good representation of amine loss due to vaporization. This type of data is scarce in open literature.

References

1. K. Thomsen and P. Rasmussen, Chem.Eng. Sci., 54(1999)1787-1802.
2. J. Addicks, Ph.D dissertation, Norwegian University of Technology, 2002.

3. A. P-S Kamps and G. Maurer, J. Chem. Eng. Data, 41(1996)1505-1513.
4. B. Sander, Aa. Fredenslund and P. Rasmussen, Chem. Eng. Sci., 41(1986)1171-1183.
5. H. Nicolaisen, P. Rasmussen and J. M. Sørensen, Chem. Eng. Sci., 48(1993)3149-3158.
6. D. S. Abrams and J. M. Prausnitz, AIChE Journal, 21(1975)116-128.
7. G. Maurer and J. M. Prausnitz, Fluid Phase Equilibria, 2(1978)91-99.
8. Sir R. Fowler and E. A. Guggenheim, Statistical Thermodynamics, University Press, Cambridge, 1949.
9. G. Kuranov, B. Rumpf, N. A. Smirnova and G. Maurer, Ind. Eng. Chem. Res., 35(1996)1959-1966.
10. V. Ermatchkov, A. P-S Kamps and G. Maurer, 45(2006)6081-6091.
11. R. Sidi-Boumedine, S. Horstmann, K. Fischer, E. Provost, W. Fürst and J. Gmehling, Fluid Phase Equilibria, 218 (2004)85-94.
12. D. M. Austgen, G. T. Rochelle and C-C. Chen, Ind. Eng. Chem. Res., 30(1991)543-555.
13. F-Y. Jou, J. J. Carroll, A. E. Mather and F. D. Otto, Can J. Chem. Eng., 71(1993)264-268.
14. S. W. Rho, K. P. Yoo, J. S. Lee, S. C. Nam, J. E. Son and B. M. Min, J. Chem. Eng. Data, 42(1997)1161-1164.
15. A. Chakma, A. Meisen, Ind. Eng. Chem. Res., 26 (12)(1987)2461-66.
16. S. Ma'mun, R. Nilsen and H. F. Svendsen, J. Chem. Eng. Data, 50 (2)(2005)630-634.
17. Y. Maham, A. E. Mather and L. G., J. Chem. Eng. Data, 42(5) (1997)988-992(5).
18. Y. Maham, A. E. Mather and C. Mathonat, J. Chem. Thermodynamics, 32(2) (2000)229-236(2).

José M. S. Fonseca

Phone: +45 4525 2858
Fax: +45 4588 2258
E-mail: jfo@kt.dtu.dk
WWW: http://www.ivc-sep.kt.dtu.dk/staff/JFO/
Supervisors: Nicolas von Solms

PhD Study
Started: January 2007
To be completed: January 2010

Multiphase Equilibrium in Natural Gas - Hydrate Inhibitor Systems

Abstract
A considerable amount of money is currently spent in the so-called "production chemicals", used in order to increase or facilitate production from a reservoir and in pipelines. Examples of such chemicals are methanol and glycols, used as inhibitors to prevent the formation of gas hydrates. As the oil price raises, the use of new, more expensive and exotic chemicals become viable, further complicating the prediction of phase equilibria and increasing environmental concern. A better knowledge of the phase equilibria in these systems will allow the reduction of the amounts used to the strictly necessary, with the inherent economical and environmental advantages. Therefore, we are working on the improvement of our experimental techniques with the designing of a new vapor-liquid-liquid-equilibria (VLLE) set-up, which will allow the collection of more accurate and reliable data in a wider range of conditions.

Introduction
Gas hydrates are crystalline compounds formed by inclusion of low molecular weight compounds in lattice structures formed by water on hydrogen bonds. Small molecules from light gases like nitrogen, carbon dioxide, hydrogen sulphide, methane, ethane, propane, n-butane or i-butane stabilize the lattice structure with the formation of stable solids at temperatures above the freezing point of water. Additionally, hydrates form more readily from real natural gas mixtures than from the pure constituent components of natural gas, representing a frequent problem for the gas industry, especially at the high pressures and low temperatures typical in North Sea gas reserves.

Blocking of lines due to the formation of hydrates presents serious issues in what safety is concerning and it has disastrous economic consequences.

Because of this, hydrate inhibitors such as ethylene glycol (MEG) or methanol are injected to the natural gas well stream, in order to prevent the formation of hydrates during transportation and further processing. In the case of offshore production, these inhibitors are transported through pipelines to the well. When a mixture of gas, water, MEG and condensate arrives onshore, all the components are distributed through all the phases, and it is essential to evaluate the amount of glycol lost in the gas phase, for environmental and for economical reasons. Also for environmental reasons it is necessary to determine the solubility of aromatics in the glycol rich phase, due to possible emissions during the regeneration process of the glycol.

However the amount of inhibitor needed is not well known and in order to avoid accidents, an excess of inhibitors is regularly used in the processes, with the inherent economical and environmental consequences.

A better knowledge of the phase equilibrium in these systems can allow the reduction of the amounts used to the strictly necessary.

This project will focus on the study of the phase equilibria in these systems, through the improvement of our experimental techniques, with the designing of a new vapor-liquid-liquid-equilibria experimental set-up which will allow the collection of more accurate and reliable data in a range of temperatures and pressures that can allow for example the replication of the polar conditions under which some pipelines are operated.

The methods for phase analysis will include the use of gas chromatography (GC), gas chromatography associated with mass spectroscopy (GC-MS), Karl Fisher and the use of adsorption columns (ATD).

This experimental part will allow establishing the basis for the posterior modeling of these systems with equations of state.

Experimental

In order to fulfill our goals, the new experimental set-up will allow measurements at high pressures (up to 40 MPa) and low temperatures (down to -60ºC or 213 K). The experimental conditions will be controlled and monitored with the high accuracy necessary to the production of high quality results. Finally, our goal is to achieve a full characterization of all the phases, including the quantification of traces of water and inhibitors in the gas phase.

The fundamental part of the experimental set-up is the equilibrium cell, depicted in Figure 1.

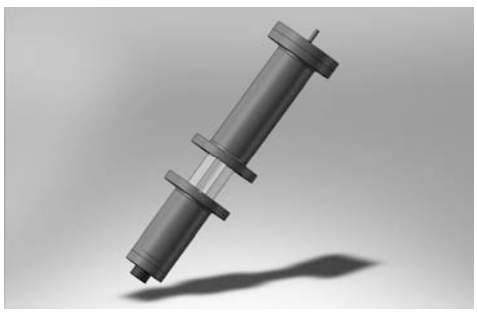

Figure 1: Three-dimensional computer generated image of the new equilibrium cell.

It is a variable volume cell specially designed for this project, equipped with two moving pistons and a 360º sapphire window. The position of the piston in the lower part of the cell can be set manually before a series of experiments, and it allocates in its interior a magnetic stirrer, while the position of the piston in the upper part is computer controlled, compensating for the pressure drop usually associated with the gas sampling.

Figure 2 shows a cut of the cell where is possible to observe the positioning of the pistons inside.

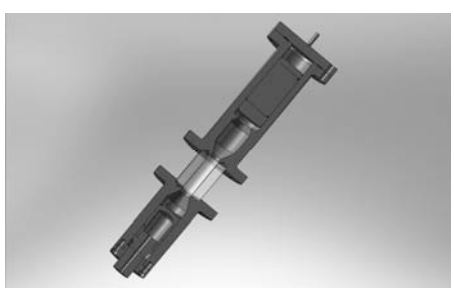

Figure 2: Cut of the new equilibrium cell, where it is possible to see the pistons inside.

The 360º window allows a good visibility of what is happening inside the cell at any moment, also permitting for example the study of phase interfaces, through optical or other kinds of measurements. The metal parts of this cell have already been built in the workshop of the department.

The cell will be placed inside a temperature controlled chamber, capable of keeping the whole system at a stable temperature down to -60ºC (213 K). This chamber is being specifically developed in a close collaboration with a Danish company specialist in this area.

Another big progress in this new set-up is the online sampling of all the phases, directly for the GC carrier gas stream. This is possible by the use of the ROLSI™ system (Rapid On Line Sampler Injector), represented schematically in Figure 3.

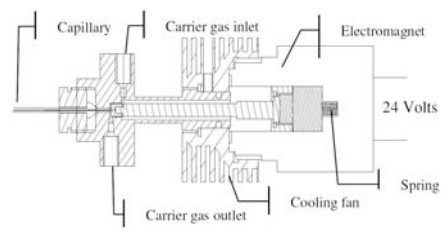

Figure 2: Schematic representation of a ROLSI™ electro-pneumatic sampler.

This system consists of electro-pneumatic valves, controlled by computer, with the ability of sampling very small amounts of liquid or gas, making possible to sample directly for the GC carrier gas without the need for dilutions.

Finally, the analysis of the samples will include different methods and techniques, in order to obtain precise results. The assessment of the composition of some of the phases will be possible by more than one method in order to test the respective accuracies.

Other necessary parts for this set-up, like a gas meter for example, are also currently being designed and built.

Acknowledgements

The author would like to thank the Danish Research Council for Technology and Production Sciences for the financial support through the project "Gas Hydrates – from Threat to Opportunity" and the Technical University of Denmark for the financial support through a Ph.D. scholarship.

Charlotte Juel Fristrup

Phone: +45 4525 6819
Fax: +45 4588 2161
E-mail: cjf@kt.dtu.dk
WWW: http://dpc.kt.dtu.dk
Supervisors: Søren Hvilsted
Katja Jankova
Rüya Eskimergen Nielsen, Novo Nordisk
Jens Thostrup Bukrinski, Novo Nordisk

PhD Study
Started: March 2007
To be completed: February 2010

Polymers for Pharmaceutical Packaging and Delivery Systems

Abstract
Materials for insulin containers and delivery systems should comply with requirements like compatibility with proteins, sterilisability, good barrier properties towards preservatives, and no toxic leachables. The number of commercially available polymer materials which can be used is rather limited. Therefore, a polymer coating containing some of the required properties may expand the use of polymers in medical devices. Initial studies have been made with model systems of poly(ether ether ketone) (PEEK) films as they can easily be functionalized. Analysis results confirm that hydrophilic polymers have been grafted from the surface.

Introduction
Polymers are replacing metals and glass in many applications. Medical applications are not an exception to that. In the field of diabetes treatment, compatibility of the polymer materials with insulin is extremely important. It has been shown earlier that the insulin hormone is susceptible to degradation due to leachables and also due to surface properties (hydrophobicity, electric charge etc.) of these materials. Moreover, the polymer material might have a high affinity to preservatives in the drug formulation or proteins might be adsorbed on the polymer surface resulting in a lower concentration of one or the other in the drug formulation.

Coatings of poly(ethylene glycol) (PEG) are known to be compatible with proteins due to their water solubility and hydrophilicity. The surfaces are in a liquid-like state with polymer chains showing high flexibility or mobility (increasing mobility with chain length up to 100). Steric stabilization and chain mobility are the mechanisms involved in protein rejection of PEG surfaces. The PEG molecules have a large excluded volume in water which makes them very effective for the steric repulsion. Additionally, the high surface mobility of PEG chains prevents protein adsorption as the contact time is shortened. [1, 2, 3]

Specific Objectives
Many polymer materials are permeable to preservatives found in the insulin drug solutions. Hence, use of polymer materials in insulin containers is quite limited. Thus, synthesis of a polymeric coating for improved barrier properties and better insulin compatibility is considered as the primary goal of the project. Throughout the PhD study initial investigations and analyses will be performed on model systems in order to establish the fundamental understanding of the barrier properties and insulin compatibility of the materials. The purpose of using model systems is either to have a very simple system or to have substrate which can easily be functionalized. The latter is the reason for selecting PEEK film as substrate. Different polymers including PEG-like materials will be investigated as coating materials. The first approach is to graft the polymers from the substrate using a technique called Surface-Initiated Atom Transfer Radical Polymerization (SI ATRP).

Results and Discussion
The surface of PEEK was functionalized by covalently bounding of hydrophilic polymer brushes of poly(ethylene glycol)methacrylate (PEGMA) from initiator-modified PEEK using SI ATRP. Surface reduction of PEEK to form hydroxyl groups [4] was performed prior to the attachment of 2-bromoisobutyrate initiating groups.

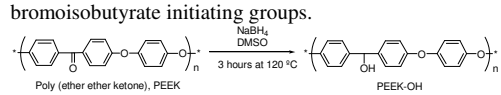

Figure 1: Surface activation of the PEEK films

SI ATRP of the monomer PEGMA was performed in aqueous media in the presence of the catalyst system 2,2'-bipyridine and copper chloride.

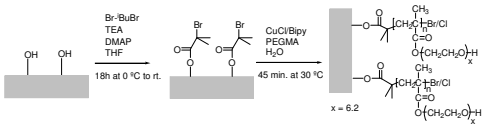

Figure 2: 1) Anchoring of the initiating groups on the hydroxyl-functionalized surface 2) Grafting of PPEGMA brushes from the PEEK films using SI ATRP

Attenuated Total Reflectance Fourier Transform Infrared (ATR FTIR) spectra were compared during the modification of PEEK. The formation of hydroxyl groups was observed as an C-O absorption band appeared at 1057 cm^{-1}. The carbonyl (C=O) absorption band at 1736 cm^{-1} indicated the presence of initiating groups on the surface. Grafting of PPEGMA from the surface resulted in an increase of the C=O band (broad band at 1730 cm^{-1}).

The advancing and receding water contact angles (CA) decreased as the films were modified, reflecting the high hydrophilicity of the hydroxyl groups and PPEGMA.

Table 1: Water contact angles measured on the smooth (S) or rough (R) side of the PEEK films

Material	S/R	CA (adv.), º	CA (rec.), º
PEEK	S	99 ± 2	58 ± 4
PEEK	R	103 ± 3	27 ± 4
PEEK-OH	S	79 ± 5	38 ± 3
PEEK-Br	S	92 ±7	59 ± 5
PEEK-*g*-PPEGMA	S	62 ± 1	25 ± 2
PEEK-*g*-PPEGMA	R	68 ± 2	19 ± 4

Thermal Gravimetric Analysis (TGA) showed that the 2 -3 % weight loss below 500 ºC for PEEK-*g*-PPEGMA originated from PPEGMA.

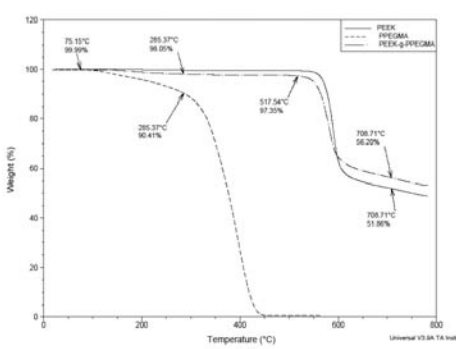

Figure 3: TGA of unmodified PEEK, PPEGMA homopolymer, and PEEK-*g*-PPEGMA

The roughness average (R_a) and root mean square roughness (R_q) were determined by Atomic Force Microscope (AFM) analysis to evaluate the surface topography.

Table 2: AFM analyses of unmodified PEEK and PEEK-*g*-PPEGMA

Roughness	PEEK	PEEK-*g*-PPEGMA
R_a (µm)	0.76 ± 0.12	0.79 ± 0.18
R_q (µm)	0.94 ± 0.14	1.0 ± 0.2

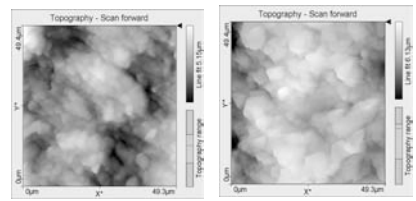

Figure 4: AFM images of unmodified PEEK (left) and PEEK-*g*-PPEGMA (right)

X-ray Photoelectron Spectroscopy (XPS) has been used to investigate the functionalization. The scan survey spectrum was used to identify and quantify the elements in the modified PEEK samples. Chemical composition information was obtained from high resolution scans (not shown).

Table 3: XPS analyses of PEEK samples

Element (%)	PEEK-OH	PEEK-Br	PEEK-*g*-PPEGMA
C	84.76	83.11	68.56
O	15.26	15.06	31.44
Br		0.98	
C/O ratio	5.56	5.52	2.18

Conclusions

Polymer brushes of PPEGMA were grafted from PEEK films via Surface-Initiated ATRP. The water contact angles were lower for the modified PEEK films; thus hydrophilization of PEEK was achieved. AFM analyses showed that the surface modification did not change the surface roughness. The C/O ratio as well as the data from the high resolution XPS confirmed the grafting from the PEEK films.

Acknowledgments

Novo Nordisk A/S, the Ministry of Science Technology and Innovation, and Technical University of Denmark are acknowledged for co-financing the PhD study. Furthermore, I thank Lene Hubert for the XPS results and P.S. Ramanujam for the AFM analyses.

References

1. D.L. Elbert, J.A. Hubbell Annu. Rev. Mater. Sci., 26 (1996) 365-394
2. J.H. Lee, H.B. Lee, J.D. Andrade Prog. Polym. Sci. 20 (1995) 1043-1079
3. M. Malmsten, K. Emoto, J.M. Van Alstine J. Colloid Interface Sci. 202 (1998) 507-517
4. O. Noiset, C. Henneuse, Y.-J. Schneider, C. Marchand-Brynaert Macromolecules 30 (1997) 540-548

Hugo Edson González Villalba
Phone: +45 4525 2912
Fax: +45 45932906
E-mail: heg@kt.dtu.dk
WWW: http://www.capec.kt.dtu.dk/People/phds
Supervisors: Rafiqul Gani
Jens Abildskov

PhD Study
Started: October 2005
To be completed: September 2008

Development of Group Contribution^{Plus} Models for Properties of Organic Chemical Systems

Abstract
In order to meet the increased demands with respect to complexity of the chemical molecular structures, wider range of chemicals and accuracy, further development of current estimation methods and techniques and/or development of new models are necessary. Hybrid models that combine molecular descriptors theory and group contribution theory for pure component properties and for mixture properties prediction have been developed using a group contribution plus (GC^{plus}) approach[1]. In this work a GC^{Plus} model for mixture property prediction for phase equilibria calculations is highligthed and analyzed.

Introduction
GC models are often used for pure component and mixture property predictions. The flexibility, reliability and simplicity of GC models make them popular for property prediction. However, GC models also exhibit some limitations: they are unable to distinguish 3D features of the molecular structures while sometimes there are not enough experimental data for the group generation. At the same time, the extended estimation methods need to be computationally simple and efficient, so they can be used routinely for process-product engineering calculations. Also, the extensions need to consider the coupling of molecular modelling with "engineering" end-use models used in process simulators. A GC^{Plus} model for mixture property prediction (UNIFAC-CI) has been developed[2] using as a basis the UNIFAC group contribution method[3] .

The main idea of this methodology is the use of connectivity indices (CI) to describe the molecular fragmentation that is characteristic for the UNIFAC group contribution method and that relates properties (molecular interactions in this case) with molecular structure. The result is the automatic generation of group interaction parameters (GIPs) for the UNIFAC group contribution method. Derivation and use of the method has been reported in a recent publication[2]. The current version of the UNIFAC-CI method includes groups formed by C, H, O, N, Cl, F and S atoms. This feature of the method implies the potential generation of a very large number of GIPs as well as filling-up the original GIPs matrix without additional experimental data. In this work, the performance of UNIFAC-CI for phase equilibria predictions including VLE (Vapor-liquid equilibrium) and SLE (Solid-liquid equilibrium) is discussed together with guidelines and recommendations for the user.

Specific Objectives
The objective of this work is to establish a methodology to generate missing group interaction parameters for the UNIFAC group contribution method, and analyze the performance of the generated parameters through VLE and SLE calculations.

UNIFAC-CI Group Contribution Method
For phase equilibrium related properties of mixtures, one of the most successful GC methods is the UNIFAC group contribution method for estimation of liquid phase activity coefficients. One of the limitations of the UNIFAC method is the missing group interaction parameters in the UNIFAC parameter table. The unavailability of experimental data is one of the main reasons for the missing group interaction parameters. Recently, González et.al[2] have proposed the use of connectivity indices for the generation of missing group interaction parameters for the UNIFAC parameter table. The basic idea is to derive a relationship (see Eq. 1) between the group interaction parameters with the CI and the atom constitution of the groups. Parameter regression is performed in order to determine the atom interaction parameters (AIP) i.e. a,b,c and d (see Eq. 2), that are then used for the generation of any missing

group interaction parameter (GIP) a_{kl} (see Eq. 2). This combined model is the UNIFAC-CI GC method. The derivation of the model equations can be found in González et.al.[2].

Once the AIPs have been regressed it is possible to: 1) Generate values for missing GIPs on the UNIFAC parameter table[3] 2) Reestimate one or more GIPs 3) Create a new group and estimate its GIPs. The UNIFAC-CI method in this work has been extended and tested for groups consisting of atoms of carbon, oxygen, hydrogen, nitrogen, chlorine, sulfur and fluorine. Based on the original UNIFAC parameter table, the following groups are covered: CH_2, C=C, ACH, $ACCH_2$, OH, CH_3OH, H_2O, ACOH, CH_2CO, CHO, CCOO, HCOO, CH_2O, DOH (ethylene-glycol), C≡C, COO, OCCOH, furfural, CNH_2, CNH, $(C)_3N$, $ACNH_2$, Pyridine, CCN, CNO_2, $ACNO_2$, ACRY (acrylonitrile), DMF (dimethylformamide), NMP (n-methyl pyrrolidone), CON, Morpholine, CCl, CCl_2, CCl_3, CCl_4, ACCl, ClCC, CS_2, CH_3SH, DMSO, CH_2S, Thiophene, ACF, CF2, CClF. With the UNIFAC-CI method, only a set of 288 AIPs need to be regressed to cover all the groups containing C, H, O, N, Cl, S, F atoms in the original UNIFAC matrix. A generic form for calculation of AIPs is highlighted through Eqs. (1) and (2):

$$\left(A_{kl}^{XY}\right)_0 = \frac{n_X^{(k)}\,{}^{v}\chi_{(l)}^{0} - n_Y^{(l)}\,{}^{v}\chi_{(k)}^{0}}{{}^{v}\chi_{(l)}^{0}\,{}^{v}\chi_{(k)}^{0}}$$

$$\left(A_{kl}^{XY}\right)_1 = \frac{n_X^{(k)}\,{}^{v}\chi_{(l)}^{1} - n_Y^{(l)}\,{}^{v}\chi_{(k)}^{0}}{{}^{v}\chi_{(l)}^{1}\,{}^{v}\chi_{(k)}^{0}} \qquad (1)$$

$$\left(A_{kl}^{XY}\right)_2 = \frac{n_X^{(k)}\,{}^{v}\chi_{(l)}^{1} - n_Y^{(l)}\,{}^{v}\chi_{(k)}^{1}}{{}^{v}\chi_{(l)}^{1}\,{}^{v}\chi_{(k)}^{1}}$$

$$\left(A_{kl}^{XY}\right)_3 = \frac{n_X^{(k)}\,{}^{v}\chi_{(l)}^{2} - n_Y^{(l)}\,{}^{v}\chi_{(k)}^{0}}{{}^{v}\chi_{(l)}^{2}\,{}^{v}\chi_{(k)}^{0}}$$

$$\begin{aligned} a_{kl} = {} & \underbrace{b_{C\text{-}C}\left(A_{kl}^{CC}\right)_0 + b_{C\text{-}O}\left(A_{kl}^{CO}\right)_0 + b_{C\text{-}N}\left(A_{kl}^{CN}\right)_0 + \ldots}_{0^{th}\text{-order interactions}} \\ & + \underbrace{c_{C\text{-}C}\left(A_{kl}^{CC}\right)_1 + c_{C\text{-}O}\left(A_{kl}^{CO}\right)_1 + c_{C\text{-}N}\left(A_{kl}^{CN}\right)_1 + \ldots}_{1^{st}\text{-order interactions}} \\ & + \underbrace{d_{C\text{-}C}\left(A_{kl}^{CC}\right)_2 + d_{C\text{-}O}\left(A_{kl}^{CO}\right)_2 + d_{C\text{-}N}\left(A_{kl}^{CN}\right)_2 + \ldots}_{2^{nd}\text{-order interactions}} \\ & + \underbrace{e_{C\text{-}C}\left(A_{kl}^{CC}\right)_3 + e_{C\text{-}O}\left(A_{kl}^{CO}\right)_3 + e_{C\text{-}N}\left(A_{kl}^{CN}\right)_3 + \ldots}_{3^{rd}\text{-order interactions}} \end{aligned} \qquad (2)$$

In Eqs. 1-2, all binary atomic interactions are combined to obtain the group interaction, a_{kl}. This is an empirical relation derived in a similar fashion as the UNIFAC model.

The group interaction parameter a_{kl} between groups k and l are predicted from calculated A_{kl}^{xy} and regressed coefficients b, c, d, e (the atom interaction parameters, AIPs) representing the atomic interactions (i.e. $b_{C\text{-}C}$, $b_{C\text{-}O}$, $b_{C\text{-}N}$, $b_{C\text{-}Cl}$, $c_{C\text{-}C}$, $c_{C\text{-}O}$, etc) from Eq. (2), In the above equations, $n_X^{(k)}$ is the number of atoms of type X in the group k, and ${}^{v}X^{m}_{(k)}$ is the m-th order valence connectivity index for the group k .

Parameter Optimization

The database used for fitting the AIPs includes 58 binary sets (462 data points) for VLE systems involving C, H, O, N atoms 86 (1325 values) binary sets for systems involving C, H, O, Cl atoms, 228 binary measurement sets (3946 values) for VLE systems involving C, H, O atoms, and 17 (217 values) binary sets for systems involving C, H, O, S atoms. The parameter estimation of this work is exclusively based on isothermal VLE data. The VLE data sets were extracted from the CAPEC database[4] and free sources, and were checked for thermodynamic consistency using the test of Van Ness[5].

The optimization algorithm used for the data fitting was the Levenberg-Marquardt[6][7] technique, which is a local optimization method. It is therefore strongly dependent on the initial guesses for the parameters. The proposed objective function is the following:

$$S = \frac{1}{N}\sum_{i=1}^{N}\left(\frac{P_{\exp} - P_{calc}}{P_{\exp}}\right)^2 + w_{reg}\sum_{j}^{N_A}\sum_{k}^{N_A}\left(AIP_{jk} - AIP_{jk}^{IG}\right)^2 \qquad (3)$$

where, N is the number of experimental data points, AIP_{jk} is the current value of the atom-interaction parameters (b, c, d, e) between atoms j and k and AIP^{IG}_{jk} the corresponding values from the previous iteration, N_A is the number of atoms involved in the optimization (excluding hydrogen) and w_{reg} a weighting value used to increase or decrease the influence of regularization in the optimization.

Correlation

Correlation results are shown on table 1. Where a comparison vs Original UNIFAC is done in terms of AARD % (average absolute relative deviation).

The AARD is defined by equation (4):

$$\text{AARD}\,(\%) = \frac{1}{N}\sum_{i=1}^{N}\left|\frac{P_{\exp} - P_{cal}}{P_{\exp}}\right| x\ 100 \qquad (4)$$

where N is the number of data points in the data system.

Table 1: Comparison of the correlation results for the VLE calculations using original UNIFAC and UNIFAC-CI in terms of AARD for the whole data systems

System	Main Groups involved	Original UNIFAC	UNIFAC-CI
Functional Groups	CH_2, C=C, ACH, $ACCH_2$, OH, ACOH, CH_2CO, CHOa, CCOO, HCOO, CH_2O, COOH	2.57	2.54
Water	CH_2, C=C, OH, H_2O, CH_2CO, CH_2O, COOH	3.71	3.34
Methanol	CH_2, OH, CH_3OH, CH_2CO, CHOa, CCOO, CH_2O	3.98	2.56
N-atom related groups	CH_2, ACH, $ACCH_2$, OH, CH_2CO, CCOO, CNH_2, CNH, $(C)_3N$, $ACNH_2$, PYRIDINE, CCN, CNO_2	4.39	2.96
Cl-atom related groups	CH_2, C=C, ACH, $ACCH_2$, OH, CH_2CO, CCOO, CH_2O, CCl, CCl_2, CCl_3, CCl_4, ACCl	4.11	3.85
Functional groups + N-atom related + Cl atom related	All of the previously listed groups except CH_3OH and H_2O	3.32	2.94
S-atom related groups	CS_2, CH_3SH, DMSO, CH_2S, Thiophene	3.31	1.12

Results and Discussion

In order to evaluate the performance of UNIFAC-CI, comparisons have been made between VLE experimental data, the prediction using original UNIFAC model and predictions using the UNIFAC model with the generated GIPs through AIPs (UNIFAC-CI). A system involving C,H,O,N atoms and a system involving C,H,O,Cl, S atoms have been chosen for illustration of this comparison. On the other hand for SLE calculations, the performance of UNIFAC-CI is tested against experimental data and the original UNIFAC model. It should be pointed out that the same parameters used for UNIFAC-VLE are used, which means that there are pure predictions.

On figure 1 a comparison between experimental data involving the system n-n-diethylamine + (2) pyridine at 323.15 K is compared with the predictions using UNIFAC-CI. It is clear that UNIFAC-CI follows the trend of the experimental data points, and, it is important to mention that the pair of GIPs parameters needed are blanks on the current UNIFAC matrix.

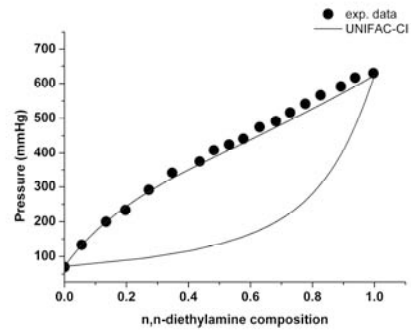

Figure 1. Comparison of VLE calculations using the original UNIFAC method ( ) towards a n,n-diethylamine/pyridine experimental data set[8] (,) at 323.15 K

For systems involving sulfur and chlorine atoms, a comparison using the system (1) CCl_4 + (2) dimethyl-sulfide is done in terms of experimental data, original UNIFAC and UNIFAC-CI. The VLE phase diagrams is shown on figure 2:

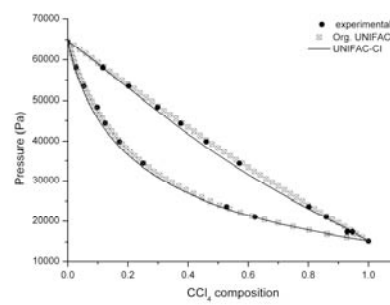

Figure 2. Comparison of VLE calculations using the original UNIFAC method (0) and UNIFAC-CI ( ) towards a CCl_4/dimethyl-sulfide experimental data set[9] (,) at 298.15 K.

It can be seen that the performance of UNIFAC-CI is similar to original UNIFAC and that both models show a good agreement with the experimental data. Even though the GIPs involved with this calculation are not missing in the original UNIFAC matrix; these data were not used for the regression of the AIPs.

The possibility of using the same set of parameters from VLE in SLE calculations is considered here. The idea is to "test" the generated GIPs for VLE in SLE systems, in order to evaluate and make conclusions whether if it is possible to use the GIPs for SLE calculations, limitations and recommendations for the user. On figure 3, four SLE systems involving aromatics, nitrogenated

compounds, hydrocarbons, alcohols and chlorinated compounds have been selected for comparisons between experimental data, Original UNIFAC and UNIFAC-CI. So far, the results are encouraging: UNIFAC-CI follows the tendency of the experimental data in all the cases. It is clear that the major discrepancies between experimental data and the proposed model occur for the benzene + pyridine and phenol + benzene systems, the explanations for this behaviour are the next step on the work for SLE.

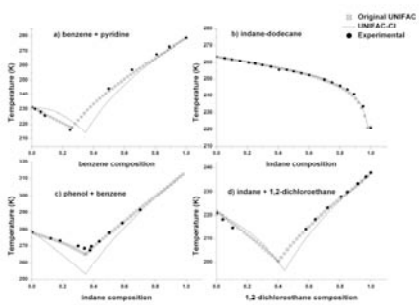

Figure 3. Comparison of SLE calculations using the original UNIFAC method (0), UNIFAC-CI ( ) towards four experimental data sets[10][11] (,): a) benzene+pyridine b) indane+dodecane c) phenol+benzene d) indane+1,2-dichloroethane.

Conclusions

The performance of the proposed GC^{Plus} models have been evaluated for VLE calculations for several systems including a wide range of compounds have been presented. Examples involving pure predictions and validations of the model are very promising. A further optimized set of GIPs is under development as well as a final analysis to define the strenghts and limitations of the proposed model. For the SLE calculations using UNIFAC-CI, the results show that the method is well suited for the tested systems up to now. An extensive test of the model for SLE calculations is needed in order to make final conclusions and recommendations to the user. Future work includes the generation of an independent set of GIPs for LLE calculations in the same way as for VLE.

Acknowledgements

Funding for Hugo E. Gonzalez Villalba through the National Council of Science and Technology (CONACyT) from Mexico is gratefully acknowledged.

References

1. González H.E, Abildskov J., Gani, R; Computer-aided framework for pure component properties and pase equilibria prediction for organic systems, Fluid Phase Equilibria, 261, 2007, 199-204.
2. González, H.E.; Abildskov,J; Gani R.; Rosseaux, P.; Le Bert, B. A Method for Prediction of UNIFAC Group Interaction Parameters, AIChE J. 2007; 53, 6, 1393-1634.
3. Hansen, H.; Rasmussen P., Fredenslund A.; Schiller M.; Gmehling J. Vapor-Liquid Equilibria by UNIFAC Group Contribution. 5. Revision and Extension. Ind. Eng. Chem. Res. 1991,30, 2352-2355.
4. The The CAPEC database, CAPEC Report. Department of Chemical Engineering, DTU, Lyngby, Denmark www.capec.kt.dtu.dk.
5. Van Ness, H.C. Thermodynamics in the treatment of (vapor + liquid) equilibria. J. Chem. Thermodynamics. 1995, 27, 113-134.
6. Levenberg, K. A Method for the Solution of Certain Problems in Least Squares. Quart. Appl. Math. 1944, 2, 164-168.
7. Marquardt, D. An Algorithm for Least-Squares Estimation of Nonlinear Parameters. SIAM J. Appl. Math. 1963, 11, 431-441.
8. Antje J., Grensemmann H., Lohmann J., Gmehling J.; Ind. Eng. Chem. Res. Vol. 45, 23, 2006.
9. Gray, D.F., Pasco N.F., Williamson G., J. Chem. Eng. Data., 33, 1998, 335.
10. Gmehling J., Anderson T., Prausnitz J., Solid-liquid Equilibria using UNIFAC, 17, 4 1978, 269-73.
11. Jakob A., Joh R., Rose C., Gmehling J., Solid-liquid equilibria in binary mixtures of organic compounds, 113, 1995, 117-126.

List of publications

González H.E, Abildskov J., Gani, R; Computer-aided framework for pure component properties and pase equilibria prediction for organic systems, Fluid Phase Equilibria, 261, 2007, 199-204.

González, H.E.; Abildskov J; Gani R.; Rosseaux, P.; Le Bert, B. A Method for Prediction of UNIFAC Group Interaction Parameters, AIChE J. 2007; 53, 6, 1393-1634.

Fengxiao Guo
Phone: +45 4525 6821
Fax: +45 4588 2161
e-mail: feg@kt.dtu.dk
www: http://www.dtu.dk/Centre/DPC.aspx
Supervisors: Martin E. Vigild
Sokol Ndoni (Risø)
Katja Jankova

Ph.D. Study
Started: November 2006
To be completed: November 2009

Hydrophilic Nanoporous Poly(acrylic acid)-*b*-Polystyrene from Di- and Triblock Copolymers

Abstract
Polymeric nanoporous materials derived from block copolymers offer great technological promise due to their many potential applications. However, many possible applications will require the nanoporous polymers to work in an aqueous environment. Nanoporous polymers with hydrophilic pores are desired. The preparation of nanoporous polystyrene with poly(acrylic acid) hydrophilic cavities from di- and triblock copolymer precursors is presented here.

Introduction
The self-organization of block copolymers has attracted considerable attention in relation to "bottom up" nanotechnology because it enables various highly ordered structures at nanometer length scale. Specific removal of a minority component from an ordered block copolymer allows for the preparation of nanoporous materials. Nanoporous polymeric materials derived from self-organized block copolymers show great potential for nanoobject templates, separation membranes, sensors, and substrates for catalysis [1]. However, many possible applications such as drug delivery, growth of bacteria and selective separation will require the nanoporous polymers to work in an aqueous environment. Only a limited number of nanoporous polymers with hydrophilic pores have been prepared to date [2-5].

Here hydrophilic nanoporous poly(acrylic acid)-*b*-polystyrene was prepared from either a poly(*tert*-butyl acrylate)-*b*-polystyrene (P*t*BA-*b*-PS) diblock copolymer or a polydimethylsiloxane-*b*-poly(*tert*-butyl acrylate)-*b*-polystyrene (PDMS-*b*-P*t*BA-*b*-PS) triblock copolymer. In these polymer precursors the PS block was the matrix material, the P*t*BA block was deprotected to provide hydrophilic PAA and at the same time generating free volume, and the PDMS block was the degradable component. Anhydrous hydrogen fluoride (HF) or trifluoroacetic acid (TFA) were employed to quantitatively deprotect P*t*BA and remove PDMS at the same time.

Experimental Work
The synthesis of P*t*BA-*b*-PS diblock copolymers through atom transfer radical polymerization (ATRP) is outlined in Scheme 1. *t*BA was polymerized with 2-EBP as the initiator at 60 °C. After purification the homopolymers were further employed as macroinitiators for a second ATRP of styrene in xylene at 100 °C.

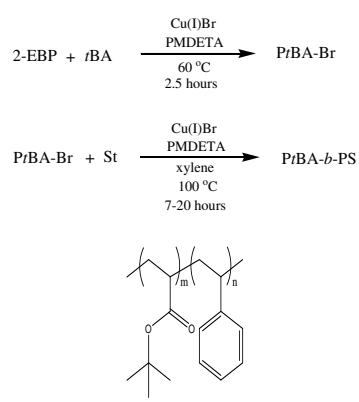

Scheme 1. Synthesis of P*t*BA-*b*-PS diblock copolymer by ATRP (the chemical structure of the obtained block copolymer is shown in the last row).

PDMS-*b*-P*t*BA-*b*-PS triblock copolymer was synthesized by a combination of living anionic

polymerization and ATRP according to Scheme 2. PDMS macroinitiators for ATRP have previously been prepared by anionic polymerization [6-8]. Here we have chosen to use a modified three-step procedure, where the product of living anionic polymerization of D_3 was endcapped with chlorodimethylsilane. The yielded PDMS-H was coupled with allyl alcohol in the presence of Karstedt's catalyst [9] (see reaction step iii in Scheme 2) producing PDMS with a hydroxyl end-group (PDMS-OH). Further reaction with α-bromoisobutyryl bromide [10] turned the obtained PDMS-OH into a bromoisobutyrate PDMS (PDMS-Br), shown in reaction step iv. The obtained PDMS-Br was used to consecutively polymerize *t*BA and St blocks by ATRP.

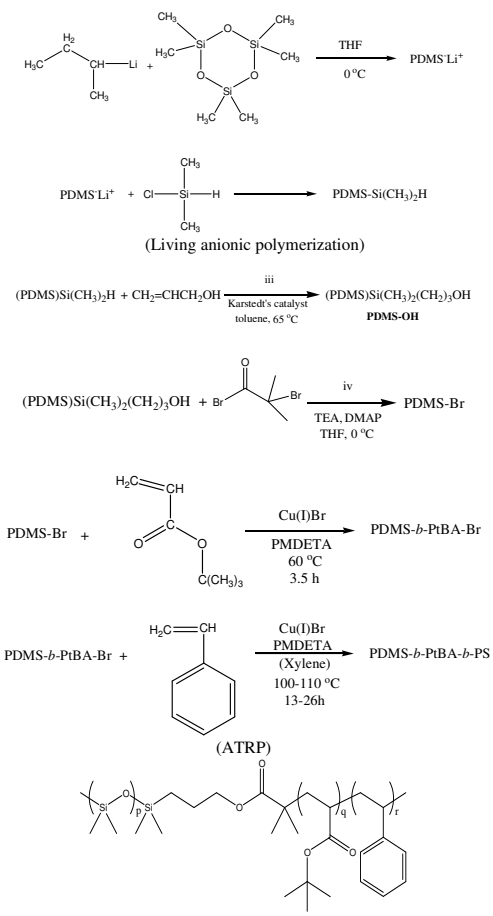

Scheme 2. Synthesis of PDMS-*b*-P*t*BA-*b*-PS triblock copolymer by a combination of living anionic polymerization and ATRP (the chemical structure of the final triblock copolymer is shown in the last row).

Deprotection and etching of diblock P*t*BA-*b*-PS or triblock PDMS-*b*-P*t*BA-*b*-PS copolymers (by HF or TFA) creates nanoporous PAA-*b*-PS. (Scheme 3)

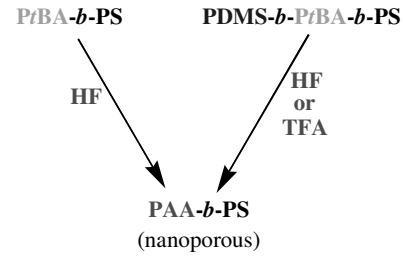

Scheme 3. Deprotection and etching by HF or TFA

Results and Discussions

Detailed information on the chemical composition changes for PDMS-*b*-P*t*BA-*b*-PS (DAS-1) after HF and TFA treatments was acquired by the FT-IR spectra shown in Figure 1. The spectrum of DAS-1 shows absorption bands related to the PDMS: CH_3 bending, Si-O-Si stretching and C-Si-C stretching peaks located at 1261, 1092-1088 and 800 cm^{-1}, respectively. C=O (ester) stretching peak at 1730 cm^{-1}, CH_3 (*t*Bu) bending peak at 1394/1368 cm^{-1}, C-C-O stretching (O-*t*Bu) at 1259 cm^{-1},and C-O (O-*t*Bu) stretching peak at 1151 cm^{-1} represent *tert*-butyl group in P*t*BA. The characteristic absorption peaks associated with PS are at 1489, 1454, 760 and 700 cm^{-1}. After deprotection and etching in HF for 2 hours (DAS-1-HF), the characteristic peaks for PS remained intact, while the peaks related to PDMS (CH_3 bending and C-O stretching) and peaks originated from *tert*-butyl group disappeared entirely. The sharp peak (**a** in Figure 1) corresponding to the ester carbonyl group (C=O) was broadened after HF-treatment due to the formation of carboxylic acid carbonyl group. The spectrum confirms that PDMS and *tert*-butyl groups were completely removed and PS was stable under HF treatment conditions. This shows that HF was also able to deprotect P*t*BA (yielding the hydrophilic PAA block) in addition to etching of PDMS. Identical chemical composition changes follow from TFA treatment (DAS-1-TFA) as shown in Figure 1.

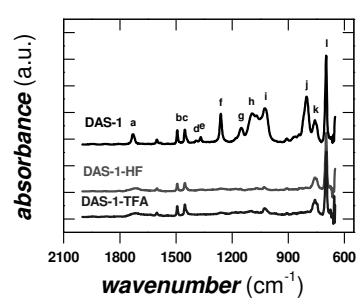

Figure 1. FT-IR spectra of DAS-1 precursor sample (top line), after HF treatment (middle line) or after TFA treatment (bottom line).

Figure 2 shows small angle x-ray scattering (SAXS) 1D profiles of P*t*BA-*b*-PS (AS-1, AS-3) and DAS-1 before and after degradation. DAS-1 was treated with TFA and HF and both curves are shown in panel (c) of Figure 2. The ratios of scattering peak positions for the HF-treated samples were identical to those for the original diblock and triblock precursors. But the scattering intensity was significantly increased after HF or TFA treatment for all three samples, though at different degrees. This is due to an increased electron density contrast as a result of replacing the removed chain parts by vacuum. The SAXS data give evidence for the creation of nanoporous structures of the same morphologies as that of the respective diblock and triblock precursors.

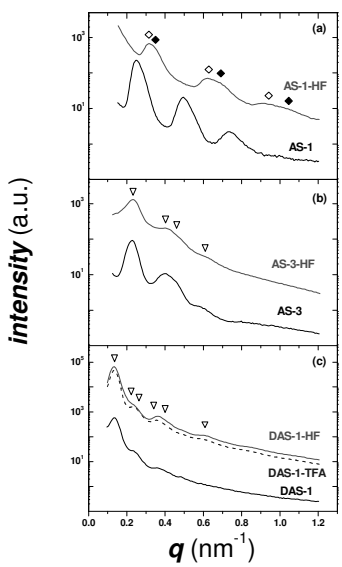

Figure 2. SAXS 1D profiles of (a) AS-1, (b) AS-3 and (c) DAS-1 before and after degradation.

SEM micrographs of AS-3-HF and DAS-1-HF are shown on the same scale of magnification in Figure 3. Both samples show hexagonal patterns of pores, with the distinct difference that the cavities for DAS-1-HF are larger and wider spread apart compared to the cavities for AS-1-HF. This is as expected from the molecular weights of the two samples and from the fact that the triblock sample sacrifices a larger portion of the molecule during degradation.

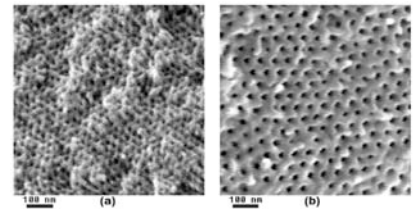

Figure 3. SEM pictures of (a) AS-3-HF and (b) DAS-1-HF.

A direct proof of hydrophilicity for the nanoporous materials presented here was the spontaneous uptake of water. The three nanoporous PAA-*b*-PS samples: AS-1-HF, AS-3-HF, DAS-1-HF were placed into glass vials containing distilled water. After soaking in water for one day, the four PAA-*b*-PS samples sank down to the bottom of their respective vials. Volumes of water uptake for AS-3-HF, DAS-1-HF and DAS-1-TFA were close to the expected volumes. This confirms that hydrophilic nanopores were created in the four PS-*b*-PAA samples.

Conclusions

Nanoporous poly(acrylic acid)-*b*-polystyrene amphiphilic diblock copolymers with hydrophilic cavity surfaces were successfully prepared from P*t*BA-*b*-PS and PDMS-*b*-P*t*BA-*b*-PS copolymer precursors. The combination of living anionic polymerization and ATRP allows synthesizing PDMS-*b*-P*t*BA-*b*-PS triblock copolymer with a center P*t*BA block, which can be modified to the hydrophilic PAA, and PDMS block that can be fully degraded. Deprotection of *tert*-butyl groups in P*t*BA and selective etching of PDMS chains was accomplished by applying HF or TFA in one step. The hydrophilic property of nano cavity surfaces in the PAA-*b*-PS block copolymers was verified by water uptake measurements. The nanoporous polymers prepared in this work are expected to broaden the spectrum of possible applications of such materials in cases, which require aqueous or biological environment.

References

1. M.A. Hillmyer, Adv. Polym. Sci. 190 (2005) 137.
2. G. Liu, J. Ding, A. Guo, M. Herfort, D. Bazett-Jones, Macromolecules 30 (1997) 1851.
3. G. Liu, J. Ding, S. Stewart, Angew. Chem. Int. Ed. 38 (1999) 835.
4. H. Mao, P.L. Arrechea, T.S. Bailey, B.J.S. Johnson, M.A. Hillmyer, Faraday Discussions 128 (2005) 149.
5. J. Rzayev, M.A. Hillmyer, Macromolecules 38 (2005) 3.
6. Y. Nakagawa, P.J. Miller, K. Matyjaszewski, Polymer 39 (1998) 5163.
7. P.J. Miller, K. Matyjaszewski, Macromolecules 32 (1999) 8760.

8. J. Kurjata, J. Chojnowski, C.-T. Yeoh, N.A.A. Rossi, S.J. Holder, Polymer 45 (2004) 6111.
9. M. Rutnakornpituk, P. Ngamdee, P. Phinyocheep, Polymer 46 (2005) 9742.
10. K. Jankova, X. Chen, J. Kops, W. Batsberg, Macromolecules 31 (1998) 538.

List of Publications

1. F. Guo, J.W. Andreasen, M.E. Vigild, S. Ndoni, Macromolecules 40 (2007) 3669.
2. F. Guo, K. Jankova, L. Schulte, M.E. Vigild, S. Ndoni, Macromolecules (accepted).

Brian Brun Hansen

Phone: +45 4525 2829
Fax: +45 4588 2258
E-mail: bbh@kt.dtu.dk
WWW: www.chec.dtu.dk
Supervisors: Søren Kiil
Jan E. Johnsson

PhD Study
Started: March 2005
To be completed: April 2008

Gypsum Crystallisation and Foaming in Wet Flue Gas Desulphurisation (FGD) Plants

Abstract
This study consists of experimental as well as theoretical investigations of gypsum crystallisation and the unexpected occurrence of foaming in wet flue gas desulphurisation (FGD) plants. The observed nucleation, growth and breakage of gypsum crystals in a wet FGD pilot plant will be used to validate models describing the particle size distribution (PSD). A survey of the gypsum quality at Danish full-scale wet FGD plants will furthermore be performed. The origin of the unexpected occurrence of foaming in wet FGD plants will be investigated. The obtained knowledge will be used to point towards methods to optimize the operation of wet FGD plants.

Introduction
A substantial part of the worlds present energy demand is based on the combustion of fossil fuels, such as coal, oil and gas. Despite an increasing interest in alternative fuel sources, the combustion of fossil fuels is expected to continue to yield a significant part of the world's energy demand in the coming years (figure 1).

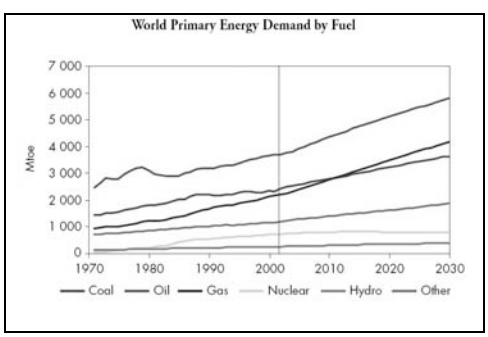

Figure 1: *Projected development of the world's primary energy demand (Mtoe = Million ton oil equivalents) [1].*

Due to the sulphur content of coals and oils, sulphur dioxide (SO_2), and to a lesser extent sulphur trioxide (SO_3), will be released by the combustion of these fuels. If emitted to the atmosphere the SO_2 can form sulphuric acid according to equation 1.

$$SO_2\,(g) + \tfrac{1}{2}O_2\,(g) + H_2O\,(l) \rightarrow H_2SO_4 \qquad (1)$$

The acidification of the environment caused by the formation of sulphuric acid in the atmosphere has been associated with a number of detrimental effects, such as

A reduction of biodiversity.
Reduced crop and forest growth.
Damage to buildings and architectural heritage.

Emitted SO_2 can furthermore contribute to the formation of aerosols in the atmosphere, affecting human health through respiratory and cardiovascular diseases.

In order to reduce these detrimental effects a range of FGD technologies have been developed and installed at power plants all over the world. The vast majority of the installed FGD capacity consists of the wet scrubber FGD technology [2] that either produces $CaSO_3$ sludge (equation 2) or $CaSO_4{\cdot}2H_2O$/gypsum (equation 3) depending on the operating conditions.

$$CaCO_3(s) + SO_2(g) + \tfrac{1}{2}\,H_2O \rightarrow CaSO_3{\cdot}\tfrac{1}{2}H_2O(s) + CO_2(g) \qquad (2)$$

$$CaCO_3(s) + SO_2(g) + 2\,H_2O(l) + \tfrac{1}{2}O_2(g) \rightarrow CaSO_4{\cdot}2H_2O(s) + CO_2(g) \qquad (3)$$

Most European power plants use the gypsum-producing forced oxidation process (equation 3), because of the sales potential of the gypsum for either wallboard or cement production. The sales potential of the produced gypsum depends on quality parameters such as the particle size distribution (PSD), the moisture content and the impurity content

A better understanding of the gypsum crystallisation process could facilitate a more consistent gypsum quality and point to ways of manipulating the gypsum properties. The incorporation of crystallisation kinetics predicting the gypsum PSD into mathematical process models is one way to obtain an increased control and understanding of the FGD process.

Non-wanted and unexpected foaming in wet FGD plants has been observed at several Danish power plants. This has caused a range of problems like scaling at the demister and FGD unit shut down, due to foam overflow from the reactor. The origin of this phenomenon is unknown and will be investigated with the aim of controlling foaming in wet FGD plants.

Specific Objectives

The overall objectives of this PhD project are:

- Derivation of crystallisation and degradation kinetics for the prediction of gypsum PSD.
- Investigation of the origin of foaming and the development of methods to control it in wet FGD plants.
- The use of the obtained results to optimize the operation of wet FGD plants

Crystallisation

The crystallisation process describes the formation and growth of solid crystals from a solution. Crystallisation can be encountered in nature or it can be used industrially as a solid liquid separation technique.

Before crystallisation can take place the solution must be supersaturated with respect to the crystallising species. Super saturation can be obtained by either changing the solubility of the solution or by a reaction yielding a product with a low solubility. The following different techniques may be used:

- Solution cooling.
- Solvent evaporation.
- Chemical reaction.
- The addition of an additional solvent (drowning out).
- Change of the pH.

The first step in the crystallisation process is the gathering of solute molecules into clusters (nuclei). Depending on whether the clusters are below or above the critical cluster size they may either redissolve or grow. The critical cluster size is a function of parameters such as super saturation and temperature. The process described above is known as homogenous nucleation, however new crystal may also be formed by heterogeneous or secondary nucleation. Heterogeneous nucleation is the formation of “new” particles by precipitation on particles of other species. Secondary nucleation is the formation of new crystals by particle attrition caused by particle/particle, particle/wall or particle/stirrer collisions.

The next step of the crystallisation process is the subsequent growth of the formed nuclei. The crystal growth process consists of transport of the solute molecule to the surface, surface diffusion and incorporation into the crystal structure. The transport of solute molecules to the crystal surface depends on the concentration gradient and thereby the super saturation. The topography of the surface offers a range of different binding sites, the most favourable ones constitute only a small fraction of the total number of binding sites. Because of this even a small amount of a species preferably absorbed on these sites may have a significant effect on the rate of molecule incorporation (crystal growth) and the resulting crystal morphology [3]. An example of the gypsum crystal morphology seen at full-scale wet FGD plants is shown in figure 2.

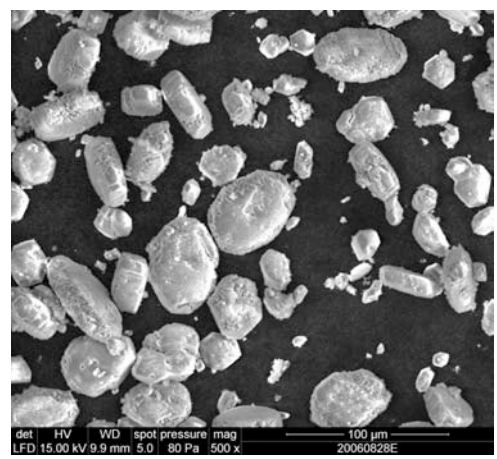

Figure 2: *Morphology of gypsum crystals from a full scale wet FGD plant.*

In addition to the nucleation rate and growth rate of cryastals factors such changes with time, breakage, agglomeration and the crystal residence time must be considered when modelling crystallisers. The population balance concpet is well suited for this purpose, it describes the number of particles as a function of their size or volume. Equation 4 shows the generel form of the population balance for a well mixed crystalliser [4].

$$\frac{\partial n(l)}{\partial t} + \frac{\partial (G \cdot n(l))}{\partial l} + \frac{n(l)_{out}}{\tau} + n(l) \cdot \frac{\partial (\log V)}{\partial t} = B \quad D \quad (4)$$

The simpler mixed suspension mixed product removal (MSMPR) model can be derived (equation 5), by

assumptions of steady state, the absence of breakage/agglomeration, a well mixed prodct stream and a size independent growth rate. This equation allows an easy extraction of kinetic date from a semilogaritmic plot of the population density as a function of the particle size.

$$\ln(n(l)) = \ln\left(\frac{B^0}{G}\right) - \frac{l}{G \cdot \tau} \quad (5)$$

Pilot-Scale

The wet FGD pilot plant, used in this investigation, simulates a single vertical channel of the packing zone in a full-scale wet FGD plant. The basic outline of the pilot plant is illustrated by figure 3. A 110 kW natural gas boiler and subsequent SO_2 addition generates the SO_2 containing flue gas. The flue gas is brought into contact with the slurry in the absorber (a 7 m pipe with multiple sampling sites). The slurry leaving the absorber is collected in a hold-up tank where air injection and reactant addition take place. The pH of the holding tank is kept constant by an on/off control of the feed stream. A timer-controlled pump removes the slurry that exceeds a given level, ensuring a constant slurry level in the holding tank. The time to reach steady state operation is roughly a week.

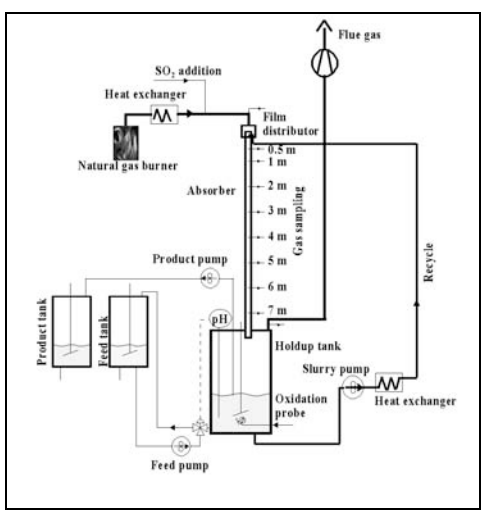

Figure 3: *Principal diagram of the wet FGD pilot plant.*

Initial experiments have been focused on the extent of crystal breakage taking place in the wet FGD pilot and its effect on the PSD. Samples of gypsum slurry have been subjected to the mechanical stresses caused by stirring, recirculation and air injection for up to 600 hrs. The development in PSD as a function of time has been monitored by laser diffraction measurements with a Malvern Mastersizer S. The long exposure times caused a decrease in the volume fraction of particles above approximately 25 µm and a corresponding increase in the volume fraction of particles below this size. The increased fraction of small particles may cause a reduced dewatering potential of the gypsum. Various breakage models are being tested against the experimental data.

Full-Scale

A survey of the gypsum quality at a range of Danish full-scale wet FGD plants is currently in progress. Samples from 3 different plants have been collected, one of these plants was monitored during several weeks of operation, in order to obtain knowledge on the effect of operational variations on the slurry composition and ultimately the gypsum quality. It is the aim of this survey to compare the gypsum PSD and morphology with operational parameters such as slurry saturation degree, slurry composition, solid residence time and slurry density.

Foaming

Bubbles in a liquid may form as a result of injected air, stirring or the flow conditions present. The balance between the arrival of new bubbles to the surface and their persistence (lifetime) determine if an accumulation of bubbles, and thereby foam formation, will occur.

The persistence of a foam will be influenced by gravity-induced drainage of the bubble walls (lamella), gas diffusion between the bubbles, the attractive/repulsive forces of the approaching surfaces and capillary flow induced by pressure differences within the lamella. Foaming agents that provide increased bubble persistence include surfactants, macromolecules (such as polymers or proteins) or finely dispersed solids [5].

Laboratory experiments with a Bikerman column will be performed to investigate the influence of the additives, ions, and particles present in a wet FGD slurry on the foamability of the slurry. The Bikerman test measures the foam height at a dynamic equilibrium between the rate of bubble formation and the rate of bubble collapse. The foam height as a function of gas flow rate is recorded and used to calculate a Bikerman/foaminess coefficient of the solution (Σ).

$$\sum = \frac{h}{v_s} \quad (6).$$

This coefficient expresses the average bubble lifetime in the foam before it bursts. The coefficient is reported to be independent of gas flow rate, the shape and dimensions of the column and the amount of solution present, provided that the evaporation (low gas velocities) and the rupture of the lamella (high gas velocities) is negligible [6].

Acknowledgements

This work is part of the MP_2T Graduate School within the CHEC (Combustion and Harmful Emission Control) Research Center funded a.o. by the Technical University of Denmark, the Danish Technical Research

Council, the European Union, the Nordic Energy Research, Dong Energy A/S, Vattenfall A.B., F L Smidth A/S, and Public Service Obligation funds from Energinet.dk and the Danish Energy Research program.

Nomenclature

B particle birth term [no m^{-1} m^{-3} hr^{-1}]
B^0 nucleation rate [no m^{-3} hr^{-1}]
D particle death term [no m^{-1} m^{-3} hr^{-1}]
G crystal growth rate [m hr^{-1}]
h foam height [m]
l characteristic particle length [m]
n population density [no m^{-1} m^{-3}]
t time [hr]
v gas velocity [m hr^{-1}]
V volume [m^3]
Σ = Bikerman coefficient [hr}
τ rresidence time [hr]

Subscript

o out
s superficial

References

1. World energy outlook, International Energy Agency (IEA) & Organisation for Economic Co-operation and Development (OECD), Paris, France, 2004, p. 570.
2. H.N. Soud, Developments in FGD, IEA Coal Research, London, U.K., 2000, p. 138.
3. R.J. Davey, J. Garside, From Molecules to Crystallizers, Oxford University Press, Oxford, U.K. 2000, p. 81.
4. A.D. Randolph, M.A. Larson, Theory of Particulate Processes 2nd ed, Academic Press Inc, San Diego, U.S.A, 1988, p. 369.
5. R. Thiele, O. Brettschneider, J. Repke, H. Thielert, G. Wozny, Experimental Investigation of Foaming in a Packed Tower for Sour Water Stripping, Industrial & Engineering Chemistry Research 42 (7) (2003) 1426-1432.
6. J.J. Bikerman, Foams, Springer-Verlag, New York, U.S.A., 1973

List of publications

1. B.B. Hansen, S. Kill, J.E Johnsson, Gypsum Crystallisation in wet Flue Gas Desulphurisation (FGD) plants, Poster, Dansk Kemiingeniør konference (DK_2), DTU, Kgs Lyngby, May-June 2006.
2. B.B. Hansen, S. Kill, J.E Johnsson, Wet Flue Gas Desulphurisation – Gypsum Crystallisation, Proceedings of the 6th European Congress of Chemical Engineering (1), 267-268, Copenhagen September 2007.

Peter Dybdahl Hede
Phone: +45 4525 2842
Fax: +45 4525 2258
E-mail: pdh@kt.dtu.dk

Supervisors: Anker Degn Jensen
Poul Bach, Novozymes A/S

PhD Study
Started: September 2005
To be completed: August 2008

Scale-Up of Fluidized Bed Coating Systems

Abstract
Fluid bed granulation is a vital operation in the pharmaceutical, enzyme and food/feed industry, and fluid beds are used extensively to form liquid formulations into solid products. Although widely used, fluid bed operations are still not fully understood or described. This means that industrial fluid bed operations and optimisation are still highly dependent on empirical approaches. Especially up-scaling of fluid bed systems is a challenging task with decisions to be made at many levels. This Ph.D. project aims at the fundamental understanding of the fluid bed granulation process in an industrial context having successful scale-up as it primary focus.

Introduction
Particle processing in fluidised beds is a key operation to many types of industries including the food and pharmaceutical industries. In the production of solid enzyme products, fluid beds are used to produce enzyme granules with the proper product properties by spraying the enzyme concentrate through nozzles onto the agitated fluidised bed often consisting of inactive filler cores. In that sense agglomeration is an unwanted phenomenon but in other applications, agglomeration is indeed desired. In either case, control of agglomeration is essential.

Proper product quality is highly dependent on the precise control and optimisation of the process. As there is more than forty parameters involved in the fluid bed coating process, and as many of these parameters interact, fluid bed optimisation is an extremely difficult exercise. The situation is further complicated by the fact that during fluid bed processing many different processes occur simultaneously including wetting, drying, chance of agglomeration, attrition and more. As, in addition, particle trajectories inside fluid beds are chaotic, modelling and simulation of the coating process with commercial products is not an easy task. Thus, fluid bed processes and products are still highly dependent on experimental results although this is tedious, time consuming and thereby expensive.

Often, optimisation of a fluid bed process is done in small- or medium-scale and then transferred to the large production-scale. This requires detailed knowledge of not just process and formulation properties but also knowledge of scaling principles and parameters; e.g. which parameters should be kept constant during scale-up and which parameters may be varied. Currently, scaling is still based on experience as reviewed by Hede (2006b). This is not a satisfactory situation - neither from an academic nor from an industrial point of view.

Commercial enzyme granules are typically coated with different types of coating layers falling into two basic categories being inorganic salt coating and polymer film coatings. A typical example of a commercial enzyme granule with both types of coatings can be seen in figure 1. This granulation process is based on a combination of mixer and fluid bed technology, where the active granulate is build around an inert carrier/core, which is produced and formulated in a high-shear mixer. Enzyme and inert functional layers are added onto the core in successive steps. First, the enzyme is added by absorption of concentrate into the carrier/core in a high-shear mixer. Then additional concentrate is added by spraying in a fluid bed to reach the specified product activity. Next, the granule is coated in a fluid bed with a layer of typically sodium sulphate. The granule is finally equipped with an outer film coating consisting of a mixture of different types of polymers. An additional layer of low-viscous polymer may be added as a lubricant to reduce attrition [1,2,3].

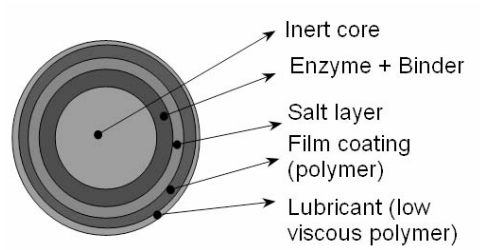

Figure 1: The build-up of a commercial enzyme granule.

In recent articles [4, 5, 6, 10] fluid bed coating processes with sodium salt solutions were treated in detail in the context of fundamentals and scale-up issues. Results are promising regarding control of the process at the same time being able to produce salt coated granules with high mechanical strength and low tendency of agglomeration during processing. Results indicate that especially nozzle conditions play an important role for the outcome of the process and that temperature and humidity conditions inside the bed during coating is of primary importance regarding agglomeration. Hede et al. [6] suggested that the bed temperature and bed humidity during steady state coating conditions were combined into a so-called Drying force parameter, according to equation 1, indicating the rate of moisture evaporation from the coated particles.

$$\text{Drying Force} = P_{sat}\big|_{T_{bed},100\%rH} - P_{actual} \qquad (1)$$

where $P_{sat}|_{Tbed,100\%rH}$ is the saturated pressure at the dry bulb temperature and P_{actual} is the actual vapour pressure of the fluidisation air at the bed temperature and the bed relative humidity conditions. P_{sat} is calculated from the Antoine equation and P_{actual} is given by equation 2.

$$P_{actual} = \frac{\text{Bed rH\%}}{100\,\text{rH\%}} \cdot P_{sat}\big|_{T_{bed}} \qquad (2)$$

The advantages of the Drying force parameter in a scale-up context were emphasized in the works by Hede et al. [6]. This paper further argues in favour of fluid bed process operation in terms of fixed nozzle conditions and fluidisation velocity throughout the coating process with conditions inside the fluidisation chamber adjusted only in terms of the inlet air temperature. Whether this fluid bed coating control approach can be used for polymer film coating has not yet been tested.

Specific Objectives

It is the objectives of the Ph.D. project to achieve a fundamental quantitative understanding at particle level of what is going on inside the fluid bed during coating/agglomeration processing. Further, it is the objective to be able to propose and test new principles for successful scale-up of the fluid bed coating process from pilot plant-scale into large-scale.

Experimental

A number of coating expereimetns were carried out using a Niro-Aeromatic Multiprocessor type MP-1 with a stainless steel fluidising chamber of 16 L allowing a particle bed load of 4000 g to be fluidized. A sketch of the general set-up in each of the three fluid bed systems may be seen from figure 2.

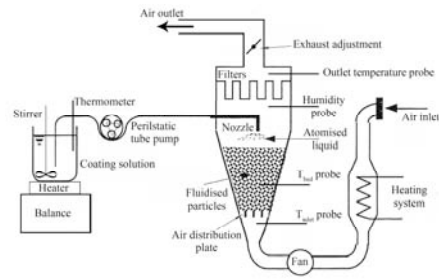

Figure 2: Sketch of the general top-spray set-up used in all three fluid bed scales.

Resembling standard coating formulations within the inorganic salt and polymer film coating solution two coating formulations were selected for comparison being a 15 w/w% Na_2SO_4 + 1 w/w% Dextrin and a 10 w/w% PVA + 10 w/w% TiO_2 solution.. Demineralised water was used as solvent.

Prior to coating, the core bed load was heated until the relative humidity inside the fluidisation chamber was constant, typically ranging from 5 RH% to 7 RH% depending on weather conditions. In each coating operation the aim was to coat until the bed load had increased 20 w/w%. This was done in order to make sure that a reasonable coating layer (~ 5 - 10 µm) had developed. After coating, the bed load was kept fluidised at identical fluidisation velocity and temperature conditions in order to dry the coated granules. This was done until the relative humidity inside the chamber was identical to the conditions prior to coating. The coated bed load was afterwards weighed in order to make sure that the bed load had gained in weight about 20 w/w%. For all the experiments the batch weight gain was in the range of 18.7 w/w% – 19.5 w/w% indicating little loss of core material as well as little loss of coating solution due to spray drying.

Results and Discussion

Result with the two types of coating solutions showed interestingly that the agglomeration tendencies distributed nicely in bonds when the corresponding Drying force value was depicted as a function of the spray rate. However, the agglomeration bonds were not similar for the two coating solutions as it can be seen from figure 3 and figure 4. Whereas the agglomeration tendency is < 5 w/w% for the Na_2SO_4 coating process over a wide range of Drying force/spray rate conditions

the agglomeration tendency was not observed to be less than 10 w/w% for the PVA/TiO_2 coating solution. Furthermore, the regime with agglomeration tendency in the range of 10-20 w/w% was quite narrow. Apparently, it is much more difficult to coat with the polymer coating solution compared with the Na_2SO_4 solution.

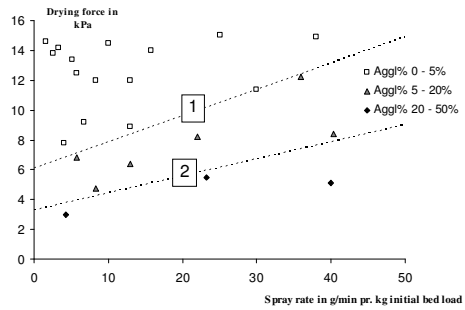

Figure 3: Resulting agglomeration tendencies for coating experiments with 15 w/w% Na_2SO_4 coating solution. The dashed lines indicate the demarcation between the different agglomeration regimes.

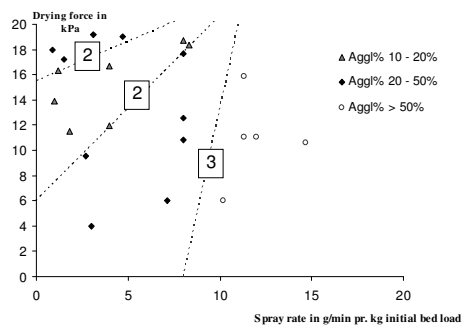

Figure 4: Resulting agglomeration tendencies for coating experiments with 10 w/w% PVA + 10 w/w% TiO_2 coating solution. The dashed lines indicate the demarcation between the different agglomeration regimes.

In order to study what causes the differences in processing the two type of coating solutions were studied in detail. Rheological characterisation of the coating solutions was performed with Physica MCR 301 Rheometer (Anton Paar GmbH, Austria) in which is was possible to measure the shear viscosity at different temperatures and shear rates.

Stickiness measurements were carried out in a TA.XT2i Texture Analyser (Stable Micro Systems, England). The probe was a standard Perspex 20 mm probe being an acrylic cylinder with sharp edges and a well-defined surface area. A specially designed stainless steel plate was designed for the coating liquid samples. For the liquid sample a cylinder-shaped hole with a diameter of 30 mm and a depth of exactly 200 µm was cut with a milling cutter into the stainless steel plate. A sketch of the texture analyser system may be seen from figure 5.

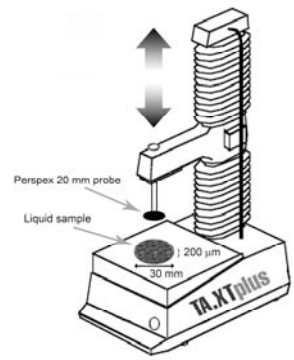

Figure 5: Sketch of the TA.XT2i Texture Analyser coating formulation screening tool.

Results from the fluid bed coating and rheology experiments indicated the following points:

It is not the bulk viscosity of the coating solution that plays an important role regarding agglomeration but rather the extent of stickiness during steady state coating.

The bulk viscosity does indeed play an important role regarding the degree of droplet penetration into the coated core. As the coating liquid bulk viscosity increased, the level of droplet penetration decreased.

It was however observed, how the tendency of agglomeration clearly decreased as the mean droplet size decreased, but also that the trends were different for the two types of coating solutions with respect to the tendency of agglomeration., i.e. the PVA/TiO_2 solution responded clearly with increased agglomeration percentage upon a small increase in the mean droplet size, whereas the agglomeration tendency for the salt solution was hardly affected in the range of the tested mean droplet sizes.

The PVA/TiO_2 solution is a colloidal system having an isoelectric point and a glass transition temperature. It was observed that the viscosity, stickiness and agglomeration tendency all could be reduced by reducing the pH to a value far from the isoelectric point.

By replacing 1/10 of the PVA and an equal amount of the TiO_2 with Neodol (a high purity C12-C13 Primary alcohol ethoxylate with an average of approximately 6.5 moles of ethylene oxide per mole of alcohol), reducing

the solution pH to 4, the resulting agglomeration tendency could be reduced by roughly 10 w/w% points. The morphology interestingly also improved significantly in terms of the formulation modifications.

Conclusions

In the pursuit of finding the causes why polymer and inorganic salt solutions cannot be processed under similar fluid bed process condition in order to result in similar tendency of agglomeration, a number of detailed studies were carried out in order to optimise process and formulation conditions. Experimental studies were based on hypotheses originating from previous experience and theoretical knowledge found in literature.

The results in the present study have clearly shown that the coating with inorganic salt solutions in a top-spray fluid bed is indeed different from coating with a polymer solution with inorganic filler particles in suspension. In comparison the salt coating process is a fairly simple process where it is possible to keep the agglomeration tendency low even at high process intensity. The salt coating process can be controlled in terms of process parameters solely as correct choices of parameters such as spray rate, bed temperature and bed humidity are sufficient to control the process.

On the contrary, the polymer coating process is much more sensitive. First of all the coating process cannot be controlled in terms of process parameters alone. Correct choices of process conditions are difficult as there is only a narrow regime in which there is a possibility that the agglomeration tendency can be kept low. The coating formulation is also of primary importance for the agglomeration tendency. The fact that a polymer solution with dispersed inorganic particles constitutes a colloidal system requires knowledge of glass transition temperature as well as surface and electrostatic phenomena for the correct optimisation of the formulation. This also means that the correct preparation (order of dispersion, temperature range, stirring, correct heating ramping etc.) of the coating liquid is of importance. The strict requirements for correct choice of process and formulation properties all together clearly make the polymer coating process a challenging exercise.

Acknowledgements

This Ph.D. project is partly funded by Novozymes A/S. The Author is a member of the Novozymes Bioprocess Academy as well as the MP_2T Graduate School in Chemical Engineering

References

1. Markussen, E.K. (1986) *Enzyme containing granulates suitable for use as detergent additives*, European Patent EP 0 170 360 B1, Novo Industri A/S.
2. Markussen, E.K. (2002) *Enzyme containing granule*, United States Patent US 6,348,442, Novozymes A/S.
3. Simonsen, O. (2002) *Lubricated Granules*, International Patent WO 02/20746 A1, Novozymes A/S.

List of Publications:

Journals:

4. Hede, P.D., Bach, P. and Jensen, A.D., Powder Technology No. 176, pp. 156-167: *Small-scale top-spray fluid bed coating: Granule impact strength, agglomeration tendency and coating layer morphology*.
5. Hede, P.D., Bach, P. and Jensen, A.D., Chemical Engineering Science, In Press, *Validation of the Flux number as scaling parameter for top-spray fluid bed systems*.
6. Hede, P.D., Bach, P. and Jensen, A.D., Powder Technology, In Press, *Top-spray fluidised bed coating: Scale-up in terms of relative droplet size and drying force*.
7. Hede, P.D., Bach, P. and Jensen, A.D., International Journal of Pharmaceutics, Submitted to Journal, *Two-fluid spray atomisation and pneumatic nozzles for fluid bed coating/agglomeration purposes: a review*.
8. Hede, P.D., Bach, P. and Jensen, A.D., Chemical Engineering Science, In preparation, *Fluidised bed particle coating with sodium sulphate or PVA/TiO_2 solutions: Differences and similarities in processing and operations*.

9. **Conference Proceedings:** Hede, P.D., Jensen, A.D., Bach, P.: *Experimental Validation of Macro- and Micro-level Scaling Laws in Small- and Medium Scale Top-spray Fluidised Bed Coaters* in Bi, X., Berruti, F., Pugsley, T. (Eds.), Fluidization XII – New Horizons in Fluidization Engineering, Engineering Conferences International, British Columbia, Canada, 2007, pp. 823-830, ISBN 978-0-918902-57-3.

10. **Internal Reports:** Hede, P.D.: *Towards Mathesis Universalis: Modern aspects of modelling batch fluid bed agglomeration and coating systems – a review*, CHEC Report R0605, Department of Chemical Engineering, CHEC Research Centre, Technical University of Denmark, pp. 1 - 101, 2006.

Michael Lykke Heiredal
Phone: +45 4525 4828
Fax: +45 4525 2258
e-mail: mlh@kt.dtu.dk
www: www.kt.dtu.dk
Supervisors: Professor Anker Degn Jensen
Associate professor Flemming J. Frandsen
Joakim R. Thøgersen, Haldor Topsøe A/S

Industrial Ph.D. Study
Started: September 2006
To be completed: August 2009

Particle Dynamics in Monolithic Catalysts

Abstract
Emission of nitrogen oxides from pulverized coal combustion is a major environmental problem today. The most used method for reduction of nitrogen oxides in the flue gas from coal fired power stations is Selective Catalytic Reduction (SCR) of nitrogen oxides with ammonia as reducing agent. A major problem using the SCR process is the risk of plugging and erosion/attrition of the monolithic catalysts because of fly ash particles in the flue gas. The objective of this Ph.D. project is to develop a model that in combination with Computational Fluid Dynamics can simulate the degree of plugging in monolithic catalysts with flue gas containing high fly ash concentration. The model should be a function of particle properties, gas velocities, angle of incidence to the monolith, geometry of the catalyst, and characteristics of the surfaces.

Introduction
The formation of nitrogen oxides (NO_x) during combustion processes takes place partly because of reaction between oxygen and nitrogen in the combustion air and partly because of reaction between oxygen in the air and nitrogen in the fuel. The formation of NO_x is an unwanted reaction because it contributes to acidifying the rain water and also is unhealthy for human beings.

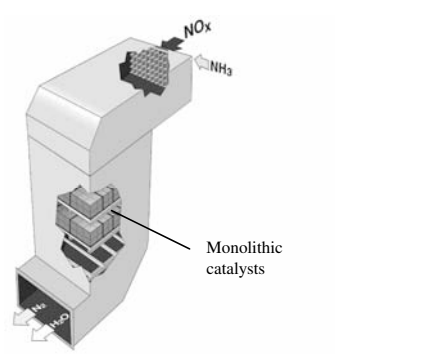

Figure 1: Illustration of a high dust SCR reactor with monolithic catalysts.

The most used method for reducing NO_x in the flue gas from coal fired power stations is Selective Catalytic Reduction (SCR) of NO_x, where ammonia (NH_3) is used as reduction agent. Figure 1 shows an illustration of a high dust SCR reactor with monolithic catalysts. The global reactions for the SCR process are:

$$4NO + 4NH_3 + O_2 \rightarrow 4N_2 + 6H_2O$$

$$6NO_2 \quad 8NH_3 \rightarrow 7N_2 + 12H_2O$$

where the products are free nitrogen (N_2) and water (H_2O) which are harmless to the environment.

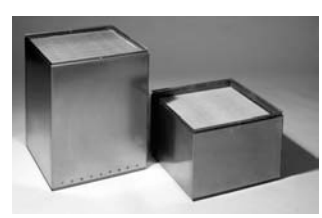

Figure 2: Picture of Haldor Topsøe A/S DeNOx SCR catalysts with corrugated monolith.

Generally industrial catalysts consist of vanadium and wolfram (V_2O_5/WO_3) dispersed on a titanium oxide (TiO_2) carrier. Figure 2 shows a picture of two Haldor Topsøe A/S DeNOx catalysts with corrugated monoliths. The high dust zone in the stationary power

stations is usually preferred for the SCR reactor. The operating temperature in the high dust zone is in the range from 300 to 400°C which is ideal for the catalytic activity. The content of NO_x in the flue gas is typically about 300 to 700 ppm, and NO_x can thereby be reduced by 80 to 90% over the SCR catalyst with an ammonia slip of a few ppm.

A major problem using the SCR DeNOx process under high dust conditions is the risk of plugging and erosion/attrition of the monolithic catalysts because of fly ash particles in the flue gas. The content of fly ash formed by the combustion processes is usually about 5-20 g/Nm^3 [1]. Monolithic catalysts are generally designed as a collection of catalytic channels, where the flue gas flows parallel to the wall to minimize the risk of plugging. Despite regular soot blowing, it is observed that a major part of the channels in the catalysts have been deactivated due to plugging. The plugging can be minimized by using larger channel diameters but as a consequence the catalyst volume has to be larger to obtain the same conversion which makes the reactor more expensive. One of the main design criteria is that the catalysts should be able to operate under heavy dust load and be compact to reduce cost, and at the same time function effectively without plugging.

Objective

To meet these design criteria it is necessary with a fundamental study (both experimental and numerical) of the particle dynamics in monolithic catalysts in order to understand the mechanisms that transport and deposit fly ash particles on the surface of the catalyst. Depending on the size of the particles, the transport can be due to Brownian diffusion [7], particle inertia, aerodynamic forces [2], turbulent diffusion [8] or thermophoresis [6]

Today a lot of models exist in the literature for transport of particles and aerosols in duct flow including deposition of these. It is also possible to use CFD to simulate transport and deposition of particles and aerosols in turbulent gas flow [3, 4]. CFD models also exist that can simulate the performance of the SCR reactor down stream in coal fired power stations regarding pressure loss, temperature and mixing of chemical species [5]. But none of these models take deposition and plugging into account in the channels of the monolithic catalysts.

The objective of this Ph.D. project is to develop a model that e.g. in combination with Computational Fluid Dynamics (CFD) can simulate the degree of plugging in monolithic catalysts with flue gas containing high fly ash concentrations. The model e.g. should be a function of particle properties, gas velocities, angle of incidence to the monolith, geometry of the catalyst and characteristic of the surface.

Methods

An experimental setup has been built for measuring deposition of submicron particles in a pipe, see Figure 3. The experimental setup consisted of a Six-Jet Atomizer Model 9306A *TSI Incorporated*, a Diffusion Dryer Model 3062 *TSI Incorporated*, an Aerosol Neutralizer Model 3054 *TSI Incorporated*, a 3m long electro polished stainless steel tube[1] for deposition of aerosol particles and two sampling lines for Scanning Mobility Particle Sizer (SMPS) measurements. The flow rate in the deposition pipe was 300 ml/min, giving an average velocity of 0.18 m/s corresponding to a Reynolds number of about 72, to ensure enough residence time for deposition of submicron particles.

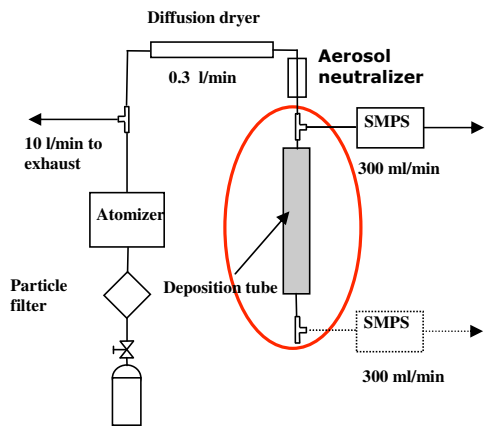

Figure 3: Experimental setup for measuring deposition of submicron particles in a 3m long electro polished pipe with a diameter of 6mm.

All fittings in the setup were Swagelok® and tubes were made of carbonized silicon material to prevent deposition due to electrostatic forces. Dimensions of the fittings and tubes in the setup were ¼" inch except for connections to the atomizer, where ½" fittings and tubes were used.

The principle of the setup was as follows. Pressurized atmospheric air at 5 bar controlled by a valve was fed to the atomizer through a particle filter. The atomizer was set to a pressure at about 4 bar giving a flow rate of about 10 l/min per nozzle which was connected to the exhaust system. Because the SMPS system was set to a flow rate of 300 ml/min controlled by an internal vacuum pump, a side stream of 300 ml/min was drawn from the atomizer main aerosol stream through the diffusion dryer and through the deposition pipe. The surplus of the aerosol stream from the atomizer was led to the exhaust system. To minimize deposition losses through the sampling lines, these were made as short as possible giving a maximum length of about 10 cm. To minimize deposition in the system due to electrical charges the setup was grounded using stainless steel and carbonized tubes.

[1] The stainless steel pipe had a surface roughness of 2 nm.

The Scanning Mobility Particle Sizer (SMPS) system consisted of a Condensation Particle Counter (CPC) model 3775 *TSI Incorporated*, and a Long Differential Mobility Analyzer (LDMA) model 3081 *TSI Incorporated* or a Nano Differential Mobility Analyser (NDMA) model 3085 *TSI Incorporated* depending on the system settings. The SMPS system measured the size distribution of a poly-dispersed aerosol in the size range between 4.4-833nm using the NDMA for particles in the size range between 4.4-168nm and the LDMA for particles in the size range between 13-833nm. The CPC counted the different classes of particles classified by respectively the NDMA and LDMA.

A dust pilot at Haldor Topsøe A/S was rebuilt with a worst case angle of incidence at 45° to the monolith for investigating fly ash deposition and plugging in monolithic catalysts as a function of different fly ash types, particle concentration in the gas flow and the linear gas velocity.

Deposition of neutral (carrying zero charge) submicron particles in the particle size range between 3-800nm in a 3m long smooth pipe has been numerically investigated using the commercial CFD solver Fluent.

Results and discussion

The particles that were generated by the atomizer were produced by a 0.002 wt% salt solution consisting of potassium chloride KCl. The size distribution of the poly-disperse KCl aerosols between 4.4-168nm was measured using the NDMA. The measurements were carried out at the top and bottom of the deposition pipe, see Figure 3. In order to analyze the effect of particles carrying a charge, the measurements were carried out both with and without using the Aerosol Neutralizer in the setup as shown in Figure 3. Using the Aerosol Neutralizer discharges the particles to a Boltzmann charge equilibrium. The size distributions of the poly-disperse KCl aerosols at the top and the bottom of the deposition pipe are shown in Figure 4.

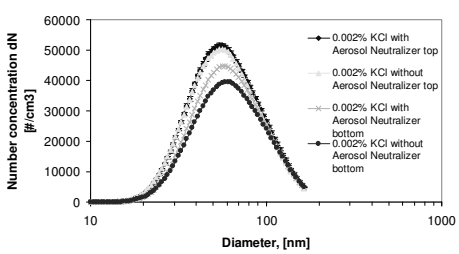

Figure 4: Size distributions of the charged and discharged poly-disperse KCl aerosols at the top and the bottom of the deposition pipe consisting of a 3m long electro polished pipe with a diameter of 6mm.

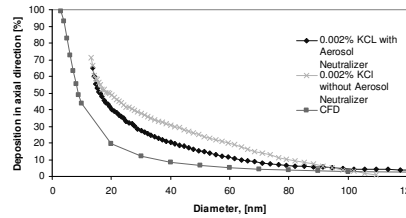

Figure 5: Comparison between charged and discharged particles including CFD simulation of neutral particles (carrying zero charge). Graph showing deposition of particles in per cent in the deposition pipe as a function of particle size, based on the measurements at the top and bottom of the deposition pipe consisting of a 3m long electro polished pipe with a diameter of 6mm.

As it can been seen from Figure 4 the concentration of the discharged particles measured at the bottom of the deposition pipe is substantially higher than the concentration of the particles which have not been discharged by the Aerosol Neutralizer. Figure 5 shows the deposition of particles in per cent in the deposition pipe as a function of particle size, based on the measurements at the top and bottom of the deposition pipe showed in Figure 4. As it can be seen the discharged (discharged to a Boltzmann charge equilibrium) particles show a lower deposition rate in the range between about 20-80nm than particles which have not been discharged. This is probably due to additional deposition from electrostatic forces as a result of the higher charge that the particles are carrying. Tsai et al. [9] have reported that the charge on NaCl particles generated by an atomizer increases with a decrease in NaCl solution. Therefore, it is probably the same effect seen here, where the KCl particles generated from a very low 0.002 wt% KCl solution carry a high charge compared to the Boltzmann charge equilibrium, which has been obtained in the case where the Aerosol Neutralizer was used to discharge the particles.

The measured deposition was also compared with CFD simulation of the deposition, of submicron particles carrying zero charge, in the particle size range between 3-800nm in a 3m long smooth pipe with a diameter of 6mm. As it can be seen from Figure 5, there is some deviation between simulation and measurements. This could probably be due to the effect of the mirror force acting on a particle from the Boltzmann charge equilibrium and the mirror force in the case where the particles are highly charged

Conclusion

Particle size distribution and deposition rate of highly charged aerosol particles generated by an atomizer from a 0.002 wt% KCl solution were measured at the top and bottom of a 3m long pipe with a diameter of 6mm. Size distribution and deposition rate were compared with particles which have been discharged to a Boltzmann charge equilibrium using an Aerosol Neutralizer. The

size distribution shows that concentrations of the discharged particles at the bottom of the deposition pipe are substantially higher than the concentration of the particles which have not been discharged. The discharged particles show a lower deposition rate in the range between about 20-80nm than particles which have been discharged. This could probably be due to an additional deposition from electrostatic forces as a result of the higher charge that the particles are carrying. CFD simulations of the deposition of submicron particles carrying zero charge in the particle size range between 3-800nm in a 3m long smooth pipe with a diameter of 6mm show lower deposition than the charged and the discharged particles. The reason could probably be that particles in the CFD simulations are fully neutral particles that are carrying zero charge.

Future work

In the next period plugging experiments using the rebuilt dust pilot at Haldor Topsøe A/S will be carried out. Further experiments will be made with the experimental setup for measuring deposition of submicron particles in a pipe, and the setup will be modified in order to investigate the effect of large particles in the micro meter range. Further investigations will be carried out in order to explain the deviation between the measured and the simulated deposition. Modelling of particle deposition from micron particles in a single pipe will be carried out taking the particle/wall interaction into account.

References

1. E. Raask, Minerals Impurities in Coal Combustion. Behavior, Problems and Remedial Measures, Taylor & Francis, 1 edition, U.K., 1985.
2. P.G. Saffman, Journal of Fluid Mechanics, 22 (2) (1965) 385-400.
3. C.M. Winkler, S.L. Rani & S.P. Vanka, Powder Technology, 170 (2006) 12-25.
4. R. Maniero & P. Canu, Chemical engineering Science 61 (2006) 7626-7635.
5. K. Rogers, M. Albrecht & M. Varner. Babcock & Wilcox, Technical Paper (2000).
6. C-J. Tsai, J-S. Lin, S.G. Aggarwal & D. Chen, Aerosol Science and Technology, 38 (2004) 131-139.
7. J.M. Frey, P. Schmitz, J. Dufreche & I.G. Pinheiro, Transport in Porous Media, 37 (1999) 25-54.
8. A. Kitamoto & Y. Takashima, Bulletin of the Tokyo Institute of Technology, No. 127 (1975).
9. C-J. Tsai, J-S. Lin, C.G. Deshpande & L-C. Liu, Part. Part. Syst. Charact, No. 22 (2005) 293-298.

Jesper Holck
Phone: +45 4525 2943
E-mail: jeh@kt.dtu.dk
WWW www.bioeng.kt.dtu.dk

Supervisors: Anne S. Meyer
Jørn Dalgaard Mikkelsen (Danisco)

PhD Study
Started: November 2007
To be completed: December 2010

Enzymatic Production of Prebiotics from Sugar Beet Pectin

Abstract
The potential importance of dietary fibres and oligo-saccharides in modulating the microbial ecology of the human colon to exert beneficial health effects is currently receiving significant attention. By targeting dietary fibre structures and prebiotics by selective enzymatic hydrolysis of complex plant substrates, such as pectin, defined poly- and oligomers can be derived.

Introduction
Dietary fibres and prebiotics are non-digestible dietary carbohydrate structures that can be health promoting by supporting the growth of beneficial bacteria in the human colon, such as *Bifidobacterium sp*. and via other mechanisms [1]. This PhD project builds on that a significant potential exists for targeting dietary fibre and prebiotics structures by selective enzymatic hydrolysis of pectinaceous plant cell wall structures present in sugar beet pulp – the byproduct stream left over from industrial production of sugar.

Specific objectives
The focus of the project will be on manufacture of the target oligomer products via intelligent reaction optimisation and combination of monoactive experimental enzymes available in the Prebiotics Center [2]. A particular focus area will be on characterising the action of these enzymes in modification of pectin rhamnogalacturonan I (rg I) (see Figure 1). Rg I is a heteropolysaccharide composed of a rhamno-galacturonan backbone with arabinan, galactan, and arabinogalactan side chains. The design of optimal enzyme reactions, including only the required activites for the particular target substrate and target product, will be done via an iteration of advanced structural substrate and product analyses in systematic enzymatic treatments using monoactive enzymes. The research will include reaction parameter optimisations of selected reactions. The experimental work will be conducted to allow obtainment of new realizations about enzyme cascade action patterns on rg I and other pectin structures, including quantitative kinetics on branched plant cell wall polysaccharides.

Figure 1. schematic structure of rhamnogalacturonan I

The first challenge is to establish methods for thorough analysis of the substrate and the product oligomers in order to design a properly targeted enzyme biocatalysis followed by construction of statistically designed combinations of monoactive experimental enzymes for contriving optimal "minimal" enzyme cocktails.

Acknowledgements
The project is anchored in the Center for Biological Production of Dietary Fibres and Prebiotics at DTU ("Prebiotics Center"), granted by DSF. The project has significant involvement from Danisco A/S which provides the sugar beet pulp.

References
1. Rastall, R.A., Gibson, G.R., Gill, H.S., Guarner, F., Klaenhammer, T.R., Pot, B., Reid, G., Rowland, I.R. and Sanders, M.E. (2005). Fems Mic. Eco. 52, 145-152.

2. Bauer, S., Vasu, P., Persson, S., Mort, A.J. and Somerville, C.R. (2006). Proc. Natl. Acad. Sci. U. S. A 103, 11417-11422.

Jakob Kjøbsted Huusom
Phone: +45 4525 2801
Fax: +45 4525 2906
E-mail: jkh@kt.dtu.dk

Supervisors: Sten Bay Jørgensen
Niels Kjølstad Poulsen (IMM)

Ph.D. Study
Started: February 2005
To be completed: June 2008

Data Driven Controller Tuning

Abstract
Optimizing process operation through model based control strategies requires ideally a control oriented identification of the plant model. Identification for control should be performed under the conditions the process is operated at i.e. under closed loop control. Identification in closed loop implies an iterative procedure where the closed loop performance is optimized. Estimation of a process model from closed loop data needs to take the correlation between the process input and the external noise signal into account.

Introduction
The increasing competition on the global market has rendered optimizing process operation a necessity for new as well as existing production in the chemical industry. Advanced control strategies based on models for a specific process plays an important role in this respect. In particular implementation of model predictive controllers (MPC) in recent years, have contributed to increase competition capabilities of the product supply chain. Control oriented process modelling is part of the frame work on application oriented modelling. System identification is an area that has received much attention but within identification for control there is still a need for development of systematic methods. Identification for control implies experiments where the collected data for identification are retrieved from a process operated under control i.e. in closed loop.

The benefits and challenges in closed loop identification has been motivated several times in the literature where a key point is, that it is the performance of the closed loop that is object for the optimization [4,9]. Since then several research groups have worked on development of suitable systematic methods for handling an iterative procedure of closed loop experiments, model parameter estimation, and enhanced control design. This project is devoted to further development of optimization methods for processes through control oriented system identification.

Closed loop identification
A stable feedback connection ***T(P,C)***, consisting of the possible unstable system ***P*** and the controller ***C***, will due to the controller reject disturbances and track set points. The performance of the loop can be evaluated through some norm of a performance cost function ***J(P,C)***. In order to excite the system to reveal the dynamics, two external perturbations signals can be introduced to the system. The closed loop system with external probing signals is shown on the figure.

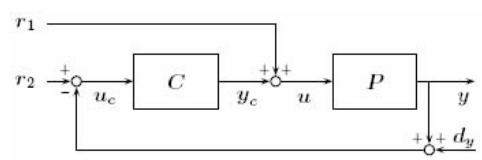

The signal r_1 introduces a deviation from the optimal control input to the system which will act as a known disturbance on the plant input. The second signal r_2 acts as a known perturbation in the reference signal and can therefore be used to move the process around to span a desired region of the output space.

Methodology
Closed loop identification is an iterative procedure due to the influence of the control. The identified plant model is used to design a new controller in order to enhance the performance of the loop. If the performance specifications are not met repeated iterations will have

to be performed according to the following scheme until the performance is satisfactory.

- Closed loop experiment
- Estimation of a plant model, $\boldsymbol{P}_i$
- Implement controller $\boldsymbol{C}_{i+1}$ based on $\boldsymbol{P}_i$
- Evaluation of closed loop performance, $\|\boldsymbol{J}(\boldsymbol{P}, \boldsymbol{C}_{i+1})\|$

Identification in closed loop through the iterative scheme involves some inherent problems and design challenges that needs to be addressed in order to ensure convergence of the procedure [1]. It must be required that the performance of the control loop is equal to or better than the performance of the loop for the previous iteration.

Estimation

Three main approaches to model estimation from closed loop data emerge, each with a number of advantages and disadvantages [8].

- Direct identification
- Indirect identification
- Joint input/output identification

In direct identification $\{\boldsymbol{u},\boldsymbol{y}\}$ are used to estimated the process model as in open loop identification. The basic principle of not having inputs that are correlated with noise are violated by this method. A consistent estimate is only produced by this method if the data are informative and the estimate contains the true model structure. This can imply that a very high model order have to be chosen in order to avoid bias. The advantages of the direct estimation is that it is simple and applicable regardless whether the controller are know and its complexity.

In the indirect identification a model is estimated using $\{\boldsymbol{r}_i,\boldsymbol{y}\}$ which prevent the problem with correlations. Given this estimate of the closed loop an estimate for the process is deduced using knowledge of the controller.

The joint input/output identification estimates the transfer from the excitation signals $\boldsymbol{r}_i$ to both $\boldsymbol{u}$ and $\boldsymbol{y}$. The system model is then equal the ratio between the two transfer functions.

Approaches to closed loop optimization

In order to ensure a robust control design based on an estimated model, it is necessary to estimate both a nominal model and its uncertainty set. In the thesis by de Callafon, [1], this is done by fractional identification through the dual-Youla parameterization and robust control design is based on μ-synthesis. Through an iterative procedure, the closed loop performance is optimized in a robust sense.

A more simple approach is to replace the robust infinity norms in the identification and control design with the 2-norm to facilitate the calculations. That could lead to a least squares identification problem and a frequency weighted LQG-control design [10]. This design does not have the same robust stability or performance properties as the infinity norm design. Given an identified model and the parameter confidence regions, stability and performance can be ensured for all systems within the confidence region. This approach will improve robustness properties but only for parametric uncertainty. If the identified model structure is wrong, stability can not be guarantied.

In the following section a data driven method will be presented which does not depend on an identified model of the system.

Iterative Feedback Tuning

This method of iterative performance enhancement does not include an estimate of the process model. The basic idea is to formulate a loop performance cost function and use an optimization algorithm to minimize this cost function with respect to the controller parameters. Evaluations of the partial derivatives of the cost function with respect to the controller parameters, $\boldsymbol{\rho}$, are based on measurements taken form the closed loop system. The algorithm was first presented in [5] and have since been extended and tested in a number of papers. See [2] and [3] for an extensive overview of the development of the method and for references to applications.

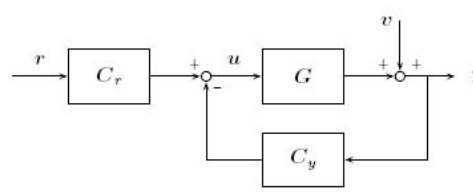

Given a description of a closed loop system as depicted on the figure above, where the two degree of freedom controller, $\boldsymbol{C} = \{\boldsymbol{C}_r, \boldsymbol{C}_y\}$, is implemented on the discrete linear time invariant system $\boldsymbol{G}$, the transfer functions are given as:

$$y = \frac{C_r G}{1 + C_y G} r + \frac{1}{1 + C_y G} v = Tr + Sv \qquad (1a)$$

$$u = \frac{C_r}{1 + C_y G} r - \frac{C_y}{1 + C_y G} v = SC_r r - SC_y v \qquad (1b)$$

where $\boldsymbol{r}$ is the reference value for the measurements $\boldsymbol{y}$, $\boldsymbol{u}$ is the actuator variable and $\boldsymbol{v}$ is a noise signal for the system which is presented in deviation variables. $\boldsymbol{S}$ and $\boldsymbol{T}$ are the sensitivity and the complementary sensitivity function respectively. Given a desired reference model for the closed loop $\boldsymbol{T}_d$, the desired response from the

loop is given as $\boldsymbol{y}_d = \boldsymbol{T}_d \boldsymbol{r}$. The performance criterion can then be formulated as a typical quadratic cost function, $\boldsymbol{F}(\boldsymbol{\rho})$, with penalty on deviations from the desired output and the control effort. The deviation of the outputs is given as

$$\tilde{y} = y - y_d$$

The optimal set of parameters will then require that the partial derivative of the cost function with respect to the controller parameters is zero and these represent the global minimum given the admissible parameter space. This optimal solution to the minimization problem can be obtained through an iterative gradient based search algorithm in case where the cost function is convex.

$$\begin{aligned}\rho_{i+1} &= \rho_i - \gamma_i R_i^{-1} \frac{\partial F(\rho_i)}{\partial \rho} \\ &= \rho_i - \gamma_i R_i^{-1} J(\rho_i) \end{aligned} \quad (2)$$

where $\boldsymbol{R}_i$ is a positive definite matrix and $\boldsymbol{J}$ is the Jacobian. The i'th step is then given by $\boldsymbol{h}_i = -\gamma_i \boldsymbol{R}_i^{-1} \boldsymbol{J}(\boldsymbol{\rho}_i)$. In case $\boldsymbol{R} = \boldsymbol{I}$ the algorithm steps in the steepest decent direction. In case $\boldsymbol{R} = \boldsymbol{H}(\boldsymbol{\rho})$ or an approximation to the Hessian, the Newton or Gauss-Newton algorithm appears. γ_i determine the step length and the choice of $\boldsymbol{R}$ and γ will thus affect the convergence properties of the method [5]. The determination of γ_i can be evaluated using a line search method.

The key contribution in Iterative Feedback Tuning is that it supplies an unbiased estimate of the cost function gradient without estimating a plant model, given that the noise $\boldsymbol{v}$ is a zero mean, weakly stationary random signal [3]. Using an estimate of the Jacobian in equation (2) instead of the analytical Jacobian as a stochastic approximation, the method will still make the algorithm converge to a local minimizer, provided that the estimate is unbiased. Given the cost function

$$F(\rho) = \frac{1}{2N} \mathrm{E} \left[\sum_{t=1}^{N} \tilde{y}_t(\rho)^2 + \lambda \sum_{t=1}^{N} u_t(\rho)^2 \right] \quad (3)$$

where the minimization criterion is

$$0 = J(\rho) = \frac{1}{N} \mathrm{E} \left[\sum_{t=1}^{N} \tilde{y}_t(\rho) \frac{\partial \tilde{y}_t}{\partial \rho} + \lambda \sum_{t=1}^{N} u_t(\rho) \frac{\partial u_t}{\partial \rho} \right] \quad (4)$$

it is seen that estimates of the gradients of deviation of the output and the control are needed in order to produce an estimate of the Jacobian. Since $\boldsymbol{y}_d$ is not a function of the controller parameters the gradient of the output is used instead of the deviation from the desired output. The partial derivatives of the in- and output with respect to the controller parameters can be evaluated based on equation (1).

$$\frac{\partial y}{\partial \rho} = \frac{1}{C_r(\rho)} \frac{\partial C_r}{\partial \rho} T(\rho) r - \frac{1}{C_r(\rho)} \frac{\partial C_y}{\partial \rho} T(\rho) y \quad (5a)$$

$$\frac{\partial u}{\partial \rho} = \frac{\partial C_r}{\partial \rho} S(\rho) r - \frac{\partial C_y}{\partial \rho} S(\rho) y \quad (5b)$$

Estimates of these two gradients can be produced given data from three separate closed loop experiments on the system. The three experiments can be designed as follows:

1. $\boldsymbol{r}^1 = \boldsymbol{r}$ i.e. the reference in the first experiment is the same as for normal operation of the process.
2. $\boldsymbol{r}^2 = \boldsymbol{y}^1$ i.e. the reference in the second experiment is the output from the first experiment
3. $\boldsymbol{r}^3 = \boldsymbol{r}$ i.e. the reference in the third experiment is the same as for normal operation of the process just as in the first experiment.

these experiments gives the following in- and outputs

$$\begin{aligned} \textbf{Ex. no 1:} \quad & y^1 = T(\rho) r + S(\rho) v^1 \\ & u^1 = S(\rho) \left(C_r(\rho) r - C_y(\rho) v^1 \right) \\ \textbf{Ex. no 2:} \quad & y^2 = T(\rho) y^1 + S(\rho) v^2 \\ & u^2 = S(\rho) \left(C_r(\rho) y^1 - C_y(\rho) v^2 \right) \\ \textbf{Ex. no 3:} \quad & y^3 = T(\rho) r + S(\rho) v^3 \\ & u^3 = S(\rho) \left(C_r(\rho) r - C_y(\rho) v^3 \right) \end{aligned}$$

The sequence of input/output data form these experiments $\{\boldsymbol{y}^i ; \boldsymbol{u}^i\}$ were i is 1,2 or 3 will be utilized as

$$\tilde{y} = y^1 - y^d \quad (6a)$$

$$u = u^1 \quad (6b)$$

$$\hat{\frac{\partial y}{\partial \rho}} = \frac{1}{C_r(\rho)} \left(\frac{\partial C_r}{\partial \rho} y^3 - \frac{\partial C_y}{\partial \rho} y^2 \right) \quad (6c)$$

$$\hat{\frac{\partial u}{\partial \rho}} = \frac{1}{C_r(\rho)} \left(\frac{\partial C_r}{\partial \rho} u^3 - \frac{\partial C_y}{\partial \rho} u^2 \right) \quad (6d)$$

It can be seen from equation (6a) and (6b) that the first experiments gives the measurement of the deviation from the desired output and the input which are needed in the estimate of $\boldsymbol{J}(\boldsymbol{\rho})$. The estimate of the gradients of the input and output can be written as

$$\hat{\frac{\partial y}{\partial \rho}} = \frac{\partial y}{\partial \rho} + \frac{S(\rho)}{C_r(\rho)} \left(\frac{\partial C_r}{\partial \rho} v^3 - \frac{\partial C_y}{\partial \rho} v^2 \right) \quad (7)$$

$$\hat{\frac{\partial u}{\partial \rho}} = \frac{\partial u}{\partial \rho} - \frac{S(\rho) C_y(\rho)}{C_r(\rho)} \left(\frac{\partial C_r}{\partial \rho} v^3 - \frac{\partial C_y}{\partial \rho} v^2 \right) \quad (8)$$

From this result it can be seen that the noise signal $\boldsymbol{v}^1$ plays an active part in the optimization of the controller parameters while only the noise terms from the second and third experiment act as nuisance.

Simulation Example
The figure and table shows the result of optimizing the setting time for a second order process with Iterative Feedback Tuning. Responses are shown for the initial, the two first iterations and for the optimal set of parameter for a PID controller with a first order derivative filter. The loop is implemented with PI action on the reference and full PID action in the feedback. The red curve $\boldsymbol{y}_d$ shows the desired response.

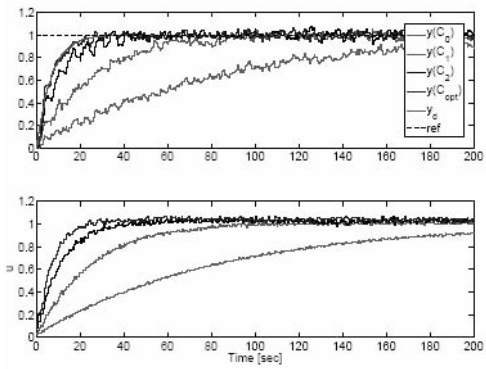

Iter.	K_c	τ_I	τ_D	α	Cost
Inital	0.0250	2.0000	1.0000	0.1000	0.0757
No 1	0.0379	0.9314	0.9976	0.0916	0.0131
No 2	0.0522	0.5525	0.9921	0.0905	0.0015
Opt.	0.0705	0.4874	4.9580	0.1184	0.0003

Recent developments.
As part of this Ph.D. project the Iterative Feedback Tuning method has been applied on control loops with other and more complicated types of control than classic PID-control. Satisfactory results were obtained from tuning a multivariable control loop with a nonlinear inventory control law on a pilot plant of a two tank system [6]. Work is being carried out on extending the method to state space model representations.

Controller tuning for disturbance rejection is notoriously difficult by Iterative Feedback Tuning due to poor signal to noise ratio in data. A methodology for improving the information content in data by use of external excitation has been developed for Iterative Feedback Tuning. Probing signals is generated from a constrained optimization [7].

Conclusion
Identification for control is a strategy of iterative performance enhancement where data are collected from the closed loop system. Several approaches exits for deriving the plant model from closed loop data and for the methods of consecutive identification and control design steps.

Iterative feedback tuning is a purely data driven approach to loop performance enhancement. In a short example it has been shown that the closed loop performance can be improved in very few iterations for a reference response time problem. Extensions are under investigation to more general model representations and to utilization of perturbation signals for ensuring suitable signal to noise ratio in tuning for disturbance rejection.

References

[1] Raymond Arnoud de Callafon. *Feedback Oriented identification for Enhanced and Robust Control - a fractional approach applied to a wafer stage*. PhD thesis, Technical University of Delft, The Netherlands, October 1998.

[2] Michel Gevers. A decade of progress in iterative process control design: from theory to practice. *Journal of process control*, **12**(4):519--531, 2002.

[3] Håkan Hjalmarsson. Iterative feedback tuning - an overview. *International journal of adaptive control and signal processing*, **16**:373--395, 2002.

[4] Håkan Hjalmarsson, Michel Gevers, Franky De Bruyne, and Juliette Leblond. Identification for control: Closing the loop gives more accurate controllers. *IEEE Proceedings of the 33rd Conference on Decision and Control*, 4150--4455, 1994.

[5] Håkan Hjalmarsson, Svante Gunnarsson, and Michel Gevers. A convergent iterative restricted complexity control design scheme. In *Proceedings of the 33rd IEEE Conference on Decision and Control*, volume 2, 1735 -- 1740, 1994.

[6] Jakob Kjøbsted Huusom, Paloma Andrade Santacoloma, Niels Kjølstad Poulsen, and Sten Bay Jørgensen. Data driven tuning of inventory controllers. In *Proceedings of the 46ed IEEE Conference on Decision and Control,* 2007.

[7] Jakob Kjøbsted Huusom, Niels Kjølstad Poulsen, and Sten Bay Jørgensen. Improving Convergence of Iterative Feedback Tuning. Submitted for Journal of Process Control*,* 2007.

[8] Lennart Ljung. System identification - Theory for the user. Prentice hall, 2 edition, 1999.

[9] Ruud J. P. Schrama. Accurate identification for control: The necessity of an iterative scheme. *IEEE Transactions on automatic control*, **37**(7):991--994, 1992.

[10] Zhuquan Zang, Robert R. Bitmead, and Michel Gevers. Iterative weighted least-squares identification and weighted LQG control design. *Automatica*, **31**(11):1577--1594, 1995.

Norazana binti Ibrahim
Phone: +45 4525 2922
Fax: +45 4588 2258
E-mail: nbi@kt.dtu.dk
WWW: http://www.chec.kt.dtu.dk
Supervisors: Prof. Kim Dam-Johansen
Assoc.Prof. Peter Arendt Jensen

PhD Study
Started: July 2007
To be completed: June 2010

Flash Pyrolysis of Agricultural Residues for Bio-oil Production and Utilisation

Abstract
The focus of this study is to optimize the flash pyrolysis process of agricultural residues such as wheat straw, rice husk, palm oil wastes, lignin residue and waste water sludge for the production of bio-oil. In a flash pyrolysis process, biomass is thermally converted to bio-oil, char and gas with high heating rate in the absence of oxygen. The flash pyrolysis process is preferred due to its ability to produce a large fraction of liquid product with low fraction of char and gas by-products. The objective of the research is to optimize the pyrolysis process and the bio-oil storage properties and to study the bio-oil combustion properties. The preliminary experiment was carried out using wheat straw as a feedstock. The results obtained will be used as a benchmark for the future works.

Introduction
Renewable energy is of growing importance in satisfying environmental concerns over fossil fuel usage. Wood and other forms of biomass including agricultural wastes and energy crops are some of the main renewable energy resources available. Biomass is unique in providing the only renewable source of fixed carbon, which is a crucial ingredient in meeting many of our fuel and consumer goods requirements.

Bio-energy could provide a large part of the projected renewable energy provisions of the future. There are many ways of utilizing biomass, including thermal and biological conversion, of which pyrolysis, and particularly flash pyrolysis, forms the focus of this study.

Pyrolysis is an oxygen deplected thermal conversion routes to recover energy from biomass whereby a liquid oil with a high energy density is provided. During pyrolysis, biomass is thermally decomposed to solid charcoal, liquid oil and gase. Lower process temperatures and longer vapour residence times favour the production of charcoal. High temperatures and longer residence times increase biomass conversion to gas, and moderate temperatures, high heating rates and short vapour residence times are optimal for producing liquids. The yields of the end products of pyrolysis are dependent on several parameters including temperature, biomass species, particle size, reactor condition, operating pressure and reactor configuration, as well as the possible extraneous addition of catalysts [1].

In flash pyrolysis, biomass decomposes to generate vapors, aerosols and some charcoal-like char. After cooling and condensation of the vapors and aerosols, a dark red liquid is formed known as pyrolysis liquid or bio-oil that has a heating value of about half that of conventional fuel oil [2]. The process produce 50-75 wt % of liquid bio-oil, 15-25 wt % of solid char and 10-20 wt % of noncondensable gases, depending on the feedstock/biomass used [3 , 4].

Specific Objectives
The main objective of this study is to optimize the flash pyrolysis process in order to produce bio-oil from different agricultural residues, waste water sludge and to investigate the storage, handling and combustion properties of bio-oils. A model to elucidate the connection between biomass structure and the bio-oil produced also will be developed.

Pyrolysis Centrifuge Reactor (PCR)
In this work, a new reactor as shown in Figure 1 developed by Bech et. al. [5] will be used. The biomass will be introduced by a screw feeder into a horizontal heated tube. Here, a three-blade rotor with close clearance to the reactor wall provides rotation of the gas phase and the biomasses particles.

The residence time in the reactor for the evolved gasses is controlled by means of a recirculation compressor. Liquids are condensed by passing the gasses through a cooler tar/water condensation after the char particles have been removed in a catch pot and a

cyclone. Aerosols are collected in a coalescer and removed by gravity. Before the gas is metered, it is cooled to ambient temperature in order to remove water. Gas for recirculation is preheated in order to avoid condensation of liquid products within the reactor.

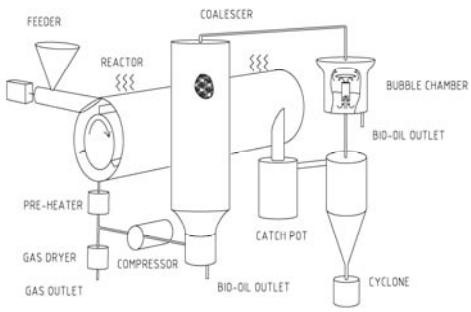

Figure 1: Schematic diagram of the developed ablative pyrolysis bench reactor system [5].

Preliminary Experiment

Some preliminary experiments have been conducted based on [5] using wheat straw as a feedstock. The operating conditions are tabulated in Table 1and Table 2 shows the results obtained from this experiment.

Table 1: Operating conditions

Operating parameters	Value
Feed weight (g)	500
Mass flow rate of straw (g/min)	24
Reactor Temperature (°C)	550
Reactor Diameter (mm)	82
Reactor Length (mm)	200
Tracing gas (°C)	400
Gas Preheat (°C)	400

Table 2: Data Analysis

Proximate Analysis of Wheat straw [5]	
Moisture (% wt)	5.8
Ash (% db)	6.8
Pyrolysis Product (daf)	**Yields**
Char (% wt)	29.3
Tar (% wt)	50.6
Gas (% wt)	17.8
Molecular weight of gas (g/mol)	37.5

db: dry basis, daf: dry ash free

Conclusion and Future Work

The preliminary experiment has shown that the yields of the pyrolysis products and molecular weight of the pyrolysis gas are agreement with the previous work [5].

In future, experimental work will include experiments with straw, rice husk and palm oil waste as a feed stock. Initially, the effect of biomass water content on the bio-oil yield and compositions will be investigated as well as the influence of particle size and final temperature.

Acknowledgement

The author acknowledges the financial support of the Ministry of Higher Education (MoHE) of Malaysia, Universiti Teknologi Malaysia (UTM) and Nordic Energy Research.

References

[1] Bridgwater, A.V. (1994). Catalysis in thermal biomass conversion. Applied Catalysis. A, General 116, 5–47.

[2] Bridgwater, A.V., and Peacocke, G.V.C. (2000). Fast pyrolysis process for biomass. Renewable & Sustainable Energy Reviews, 4, 1–73.

[3] Mohan, D., Charles, U., Pittman, J., and Philip, H.S. (2006). Pyrolysis of wood/biomass for bio-oil: Critical Review. Energy & Fuels, 20, 848–889.

[4] IEA - International Energy Agency (2006), www.ieabioenergy.com.

[5] Bech N, Jensen PA, Dam-Johansen K. Ablative Flash Pyrolysis of Straw and Wood: Bench-Scale Results. Proc 15th European Biomass Conference and Exhibition, Berlin, 7-11 May, 2007 (in press).

Irakli Javakhishvili
Phone: +45 4525 6818
Fax: +45 4588 2161
E-mail: irj@kt.dtu.dk
WWW: www.polymers.dk
Supervisors: Prof. Søren Hvilsted

PhD Study
Started: September 2007
To be completed: August 2010

Gold Nanoparticles for Bladder Cancer Treatment

Abstract
Bladder cancer is one of the most widespread diseases. Short residence time of the drug in the bladder renders anticancer treatment ineffectual. The project aims to design and characterize gold nanoparticles that exhibit mucoadhesive properties, and hence have potential to be exploited as drug delivery devices in bladder cancer therapy.

Introduction
Bladder cancer is amongst the most abundant malevolent diseases in the western world. It is the second most common urologic malignancy with approximately 336,000 new cases reported every year, the majority of which occur in the industrially developed countries – mainly in Europe and the United States. While occurrence of bladder cancer across Europe is marked with steady rate, Denmark has the highest incidence amongst women and Italy the highest amongst men.

Superficial tumors luxuriating on the inner lining of the bladder are characteristic for about 70-80 % of the new cases. Resection, combined with intravesical therapy, is one of the forms of treatment administered currently. Numerous drugs such as Paclitaxel, Doxorubicin and Mitomycin have been employed. The major drawback of such a treatment is rapid and almost complete expulsion of the drug from the bladder on the first void of urine, which dramatically reduces the exposure of the therapeutic agent to the tumor sites in the mucosal tissues of the bladder lining. Moreover, poor water-solubility of anticancer drugs raises difficulties in their delivery [1,2], results in low bioavailability, and may lead to undesirable side effects due to high local concentrations upon aggregation [2].

To alleviate problems such as premature drug decomposition, adverse effects of cytotoxic drugs, and to improve drug bioavailability at desired sites by prolonging the residence time and making use of specific interactions, various drug delivery systems such as synthetic polymers, micelles, microcapsules, etc. have been constructed and are under development [1,3]. A polymer-based drug delivery system, which is marked with mucoadhesive properties, has capacity to carry sufficient chemotherapeutic payload, and exhibits controlled release of the drug over an extended period, could be a significant improvement in bladder cancer therapy.

Scope of the Project
The purpose of the project is construction and characterization of gold nanoparticles of micellar architecture which display mucoadhesion, and hence have potential of being employed as a drug delivery system in bladder cancer treatment. Such a system may also find application in other cases where combination of mucoadhesion and controlled drug release is desirable.

Block copolymers have been vastly employed as building blocks of drug carries such as polymer-drug conjugates, micro- or nanoparticles. Amphiphilic block copolymers are of significant interest due to their unique structural characteristics that may be altered to provide drug carriers with predetermined properties. Many low molecular weight lipophilic drugs have been successfully incorporated in the hydrophobic core of micelles prepared from amphiphilic block copolymers [4].

Entrenched in the micelle, the drug is protected from possible inactivation in biological environment, and is debarred from being accumulated in non-target organs and tissues [2].

Mucoadhesion facilitates local delivery of therapeutic agents, and thus bolsters their efficiency. Also, mucoadhesive controlled-release device maintains constant effective drug concentration in the body by inhibiting dilution of drugs in body fluids, and allowing

targeting and localization of drugs at specific sites [5,6,7,8].

Combination of two factors, such as direct drug adsorption and decrease of excretion rate, boosts efficiency of small dosages and less frequent administration due to increased bioavailability of the drug [6].

For further development of drug delivery systems it is necessary to gain insight about the interactions amongst cells and carriers. Since gold nanoparticles provide enough contrast for imaging with electron microscopy they have been subject of increased attention. Gold nanoparticles incorporated in biodegradable and biocompatible core-shell structures have potential in drug delivery as well as for labeling micelles for localization studies [4].

Taking into consideration all the abovementioned points, the drug carrier will be designed as follows. Food and drug administration (FDA) approved biocompatible and biodegradable poly(ε-caprolactone) (PCL) [9] is chosen for building the core, while biocompatible and mucoadhesive poly(acrylic acid) (PAA) [5] constitutes the shell of the micelle. PCL exhibits high permeability to small drug molecules, does not alter natural pH of the environment after degradation, and may be employed for long-term delivery due to low erosion rate [9].

The diblock copolymer is fastened on gold nanoparticles to achieve enhanced stability against sink conditions and severe dilution upon administration. The nanoparticle thus obtained provides splendid habitat for drug molecules, and features mucoadhesive properties. It may be considered as an excellent candidate for drug delivery in bladder cancer treatment. On the other hand, such a system may provide means of monitoring interaction between the carrier and biological tissues, drug release behavior, etc. by using electron microscopy.

Controlled polymerization techniques (CPT) such as anionic ring-opening polymerization and atom transfer radical polymerization (ATRP), are employed to attain desired macromolecular architecture (Figure 1).

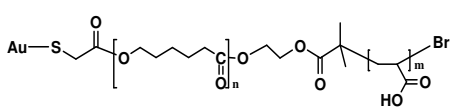

Figure 1: Amphiphilic block copolymer.

CPT allows synthesis of polymers with well-defined structure, chain length and functionality. This eventually leads to predetermined loading capacity, steady drug release profile, and robustness - no lysis due to structural defects. Well-defined system with very narrow polydispersity is essential for the approval of new therapeutic agents [10].

Characterization techniques such as Nuclear Magnetic Resonance Spectroscopy (NMR), Fourier Transform Infrared Spectroscopy (FT IR), and Size Exclusion Chromatography (SEC) are employed to obtain information about the structure and composition of the building blocks. Transmission Electron Microscopy (TEM) and light scattering experiments will be conducted to determine shape and size distribution of the nanoparticles.

Further investigation is necessary to gain insight about compatibility, drug release kinetics, residence time, extent of accumulation in tumor cells, as well as decay and eviction of residues by the living organism.

Acknowledgments

The project is funded by technical University of Denmark.

References

1. M. L. Adams, A. Lavasanifar, G. S. Kwon, J. Pharmaceutical Sciences 92 (2003) 1343-1355.
2. V. P. Torchilin, Pharmaceutical Research 24 (2007) 1-16.
3. C. Allen, D. Maysinger, A. Eisenberg, Colloids and Surfaces: Biointerfaces 16 (1999) 3-27.
4. T. Azzam, A. Eisenberg, Langmuir 23 (2007) 2126-2132.
5. N. A. Peppas, Y. Huang, Adv. Drug Deliv. Rev. 56 (2004) 1675-1687.
6. Y. Huang, W. Leobandung, A. Foss, N. A. Peppas, J. Controlled Release 65 (2000) 63-71.
7. F. Cui, F. Qian, C. Yin, Int. J. Pharmaceutics 316 (2006) 154-161.
8. B. S. Lele, A. S. Hoffman, J. Controlled Release 69 (2000) 237-248.
9. P. P. Ghoroghchian, G. Li, D. H. Levine, K. P. Davis, F. S. Bates, D. A. Hammer, M. J. Therien, Macromolecules 39 (2006) 1673-1675
10. H. R. Ihre, O. P. Padellia De Jesús, F. C. Szoka, Jr., J. M. J. Fréchet, Bioconjugate Chem. 13 (2002) 443-452.

Jacob Skibsted Jensen
Phone: +45 4525 2943
Fax: +45 4525 2258
E-mail: jsk@kt.dtu.dk
WWW: www.kt.dtu.dk
Supervisors: Anne S. Meyer, BioProcess Engineering
Max Egebo, FOSS A/S

Industrial PhD Study
Started: February 2005
To be completed: January 2008

Prediction of Wine Quality from Phenolic Profiles of Grapes

Abstract
Assessment of the phenolic content of red grapes is an important prerequisite for understanding how grape phenolics impact wine quality. In the search for a rapid and robust extraction method for grapes we have investigated the influence of selected factors on extraction efficiency of phenolics from eight different red wine grape cultivars. By applying optimized extraction conditions we found that it was possible to extract an average of 81.8 % total phenolics and 91.5 % of the anthocyanins from the grapes with only five minutes of solvent contact time. Using the developed protocol it was possible to establish a relation between grape anthocyanins and total wine color, thereby allowing the prediction of a wine quality parameter (color) from measurement grape phenolics. The future work will focus on applying infrared spectroscopy for rapid measurement of the phenolics.

Introduction
Phenolics in red wine are closely related to wine characteristics, especially wine color and astringency. The color and astringency of a red wine play an important role of wine quality and depends on the concentration and profiles of the phenolics in the wine [1]. The phenolics in wine originate mainly from the grapes, but also to a smaller degree the oak used in the wine production.

The two most abundant groups of phenolics found in grapes are anthocyanins and flavanols (**Figure 1**). Anthocyanins are almost exclusively found in the outer layers of the grape skin and are under acidic conditions highly colored compounds, which are responsible for most of the color in young red wines [2]. Flavanols are mainly found in the skins and seeds of the grapes and are important for both the astringency and the color stability of wines [2, 3].

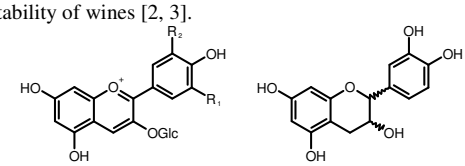

Figure 1: Most abundant phenolics in red wine.

Due to various physico-chemical phenomena and chemical reactions that occur during wine production [4], and the significant influence of various factors on these reactions, the relationship between the grape's phenolic profiles and the phenolic profiles and quality of wines is not straight forward. Nevertheless, a main hypothesis in our ongoing work on grape and wine phenols is that the phenolics present in the grapes have a significant influence on the quality of the finished wine and that it may be possible to predict the wine quality from analysis of the phenolics in the grapes

The overall aim of the PhD study is to unravel the relation between grape and wine phenolics to be able to predict red wine quality from the phenolic profiles of grapes.

Specific Objectives
A first requirement for quantification of grape polyphenols is to find an optimal procedure for extracting the polyphenols from grapes. The first objective is to investigate how different extraction conditions affect the extraction efficiency and robustness on different grape cultivars. This has been investigated using statistically designed experiments and used to find the optimal extraction conditions for future experiments.

A second objective is to determine the relation between grape and wine phenolics. For this purpose grape extractions on different grape cultivars have been compared with parallel wine extractions under controlled experimental fermentation conditions.

The last objective is to investigate rapid measurement of grape and wine phenolics with infrared spectroscopy.

Results and Discussion

The first requirement of a robust and efficient protocol for the extraction of grape phenolics has been investigated for selected parameters in solvent extractions on grape homogenates. The experiment was conducted as a full factorial design and the responses were fitted to a linear model accounting for main and interaction effects [5]. The response levels y_i for all i observations were estimated in a linear model of the factor levels (x_1, x_2 and x_3) accounting for main and interaction effects (**equation 1**).

$$y_i = \beta_0 + \beta_1 x_1 + \beta_2 x_2 + \beta_3 x_3 + \beta_{12} x_1 x_2 + \beta_{13} x_1 x_3 + \beta_{23} x_2 x_3 + \varepsilon_i \quad \textbf{(1)}$$

It was found, that extraction temperature (20 to 60 ºC), aqueous solvent levels of ethanol (0 to 50 % v/v) and hydrochloric acid (0 to 0.1 M) had a high significant impact on the extraction efficiency of total grape phenolics (**Table 1**).

Table 1: Impact of selected extraction parameters on the mean extraction degree of total phenolics.

Term	Total phenolics (model fit: $R^2 = 0.99$)		
	Prob > F	β estimate	Std Error
Intercept	<.0001	66.49	0.36
EtOH	<.0001	18.75	0.48
HCl	<.0001	6.69	0.39
Temp	<.0001	6.63	0.48
EtOH*HCl	0.446	-0.37	0.48
EtOH*Temp	0.425	0.48	0.58
HCl*Temp	0.367	0.45	0.48

These findings were used to design an optimal extraction protocol. Using 50 % v/v acidified aqueous ethanol (0.1 M HCl) and a 1:1 ratio of solvent to grape, we found that it was possible to extract an average of 81.8 % total phenols and 91.5 % anthocyanins from the grapes with only five minutes of solvent contact time at 40 ºC, followed by sample neutralization and work up. The protocol allows high extraction of grape phenolics with an acceptable standard deviation across different cultivars (**Table 2**).

Table 2: Fast extraction of grape phenolics.

	Mean extraction degree	Relative standard deviation
Anthocyanins	91.5 %	3.8 %
Total phenolics	81.8 %	6.0 %

The relation between grape phenols and wine color was investigated applying the optimized extraction conditions. The phenolic composition of 55 grape extracts were compared with the wine color of pH normalized experimental wines made from the same grapes. The results revealed that the anthocyanin levels in the grapes were highly correlated with the total wine color of the experimental wines (**Figure 2**).

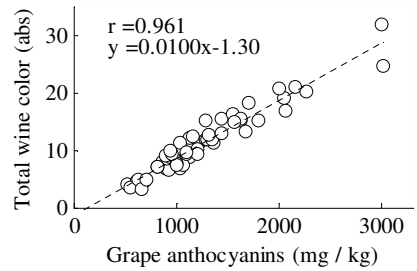

Figure 2: Direct relation between grape anthocyanins and total wine color.

The relation between grape anthocyanins and wine color thus provides the basis for being able to predict a wine quality parameter (color) from the composition of grapes.

Conclusions and future work

In the search for a tool to predict wine quality from grape phenolics a fast solvent extraction protocol for grape homogenates has been developed. The utility of the developed extraction protocol for prediction of wine color shows good promise. The future work will be focused on measuring grape and wine phenolics with infrared spectroscopy.

Acknowledgements

The Danish ministry of Science and Technology are acknowledged for their financial support for the project.

References

1. S. Preys, G. Mazerolles, P. Courcoux, A. Samson, U. Fischer, A. Hanafi, D. Bertrand and V. Cheynier. Anal. Chim. Acta 563 (2006) 126-136.
2. J.A. Kennedy, M.A. Matthews and A.L. Waterhouse. Phytochemistry 55 (2000) 77-85.
3. D.O. Adams. Am. J. Enol. Vitic. 57 (2006) 249-256.
4. K.L. Sacchi, L.F. Bisson and D.O. Adams. Am. J. Enol. Vitic. 56 (2005) 197-206.
5. D.C. Montgomery. Design and Analysis of Experiments. John Wileys & Sons, New York, NY. 2001.

List of publications

1. J.S. Jensen., B. Blachez, M. Egebo, A.S. Meyer, Am. J. Enol. Vitic. 58 (2007) 451-461.
2. R. Gani, K.D. Johansen, ECCE-6 Book of abstracts, Department of Chemical Engineering, Kgs. Lyngby, Denmark, 2007, Volume 2, p. 937.
3. R. Gani, K.D. Johansen, ECCE-6 Book of Abstracts , Department of Chemical Engineering, Kgs. Lyngby, Denmark, 2007, p. 1123.
4. J.S. Jensen., B. Blachez, M. Egebo, A.S. Meyer, Am. J. Enol. Vitic. 58 (2007) 413.

Lars Jensen
Phone: +45 4525 2858
Fax: +45 4588 2258
E-mail: lje@kt.dtu.dk
WWW: http://www.ivc-sep.kt.dtu.dk
Supervisors: Nicolas von Solms
Kaj Thomsen

PhD Study
Started: March 2007
To be completed: March 2010

Gas Hydrate Kinetics in Realistic Reservoir Systems – Formation and Inhibition

Abstract
The goal of this PhD project is to study the formation kinetics of natural gas hydrates. Preliminary experimental studies on the nucleation of propane hydrate have been performed. The results showed that the driving force in terms of the supersaturation highly influences the hydrate induction time while the stirring rate influence the induction time less. Addition of polyvinylpyrrolidone to the aqueous phase was found to prolong the induction times quite substantially.
The induction time data were correlated using a newly developed induction time model based on crystallization theory. In most cases reasonable agreement between the data and the model could be obtained. The results revealed that especially the effective surface energy between propane hydrate and water is likely to change when the experimental conditions are changed. Changing the stirring rate resulted in slight changes in the surface energy while the addition of polyvinylpyrrolidone caused the effective surface energy to more than double.

Introduction
Gas hydrates are crystalline compounds formed as a result of combination of water and suitably sized guest molecules at elevated pressure and low temperature. Light hydrocarbons; methane-pentane, carbon dioxide and hydrogen sulphide are the guest molecules of interest to the oil and natural gas industry [1]. Depending on the pressure and gas composition, gas hydrates may build up where water coexists with natural gas at temperatures as high as 300 K. Especially long gas transmission lines at cold weather conditions and process equipment are vulnerable to being blocked by hydrate formation causing potential hazards or economical loss.
Inhibition of gas hydrates is a necessity in the oil and gas industry in order to assure a continuous flow of reservoir fluids from the production well to the platform. Traditionally methanol or glycol has been used to inhibit the formation of gas hydrates by shifting the hydrate equilibrium to lower temperatures and higher pressures. Due to the relative large amounts (10-50 wt%) of methanol or glycol needed in the process of hydrate prevention [2] other chemicals capable of inhibiting hydrate formation at much lower doses (<1 wt%) have gained interest [3]. These impact the kinetics of hydrate formation, in contrast to the thermodynamic inhibitors, thus the chemicals are known as kinetic inhibitors.
Kinetic information of hydrate formation is very important if kinetic inhibition is applied as a mean of preventing hydrate formation in transmission lines, valves etc.
The goal of this project is to study the formation kinetics of gas hydrates in realistic reservoir fluid systems. The impact on the formation kinetics when adding small amounts of kinetic inhibitors will be investigated. This will be done using already available equipment for hydrate investigation and spectroscopic techniques like Raman. It is also the hope that new equipment for investigating hydrate phenomena can be designed.
The work that has been done until now concern investigating the effect that the driving force in terms of supersaturation, has on nucleation of structure II (sII) propane gas hydrate. The nucleation time (the time until a critical sized crystal appear) has been measured at different degrees of supersaturation. The influence of stirring rate and the addition of a kinetic inhibitor (polyvinylpyrroldidone, PVP) on the nucleation is likewise investigated. The experimental data has been correlated to a newly developed model for gas hydrate nucleation.

Driving force for Hydrate Nucleation

The expression for the driving force for nucleation of simple hydrates has been described on the basis of the following phase reaction occurring in the aqueous solution.

$$G + n_w H_2O \Leftrightarrow G \cdot n_w H_2O \qquad (1)$$

Where n_w is the number of water molecules in a hydrate building unit. The resulting expression for the driving force in terms of supersaturation is given below.

$$\Delta \quad = kT \ln\left(\frac{f(P,T)}{f(P_e,T)}\right) + \Delta v_e (P - P_e) \qquad (2)$$

Where k is Boltzmann's constant, f is the fugacity of the gas in the gas phase and Δv_ε is the volume difference between a water molecule in solution and a hydrate building unit in the hydrate lattice.

Linearized Nucleation Time Model

Based on crystallization theory the following expression describing the relation between nucleation time and the supersaturation ratio, S, is proposed:

$$\ln\left[S^{1/4}(S-1)^{3/4} t_i\right] = \ln K + \frac{B}{4\ln^2 S} \qquad (3)$$

Where K is a kinetic parameter and the supersaturation ratio S, and the B parameter is given as:

$$S = \left[\frac{f(P,T)}{f(P_e,T)}\right] \cdot \exp\left[\frac{\Delta v_e (P - P_e)}{kT}\right] \qquad (4)$$

$$B = \frac{4c^3 v_h^2 \sigma_{ef}^3}{27(kT)^3} \qquad (5)$$

where c is a shape factor, v_h is the volume of a hydrate building unit σ_e and is the effective surface energy between hydrate and solution.

Experimental Equipment

The kinetic measurements were performed in a stainless steel hydrate equilibrium cell with a fixed volume of 66.5 cm^3 and a maximum working pressure of 150 bar. The cell allows for visual observation of hydrate formation through two sapphire windows. The cell is attached with a gas reservoir and a vacuum pump. The temperature in the cell was controlled by circulating coolant (water-ethanol solution), in a jacket surrounding the cell. The temperature was monitored by using a platinum resistance probe (±0.01 K) placed inside the cell. The pressure of the cell was monitored by a single pressure transducer (BD Sensors, 0-40 bar). The cell was placed on a stir plate which allowed a stirring bar (L = 4 cm) to rotate within the cell. The pressure and temperature in the cell was recorded continuously on a computer. A schematic layout of the experimental equipment used to investigate gas hydrate nucleation is showed in figure 1.

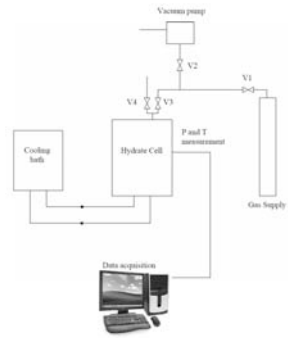

Figure 1: Layout of experimental equipment used in the study of gas hydrate nucleation. The hydrate cell is attached to a gas supply unit and a vacuum pump. The temperature is controlled by a cooling bath. Data is collected continuously on a computer.

Experimental Procedure

The cell was cleaned with distilled water and loaded with distilled water or distilled water containing PVP. A stirring bar was placed in the cell. The cell lid was screwed on and the cell evacuated using a vacuum pump for approximately 1 hour. The temperature bath was adjusted so the temperature in the cell was 273.75 K. When the temperature in the cell was constant the propane gas was injected through the inlet until the desired pressure at the chosen temperature was obtained. Three experimental series using distilled water were performed. For each series the stirring rate was altered in the range 200-500 rpm in order to investigate the effect of the stirring rate on the nucleation kinetics.

For nucleation experiments involving PVP as a kinetic inhibitor two experimental series at PVP concentrations of 0.05 wt% and 0.025 wt% were performed both at a stirring rate of 500 rpm. In all the experiments the pressure and temperature was recorded in a time interval of 5 s. The data obtained in an experimental run can typically be represented from the pressure-time relationship provided in figure 2.

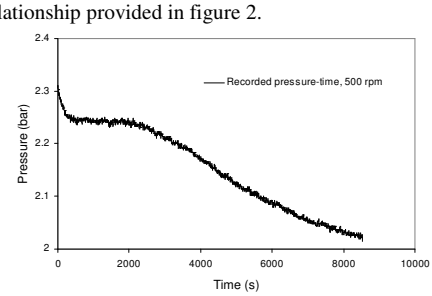

Figure 2: Typical pressure-time recording for the propane hydrate forming system. The initial pressure drop is due to gas dissolution followed by an isobaric period where nucleation takes place. The sudden pressure drop during the nucleation period is caused by hydrate formation.

Results and Discussion

The measured induction times have been plotted as a function of the supersaturation for different stirring rates in figure 3 and for different concentrations of PVP in figure 4. The induction periods can be seen to be more or less independent of the stirring rate when this is varied in the range of 300-500 rpm. At lower stirring rates a less regular tendency is observed i.e. there is quite more scattering among the data points. This indicates that in case of low convection, the system will act more randomly which could be due to lower V-L_w interfacial area or a less favorable distribution of gas in the bulk liquid phase.

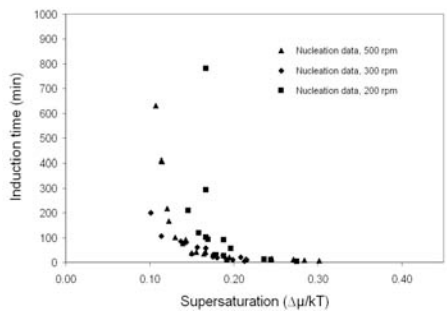

Figure 3: Nucleation period vs. driving force at 273.75 K for propane hydrate. The induction times measured at stirring rates of 500 and 300 rpm are very similar. At 200 rpm more scattering among the measured induction times is observed. At this stirring rate the induction times are also seen to be prolonged a little.

When PVP is added in even very small amounts the induction time/supersaturation relationship is shifted to the right as can be observed in figure 4. There seems to be quite steady agreement among the two data sets, i.e. the higher PVP concentration data are shifted to the right with the same Δμ value compared to the data for the lower PVP concentration.

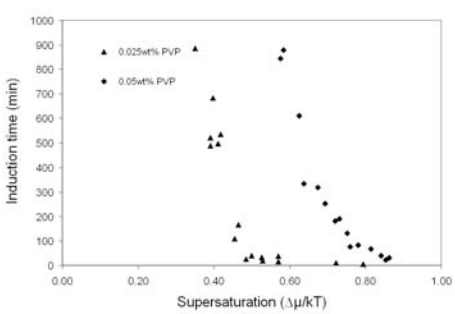

Figure 4: Plot of nucleation period vs. driving force at 273.75 K for propane hydrate for two different concentrations of PVP and a stirring rate of 500 rpm. PVP is seen to cause longer induction times compared to nucleation of propane hydrate from a pure aqueous phase.

Using (3) the dependence of the induction time on the supersaturation ratio for propane hydrate has been investigated. The results using the experimentally obtained induction periods at different supersaturation ratios at a stirring rate of 500 and 200 rpm and the best linear fit is presented in figure 5. As expected the linear fit for the higher stirring rate is better. The model parameters for the linear fit at all three stirring rates are presented in table 1. It can be seen that the surface energy between hydrate and solution increases slightly when the stirring rate is decreased. The kinetic constant, K, does not seem to follow any pattern.

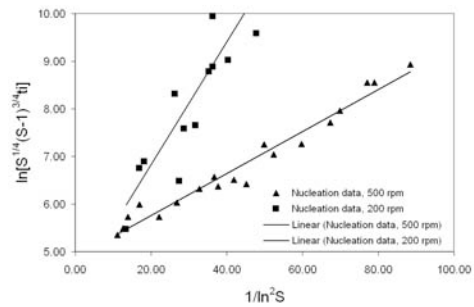

Figure 5: Linearized dependence of the induction time on the supersaturation ratio for nucleation of propane hydrate in aqueous solution at T = 273.75, 500 rpm and 200 rpm . Changing the agitation speed causes small changes in nucleation periods.

Table 1: Fitted parameters of the nucleation model. The resulting effective surface energy is not heavily influence by a change in the stirring rate which explains why similar nucleation periods at different stirring rates are observed.

RPM	K (s)	B	σ_{ef} mJ/m^2
500	130.92	0.176	1.11
300	67.60	0.258	1.26
200	69.85	0.516	1.58

The result of using the linearized induction time model for the data obtained in the nucleation experiments with PVP are shown in figure 6. As seen there is a reasonable good linear relationship for the two data sets. The calculated effective surface energies and the kinetic constants are given in table 2.

The addition of PVP to the aqueous phase is seen to cause more change in the model parameters compared to the parameters of the uninhibited nucleating system. Again the K value, as in the case when changing the stirring rates, has no defined pattern when going from 0-0.050 wt% PVP. B increases as the PVP concentration is increased thus the effective surface energy increases as well.

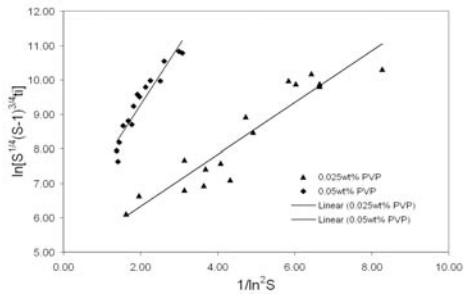

Figure 6: Linearized dependence of the induction time on the supersaturation ratio for nucleation of propane hydrate in dilute polymer solutions at 273.75 K and 500 rpm. Small changes in polymer concentration changes nucleation conditions significantly.

Table 2: Fitted parameters of the nucleation model. The resulting effective surface energy is significant influence by the concentration of the polymer.

RPM	[PVP] (wt%)	K (s)	B	σ_{ef} mJ/m^2
500	0	130.92	0.176	1.11
500	0.025	125.15	3.01	2.85
500	0.050	339.75	6.91	3.76

Conclusions

Nucleation time data have been obtained for propane hydrate at 273.75 K as a function of the driving force in terms of supersaturation. The effect of changing stirring rate and adding a kinetic inhibitor (PVP) were investigated. The main conclusions are:

The consistency in the measured nucleation data was relatively good, especially at high convection due to better distribution of the gas in solution.

At low stirring rates nucleation of propane hydrate becomes more stochastic i.e. more scattering in measured nucleation periods is observed.

Reasonable agreement between the nucleation model and the measured data can be obtained. Especially at high stirring rates.

Polymers like PVP effectively prolong the nucleation periods of propane hydrate.

The mechanism by which PVP inhibits the nucleation of propane hydrate is by increasing the effective surface energy between the hydrate surface en the surrounding solution.

Acknowledegements

The authors would like to thank the Danish Research Council for Technology and Production Sciences for financial support through the project "Gas Hydrates – from Threat to Opportunity" and the Technical University of Denmark for financial support through a Ph.D. scholarship.

References

1. Sloan, E.D. (1998). Clathrate Hydrates of Natural Gases, Marcel Dekker, New York.

2. Kelland, M., (1995). Studies on New Gas Hydrate Inhibitors, SPE 30420, 531-539.

3. Sloan, E.D., Lederhos, J.P., Long, J.P., Sum, A., Christiansen, R.L. (1996). Effective Kinetic Inhibitors for Natural Gas Hydrates, Chem. Eng. Sci., 51, 1221-1229.

Mette Krog Jensen
Phone: +45 4525 6809
Fax: +45 4588 2161
E-mail: mkj@kt.dtu.dk
WWW: http://www.dtu.dk/Centre/DPC.aspx
Supervisors: Ole Hassager
Anne L. Skov
Anders Bach, Coloplast A/S

PhD Study
Started: November 2006
To be completed: November 2009

Polymer Network as Pressure Sensitive Adhesives – Viscoelastic Guidelines

Abstract
The present work focuses on the use of polymer networks as pressure sensitive adhesives (PSA). The purpose is to achieve an adhesive which adhere well on a given substrate, while easy to remove without leaving traces. A polymer/cross-linker system with changing degree of cross-linking is used, and small amplitude oscillatory shear (SAOS) experiments are used to address the fundamental viscoelastic parameters that govern the PSA performance. The adhesive performance is tested with 90^o peel tests, and an empirical relation between the measured peel forces and the viscoelastic data is suggested.

Introduction
Pressure sensitive Adhesives (PSAs) are probably the most common class of adhesives in consumer products, e.g. self-adhesive tapes and labels of all kinds are ubiquitous products in everyday life. However, the understanding of the rheological properties of the material upon application is limited [1]. It is especially the rheological properties upon removal/debonding of the adhesive that remain as a challenge, and although several studies have focused on such relations there is still a lack of knowledge on the field of interfacial failure mode upon debonding [2].

Most modern PSAs are made of cross-linked polymers to avoid flow. The unique property is simply that there is a difference in the energy gained in forming the interfacial interactions and the energy dissipated during debonding, and it is this property that will be investigated in this paper.

Sample Preparations
A Vinyl-terminated linear polymer is cross-linked with a silyl-terminated f-functional cross-linker with $f > 2$. Three samples are prepared with different degree of cross-linking, r, defined as the ratio of silane to vinyl groups, $r = silane/vinyl$. The samples should be soft viscoelastic solids, why r should be close to, but larger than the critical degree of cross-linking [3, 4, 5] given by eqn. (1.1)

$$r > r_c = \frac{1}{f-1} \qquad (1.1)$$

The functionality, f, is taken as the average functionality of all chains, which is around 3.5, hence r_c ; 0.4. The degrees of cross-linking for the three prepared samples are listed in Table 1.

Table 1: The ratio of silane to vinyl groups.

Spox.01.	01	02	03
r	0.46	0.50	0.53

All the samples are prepared in a static mixer to avoid air-bubbles. They are hereafter pressed in desired thicknesses in a 100^oC hot-press between

1. two sheets of release liner for dynamic mechanical analysis (DMA)
2. one sheet of release liner and one backing folio for peel tests

All samples are then cured at 100^oC for one hour to make sure that they are fully reacted before further analysis.

Experimental Work
Small amplitude oscillatory shear (SAOS) experiments are performed on an AR2000 rotational rheometer with plate-plate geometry, to measure the linear viscoelastic data. The rheological master curves for the three

samples are reported in Figure 1, where it is seen that the loss modulus (crosses) follows a power law behavior while the storage modulus (circles) reaches a plateau at low frequencies. The solid lines represents a fit of the gel equation (eqn. (1.2)) with respect to the three material constants, n, S and G_0, representing the slope of the loss modulus, the stiffness of the network and the plateau modulus at low frequencies respectively [6,7].

$$G(t) = St^{-n} + G_0 \tag{1.2}$$

The fitted data from the gel eqn. are listed in Table 2, where it is seen that as r increases the elastic part of the sample increases (S, G_0), while the slope of the loss modulus decreases.

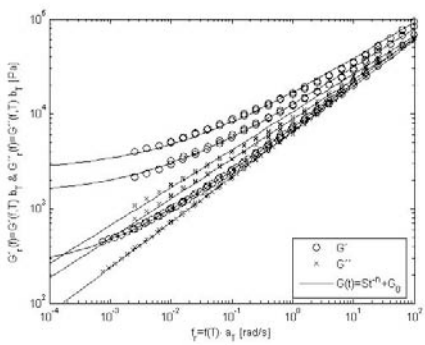

Figure 1: Dynamic moduli for the three samples. Circles represent the storage modulus while crosses represent the loss modulus

Table 2: Obtained data from the gel eqn. fit to the dynamic data given in Figure 1

Spox.01.	**01**	**02**	**03**
n	0.48	0.42	0.39
$S\left[Pa\,s^n\right]$	5630	9360	11700
$G_0\left[Pa\right]$	247	1390	2650

The adhesive performance is investigated using peeling experiments. The adhesive is applied with pressure (2 kg) on a steel plate and left at rest for 30 min. The backing folio is supported by an extra backing tape to avoid stretching of the backside of the sample. The peeling system consists of two micrometric tables X and Z both moving with velocity V. The adhesive strip is attached on a force transducer located in the vertical micrometric table moving in the Z-direction with velocity V. The substrate is located in the XY-plane and moves in the X-direction with velocity V. A 2D sketch of the XZ-plane is shown in Figure 2 where the peel strip is being peeled off the substrate in the vertical Z-direction to obtain a 90^o peel. During the experiment the peel force is measured at different thicknesses, d, and velocities, V.

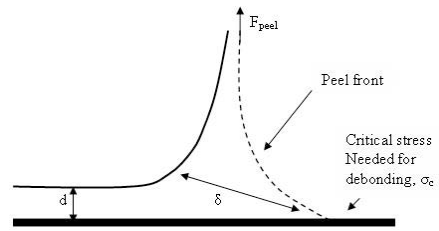

Figure 2: sketch of a 90^o peel test setup in the XZ-plane

The outcome of one peel test is seen in Figure 3. As seen in the figure the peel force is measured by triple determination and at three velocities during each run. Each peel experiments starts with $V = 0.1mm/s$ then 1 and finally $5mm/s$. In Figure 3 it is seen that there is a start-up region each time the velocity is changed, which is because the force starts to build up until it reaches a value where the adhesive detaches from the surface. Hereafter follows the operation region, where the peel force varies moderately. The measured peel force, $F_{peel}(V)$, is taken to be the average of the regions marked with the vertical borders.

During the peel experiments it was observed that the peel force increases with both increasing velocity and sample thickness. This dependency does however not give a clear picture of the rheological behavior of the samples during peeling, and there is furthermore no relation that combines spox.01.01, 02 and 03. In the following section it is discussed whether such a relation can be found.

Theoretical Considerations and Data Analysis

Upon peeling there is a loss of energy due to the viscous nature of each sample. Hence, the peel force must be proportional to the dissipated energy at the peel frequency, which is related to the loss modulus. The peel force does furthermore depend on the dimensions of the peel strip as proposed in eqn. (1.3).

$$\frac{F_{peel}}{dW} \propto G''(\omega_{peel}) \tag{1.3}$$

Eqn. (1.3) does not include any dependency on r. This parameter does have a clear effect on the peel force since it changes the balance between elastic and viscous parts in each sample. It is however, not obvious how to include this in the peel force.

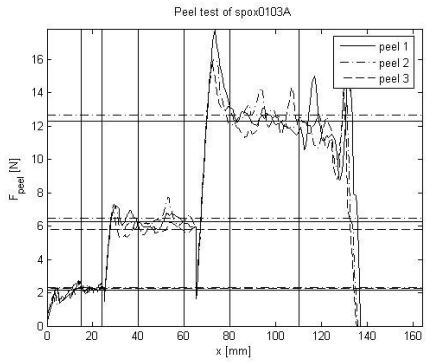

Figure 3: Outcome of one peel test. The peel force is measured by comparing peel data obtained from three identical runs.

Eqn. (1.3) only includes viscous effect to the peel force, but the elastic network must have an influence too. One way to include the elastic contribution is by exchanging the loss modulus in eqn. (1.3) with the loss tangent. This introduces the elastic effects upon deformation. However, r, also changes the ability to adapt to a given substrate. The plateau modulus could be a measure for this property, since it is taken to be the storage modulus measured at the bonding frequency. The plateau modulus is thus used to normalize the peel force as follows:

$$\frac{F_{peel}}{dWG_0} \propto f\left(\tan\delta_{\omega_{peel}}\right) \qquad (1.4)$$

The peel frequency is defined as $\omega_{peel} = V_{peel}/(2\pi d)$, and $\tan\delta_{\omega_{peel}}$ is obtained from the DMA data as shown in Figure 4, which shows the measured loss tangent for spox.01.03. The large crosses marks the peel frequency when $d = 1mm$. It is obvious that as d decreases the peel frequency increases and thus, the loss tangent. Each thickness, 1, 0.3 and 0.1 mm, will in the following be denoted A, B and C respectively.

In Figure 5 the normalized peel force is plotted vs. the loss tangent at the peel frequency. Looking at the data for spox.01.02 and 03 they fall into one curve. This curve seems to have a power-law relation in this intermediate regime for $\tan\delta_{\omega_{peel}}$. It is not clear whether this trend will hold when $\tan\delta_{\omega_{peel}} \to 0$, for which the sample is almost 100% elastic. It could be expected that the peel force at some lower critical point for the loss tangent will drop very rapidly to zero. In contrast, $\tan\delta_{\omega_{peel}} \to \infty$ represents a liquid rather than a viscoelastic material and thus result in some upper limit for which the peel experiment will result in a different failure mode. In peel experiments it is common to distinguish between two types of failure modes:

1. Adhesive failure mode – interfacial detachment
2. Cohesive failure mode – the sample will break in the bulk and leave residue on the substrate

PSAs are more likely to perform adhesive failure the stronger the network is. The network strength, is however not the only factor determining the failure mode. It has been shown that the peel velocity also influences the type of failure [6]. Hence, it is difficult to ascribe a specific point of transition to the failure mode.

In Figure 5 a shift in material properties are observed from the spox.01.02 and 03 samples to the spox.01.01 sample. This change in material properties indicates a transition in failure mode. Spox.01.01 has the lowest stoichiometric ratio of the three samples, and thus the weakest network. The dynamic moduli for spox.01.01 (see Figure 1) are parallel over several decades of frequencies, indicating that it is very close to the gel point [7, 8]. Hence, it is not surprising if this sample would result in a cohesive failure, which is actually the case observed.

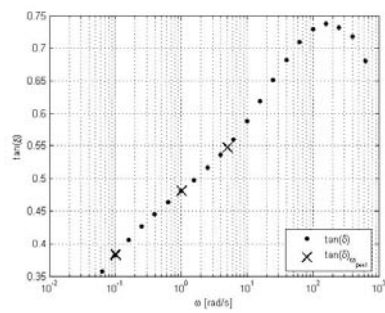

Figure 4: The loss tangent for spox.01.03. The crosses are the values obtained at the peel frequency when $d = 1mm$ and $V = [0.1, 1, 5]mm/s$.

Conclusion

It is shown experimentally that the peel force in 90° peel tests correlates very well with the loss tangent at the peel frequency and the plateau modulus. This behavior is however not intuitively clear.

It is possible to give an empirical relation between the peel force and the loss modulus, but this relation does not include any dependency on the strength of the network. This property is however found to have a large influence on the peel performance; 1) it changes the mechanisms of deformation at the peel frequency (high frequencies), and 2) it changes the ability to adapt to the substrate at the bonding frequency (low frequencies).

In eqn. (1.4) a relation between the peel force and the loss tangent is given, and it is found experimentally to be very good (see Figure 5). A brief explanation to that could be:

1. The loss tangent at the peel frequency is a good measure for the balance between the viscous and elastic parts of the sample upon deformation.
2. The plateau modulus is the storage modulus measured at the bonding frequency, and thus relevant when looking at the property of adapting to a given substrate.

It was also found experimentally that it is necessary to distinguish between types of failure mode. In this case cohesive vs. adhesive. The data points seem to separate into two curves, one for each failure mode. This is a good result, since the two failure modes are expected to be caused by a different set of mechanisms.

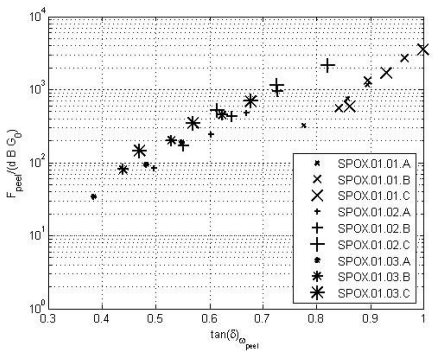

Figure 5: Normalized peel force vs. the loss tangent obtained at the peel frequency. A, B and C represents $d = [1, 0.3, 0.1]\ mm$ respectively

Acknowledgements
This study is supported by Coloplast A/S, the Graduate School of Polymer Science and the Technical University of Denmark

References

1. C. Creton, Mrs. Bulletin, 28(6):434-439, 2003
2. C. Verdier, G. Ravilly, J. Pol. Sci. B, 45:2113-2122, 2007
3. P. J. Flory , 63:3083–3090, 1941
4. C. W. Macosko and D. R Miller, 9(2):199–205, 1976.
5. D. R Miller and C.W. Macosko, 9(2):206–211, 1976.
6. D. Satas, Handbook of Pressure Sensitive adhesives. Van Nostrand Reinhold, New York, ISBN: 0-442-28026-2, 2nd edition, 1989, Chapter 5
7. H. Winter and F. Chambon, 30(2):367-382,1986
8. F. Chambon and H. Winter, 31(8):683-697,1987

Jens Lolle Laursen
Phone: +45 2230 4862
Fax: +45 4588 2161
e-mail: jlo@kt.dtu.dk
www: www.dtu.dk/centre/DPC
Supervisors: Martin E. Vigild
Andy Horsewell, IPL, DTU
Ion M. Sivebæk, Novo Nordisk A/S
Lasse Christoffersen, Novo Nordisk A/S

Industrial Ph.D. Study
Started: December 2005
To be completed: December 2008

Processability and Fracture Mechanical Performance of Tribologically Modified Plastics

Abstract
The present project deals with the influence of friction-modifying additives on processing and fracture mechanical performance of selected polymeric grades, used in the medico-device industry. The processing and test procedures are chosen to simulate the state and conditions under which the materials are used. The project will potentially make possible the safe use of new tribologically superior plastic grades, providing reduced frictional losses in the device mechanisms, without compromising product safety and failure rates.

Introduction
Plastics with friction-reducing additives are to an increasing extent being used as replacement for external lubrication of mechanisms in medico-technical devices. Novo Nordisk A/S (NNAS) is active in research within combinations of new plastics with friction-reducing additives especially developed for the conditions under which the materials operate in prefilled injection devices, such as insulin pens. Current results indicate an appreciable reduction in coefficient of friction compared to the best constellations of commercially available grades. The studies have, however, also indicated some processing difficulties when injection molding these new plastic grades, such as weak weld lines, poor surface quality and internal zones of reduced coherence. An effort towards the understanding of the underlying phenomena is crucial for the potential application of these new grades and also provides procedures for characterization and benchmarking of future plastic materials.

Specific Objectives
The primary project objectives are to provide understanding of the mechanisms behind the observed processing difficulties, to make possible quantification of the extent to which these difficulties occur for a given grade and to quantify the reduction in specific mechanical performance induced hereby. Based on these studies, a design guideline will be prepared for use in future in-house formulation of low-friction grades.

Tool and Means Overview
The processing properties of the materials (the "processability") will be investigated by injection molding and analysis of test specimens with a simplified geometry. A major project task is the development of a test geometry, which reflects processing conditions in large-scale industrial production, allows for monitoring of relevant molding parameters in the melt, and makes possible the subsequent analysis of the mechanical and tribological properties of the materials. The latter will be tested according to internal NNAS procedures, simulating field conditions for device use.

Another aspect of the project is to define and test the characterization means for the described failure mechanisms and geometries. The mechanical performance will be investigated through fracture mechanical studies, providing high sensitivity towards inherent and induced material flaws, combined with genuine information on constitutive material behavior.

A third aspect of the project is to describe the correlation between processing parameters and functional properties through models, based on the composition and microstructure of the material, in combination with the physical and chemical context in which they perform. Microstructure and morphology will be analyzed by polarized light-optical microscopy (PLM), scanning electron microscopy – energy dispersive x-ray analysis (SEM-EDX), Fourier transformed infrared spectroscopy (FTIR) and mechanical micro/nanoindentation measurements.

Model Materials and Process Factors

A semi-crystalline polymer is used as base material (matrix), namely polyoxymethylene (POM). This material is widely used in medical devices, when the properties of the traditional commodity plastic used, polypropylene (PP), do not suffice. The tribological additives chosen are polydimethylsiloxane (PDMS) as an all-liquid state additive (liquid during both material processing and usage phases) and polytetraflouroethylene (PTFE) as an all-solid state additive. Polyethylene (PE) as a liquid-solid state additive may be incorporated in the experiments at a later stage.

The process factors include injection molding shear rate, temperature gradients and holding pressure.

Test Plate Geometry and Injection Molding Tool

All experiments are based on plate-shaped blanks. The blanks are molded in an injection molding tool procured as part of the project. The tool is designed to simulate large-scale industrial production, utilizing hardened tool steel (realistic cooling conditions) and needle-valve hot runners (realistic runner conditions). The plate part of the blanks (60×60 mm^2) are filled through an ejector pin zone (Figure 1) and a straight flow front perpendicular to the primary flow direction is realized by means of three-dimensional double curving profiling of a fan-shaped geometry going from the injection point to the ejector pin zone. The midplane surface of this geometry was modeled by a 4th order polynomial in a cylindrical coordinate system, with origo in the point of injection:

$$z(r) \quad Kr^2\left(r^2 - 2r + 1\right)$$

The surface was defined in the CAD software (Pro/Engineer) through ten trajectories with different values of the angular coordinate and the scaling parameter *K*. The latter was determined for each trajectory numerically, so to keep the curve length *s* constant and equal to that at the maximum angle (corresponding to the gate width) with $K = 0$, where

$$s = \int_0^1 \left(1 + (dz/dr)^2\right)^{1/2} dr$$

and r_1 is the distance from the injection point to the gate. The result is a flow-path independent pressure drop throughout the inlet and gate, and predominantly unidirectional flow in the plate. This fact was rendered probable in the design stage by process simulation using Moldflow injection molding simulation software (Figure 1) and verified for the realized mold through a series of short shots (Figure 2).

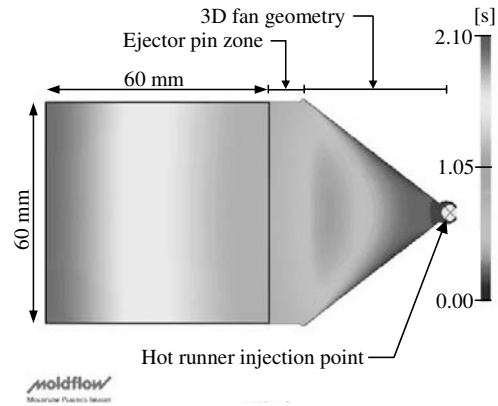

Figure 1: Fill time simulation in Moldflow software with a standard flow POM as model material (M. Papsøe, Device Simulation, Novo Nordisk A/S).

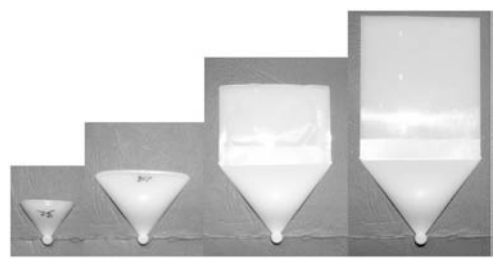

Figure 2: Short shots in 1.5 mm thickness with high-flow polyamide, ending with a fully molded blank (right).

The tool is modularly build and features possibility of plate thicknesses of 1.5 or 6 mm, molded-in notches, cavity vacuum evacuation and two surface roughnesses. The latter come about using inserts either polished with diamond paste 7 µm or spark eroded to Charmille 30. A secondary mold setup with a two-drop hot half provides gating from both of two opposing side edges. The result is test plates with a central weld line, so also studies with of this deficiency can be made. Three combined cavity pressure and temperature transducers makes possible monitoring of realized process conditions during both injection and holding phases, and also provide data for comparison against injection molding simulation software.

Friction Testing

A study has been made to addresses the processing dependence of friction for POM, neat and with PDMS and/or PTFE additives, slid against neat PP. The POM plates were processed under conditions simulating actual molding conditions from large-scale production of a POM component in a particular prefilled insulin pen. Two process factors were varied in two levels; nominal mold temperature and injection melt flow.

Friction testing was performed under conditions simulating end use in said insulin pen.

Frictional properties are expressed by the coefficient of friction (CoF). The CoF is defined as the ratio between the force that opposes relative movement between two surfaces in contact, and the normal force between them. The CoF was measured using a ring-on-disc type tester, called the TriboTester, described in detail in [1]. A close-up from a test is shown in Figure 3.

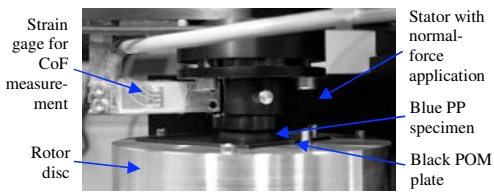

Figure 3: Close-up of TriboTester modified for plate specimens.

The influence of molecular orientation on CoF can be examined by measurements under translational sliding. Such measurements can be made using a standard tensile testing machine and comparing data from movement parallel and perpendicular to the direction of injection melt flow, respectively.

Fracture Mechanical Testing

The fracture mechanical tests will be based on a single edge notched beam geometry (SENB), milled from the molded plate blanks to standardized width and length. Specimens from 1.5 mm blanks represent a realistic thickness for components in medico-devices and will thus also be used for microstructure studies. Milling 6 mm blanks to different thicknesses can be used to assess the thickness dependence of the fracture mechanical properties. This can serve as verification of applicability of the applied testing approach. 6 mm blanks also make possible comparison of 1.5 mm specimens milled to thickness with material of same thickness as-molded. The difference would mainly represent the effect of the skin layer naturally developed during injection molding, so that the contribution from this can be isolated. Testing in 6 mm thickness can also be used for linear elastic fracture mechanical testing (LEFM) of materials which, under the testing conditions, do not comply with the requirements posed by this approach if tested in 1.5 mm thickness.

The influence of molecular orientation will be examined by comparing SENB specimens milled to having their length axis parallel and perpendicular to the direction of melt flow, respectively.

Specimens molded with the double inlet system, i.e. with a weld line across the plate, provide for fracture mechanical characterization of e.g. mold venting conditions, holding pressure or imposed under flow during weld line formation. Comparison with data from specimens without the weld line can be used to quantifying the weld line severity through the so-called weld line-induced crack length.

To simulate the impact conditions under which the materials are most likely to fail in use, a LEFM procedure will be adopted through the use of ISO standard 17281:2002 [1], which specifically addresses fracture mechanical characterization of plastics at relevantly high displacement (and thus strain) rates. The standard deals with determination of two LEFM measures, the critical strain energy release rate G_{Ic} and critical stress intensity factor K_{Ic}, given by:

$$G_{Ic} \equiv -\partial\Pi/(b\partial a)$$

where b is sample thickness, Π is elastically bound energy and a is crack length, and:

$$K_{Ic} \equiv \lim_{x_1 \to 0} \sigma_{22}(x_1)(2\pi x_1)^{1/2}$$

where σ_{ij} is the stress tensor in a Cartesian coordinate system $\{x_1..x_3\}$ with origin at the tip of the crack.

For grades where LEFM turns out to be insufficient as means for determining onset of unstable crack propagation (ineligible plasticity under posed conditions) a J-integral approach will be adopted, based on the ASTM E1820-99-standard [2] and the work by e.g. Fasce et al. [3].

The force/displacement data, which forms the basis for calculation of either of the characteristic fracture mechanical properties, will be measured by means of an instrumented drop tower impact tester, equipped with a 4.1 MHz PC based data sampling unit. As this apparatus makes possible logging of the full force and displacement time-traces, it also provides means for additional verification of the data analysis method used.

Fracture mechanical test variables include specimen thickness, load point displacement rate and material temperature. Testing at around 5°C would simulate the refrigerator conditions prefilled insulin pens are stored under. Such low temperature testing is especially relevant if PP grades are also to be tested, since this temperature is close to its glass transition.

Results and Discussion

The results of the friction study performed are discussed in the following.

The measured friction data are exemplified in Figure 4 through graphs of two extreme cases of POM with and without the PDMS and PTFE additives, respectively. The former is seen to yield markedly lower values of both transient and steady-state CoF (the so-called static and kinetic values, respectively). The large difference between the two values for the neat POM indicates that this constellation is prone to ‘stick-slip’, a phenomenon that is highly limiting its use for certain components. The POM grade with both additives on the other hand would operate smoothly against PP and could thus also be used for components where ‘stick-slip’ is critical.

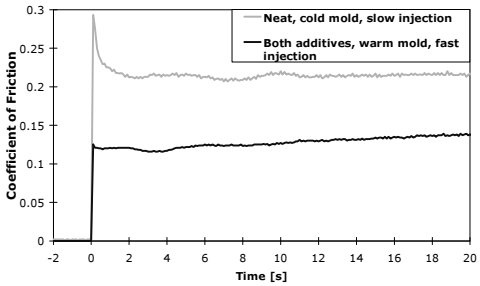

Figure 4: Friction testing data for 387 N distributed on 209 mm^2, providing 3 MPa as nominal surface pressure.

The friction testing study is summarized by Figure 5, showing the result a statistic effect screening on 5% level of significance. Non-significant effects and interaction were successively removed from the original 3rd-degree linear model. The two response variables used are the static CoF and the minimum value of the kinetic CoF measured during 20 seconds of testing. The effect of the significant variables are given as relative change in the two response variables, when changing factor level from low (0) to high (1). Other factors and interactions are kept at the intermediate level (0.5) in the comparison. For interactions the stated value represents only the interaction part of the low-high change of the constituents. Statistic *p*-values from Student's t-tests indicate the strength of each factor and interaction.

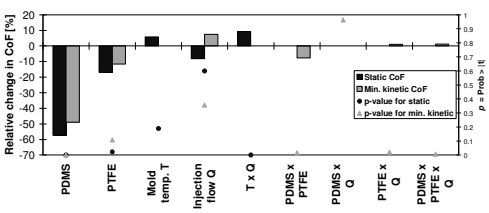

Figure 5: Statistic effect screening with α = 0.05.

Preliminary impact testing data have been measured using SENB specimens milled from POM tensile testing bars (4×8×34 mm^3) (Figure 6). The specimens were notched to half their cross-sectional height by milling and sharpened with a razor blade, confer [2]. To reduce the initial force peak, which causes high frequency oscillations in the signal, a 0.5 mm thick piece of silicone rubber was placed between the specimen and tup prior to testing. This procedure of reducing mechanical noise is in accordance with the standard and a comparison with the results of an undampened test confirmed that the time to fracture was unaffected by the applied damping. With the dampened setup, the level of mechanical oscillations was found to be within the limits prescribed by the standard. Tests with specimens milled from plate blanks are scheduled for January 2008.

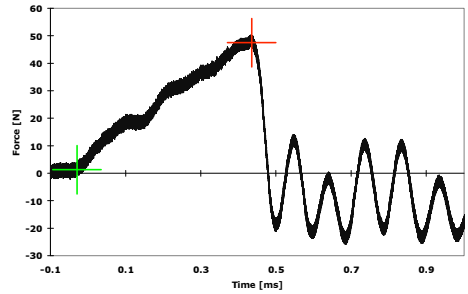

Figure 6: Preliminary impact testing data with 1 m/s impact velocity and 1.09 kg mass of falling weight. Green and red crosses indicate impact and beginning of unstable crack propagation, respectively.

Conclusions

The friction study showed the addition of PDMS and/or PTFE to have far more effect on friction than the processing factors. Some changes in processing factors were however found to be statistically significant. Future work within the friction studies include microstructural and morphological investigations into the different mechanisms behind 'good' and 'bad' processing.

Based on the presented framework, a thorough analysis of causes for the performance deterioration brought about by the friction-modifying additives will be made possible, as will establishment of procedures for comprehensive benchmarking of new grades and guidelines for the composition hereof.

Acknowledgements

The author greatly acknowledges the stated supervisors, as well as co-supervisors Povl Brøndsted, Risø-DTU, and Mogens Papsøe, Novo Nordisk A/S, for their invaluable sparring during the project. .

References

1. T. Ruby, T.J. Herslund, I.M. Sivebaek, New tribotester for polymeric materials, NordTrib 2006 proceedings, NT2006-13-52
2. ISO 17281:2002, Plastics – Determination of Fracture toughness (G_{Ic} and K_{Ic}) at moderately high loading rates (1m/s)
3. ASTM E1820-99, Standard Test Method for Measurement of Fracture Toughness
4. Fasce, V. Pettarin, R. Seltzer, P. Frontini, Polymer Engineering & Science 43 (5) (2003) 1061
5. Y. Yamaguchi, Tribology of Plastic Materials – Their Characteristics and Applications to Sliding Components, Elsevier, 1990
6. W. Brostow, R. Corneliussen (Eds.), Failure of Plastics, Hanser Publishers, 1986

Rasmus Lundsgaard
Phone: +45 4525 2869
Fax: +45 4525 2258
E-mail: ral@kt.dtu.dk
WWW: http://ivc-sep.kt.dtu.dk
Supervisors: Georgios M. Kontogeorgis
Bjarne Nielsen, Danisco A/S
Ulrik Aunskjær, Danisco A/S

PhD Study
Started: July 2007
To be completed: July 2010

Migration of Plasticisers from PVC and Other Polymers

Abstract
The major objective of this project is to develop an enhanced understanding of the mechanism of migration of plasticisers and similar polymer additives from PVC (and other polymers) into various environments and under varying conditions. The final deliverable of the project will be a model which can not only describe existing experimental migration data but also predict the migration of existing and new plasticisers with very little or no experimental data, thus assisting in the development of new formulations. A qualitative and quantitative understanding of the effect of various factors on migration will be achieved.

Introduction
The most commonly used plasticisers for Polyvinyl Chloride (PVC) are the phthalates, especially the plasticizer DEHP (Di-2-ethylhexyl phthalate) [1]. Several of these phthalates are being suspected of having carcinogenic properties and are furthermore very slowly biodegradable; this means that there is a need to develop safe substitutes of these plasticisers. The Danish food-additive manufacturer Danisco has recently developed such an alternative, the GRINDSTED® SOFT-N-SAFE plasticiser (SNS) which is based on a fully acetylated glycerol monoester on hardened oil from the castor bean. Being based on a natural product, the composition of SNS can exhibit small changes from batch to batch, but the two main components are the fully acetylated glycerol monoester based on 12-hydroxystearic acid (85%) and stearic acid (10%), as shown in figure 1[2].

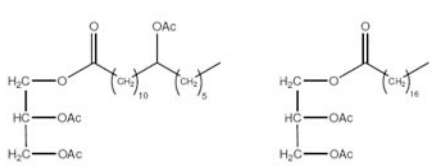

Fig. 1
Fully acetylated glycerol monoester based on 12-hydroxystearic acid (85%, left) and on stearic acid (10%, right), the two main components of GRINDSTED® SOFT-N-SAFE.

The product is now approved for use in the European and North American market and moreover preliminary results show smaller migration to specific food simulants (aqueous acetic acid, water-ethanol and sunflower oil) compared to standard plasticisers like DEHP and Diisononyl phthalate (DINP) [3]. In addition, SNS has shown to be a non-toxic, fully biodegradable substitute, but is substantially more expensive than DEHP (3-4 times).

As there has been great attention on the use of plasticisers in the later years, especially the use of phthalates, many new migration limit regulations have appeared, e.g. Commission directive 2005/79/EC [4] by the European Union (EU). The experimental tests needed in order to check whether the migration of the plasticiser is within the regulations are very time consuming or difficult to carry out. For this reason in 2002 EU made it possible to use food simulants and even generally recognised migration models to estimate the complete migration into different foods [5]. Two such models are presented in equations 1 and 2:

$$M_t = 2C_{p0}\sqrt{\frac{Dt}{\pi}} \quad (1)$$

$$\frac{M_t}{M_\infty} = \frac{\alpha}{1+\alpha}\left[1-\sum_{n=1}^{\infty}\frac{2\alpha(1+\alpha)}{1+\alpha+\alpha^2 q_n^2}\exp\left(\frac{-Dtq_n^2}{L^2}\right)\right] \quad (2)$$

Model 1 (Eq. 1) and model 2 (Eq. 2) are both derived from the work by Crank in 1956 [6], and they are widely accepted as migration models, though with some limitations. Model 1 is only applicable in the first part of the migration where the difference between migrant (plasticiser) concentration in the polymer and in

the solvent is very large. This means that this model can be used for large volumes of solvent compared to the volume of polymer with infinite well agitation. In practical conditions this could for instance occur with migration from a polymer hose into the constant moving solvent inside the hose. In this case the concentration of the migrant in the solvent next to the polymer can be seen as almost constant and very close to zero, and thus leads to the fastest possible migration of the migrant into the solvent.

In contrast, model 2 is applicable in the later part of the migration, where the migration is coming close to the final equilibrium i.e. the diffusion from polymer to solvent is equal to the diffusion from solvent to polymer. The value of n defines how large the error of the model for $t \rightarrow 0$ is; higher n values imply smaller errors but also need for more computational power. The parameter α is the ratio of the solvent volume over the polymer volume, and q_n is the positive roots of $tan\ q_n = -\alpha q_n$.

This suggests that model 1 is very useful as long as M_t/M_∞ is less than 0.5 (here M_∞ is the final equilibrium of the migration system and not necessarily equal to C_{p0}), whereas model 2, even with $n = 1$, is useful for M_t/M_∞ greater than 0.5. However, in many practical cases the migration will not follow model 2 completely, but will reach a higher final value due to some additional concentration difference of the migrant in the solvent next to the polymer barrier, caused by agitation or stirring of the solvent. This agitation or stirring of the solvent will lead to an induced lowering of the concentration of the migrant in the solvent next to the polymer, and as the migration is driven by the concentration difference on each side of the polymer-solvent barrier, this will lead to a faster migration.

In 1993 a solution to this problem was suggested by Kontominas [7] (Eq. 3), by introducing an agitation parameter into the solution of the differential equation of Fick's second law of diffusion. This new agitation parameter "u" indicates the probability for the migrant molecule to go in the direction perpendicular to the polymer-solvent barrier plane towards the solvent. Even though this mathematical migration model has some potential, it has not been possible to obtain a fully satisfactory fit to the experimental migration data with and without agitation so far. This may indicate that modelling systems where the migration is partly influenced by agitation in the solvent is rather complex.

$$\frac{M_t}{M_\infty} = \frac{ut}{2L} erf\left(\frac{ut}{2\sqrt{Dt}}\right) + \frac{ut-L}{2L} erf\left(\frac{L-ut}{2\sqrt{Dt}}\right) + \frac{\sqrt{Dt}}{L\sqrt{\pi}}\left[\exp\left(-\frac{(ut)^2}{4Dt}\right) - \exp\left(-\frac{(L-ut)^2}{4Dt}\right)\right] + \frac{1}{2} \quad (3)$$

The purpose of the current work was initially to estimate diffusion coefficients of Danisco's new plasticiser SNS at different temperatures. This was possible by utilising the data from a migration experiment Danisco had conducted on this new plasticiser for other purposes [8]. This migration experiment was set up to measure the migration of three plasticisers (GRINDSTED® SOFTN-SAFE (SNS), GRINDSTED® ACETEM 95 CO (Acetem) and Epoxidised Soybean Oil (ESBO)) from three different PVC compounds at three different temperatures (20ºC, 40 ºC and 60 ºC) into iso-octane.

Furthermore, the purpose of this work was to investigate whether it is possible to estimate the migration utilising the two simple migration models (model 1 and 2). If agitation proved to be an important parameter for the conducted experiments, the mathematical migration model of Kontominas should be tested and preferably optimised based on the recent experimental migration data.

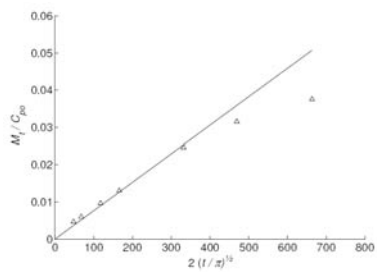

Fig. 2
The linear regression on the data points from the migration of GRINDSTED® SOFT-N-SAFE from PVC compound 2 at 40ºC into iso-octane. Only the 5 first data points are used for the regression as the last two points clearly not are following the linear model

Results

It was possible by utilising the simple model for the first part of migration (model 1, Eq. 1), to estimate diffusion coefficients for all the migration experiments by plotting M_t/C_{p0} against $2(t/\pi)^{1/2}$, which makes it possible to estimate the diffusion coefficient by linear regression (see figure 2).

All the estimated diffusion coefficients are listed in table 1.

Table 1
The estimated diffusion coefficients from the Danisco migration experiment on SNS, Acetem and ESBO from PVC into iso-octane. data points = data points used for linear regression / total number of data points in experiment.

	20ºC [cm^2/s] (data points)	40ºC [cm^2/s] (data points)	60ºC [cm^2/s] (data points)
SNS			
Comp. 1	$1.30 \cdot 10^{-9}$ (5/7)	$1.10 \cdot 10^{-9}$ (4/7)	$2.49 \cdot 10^{-9}$ (5/5)
Comp. 2	$5.95 \cdot 10^{-9}$ (5/7)	$5.84 \cdot 10^{-9}$ (5/7)	$2.67 \cdot 10^{-9}$ (5/5)
Comp. 3	$6.39 \cdot 10^{-9}$ (5/7)	$5.81 \cdot 10^{-9}$ (4/7)	$4.95 \cdot 10^{-9}$ (5/5)
Acetem			
Comp. 1	$6.17 \cdot 10^{-9}$ (7/7)	$6.42 \cdot 10^{-9}$ (4/7)	$1.07 \cdot 10^{-9}$ (5/5)
Comp. 2	$1.66 \cdot 10^{-8}$ (5/7)	$3.30 \cdot 10^{-8}$ (4/7)	$1.49 \cdot 10^{-9}$ (5/5)
Comp. 3	$3.07 \cdot 10^{-8}$ (4/7)	$6.63 \cdot 10^{-8}$ (4/7)	$7.67 \cdot 10^{-9}$ (5/5)
ESBO			
Comp. 1	$7.07 \cdot 10^{-11}$ (5/7)	$2.43 \cdot 10^{-10}$ (3/6)	$6.21 \cdot 10^{-10}$ (5/5)
Comp. 2	$1.25 \cdot 10^{-10}$ (5/7)	$7.25 \cdot 10^{-10}$ (6/7)	$8.59 \cdot 10^{-10}$ (4/4)
Comp. 3	$3.09 \cdot 10^{-10}$ (5/7)	$9.47 \cdot 10^{-10}$ (5/7)	$1.78 \cdot 10^{-9}$ (4/4)

The dependence between temperature and diffusion coefficient is normally seen to follow an Arrhenius type equation, where D_0 is the temperature independent diffusion constant, E_a is activation energy of diffusion, R is the ideal gas constant and T is the temperature:

$$D = D_0 \exp\left(\frac{-E_d}{RT}\right) \quad (4)$$

As displayed on figure 3, there is good agreement between the estimated diffusion coefficients of ESBO and the temperature dependence suggested by the Arrhenius equation (equation 2). The diffusion coefficients tend to reach higher values (faster migration) at higher temperatures, as it would be expected.

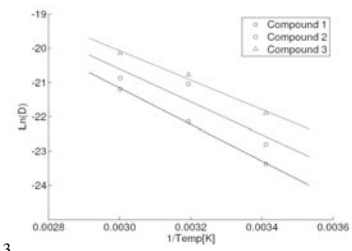

Fig. 3
The temperature dependence of ESBO diffusion coefficients from three different PVC compounds into iso-octane.

Unlike ESBO, the estimated diffusion coefficients of SNS (migration from PVC into iso-octane) seems to be temperature independent (figure 4). It is difficult to explain this behavior, as higher temperatures means faster Brownian movement of the molecules, thus the molecules will reach the lowest energy state of the system (equilibrium, M_t=M_∞) faster. Further migration experiments must be performed in order to investigate this unusual temperature behavior of SNS's diffusion coefficients.

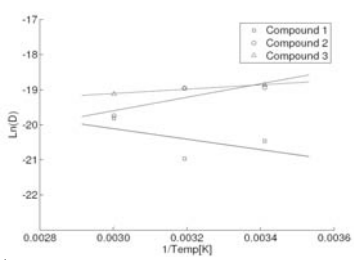

Fig. 4
The temperature dependence of SNS diffusion coefficients from three different PVC compounds into iso-octane.

Model development

The math model in the original form given by Kontominas[7] (see eq. 3) goes towards a value of 0.5 when there is no agitation of the solvent (u = 0), this means that either the migration always goes towards the final equilibrium where only 50% of the start concentration migrates (as the lower model 2 in figure 5), or that M_∞ is defined as $2{\cdot}C_{p0}$. But, as displayed in figure 5, the math model does not estimate the same migration as model 2 even though they both go towards the same limit of 50% at infinite time (the lower model 2 in figure 5).

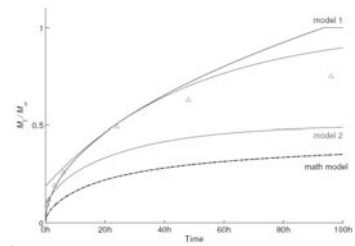

Fig. 5
The migration of SNS from PVC compound 2 into iso-octane at 40ºC. It is clear that the math model in its original form is far from estimating the same migration as the lower model 2.

If M_∞ is defined as $2{\cdot}C_{p0}$ then by multiplying the model by 2 it should be set up with the same definition of M_∞ as the other models (M_∞ = C_{p0}). This corrected math model now goes towards $2(Dt)^{1/2}/(L\pi^{1/2})$ for $t \rightarrow 0$, as would be expected (figure 6).

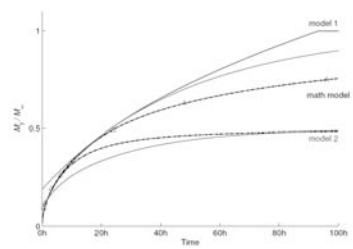

Fig. 6
The migration of SNS from PVC compound 2 into iso-octane at 40ºC. The new corrected model makes a complete fit to the experimental data, while the corrected math model for migration with no agitation goes towards 0.5.

The reason why M_∞ should have been defined as $2C_{p0}$ is not very clear, as the migration at infinite time never exceeds the total amount of migrant (C_{p0}). The corrected math model with M_∞ defined as C_{p0} is expressed as:

$$\frac{M_t}{M_\infty} = \frac{ut}{L} erf\left(\frac{ut}{2\sqrt{Dt}}\right) + \frac{ut-L}{L} erf\left(\frac{L-ut}{2\sqrt{Dt}}\right) + \frac{2\sqrt{Dt}}{L\sqrt{\pi}}\left[\exp\left(-\frac{(ut)^2}{4Dt}\right) - \exp\left(-\frac{(L-ut)^2}{4Dt}\right)\right] + 1 \quad (5)$$

It was found that further optimization of the math model for making it go towards the limit of $M_t/M_\infty=0.5$, when the agitation parameter "*u*" was set to zero, did mean a loss in the good fit of the model to the experimental data. For this reason is it suggested to use the corrected math model (Eq. 5) when there is agitation of the solvent, and the optimized model (Eq. 6) when there is no agitation.

$$\frac{M_t}{M_\infty} = \frac{1}{2} erf\left(\frac{L}{2\sqrt{Dt}}\right) \quad \frac{2\sqrt{Dt}}{L\sqrt{\pi}}\left[1-\exp\left(-\frac{L^2}{4Dt}\right)\right]+\frac{1}{2} \quad (6)$$

Conclusion

Diffusion coefficients for the three plasticisers SNS, Acetem, and ESBO were estimated for all the migration experiments conducted by Danisco. It was found that SNS has a diffusion coefficient approximately a factor 10 higher and Acetem almost a factor 50 higher by average, compared to ESBO. A good relationship between temperature and the estimated diffusion coefficients was seen for ESBO utilising an Arrhenius equation. This was not the case for Acetem and SNS. The diffusion coefficient of SNS seems to be independent of temperature, but further migration experiments at larger temperature intervals have to be conducted to verify this tendency. Two generally recognised migration models derived from Fick's second law of diffusion were tested against the migration data obtained from the Danisco migration experiments. These two general models are only able to estimate migration into a static solvent or an infinitely well agitated solvent. For this reason these two models are not necessarily suitable candidates for a migration model capable of estimating the full migration in practice. A more complex migration model was tested, in which a parameter for agitation of the solvent was incorporated. However this math model is not following model 1 for $t \rightarrow 0$ as it is generally agreed for migration models[9], but by defining M_∞ as $2 \cdot C_{p0}$ this problem was overcome. This correction led to a math model going towards 1 instead of 0.5 when the agitation parameter was set to zero. By optimising the corrected math model on one of the three contributing parts of the model, it was possible to propose a new model that almost completely followed the same estimation of migration as model 2 (no agitation and $M_\infty = ½C_{p0}$). It was found that the corrected math model had a more accurate fit to the experimental data than the optimised model, but further experimental data under different agitation conditions are needed in order to investigate the capability of the math model.

Acknowledgement

I would like to acknowledge Danisco for making this project possible, and especially Jørgen Kirk Kristiansen and Torkil Fischer Jensen at Danisco for their help and support. Furthermore I would like to acknowledge Danisco and especially Bjarne Nielsen and Ulrik Aunskjær for making it possible for me to continue this research project by partly funding of a newly started PhD project. I would also like to acknowledge Georgios Kontogeorgis for his help and guidance, especially on keeping me focused on the most important parts of this project.

List of abbreviations

Acetem	GRINDTED® Acetem 95 CO
Compound 1	50phr plasticiser, 2.5phr surfactant and stabiliser.
Compound 2	50phr plasticiser, 2.5phr surfactant and stabiliser, 7phr lubricant.
Compound 3	67phr plasticiser, 2.5phr surfactant and stabiliser
DEHP	Di-2-ethylhexyl phthalate
DINP	Diisononyl phthalate
ESBO	Epoxidised Soybean oil
PVC	Polyvinyl Chloride
SNS	GRINDTED® SOFT-N-SAFE

List of symbols

α	Ratio of solvent volume over polymer volume
C_{p0}	Initial concentration of plasticiser in polymer [mg/cm^3]
D_0	Temperature independent diffusion constant [cm^2/s]
D	Diffusion coefficient [cm^2/s]
E_d	Activation energy of diffusion [J/mol]
erf	Error function, $erf(x) = \frac{2}{\pi}\int_0^x e^{-t^2} dt$
L	Thickness of polymer [cm]
M_∞	Migration at infinite time [mg/cm^2]
M_t	Migration at time t [mg/cm^2]
phr	Parts per hundred resin.
q_n	positive roots of $tan\ q_n = -\alpha q_n$
t	Time [s]
u	agitation parameter [cm/s]

References

[1] Braucks, S. *Green paper: Environmental issues of PVC*; The Commission of the European Communities. **2000**.

[2] Jensen, T.F. *Complete composition of GRINDSTED® SOFT-N-SAFE*; Danisco research report.

[3] Danisco A/S. *GRINDSTED® SOFT-N-SAFE - The sustainable plasticiser for PVC*. **2006**.

[4] Kyprianou, M. *Commission Directive 2005/79/EC of 18 November 2005 amending Directive 2002/72/EC relating to plastic materials and articles intended to come into contact with food.* Official Journal of the European Union. **2005**, *302*, 35

[5] Byrne, D. *Commission Directive 2002/72/EC of 6 August 2002 relating to plastic materials and articles intended to come into contact with foodstuffs*. Official Journal of the European Union. **2002**, *220*, 18

[6] Crank, J. *Mathematics of diffusion*; 1st edition, Clarendon press: Oxford, **1956**.

[7] Kondili, E.; Kontominas, M.; Kosmas, M. *The effect of stirring on the diffusion of small molecules from a polymer matrix into a solution*. Polymer. **1993**, *34*, 2592.

[8] Jensen, T.F., *Migration of plasticizers from PVC to iso-octane*. Danisco research report. **2006**.

[9] Piringer, O.G.; Baner, A.L. *Plastic packaging materials for food: barrier function, mass transport, quality assurance and legislation*. Wiley-VCH: Weinheim, **2000**.

Piotr Tomasz Mitkowski

Phone: +45 4525 2910
Fax: +45 4525 2906
E-mail: ptm@kt.dtu.dk
WWW: http://capec.kt.dtu.dk
Supervisors: Rafiqul Gani
Gunnar Jonsson

PhD Study
Started: February 2005
To be completed: February 2008

Computer Aided Design and Analysis of Hybrid Processes

Abstract
In the design of hybrid processes the performance of each constituent element need to be taken into account and the design must take into consideration their interdependency. Focus of this paper is on the reaction – separation hybrid processes. The general systematic methodology for design of hybrid processes along with used computer aided techniques is presented with a supporting experimental case study of synthesis of n-propyl-propionate.

1. Introduction

Equilibrium or kinetically controlled reactions are common in chemical and biochemical manufacturing. This type of reaction is usually characterized by low product yield or low selectivity towards the desired product, when parallel reactions occur. Irrespective of the controlling factor of reaction(s), on-site removal of product(s) enhance the yield, leading to simple product purification, reduced processing time and may also reduce undesired side reaction(s) if they occur. In most of the cases, to increase process economics the recycle of unreacted reactants is looked for what imply use of separation step(s).

Combination of at least two unit operations based on different physical phenomena leads to a hybrid process since they jointly contribute to fulfil the process step [1]. In general, two types of hybrid processes are distinguished: reaction-separation (R-S), for example, the combination of batch reaction and membrane-based separation, and, separation-separation (S-S) such as the coupling of distillation with pervaporation. Design of hybrid process needs to take into account interdependency of linked processes in terms of process conditions like temperature, pressure and compositions to find out the feasible operation window. Models describing each of the constituent process (like reactor, pervaporation, nanofiltration, distillation) are usually available in literature; therefore their quantitative and qualitative analysis can lead to efficient process design. Based on the model-based computer-aided techniques it is possible to identify feasible design alternatives, saving thereby valuable experimental resources.

2. Design methodology of hybrid processes

A systematic model based framework for analysis and design of hybrid R-S and S-S processes were already presented by author in [2]. The objective of the methodology is to identify the best possible process set-ups configuration for R-S and S-S systems with wanted constraints of process parameters like process yield, reaction time, residence time, selectivity and product purity. The design algorithm is depicted in Figure 1 along with associated for each step data, specific models and computer-aided tools from ICAS family. Step 1A consist of analyzes of separation or reaction task. At that step, for separation task analyzes includes identification of azeotrope points, phase split, etc. In case of reaction task, condition of reaction are defined in terms of temperature, pressure, catalyst and concentration of compounds, which also includes analysis of reaction kinetics. In step 1B the need of solvent is considered. In step 2 the objective of design is specified in term of process parameters. Step 3 now combines all collected knowledge from step 1 with appropriate separation models to generate the feasible hybrid process design alternatives. Separation techniques are compared by means of driving force approach [3]. If step 1B pointed out need of solvent, the solvent is selected using method given by Gani et. al [4]. In the last step (step 4), the generated hybrid process alternatives are tested under different operational scenarios. Based on which feasible alternatives are identified.

2.1. Process alternatives

In the last step (step 4) based on superstructure (Figure 2) the specific process scenarios are generated. Depending on batch or continues process is selected in step 2 and dynamic or steady state models are generated for each process scenarios. A generic model giving the balance equations ((1)-(2)) for hybrid process are derived based on superstructure given in Figure 2. The differential equations represent the states of the process

system at discrete time points.

$$\left[\frac{\partial n_i}{\partial t}\right] = \left[F_i\right] + \left[F_i^{(1\alpha R)}\right] + \left[F_i^{(1\beta R)}\right] + \left[F_i^{(2\alpha R)}\right] + \left[F_i^{(2\beta R)}\right] \quad \left[F_i^{(1\alpha P)}\right] - \left[F_i^{(1\beta P)}\right] - \left[F_i^{(2\alpha P)}\right] - \left[F_i^{(2\beta P)}\right] \quad \left[\sum_{k=1}^{NKR} \nu_{i,k}^{1\beta} r_k^{1\beta} V^{1\beta}\right] \quad (1)$$

$$\left[\frac{\partial H}{\partial t}\right] = \left[Fh^{(F)}\right] + \left[F_i^{(1\alpha R)}{}_h{}^{(1\alpha R)}\right] + \left[F_i^{(1\beta R)}{}_h{}^{(1\beta R)}\right] + \left[F_i^{(2\alpha R)}{}_h{}^{(2\alpha R)}\right] + \left[F_i^{(2\beta R)}{}_h{}^{(2\beta R)}\right] - \left[F_i^{(1\alpha P)}{}_h{}^{(1\alpha P)}\right] - \left[F_i^{(1\beta P)}{}_h{}^{(1\beta P)}\right] - \left[F_i^{(2\alpha P)}{}_h{}^{(2\alpha P)}\right] - \left[F_i^{(2\beta P)}{}_h{}^{(2\beta P)}\right] + \left[\sum_{k=1}^{NKR} r_k^{1\beta} \Delta H_k^R\right] \quad [Q] \quad (2)$$

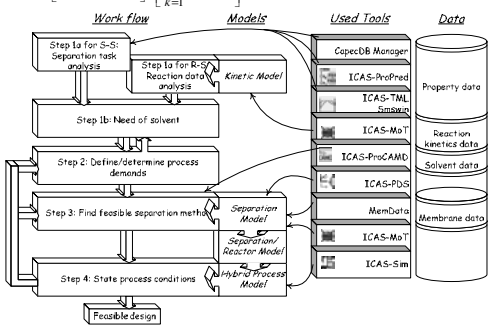

Figure 1: Methodology of design/analyze hybrid process system

Using the generic model and the particular details of any problem, the specific hybrid R-S or S-S process can be generated. Then, the generated feasible process alternatives are tested under different process conditions by means of process simulation.

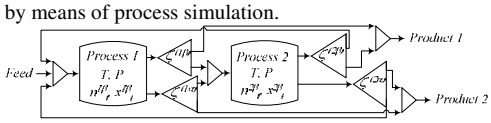

Figure 2: Hybrid process superstructure

3. Case study: Reaction-Separation

The methodology is applied here to the case of synthesis of n-propyl-propionate (ProPro). ProPro is used as paint thinner, food additive and essence for perfumes by giving apple-like, fruity taste.

Step 1: Reaction task analysis

Esterification reaction of 1-propanol (POH) and propionic acid (PAc) to ProPro and H2O follow Eq. (3). Reaction is taken place in the liquid phase with use of a heterogeneous catalyst Amberlyst 46. The use of this very selective catalyst eliminates competing etherification reaction to di-n-propyl ether and dehydration of propanol to propene.

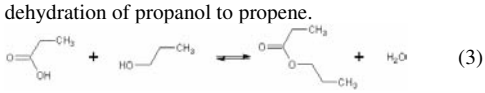

(3)

The reaction kinetics of this heterogeneous esterification reaction has been studied by Duarte et al. [5] at pressure of 5 atm and temperature range varying from 363.15K to 383.15 K. The equilibrium of reaction (3) is expressed in terms of component activities [5]:

$$K_{eq} = \frac{a_{ProPro} \cdot a_{H2O}}{a_{PAc} \cdot a_{POH}} \quad (4)$$

Separation of components present in the reaction mixture is difficult since two binary and one ternary heterogeneous azeotropes as well as one homogeneous azeotrope are found (see Table 1).

Table 1: Reaction mixture analysis (SMSwin)

Composition	Molar fraction [%]				T_b [K] @ 1atm.
	POH	H_2O	PrPr	PAc	
POH – H2O – PrPr (Hetero)	24.50	57.82	17.68	-	359.46
PrPr – H_2O (Hetero)	-	68.63	31.37	-	363.14
H_2O – PAc (Homo)	-	6.666	-	93.34	372.69
H_2O – POH (Hetero)	57.26	42.74	-	-	361.88

Initial experimental compositions reported by Duarte et. al. [5] were used as an input to reactive flash calculations [6]. The obtained results proved that the system is reaching its chemical and physical equilibrium. Based on results obtained from reactive flash calculation in ICAS-PDS (Figure 3) the maximum operating temperature at P = 1 atm. is set to 363.4 K.

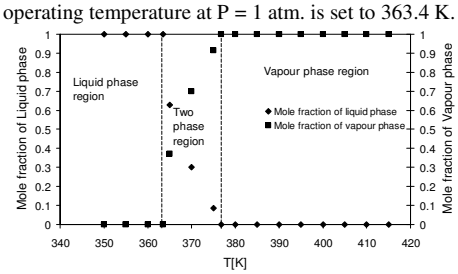

Figure 3: Phase fraction distribution at P = 1 atm., substrate ratio 1:1

Step 1B: Need of solvent

In this study incorporation of solvent has not been investigated since all reactants are liquid and miscible in the operation window. However, it is foreseen that addition of non-reactive solvent to create the second water phase would decrease the activity of the products and move reaction to the right-hand side of Eq. (3).

Step 2: Process demands

The main goal of that synthesis is to obtain as high as possible conversion of PAc close to 100% in the batch operation of 12h.

Step 3: Separation method selection

The continuous removal of product and/or products will enhance the conversion of reactants; therefore in this step separation technique needs to be selected. Many membrane-based separation processes offer selective removal of a specific chemical, for example, pervaporation and vapour permeation are widely used for dehydration of organic mixture [7]. Based on a superstructure (Figure 2) the configuration is generated where process 1 is a reactor and process 2 is membrane-based separation for selective removal of water. Since Amberlyst 46 is a heterogeneous catalyst, the packed bad reactor with additional tank to maintain hold-up in the process system is required (see Figure 4-A). The packed bed reactor and membrane-based separation can

be more integrated as is shown on Figure 3-B where the reaction and separation zones are in one piece of equipment. In order to utilize the catalyst the liquid feed is required in reaction zone therefore it is important to highlight that in the first configuration pervaporation or vapour permeation are possible alternatives since in the second configuration only pervaporation is feasible.

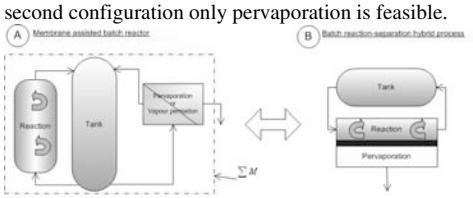

Figure 4: Conceptual process configurations

Step 4: Process conditions and feasible design

In the last step of the methodology the separation model is combined with the batch reactor model into the hybrid dynamic process model. The specific model for membrane assisted batch reactor (Figure 3-A) is written under assumptions: (1) reaction occur only with the use of catalyst and in liquid phase, (2) constant trans-membrane component flux and (3) short resident time in reaction and separation zones. Model consists of following equations:

mole balance: $$\frac{dn_i}{dt} = -R_i \quad v_i\, r\, m_{CAT} L \tag{5}$$

constitutive equations:

$$r = k_f \left(a_{POH} a_{PAc} - \frac{1}{K_{eq}} a_{ProPro} a_{H2O} \right) \tag{6}$$

$$k_f = k_0 e^{\left(\frac{-E}{RT}\right)} \tag{7}$$

$$K_{eq} = K_{0,eq} e^{\left(\frac{-E_{eq}}{RT}\right)} \tag{8}$$

In this paper Modified UNIFAC (Lyngby) [8] has been used. The kinetic parameters have the following values: k_0 = 7.872.109 [mol·eq^{-1}·s^{-1}], E =63080 [J·mol^{-1}], $K_{0,eq}$ = 3.511, Eeq = -4631.4 [J·mol^{-1}]. The process efficiency is quantified here by process yield with respect to ProPro and it is defined as:

$$Y^t_{ProPro} = \frac{\left(n^t_{ProPro} - n^{in}_{ProPro}\right)}{n^{in}_{PAc}} \tag{9}$$

The introduction of access of 1-propanol will shift the reaction towards higher conversion of acid. The batch simulations with varying molar ratio of POH:PAc from 1:4 were performed in ICAS-MoT [9] and the results of this study in terms of process yield are presented on Figure 5. The increase of molar ratio above 3 does not give significant increase in yield, therefore a range between 2 and 3 is recommended. When the batch reactor is combined with the pervaporation unit it is important to observe the influence of the amount of catalyst as well as the switching time from batch reaction into integrated mode, since water is absent in the beginning of the batch. The increase in the ratio of catalyst mass, m_{cat}, and reaction mixture, m_{mix}, increases the yield in the given processing time (in that case we limit to 12h). Note that the switching time from batch reaction to the combined operation within the first two hours of the operation does not influence significantly the process yield (see Figure 6).

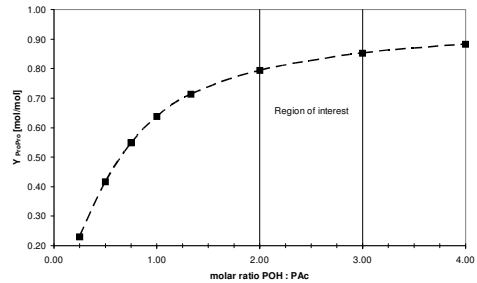

Figure 5: Yield of propyl-propionate versus molar ratio POH : PAc at T = 353.15 K

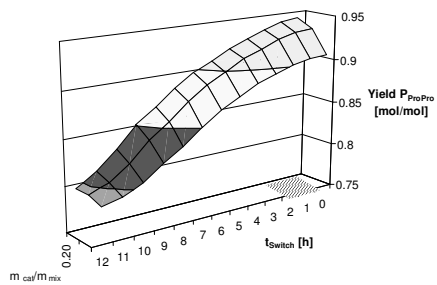

Figure 6: Yield versus switching time and mass ratio of catalyst and reaction mixture; POH : ProAc = 2:1, T = 353.15 K, m_{mix} = 1393 g, $R_{PAc} = R_{POH} = R_{PrPr} = 0$ mol/s, R_{H2O} = 0.13 mol/s

Experimental investigation

After theoretical investigation (steps 1-4) the set of experiments have been performed to verify behavior of the membrane assisted batch reactor. All experiments were conducted in a multipurpose lab-scale plant at the Chair of Fluid Separation Processes at the University of Dortmund (schematically presented on Figure 4-A).

During the pervaporation experiments the flat membrane PERVAP® 2201-D from Sulzer Chemtech with an active layer of polyvinyl alcohol (PVA) and a support layer of poly(acrylonitrile) (PAN) were used. The tank has a maximum volume of 1.7dm^3. The side packed-bed reactor (PBR) is constructed in such a way that various amount of catalyst could be introduced (varying from 130 to 300 g).

Before performing the membrane reactor experiments models for reaction kinetics and pervaporation were checked in independent experiments. In order to describe accurately the pervaporation a semi-empirical Meyer-Blumenroth model was used [10]. Both models gave very good agreement with experimental data.

Several processes operational conditions have been studied experimentally which are summarized in

Table 2: Membrane reactor: experimental process conditions, result and comparison with batch reactor

Exp No	E6	E5	E4	E3	E2	E1
T_R (av) [K]	336.21	354.11	346.24	344.85	351.87	346.83
T_M (av) [K]	334.11	353.09	343.19	343.48	349.36	347.65
m_{cat}/m_r (initial) [g/g]	0.21	0.23	0.23	0.23	0.24	0.12
POH : PAc [mol:mol]	3:1	3:1	2:1	2:1	2.2:1	2:1
Switching time [min]	61.37	61.37	60.00	134.95	135.50	75.80
Y_{ProPro}(reaction) [mol/mol] @720 min	59.9%	78.7%	73.2%	76.4%	75.0%	79.1%
Y_{ProPro} (Membrane reactor) [mol/mol] @720 min	88.8%	95.6%	93.2%	91.6%	90.2%	93.5%
Difference	**28.9%**	**16.9%**	**20.0%**	**15.3%**	**15.2%**	**14.5%**

Table 2. The switching time varying between 1 to 2 hours does not have significant influence on process yield (E3 and E4). Increase of ratio m_{cat}/m_{mix} by double, the yield increase insignificantly (E1 and E4). All tested membrane reactors scenarios gave significant improvement to batch reactor by overcoming equilibrium and kinetically controlled process (see Table 2). The best result, yield of 95.6%, has been achieved for highest temperature (354 K) and reactant ratio of 3:1 (E5). The weight fraction profiles of reactants in time of experiment E5 are presented on Figure 7. The weight fraction of PAc and POH decreased since fraction of products (ProPro, H20) increase until 61min. After the switching time weight fraction of H20 started decrease when ester fraction increased reaching 47w% in 12h. In batch reaction it would be possible to obtain only 38w% (simulation).

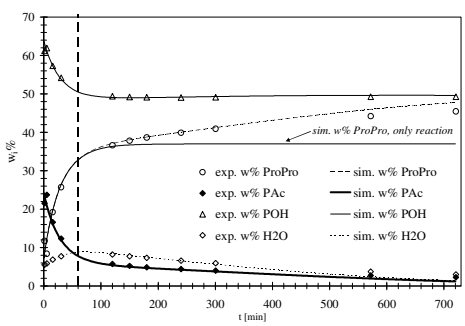

Figure 7: Membrane reactor. T_R = 354.11 K, T_M = 353.09 K, m_{CAT}/m_r = 0.23, POH:Pac = 3:1, t_{switch} = 61.37min; (E5)

Conclusions

A model-based methodology along with computer-aided techniques for systematic investigation of hybrid process systems have been presented with the application of the technique to the study of an esterification of n-propyl propionate. The reaction kinetic model and trans-membrane solution-diffusion flux model gave good agreement with simulation result. The feasibility of membrane reactor has been illustrated not only by simulation but also through experiments at different temperature, reactant molar ratio and amount of catalyst. The process temperature has the biggest influence among the investigated parameters. The increase of amount of catalyst leads to faster achievement of equilibrium. As the simulation results indicate the switching time until second hour does not influence significantly the process yield.

From this work, it is clear that processes consisting of a reactor and a highly selective membrane separation unit show advantages with respect to achieving increased product yield by overcoming limitations of equilibrium and kinetically controlled reaction.

Acknowledgements

P.T.Mitkowski is pleased to acknowledge funding to the PRISM the Marie Curie Research Training Network, EC's Sixth Framework Program.

Author is grateful to Ing. C. Buchaly, Dr. P. Kreis and Prof. A. Górak form UniDort for fruitful collaboration.

Nomenclature

a_i – activity [-],
A_m – membrane area [m^2],
J_i – component flux [mol/s/m^2],
K_{eq} – reaction equilibrium constant [-],
k_f – reaction rate constant [mol/s/eq],
L – concentration of active sides 0.95 eq/kg,
r – reaction rate [mol/s/eq],
R – universal gas constant, 8.3144 [$J \cdot K^{-1} \cdot mol^{-1}$],
R_i – component removal [$mol \cdot s^{-1}$],
ν_i - stechiometric coefficient [-],
Superscripts
R – reactor,
M – membrane unit.

References

[1] F. Lipnizki, R.W. Field, P-K. Ten, J. of Membrane Science, 155, (1999), 183-210
[2] P.Mitkowski, G.Jonsson, R.Gani, Comp.-Aided Chem.Eng., 24, (2007), 395-401
[3] E. Bek-Pedersen, PhD thesis, CAPEC, Technical University of Denmark (DTU), 2002
[4] R.Gani, C.Jim'ene-Gonz'alez, D.J.C.Constable, Comp.&Chem. Eng., 29,(2005),1661-1676
[5] C. Duarte, C. Buchaly, P. Kreis, J.M. Loureiro, Inżynieria Chemiczna i Procesowa, 27, (2006)
[6] E.S.P. Pérez-Cisneros, R. Gani, M.L. Michelsen, Chem. Eng. Science, 52, (1997) 527-543
[7] Z. Koszorz, Z. Ziobrowski, K. Belafi-Bako, R. Krupiczka, Desalination, 162, (2004), 307-313
[8] B. L. Larsen, P. Rasmussen, A. Fredenslund, Ind. Eng. Chem. Res., 26, (1987), 2274-2286.
[9] M.Sales-Cruz, R. Gani, 2003, Eds. S.P. Asprey and S. Macchietto, Elsevier, Amsterdam
[10] F. Lipnizki, G. Trägårdh, Sep. and Pur. Methods, 30, (2001), 49-125.

David Mogensen

Phone:	+45 4525 2922
Fax:	+45 4525 2258
E-mail:	dam@kt.dtu.dk
WWW:	http://www.kt.dtu.dk
Supervisors:	Prof. Kim Dam-Johansen
	Prof. Jan-Dierk Grunwaldt
	Thomas R.-Nielsen,Topsøe Fuel Cell A/S

PhD Study

Started:	November 2007
To be completed:	October 2010

Mathematical Modeling of Solid Oxide Fuel Cells

Abstract

Solid Oxide Fuel Cells (SOFC) is a technology on the brink of commercialization. In order to facilitate continuous optimization of the SOFC stack operation, improve its competitiveness and to integrate it with other technologies, an experimentally verified model is required. The aim of this project is to obtain such a model and implement it in a commercial simulation program. One important aspect embraces internal steam reforming that cannot be modeled with present literature data, and therefore steam reforming kinetics at the conditions of SOFCs will be investigated.

Introduction

The fossil fuel reserves are limited and because of this, it is necessary to investigate technologies that can be used to make our society independent of fossil fuels [1][2]. SOFC is a highly versatile technology, which can use a large number of different fuels either from fossil or renewable sources, such as H_2, CH_4 and NH_3, methanol, dimethylether and diesel [3]. This way the technology facilitates the transition between these energy sources. SOFCs combined with a gas turbine, which utilizes the high temperature exhaust gasses from the SOFC, can achieve electrical efficiencies of 65%-70% and about 90% total efficiency for a cogeneration plant [4][5][6]. It can also be used to design a decentralized power supply system since even relatively small units can provide high efficiencies i.e. 60% electrical efficiency and 80% total efficiency for a 3-400 kW system [7].

A SOFC produces electricity by an electrochemical cell, which is continuously supplied with separated streams of gaseous fuel and air/oxygen. The species that is transported through the solid electrolyte is O^{2-}. Both electrolyte and electrodes in the cell is made of ceramic materials and in order to obtain a sufficient rate of oxygen ion transport through the electrolyte a temperature in the range 600 K to 1000 K is needed. The configuration and materials of a SOFC can be seen in Figure 1. In this case the cathode is composed of strontium doped $LaMnO_3$ (LSM) and LSM on yttria-stabilized zicronia (YSZ), the electrolyte of YSZ, and the anode side of NiO/YSZ [8].

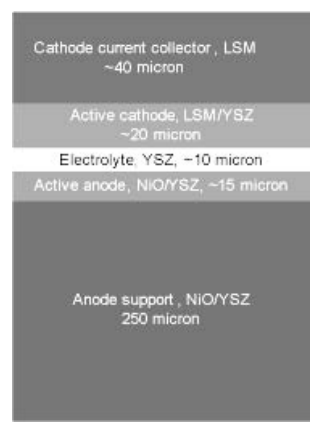

Figure 1: An illustration of an SOFC as produced by Topsøe Fuel Cell A/S [8].

The two main electrode reactions taking place in the cell are shown below.

Anode:

$$H_2 + O^{2-} \rightarrow H_2O + 2e^-$$

Cathode:

$$\tfrac{1}{2}O_2 + 2e^- \rightarrow O^{2-}$$

If methane is used as the fuel, it has to be catalytically converted into hydrogen internally in the SOFC by the NiO present in the anode material. [9]

Specific Contents
This project will cover both experimental work and modeling work. Furthermore a literature study will be made on the subjects relevant for the project.

The experimental work will cover the kinetics of internal steam reforming and include temperature and pressure effects for a planar SOFC stack.

Modeling Work
The modeling work will be a continuation of the work performed previously [10]. The effects that should be added or described in more detail are as follows:

- Stack model
  - Heat transfer
  - Single cell
    - Pressure effects
    - Electrochemical kinetics
    - Methane reforming kinetics
- Transient model

Methane Reforming
The methane reforming reaction as well as the water gas shift reaction is shown below

Methane reforming:

$$CH_4 + H_2O \rightleftarrows 3H_2 + CO$$

Water gas shift:

$$CO + H_2O \rightleftarrows H_2 + CO_2$$

The kinetics of these two reactions in conventional large scale catalytic reactors are well known [11]. The geometry and catalytic material inside a SOFC is however very different from a traditional system and therefore a series of experiments are planned to determine internal methane reforming kinetics for a SOFC, catalyzed by NiO.

The experiments will include tests in a tubular reactor with crushed anode material as the catalyst. It will also be attempted to design a setup where the reforming kinetics can be investigated in a cell without electrochemical reactions.

Pressure Effects
From the Nernst equation, an increase in total pressure from 1 atm to 5 atm is expected to increase the open cell voltage with about 5%. For tubular SOFCs it has been observed that the increase in performance at increased pressure is considerably higher than expected from the Nernst equation. Furthermore, the relative effect increases at high load as shown in figure 2 [12].
For the combined SOFC-gas turbine system there is the additional advantage of high pressure operation that it will also result in an improvement in the performance of the turbine [13].

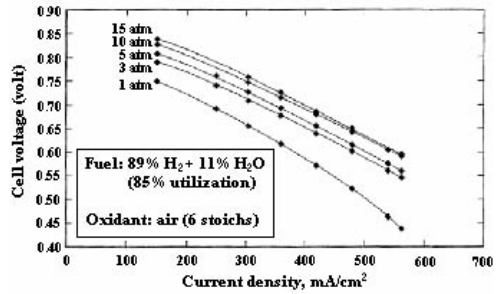

Figure 2: Effect of pressure changes on the performance of a tubular SOFC [12].

Acknowledgements
The author acknowledges Topsøe Fuel Cell A/S, DTU and the Graduate School in Chemical Engineering: MP_2T for financial support and supplying equipment.
Risø DTU is acknowledged for valuable discussions and practical support.

References

1. M. Asif, T. Muneer, Renewable and Sustainable Energy Reviews 11 (2007) 1388-1413.
2. http://www.iags.org/futureofoil.html, 30/11-2007.
3. N.Christiansen, J. B. Hansen, H. Holm-Larsen, S. Linderoth, P.H. Larsen, P.V. Hendriksen, M. Mogensen, Fuel Cells bulletin 8 (2006) 12-15.
4. A. Selimovic, Solid Oxide Fuel Cell Modelling for SOFC/Gas Turbine Combined Cycle Simulations, doctoral thesis, Lund University, 2002.
5. J. Pålsson, A. Selimovic, L. Sjunneson, Combined solid oxide fuel cell and gas turbine systems for efficient power and heat generation, Journal of Power Sources 86 (2000) 442-448.
6. V. Dorer, R. Weber, A. Weber, Energy and Buildings 37 (2005) 1132-1146.
7. A. F. Massardo, Transactions of the ASME. Journal of Engineering for Gas Turbines and Power 124 (2002) 110-116.
8. http://www.topsoefuelcell.com/, 27/11-2007.
9. W. Vielstich et al., Handbook of Fuel Cells, John Wiley & Sons Ltd, 2003 ISBN: 0-471-49926-9.
10. D. Mogensen, Mathematical Modelling of Solid Oxide Fuel Cells, Master thesis at Department of Chemical Engineering, DTU, 2007.
11. J. R. H. Ross, Catalysis Today 100 (2005) 151-158.
12. EG&G Technical Services, Inc., Fuel Cell Handbook, U.S. Department of Energy, Office of Fossil Energy.
13. S.K. Park, T.S. Kim, Journal of Power Sources 163 (2006) 490-499.

Ricardo Morales Rodríguez

Phone: +45 4525 2911
Fax: +45 4525 2906
E-mail: rmr@kt.dtu.dk
WWW: http://www.capec.kt.dtu.dk/
Supervisors: Rafiqul Gani

PhD Study
Started: February 2006
To be completed: January 2009

Computer-Aided Multiscale Modelling for Chemical Product-Process Design

Abstract
Nowadays, the key to success in product-process design/development is first to identify the end-use properties of a product and then to control product quality by manipulating the structure of the chemical. To match the desired product usually many repetitions of experiments are performed with considerable expenses of time and resources. A computer-aided modelling framework for product-process design is proposed as supplementary tool, where many of the tasks related to product-process is development can be performed systematically through an established set of work and data-flows. Because of the nature of the product-process design problems, multiscale modelling options need to be available within the framework.

Introduction
The design, development and reliability of a product and the process to manufacture it, need to be consistent with the end-use characteristics of the desired product. One of the common ways to match the desired product-process characteristics is through trial and error based experiments which can be expensive and time consuming. An alternative approach is the use of a systematic model-based approach according to an established work-flow in product-process design, replacing some of the time consuming and/or repetitive experimental steps. For many chemical products the appropriate models for product-process design needs to have multiscale features as the properties defining the chemical structure and end-use characteristics of the product are dependent on parameters of different size and time scales. The advantages of the use of multiscale modelling approach is that the design, development and/or manufacturing of a product-process can be described at different scales of length and time, providing thereby the knowledge of the applied phenomena at diverse degrees of abstractions and details.

The development of a framework for product-process design including a multiscale modelling option is very important analysis/design/identification of feasible chemical product candidates because it allows one to consider processing issues during the development of the product. The framework should include the product design and process design components, modelling tools and templates (work-flow) for guiding the user through the design steps. The integration of computational tools is necessary to increase the application range of the computer-aided product-process framework; where the connection between computational tools is established through COM-objects or following the rules for CAPE-OPEN standards.

Specific Objectives
The objective of this PhD project is to develop a new computer-aided model-based framework for product-process design that also includes multiscale modelling features. To develop this computer-aided framework, a combination of different computational tools, such as, property prediction packages, modelling tools, simulation engines, process simulators, solvent selection software, etc. is necessary; this integration of the different computational tools, allows the user to cover a wide variety of problems at different scales (of length and time) and disciplines concerned in chemical engineering in a easy manner; achieving in this way the development of a product-process with the desired end-use characteristics.

Computer-Aided Multiscale Product-Centric Process Design Framework
As product-process design problems are multidisciplinary and multiscale in nature, the gaps among the different disciplines/scales need to be bridged before a framework can be developed. A

Product-process design modelling framework would require the interaction between human and computer, where the human is handling and controlling the work-flow while the computer is carrying out the calculations in the work-flow and most of the tasks in the data-flow. It is important to highlight that the computer-aided framework performance will depend of the availability of appropriate models and the development of them.

A Work-Flow for product-process design is shown in figure 1; this work-flow covers various product-process design problem formulations and point out the needs for modelling tools, simulation engines, design tools, property packages, etc. Chemical product-process design starts with problem definition, desired properties, needs and quality of the product-process. Then documentation concerning the mathematical model of the new/redesigned product-process should be done in order to avoid the duplication of generation and storage.

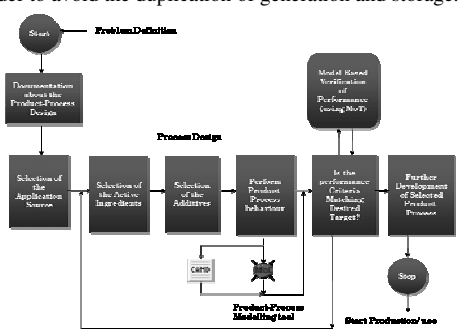

Figure 1 Work-Flow in Product-Process Design

The next step involves the selection of the application source, active ingredient and additives; here, documentation, databases and search engines are useful to verify some properties and available information during the creation and development of the product, as well as the calculation of the necessary properties embedded in the behaviour of the product. Frequently, the information needed to perform the simulation of the behaviour of the product is not found; so to overcome these gaps of information, computer-aided tools for property predictions (ProPred), solvent selection (CAMD), compound database (Database Manager) and simulation engines are applied to provide the missing data; all of these software suites are available in the Integrated Computer Aided Software (ICAS) developed by Computer Aided Process Engineering Center (CAPEC) DTU.

Once, the complete information and characteristics about the product have been chosen; simulations for analysis of product behaviour and performance are carried out. Here, modelling tools can assist in the simulation, generation of alternatives and verification of the formulation properties through the use of solvent selection tool (CAMD), and ICAS-MoT (available in ICAS software) that is a modelling tool able to perform the generation/analysis/simulation of mathematical models without extra programming effort.

Subsequently, simulation results of product behaviour is compared with the desired target and it is decided if the target has been matched; if it "No", new designs of the product are generated. Otherwise, simulations are made for model verification through the use of the modelling tool to verify if the product can be produced and the process.

Multiscale Modelling, what is it?

Multiscale modelling approach basically consists of the division of a complex problem/model into a set of sub-problems/models that are described at different scales on length or/and time, in order to improve the degree of details of the phenomena that the set of mathematical model is describing in product-process design.

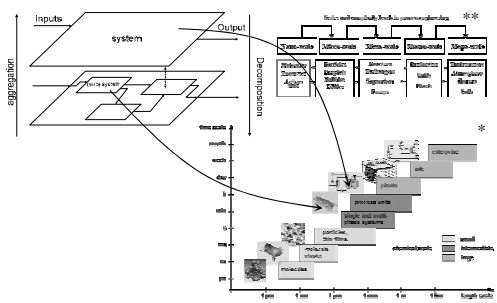

Figure 2. Multiscale modelling structure, chemical supply chain [1]*, scales and complexity levels in process engineering [2]*

Figure 2 illustrates the classical multiscale modelling structure, chemical supply chain and finally, the scales and levels in process engineering. This figure is useful to explain how multiscale modelling works; for example, block-system is depicting an unit operation at the meso-scale level (reactors, exchangers, separators, pumps and so on) what is described for a mathematical model and also provided results of the behaviour of the unit operation. Further details of some properties included in this unit are obtained if a connection between block-system and sub-system exist. This further description at the micro-scale level (particles, droplets, bubbles, eddies and so on) allow to get more fundamental knowledge with more details of the phenomena taking place at different scales.

Multiscale modelling example: DMFC

A flow-diagram for a Direct Methanol Fuel Cell (DMFC) modeled through the multiscale approach is shown in figure 3. It is possible to observe that two different scales are involved: meso-scale and micro-scale. The meso-scale involves the modelling of the anode and cathode compartments while the micro-scale is employed to model, the behaviour of the anode and cathode catalyst layers and the proton membrane exchange.

In order to highlight the differences between the results of the multiscale modelling and single-scale modelling, two scenarios have been chosen:

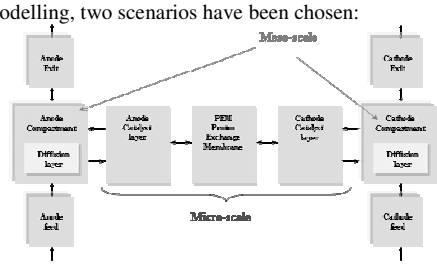

Figure 3. Multiscale Scheme for a DMFC.

For the multiscale modelling approach: the entire set of equations, for meso-scale and micro-scale were considered.

Table 1. DMFC multiscale model classification

Scale	Comp	Equation	
Level 3 (Meso-scale)	Anode compartment	$\frac{dc_{CH_3OH}}{dt}=\frac{1}{\tau}\left(c^{F}_{CH_3OH}-c_{CH_3OH}\right)-\frac{k^{LS}A^{S}}{V_a}\left(c_{CH_3OH}-c^{CL}_{CH_3OH}\right)$	(1)
		$\frac{dc_{CO_2}}{dt}=\frac{1}{\tau}\left(c^{FA}_{CO_2}-c_{CO_2}\right)-\frac{k^{LS}A^{S}}{V_a}\left(c_{CO_2}-c^{CL}_{CO_2}\right)$	(2)
Level 2 (micro-scale)	Anode Catalyst Layer	$\frac{dc^{CL}_{CH_3OH}}{dt}=\frac{k^{LS}A^{S}}{V^{CL}_a}\left(c_{CH_3OH}-c^{CL}_{CH_3OH}\right)-\frac{A^{S}}{V^{CL}_a}n^{M}_{CH_3OH}-\frac{A^{S}}{V^{CL}_a}r_1$	(3)
		$\frac{dc^{CL}_{CO_2}}{dt}=\frac{k^{LS}A^{S}}{V^{CL}_a}\left(c_{CO_2}-c^{CL}_{CO_2}\right)+\frac{A^{S}}{V^{CL}_a}r_1$	(4)
	Mem model	$\frac{\partial c^{M}_{CH_3OH}(t,z)}{\partial t}=-D^{M}\frac{\partial c^{M}_{CH_3OH}(t,z)}{\partial z}+vc^{M}_{CH_3OH}(t,z)$	(5)
	Anode Catalyst Layer	$\frac{d\eta_a}{dt}=\frac{1}{C_a}\left(-i_{cell}-6Fr_1\right)$	(6)
	Cathode Catalyst Layer	$\frac{d\eta_c}{dt}=\frac{1}{C_c}\left(-i_{cell}-6F\left(r_5\quad n^{M}_{CH_3OH}\right)\right)$	(7)
	Electrode kinetics	$r_1=k_1\exp\left(\frac{\alpha_1 F}{RT}\eta_a\right)\left\{\theta^{3}_{Pt}c^{CL}_{CH_3OH}-\frac{1}{K_1}\exp\left(-\frac{F}{RT}\eta_a\right)\theta_{Pt-COH}\right\}$	(8)
		$r_5=k_5\exp\left(\frac{\alpha_5 F}{RT}\eta_c\right)\left\{1-\exp\left(-\frac{F}{RT}\eta_c\right)\left(\frac{p_{O_2}}{p^{0}}\right)^{3/2}\right\}$	(9)

For the single-scale scenario: equations at the meso-scale level were solved while as far as micro-scale equations are concerned, values for the dependent and explicit variables values were given as known (that is, values at a specific point are known or obtained from experiment or simply as data from the literature). In this case study, the values for these variables were taken from the multiscale steady state simulation.

Methanol bulk concentration, which are variables at the meso-scale level were chosen to illustrate the different results obtained for each scenario. Figure 4 shows the bulk composition of methanol present in the fuel cell obtained with the mutiscale (MS) and Single-multiscale (S-MS) models. As it can be seen from figure 4, the values of these variables at the steady state are quite similar, but they are not the same for the transient state where some differences in the composition along the time can be noted. Those details are the extra information that can be obtained through the use of the multiscale modelling approach. Certainly, it is possible to add further details of the phenomena that is occurring in the process depending on whether the model for lower or higher scales are available or necessary for the study. The multiscale modelling framework is useful for the integration, connection and description at different scales, but the mathematical model to use will depend on the scenario and objectives of the model-based study.

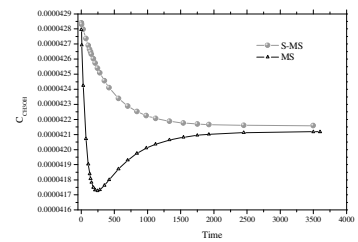

Figure 4. Bulk concentration of methanol

Interaction of Computational Tools

The combination of different computational tools in the development of the computer-aided multiscale product-centric process design framework is a very important issue for modelling (generation, analysis and solution), which is provided with varying levels of granularity (multiscale modelling) to enhance the prediction of the behaviour of the process under study.

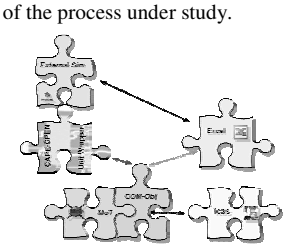

Figure 5. Integration of computational tools

The Model Test-bed (MoT) is an equation based modelling/simulation tool and allows the user to perform simulations of mathematical process models without having to write any source code. After the model equations have been successfully solved, the user has the option to generate a COM-object of the model to transfer and use it in an external software. On the other hand, the connection of these COM-Objects with external software or commercial simulator (such as ProSim) can be done through CAPE-OPEN standards (interfaces). Also, MoT-COM is able to interact with the ICAS simulation environment generating a new unit operation-model that can be used with other already available models and used with other ICAS features. Furthermore, some of the external simulators operating

with EXCEL at the same time can work with MoT-COM without additional work, provide a high-quality interaction between them (see figure 5) is available. But, *why do we need to use MoT together with other external software as a new modelling framework?* Because through their interaction, model equations for a specific equipment, process or operation can be developed, translated, analyzed and solved through MoT with almost zero programming effort with the multiscale modelling approach embedded in the final model equation.

CAPE-OPEN example

A test of the interoperability between ProSimPlus and ICAS-MoT has been carried out using CAPE-OPEN standards. A new unit operation (DMFC) model employing a multiscale modelling approach is combined with unit operations that can be found in the model library of ProSimPlus. The first step is to understand the interoperability between the different computational tools.

Figure 6 illustrates a "Generic CAPE-OPEN Unit Operation" where objects are wrapped by an ICAS-MoT object (COM object) representing a model generated through ICAS-MoT (a ICAS-MoT file) and where all the necessary interfaces for connection to other tools are CAPE-OPEN compliant. An XML configuration file describes the mapping between variables of the ICAS-MoT model and variables required by CAPE-OPEN specifications.

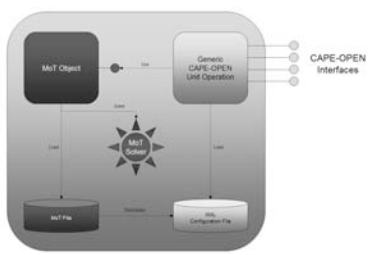

Figure 6. ICAS-MoT CAPE-OPEN Unit Operation

The input Material Objects must, at least, provide the following variables: temperature, pressure, composition (either total flowrate and molar fractions, either partial flowrates) through the COM interfaces. More generally, the wrapper will provide/ask to MoT Objects for each property is described in the XML configuration file. The values of the variables are obtained using the ICAS-MoT model and calculated by the ICAS-MoT Solver. As output Material Objects, the same variables should be described and returned together with the enthalpy of the stream.

The flowsheet shown in figure 7 illustrates a small part of the industrial production of methanol where this product is generated in the reactor by chemical reaction between carbon dioxide and hydrogen. The outstream of the reactor is composed of methanol, water (as the reaction products) and the reactants. This mixture is fed to a unit operation representing a membrane unit operation where pure methanol is obtained as the top and the mixture of the four compounds is located on the bottom. The top product is feed in the Generic CAPE-OPEN unit operation that is representing a DMFC unit operation and its mathematical model is generated and represented by ICAS-MoT file, producing a customized simulator/flowsheet for our process.

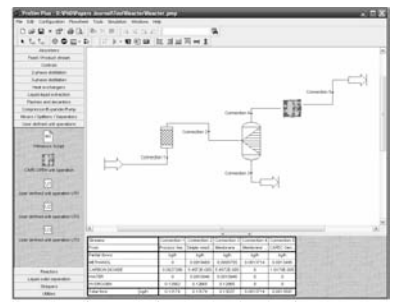

Figure 7. Flowsheet in ProSimPlus including the CAPE-OPEN unit operation using an ICAS-MoT model.

Current and Future Work

Further developments on the computer-aided multiscale product-process design framework will be carried out in terms of development of a friendly interface for users that are not so familiar with modelling tools. Work and data flows for process-product design implemented into de model-based framework. Case studies highlighting product-process design problems, including model generation and manipulation will be developed.

References

[1]. Grossmann, I.E., (2004) *Computers and Chemical Engineering*, 29, 29-39.

[2]. Charpentier, J.C., (2002) *Chemical Engineering Science*, 57, 4667-4690.

List of Publications

1. **Journals:**
   - R. Morales-Rodriguez, R. Gani, S. Déchelotte, A. Vacher, O. Baudouin, Chem Eng Res Des: part A. Submitted
2. **Conference Contributions:**
   - R. Morales-Rodriguez, A.M. Sales-Cruz, R. Gani, S. Déchelotte, A. Vacher, O. Baudouin, AIChE meeting (2006)
   - R. Morales-Rodriguez, R. Gani, CACE 24 (2007) 207-212
   - V. Soni. R. Morales-Rodriguez, E. Conte, R. Gani, AIChE meeting (2007)
   - R. Morales-Rodriguez, R. Gani, A. Vacher, P. Castelain, S. Dechelotte, AIChE meeting (2007)

Merlin Alvarado-Morales
Phone: +45 4525 2981
Fax: +45 4593 2906
E-mail: mal@kt.dtu.dk
WWW: http://capec.dtu.dk
Supervisors: Professor Rafiqul Gani
Professor John M. Woodley
Associate Professor Krist V. Gernaey

PhD Study
Started: April 2007
To be completed: March 2010

Process-Product Synthesis, Design and Analysis through a Group-Contribution Approach

Abstract
Modelling and simulation of a chemical process usually involve identifying the structure of the flowsheet representing the process, deriving model equations to represent each unit operation and solving the resulting total model equations according to one of various available simulation strategies. Recently, the group contribution (GC) concept used to represent a fraction of a molecule has been extended to represent a chemical process operation or a set of operations in a chemical process flowsheet. The core idea of this project is to develop simple, fast yet reliable methods for synthesis, design and analysis of various types of products and their corresponding processes related to the chemical, food and bio industries and extend the GC-concept to more complex process where enough systematic data may not always be found.

Introduction
Modelling and simulation of a process flowsheet usually involve identifying the structure of the flowsheet, deriving model equations to represent each operation, and solving the resulting total model equations according to one of various available simulation strategies. The flowsheet synthesis problem determines the type of operations and their sequence needed to achieve the conversion of raw materials to some specified set of products. The flowsheet design problem determines the optimal values for the conditions of operation and other operation/equipment related variables for the synthesized flowsheet. The flowsheet modelling, synthesis, and design problems are related since for generation and screening of alternatives, and for verification of the solutions of the synthesis/design problem, some flowsheet models are needed.
In contrast, a group-contribution (GC) based pure component property estimation of a molecule requires knowledge of the molecular structure and the groups needed to uniquely represent it. An example of such a method is the Marrero and Gani method [5] for pure component property estimation. The needed property is estimated from a set of *a priori* regressed contributions for the groups representing the molecule. Having the groups and their contributions together with a set of rules to combine the groups to represent any molecule therefore provides the possibility to predict properties of the molecule and/or a mixture of molecules. This also means that the reverse problem of property estimation, that is, the synthesis/design of molecules having desired properties can be solved by generating chemically feasible structures and testing for their properties. This reverse problem is also known as computer aided molecular design (CAMD) [2].
Any application of group contribution relies on availability of groups to describe the structure as well as tables giving the contributions of each group. Group contribution models are expressed as a linear combination of the group contributions of the groups:

$$f(p,C) = \sum_{i=1}^{N} n_i \times a_i \qquad (1)$$

Where p is the property to be predicted, N the total number of distinct groups in the molecular structure, n_i the number of each group i in the molecular structure, a_i the contribution of group i to the property p and C a constant. The group contribution a_i and the C are regressed parameters from experimental data.

Group contribution methods (GC), which provide the basis for molecule and mixture design, can also be applied in process synthesis/design. Recently, the group concept has been extended to represent a chemical process operation or a set of operations in a chemical process flowsheet [1]. The main idea behind this

approach is that each group used to represent a fraction of a molecule could also be used to represent an operation in a process flowsheet. In this way a set of process-groups representing different types of process operations (distillation, flash separation, absorption, solvent based azeotropic distillation, conversion reactor, etc) may be developed and the "properties" of a specified flowsheet may be estimated by first identifying the process-groups that will uniquely represent it and then by computing their contribution to the needed "property". Consequently, flowsheet synthesis/design problems can be solved through a CAMD-like approach, which can be adapted to computer aided flowsheet design (CAFD) [1]. It is important to keep in mind that the GC-concept by definition is predictive since the same groups used in the regression step can be used to represent other structures as well as to predict their behavior. Hence, the GC-concept is ideally suited to identify and analyze truly novel and innovative product-process design. The earlier work has established the GC-concept through proof of concept examples and processes from the chemical industry [1].

The process-group concept

To illustrate the process-group concept consider the simple process for the separation of a mixture of three components A, B, and C. for the process shown in figure 1. According to the framework developed in earlier work [1], the feed mixture is represented by inlet process-groups (groups with one attachment), such as, *i*ABC. The end products (also groups with one attachment) are outlet process-groups, such as, *o*A (a pure product or purity ≥ 98%) or *o*BC (a mixture of products). An intermediate-product (groups with two or more attachments) is a product from one unit operation that serves as the inlet stream for another unit operation, such as, (AB) or (BC). From the list of available process-groups like *i*ABCD; (A)(BC); (B)(C); *o*A, *o*B, etc., a feasible flowsheet structure can be created as shown in figure 1, where the mixture of three components is separated into pure components through two separation operations (A)(BC) and (B)(C).

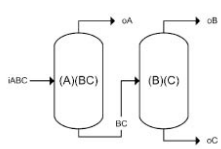

Figure1: Simplified process-group flowsheet representation [1].

Having the process flowsheet represented by a set of process groups, the next step is to predict some characteristic properties of the flowsheets in order to identify the optimal flowsheet according to a performance criteria (energy consumption, environmental impact, etc). Recently a property model has been developed to predict the energy consumption of a unit operation (in this case, any distillation column with one feed stream and two product stream) given the process-groups representing the distillation column, the driving force (related to the key compounds), and the group contribution [1].

$$E = \sum_{k=1}^{NG} \left(\frac{1 + p_k}{d_{ij}^k} a_k + A \right) \qquad (2)$$

Where, E is the energy consumption of the flowsheet (MkJ/h), NG is the number of process-groups, d_{ij}^k the maximum driving force of the process group k, a_k the contribution of the process-group k, A a constant and p_k, the topology factor.

The earlier work has established the process-group concept for distillation operations, mainly, providing rules for process-groups representation of flowsheets, a property model for separation process flowsheets, and a reverse-approach based method for flowsheet synthesis/design [1]. However, the method can be seen as an integrator since by adding new process-groups it is possible to simultaneously model, design, and synthesize products and processes that can produce them. Therefore, the scope and significance of this method is potentially very large, on one hand if a large and reliable set of process operations and atomic groups representing a wide range of process-product types can be developed, and on the other hand to develop more property models for the process groups and the representation of complex unit operations. This will require a good understanding of the processing steps involved in transforming the raw materials to a finished chemical (including bio and food) product; analysis of the behavior of the process under different conditions of operation (so that GC-based behavior models can be developed); collection, evaluation, and use of available product-process data to define the groups and to regress their contributions, and finally algorithms to synthesize, design and analyze molecular as well as process-flowsheet structures through the developed groups (using the CAMD technique).

Specific objectives

The main objective of this PhD project is to develop simple, fast yet reliable methods for synthesis, design and analysis of various types of products and their corresponding processes related to the chemical, food and bio industries using the GC-concept and extend it to synthesis, design and analysis of processes where enough data or information may not always be available.

The applicability of the developed methods and tools will be highlighted through a set of case studies from the food and bio industries, mainly. In particular as a first study case, the biorefinery concept for production of lactic acid, 1, 3-propandiol, succinic acid and ethanol,

is being studied in order to generate and test all possible sustainable design alternatives.

Product-process analysis: biorefinery

Considering the concept of biorefinery –a facility that integrates biomass conversion processes and equipments to produce chemicals, fuels and power –the four chemical products mentioned above can be identified from multiple products that are commonly attributed to a biorefinery. A biorefinery might, for instance, produce one or several low-volume, but high-value, chemical products and low-value, but high-volume products such as intermediate chemicals and/or liquid transportation fuel, while generating electricity and process heat for its own use. The high-value products enhance profitability while the high-volume products may also enhance the profitability by producing other high value chemicals in the product supply chain, or, as fuel to help to meet the energy needs of the society and industry. Also, the power production reduces over-all production costs and avoids greenhouse-gas emissions. Based on this, four chemicals products (as listed in table 1) have been selected.

Results and discussion

The first step is to evaluate a base case design and define the targets for generation of more sustainable alternatives. Figure 2 shows a simplified version of the flowsheet for the conversion of corn as the raw material to produce the four chemicals listed in table 1. Figure 1 also shows the results of the mass balance based on the amount of products obtained per kilogram of corn and the amount of water used in the principle processing steps using collected data from open literature. Based on this mass balance and an added energy balance, a cost analysis for the four products biorefinery has been performed. The results are summarized in table 1. It can be noted that three high value products have an acceptable rate of return while the low value product is not economically feasible for the production rates listed in table 1. This means that the targets for more sustainable design alternatives should be focused on production of ethanol for this biorefinery. From figure 2 it can be seen that economic feasibility of the process for ethanol can be improved through higher product yields and/or more efficient product recovery.

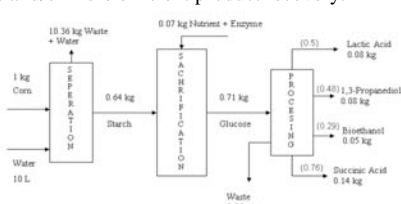

Figure 2: Simplified flowsheet for the production of bio-based chemicals from corn.

As the next step from this analysis we have considered alternative product recovery strategies for ethanol and succinic acid (to identify another alternative to crystallization for product recovery).

From an analysis of the succinic acid-water binary mixture using the driving force concept [3], it is clear that solvent based separation is an option worth considering, for example liquid-liquid extraction (LLE). ProCAMD [2] has been used to find the solvents for LLE of succinic acid from water. Figure 3 shows the LLE driving force diagram for succinic acid-water-solvent (butyl acetate and propyl acetate) on a solvent free basis. From figure 3, it can be seen that between the two solvents that have been identified, butyl acetate is better as it provides a larger driving force.

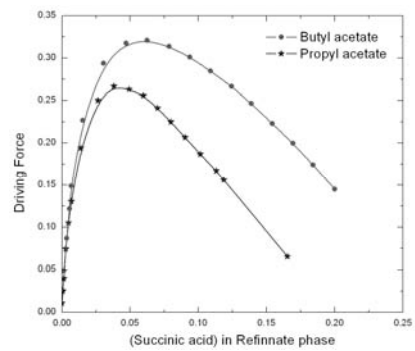

Figure 3: Solvent-free driving force curves for succinic acid-water mixture based on LLE.

For the case of ethanol purification, we are highlighting the process with lignocellulose as the raw material (see bottom row of table 1).

Table 1: Cost analysis of four products biorefinery; (1) production rate, (2) profit, (3) payback-time, (4) sell price, (†) from corn, and (‡) from lignocellulose.

Product	kg/h[(1)]	$/kg[(2)]	yr[(3)]	$/kg[(4)]
Lactic acid	1271.23	0.042	6	1.10
1, 3-propandiol	1256.76	0.058	4.1	1.34
Succinic acid	1226.67	0.043	7.4	1.10
Ethanol†	1135.25	0.019	11.6	0.75
Ethanol‡	18857	-0.166	-	0.75

Here also we can use the driving force concept [3] to investigate the different separation techniques. From figure 4 it can be seen that it is impossible to obtain anhydrous ethanol in a single distillation column (curve 1). Therefore, solvent-based or hybrid separation process are necessary. By solvent-based distillation using ethylene-glycol (curve 2) or ionic liquid (curve 4), it is possible to achieve the desired purity. Distillation followed by pervaporation (curves 1 and 3) is also a feasible separation process. A saving in overall heat duty of 24% can be achieved by using ionic liquid (curve 4) compared with the organic solvent-based

separation which uses ethylene-glycol (curve 2) [4]. This can be very quickly verified through the driving force based process group contribution [1]. From table 1, it can be seen that the ethanol from lignocellulosic biomass has a negative profit value. However, with the ionic liquid based distillation process, an improvement to the profit (-0.099 $/kg) can be achieved. This however is still not enough to produce a positive profit, indicating there are costs related to pretreatment and water use that also need to be targeted.

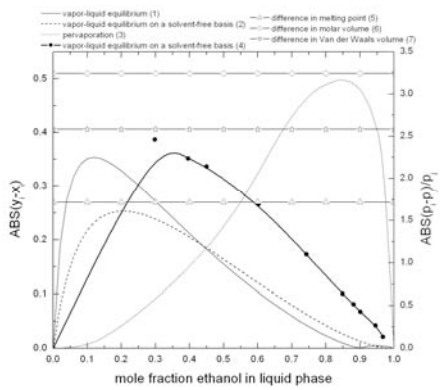

Figure 4: Curves for driving force as a function of composition (curves 1-4) and as constants (curves 5-7) for ethanol-water mixture.

Conclusions

From the above analysis, it is clear that applying solvent-based liquid-liquid extraction for recovery of succinic acid and ionic liquid based ethanol purification will lead to lower operating costs without increasing the environmental impact. In addition, the use of resources would be improved through better and more efficient solvents. Thus, these alternatives will improve sustainability metrics related to waste, environmental impact and economics. The final optimal design, however, is not possible to obtain until the production rates for each of the four products are simultaneously optimized. Note that as listed in table 1, the production rate of ethanol is not particularly high, due to imposed constrains on the availability of biomass as the raw material.

The next step in the project will be to apply the GC-concept to identify the better alternatives for ethanol recovery. For example, among the feasible alternatives to achieve the target (ethanol with a concentration ≥ 99.5 wt %) solvent based azeotropic separation process group can be used, which represents the separation of an azeotropic mixture with a solvent. According to the property dependence of this process group, the solvent free maximum driving force between the two components to be separated should be within the driving force range of the solvent based azeotropic separation. This implies the availability of an adequate solvent for the separation of the mixture [1]. According to initialization procedure for this process group, two cases are possible. Both the binary mixture and the corresponding solvent are known and matching the property dependence or the binary mixture is matching the property dependence but a corresponding solvent is not known. For the first case, the solvent based separation process group is initialized with the binary mixture and the solvent to determine the energy index (eq. 2). For the second case, as no solvent is known, the following procedure is applied to find a matching solvent. First a database search is performed to look for a potential solvent. If no solvent is found, a CAMD problem formulation is setup with the targets being to match the solvent free driving force. If more than one potential solvent is found, some constraints can be imposed to select the best solvent. Finally, having identified the appropriate solvent, the process group is initialized as the first case. The work of this project is currently at this stage. However, as the analysis of the mixture shows the solvent based azeotropic separation is a feasible alternative but others feasible alternatives can also be generated.

Acknowledgements

The author acknowledges the financial support of the Technical University of Denmark.

References

[1] L. d' Anterroches. Process Flow Sheet Generation & Design through a Group Contribution Approach, PhD Thesis, Technical University of Denmark, 2005.

[2] P. M. Harper, R. Gani, Computers and Chemical Engineering 24 (2-7) (2000) 677-683.

[3] R. Gani, E. Bek-Pedersen, American Institute of Chemical Engineers Journal 46 (6) (2000) 1271-1274.

[4] M. Seiler, C. Jork, A. Kavarnou, W. Arlt, R. Hirsch, American Institute of Chemical Engineers Journal 50 (10) (2004) 2439-2454.

[5] J. Marrero, R. Gani, Fluid Phase Equilibria 50 (183-184) (2001) 183-208.

List of Publications

[1] M. Alvarado-Morales, N. Al-Haque, K. V. Gernaey, J. M. Woodley, R. Gani, ESCAPE 18, CAPE Methods and Tools for Systemathic Analysis of New Chemical Product Design and Development, Lyon, France, 2008 (to be presented).

Martin Nordvig Mortensen
Phone: +45 4525 6819
Fax: +45 4588 2161
E-mail: mnm@kt.dtu.dk
WWW: http://www.polymers.dk
Supervisors: Søren Hvilsted
Jens Glastrup, the Danish National Museum

Ph.D. Study
Started: June 2005
To be completed: May 2008

Stabilisation of Polyethylene Glycol in Archaeological Wood

Abstract
Formic acid is a product of polyethylene glycol (PEG) degradation and it has been detected in PEG treated wooden archaeological objects. A procedure for isolating formic acid from such samples has been devised in order to measure its ^{14}C content. This can reveal the origin of the formic acid since PEG and wood have different ^{14}C signatures in this specific case. The recovery of in procedure is decent, and it is specific for formic acid. However, a ^{14}C contamination is causing problems.

Introduction
It is normal to impregnate waterlogged wooden archaeological objects with polyethylene glycol (PEG) after salvage. This is done to prevent the wood from cracking and shrinking when dried. PEG has proven useful for this purpose many times, a few examples include the Vasa (SE), the Hjortspring boat (DK), the Batavia (AU), the Skuldelev ships (DK) and the Bremen cog (D), which are all PEG treated wooden shipwrecks on exhibition today. During re-conservation of the Hjortspring boat, indications that PEG had degraded in the wood were observed [1]. This caused concern that PEG degradation could be taking place in other objects that have received a similar impregnation. If this turns out to be the case, many important objects around the world will be affected.

It is well established that PEG itself degrades at highly elevated temperatures, in the presence of air [2-8]. At lower temperatures (70 °C) the oxidative degradation of tetraethylene glycol, a PEG model molecule, led to the formation of formic acid and formate esters of mono-, di-, tri-, and tetraethyleneglycols that were also produced during the degradation [9]. Thus formic acid and shortened PEG chains should be in the wood if PEG degradation takes place. Shortened PEG chains were observed in a sample from the Skuldelev 2 Viking ship using Matrix Assisted Laser Desorption Ionization-Time of Flight Mass Spectrometry (MALDI-ToF MS) [10]. The presence of formic acid in a large series of PEG impregnated wooden archaeological objects including the Vasa and the Skuldelev ships, were also established using Solid Phase Micro Extraction - Gas Chromatograpy Mass Spectrometry (SPME-GC MS). The samples contained a little less than 1 $^{0}/_{00}$ formic acid by weight [11]. With this information it is our intention to devise a method that allows the distinction between formic acid produced by PEG degradation and formic acid produced naturally in archaeological wood. These ideas are based on the different ^{14}C contents of PEG, which is ^{14}C depleted, and formic acid from the wood components of the Vasa, which contains ^{14}C.

Specific Objectives
It is the aim to characterize PEG and possible PEG degradation products in the Vasa and in other PEG treated artefacts using appropriate analytical techniques. Based on this information a method that can show if PEG degrades or not, should be devised. If degradation is taking place then ways of inhibiting the process should be investigated.

Results and Discussion
In order to measure the ^{14}C content of formic acid in the Vasa, formic acid must be isolated. A procedure has been developed for this. An aqueous extract of the sample is prepared. The extract is vacuum distilled (VD1) at app. 0 °C, formic acid is collected at -196 °C. The distillate is passed through an anionexchange column (IE) to isolate formate. To remove the chemicals added in the ionexchange procedure a second vacuum distillation is performed (VD2). After this the formic acid is oxidized to carbon dioxide (OX) in a

specific reaction [12]. The carbon dioxide is collected for ^{14}C measurement by Accelerator Mass Spectrometry (AMS).

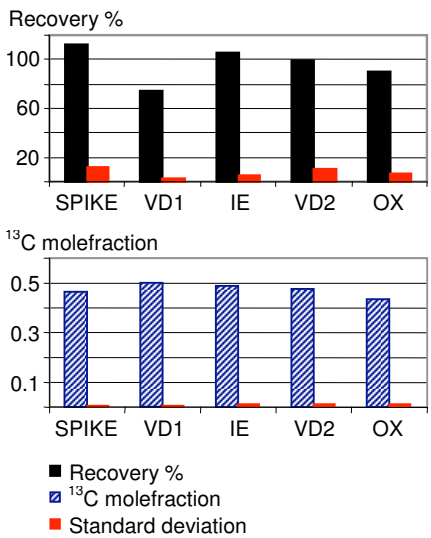

Figure 1. Top: Black columns represent the recovery (average over three samples). The recovery is shown for the four steps in the purification; first vacuum distillation (VD1), ion exchange (IE), second vacuum distillation (VD2) and oxidation to CO_2 (OX), SPIKE is the name of the initial formic acid solutions. Bottom: blue columns (hatched) represent ^{13}C molefractions in the purification steps (average over three samples). The standard deviation is shown as red columns.

As seen from figure 1 top, the recovery is close to 100% in the four steps (VD1, IE, VD2 and OX) when a solution of formic acid (called SPIKE) is processed. In the bottom of figure 1, another experiment is illustrated. The stable isotope $D^{13}COONa$ was added to an aqueous extract of a Vasa sample, already containing natural $H^{12}COOH$. The ^{13}C isotope was added in an amount equal to that of the ^{12}C formic acid already present in the solution. The resulting solution (called SPIKE) was processed and the ^{13}C molefraction measured after each step by GC MS. It is seen that this number changes very little over the purification steps. If compounds other than formic acid ended up in the purified sample as CO_2, it would be as $^{12}CO_2$ (the natural isotope) thus lowering the ^{13}C molefraction. However this is not the case, it can thus be concluded that the procedure for isolating formic acid is specific for formic acid.

The first real sample from the Vasa has been processed. The ^{14}C result from AMS measurement shows a much higher ^{14}C level than possible with natural isotopes. This means that the laboratory facilities or the chemicals used in the purification process are contaminated with an artificial isotope, enriched in ^{14}C. Current efforts focus on identifying the source of the ^{14}C contamination, since no useful information can come from analysing contaminated samples.

Conclusions

A procedure for isolating formic acid from PEG treated archaeological wood has been devised in order to measure ^{14}C in this formic acid. The recovery in the procedure is decent and it is specific for formic acid. However, a ^{14}C contamination somewhere in the laboratory or chemicals used, is hampering the analysis.

Acknowledgements

This project is funded by the National Maritime Museums of Sweden research project “Save the VASA” sponsored by The Bank of Sweden Tercentenary Foundation, The Swedish National Heritage Board, The Swedish Foundation for Strategic Research (SSF), The Swedish Research Council for Environment, Agricultural Sciences and Spatial Planning (FORMAS), and The Swedish Agency for Innovation Systems (Vinnova). The Danish Ministry of Culture and the Danish National Museum are also kindly acknowledged for funding.

References

1. T. Padfield, J. Winsløw, W. B. Pedersen, J. Glastrup, in: 9th Triennial Meeting Dresden, German Democratic Republic 26-31 August 1990, ICOM Committee for Conservation, Los Angeles, (1990) 243-245.
2. J. Glastrup, Polym. Degrad. Stabil., 52 (1996) 217-222.
3. A. D. Dale, M. B. Evans, J. Chromatogr., 552 (1991) 161-167.
4. L. Costa, A. M. Gad, G. Camino, G. G. Cameron, M. Y. Qureshi, Macromolecules, 25 (1992) 5512-5518.
5. S. Morlat, J.-L. Gardette, Polymer, 42 (2001) 6071-6079.
6. L. Yang, F. Heatley, T. G. Blease, R. I. G. Thompson, Eur. Polym. J., 32 (1996) 535-547.
7. O. A. Mkhatresh, F. Heatley, Macromol. Chem. Phys., 203 (2002) 2273-2280.
8. O. A. Mkhatresh, F. Heatley, Polym. Int., 53 (2004) 1336-1342.
9. M. N. Mortensen, Graduate Schools Yearbook, (2005) 139-141.
10. M. N. Mortensen, H. Egsgaard, S. Hvilsted, Y. Shashoua, J. Glastrup, Journal of Archaeological Science, 34(8) (2007) 1211-1218.
11. J. Glastrup, Y. Shashoua, H. Egsgaard, M. N. Mortensen, Holzforschung, 60(3) (2006) 259-264.
12. M. Glasius, S. Wessel, C. S. Christensen, J. K. Jacobsen, H. E. Jorgensen, K. C. Klitgaard, L. Petersen, J. K. Rasmussen, T. S. Hansen, C. Lohse, E. Boaretto and J. Heinemeier. Atmospheric Environment, 34(15) (2000) 2471-2479.

Hanne Hostrup Nielsen
Phone: +45 4525 2838
Fax: +45 4525 2258
E-mail: hhn@kt.dtu.dk
WWW: www.kt.dtu.dk/Centre/CHEC
Supervisors: Peter Glarborg
Stefan Mayer, MAN Diesel A/S
Sønnik Clausen, Forskningscenter RISØ

Industrial Ph.D. Study
Started: March 2006
To be completed: February 2009

In-Situ Investigations of the Combustion in Large, Two-Stroke, Diesel Engines

Abstract
Due to restrictions on the emission levels from marine engines, MAN Diesel A/S is conducting thorough research in areas connected with combustion optimization and emission reduction. An important tool in the combustion investigations is numerical analysis of the various combustion phases, but a lack of reliable experimental data provides an obstacle in validation and optimization of the developed code. For years, various optical analysis methods have been applied for investigations of the combustion in smaller engines, but due to the more restricted access, extremely sooting combustion, and very high pressures, similar investigations have not been undertaken at larger engines under realistic combustion conditions.
This project considers optical in-situ investigations on a large, two-stroke Diesel engine. The aims of the investigations are to provide experimental data for the combustion under realistic running conditions and to use these data for validation and optimization of an existing CFD-code.

Introduction
Large, marine engines are responsible for approximately 2 % of the total world fuel consumption, and many of these engines are two-stroke Diesel engines. Strong restrictions are expected to be imposed on the industry in near future, thereby forcing the leading engine manufactures to focus further on emission reduction and engine performance optimization in general.
The costs of performing physical tests on marine engines are very large, which makes numerical analysis a natural choice. Obviously, some tests are necessary for validation of the numerical codes, and the developments in optical methods within the areas of measurements of complex flows make these a natural choice. These methods have been used for several years in smaller engines, though the transient characters of the combustion and the large and fast variations in pressure and temperature have provided several challenges in the design of both optical accesses and experimental equipment.
Unfortunately, the results obtained on smaller engines cannot be scaled up to the conditions present in the larger engines. This is mainly due to large difference in both length and time scale of the engine processes and the use of different types of fuel.

Specific Objectives
The aim of the present Industrial Ph.D.- project is to develop an optical access to the Test Diesel engine located in the Test Centre at MAN Diesel A/S in Copenhagen, and with this to provide experimental data from the Diesel combustion for validation and optimization of the in-house developed numerical models.
As opposed to many of the investigations undertaken so far, this project focuses on in-situ measurements under realistic conditions, thereby enabling validations of local character for actual marine engines.

Diesel combustion and light emission
The combustion cycle in a two-stroke, marine Diesel engine is complex and consists of several different stages. The following paragraph will give a very short introduction to these, in order to demonstrate the many different aspects of the Diesel combustion.
During the compression of the last parts of the scavenging air from the former cycle, the Diesel fuel is sprayed into the combustion chamber at a high pressure. Subsequent further compression and swirling motion of the scavenging air ensures that fuel and oxygen is mixed which causes the ignition processes to proceed.
The fuel and air mixture often ignites several different places in the combustion chamber more or less at the

same time, and spreads quite fast to the remaining parts. During this premixed, turbulent combustion, more fuel is still being injected into the combustion chamber. The vaporized parts of this spray now ignite, causing a turbulent, non-premixed, diffusion flame. When the injection is stopped, the last parts of the spray is mixed with air and finally burned out. Subsequent scavenging with air removes the combustion gases from the cylinder.

The dynamic and complex manner of the Diesel combustion illustrates the troubles encountered when trying to either control the formation of unwanted components or describing it numerically. It also emphasizes the possible shortcomings of the data obtained from simplified laboratory equipment or ideal reference fuels, and hence confirms the need for reliable data recorded at real engines under realistic conditions.

Optical investigations in engines

The predominant method for optical investigations of the combustion in engines is by use of a special designed laboratory 1-cylinder engine constructed with large parts of the cylinder walls made of a transparent material. Due to the very large heat stresses in the larger engines, this approach is impossible. Alternatively, an endoscope can be used for looking into a more limited space of the engine. Using endoscopy enables using all ready existing openings in the engine, but also limits the view of the combustion chamber, when comparing to ideal laboratory cylinders. This can though partially be solved by the wide range of industrial endoscopes available today, allowing for various directions and angles of view. Further, using existing openings, the modifications of the engine from the standard set-up are minimized, thereby providing experimental data obtained under as realistic conditions as possible.

Due to the large air excess values, the final engine out emissions of soot in heavy marine engines is quite low, especially when comparing to smaller Diesel engines. During the diffusion limited combustion, the conditions though favour an intense soot production, thereby providing considerable amounts of light end enabling optical investigations without external light sources.

Also other light emissions from the other combustion reactions might be of interest, for example those leading to ignition of the fuel. With the increased focus on the formation of pollutants on combustion, the chemistry of all of the reactions going on during a combustion cycle are being investigated, in order to understand the complicated interactions between fuel spray, gas phase components and the turbulent environment in the cylinder.

Production of components like OH-radicals, formaldehyde and C_2H_2 can be investigated by combining spectroscopic techniques with the developed optical accesses. These components are of specific importance when looking into the chemical reactions between the vaporised fuel and air, leading to the auto ignition of the fuel. Further, the position of OH-radicals in the combustion chamber gives valuable information on the spread of the turbulent Diesel diffusion flame [1, 2, 3 and 4].

There are though a number of practical concerns to take into account, mainly due to the severe soot luminosity, which is many orders of magnitude larger than the chemiluminescence of these minor species.

Experimental set-up

The investigations are undertaken at the MAN Diesel Test engine in Copenhagen. This is a real engine run under realistic conditions, but also heavily equipped for various experiments. In Table 1, a few data for the test engine can be found

Table 1: A few characteristic data for the MAN Diesel test engine used for investigations.

Characteristic	Data
Engine type	Diesel, 2-stoke
No. of cylinders	4
Cylinder diam. [cm]	50
Stroke [cm]	220
Power [MW]	~ 8
Power [hp]	~ 10.000
Max. speed [rpm]	123
Max. gas temp. [°C]	~ 2400
Max pressure [bar]	~ 190
Air excess ratio [-]	~ 2

Simply establishing a useful and reliable optical access to an engine like this is rather troublesome, due to the very harsh environment inside the engine cylinder during the combustion cycle.

Challenges includes the fast, swirling flame, the high pressures, high temperatures, heavily sooting combustion, harsh chemical environment (caused by the heavy fuel oil), turbulence and large temporal and spatial gradients in many of the factors of interest.

Further, having to work with a real engine and trying to keep the modifications of the engine to a minimum induces stringent limitations on the possibilities for optical access. It has hence been determined to use existing openings in a manner that still allows for running the engine under realistic conditions. This means using valves which normally has another function, and inserting a window in the part that penetrates into the combustion chamber. Obviously, these valves will not be able to perform their normal function during operation, so selection must be made carefully.

Two different accesses have been developed to permit optical investigations of the combustion scenarios in the 4T50ME-X test engine at MAN Diesel in Copenhagen. One uses existing openings for fuel injection (fuel dummy valve) and the other type uses the entrance for the starting air (air dummy valve). An example of the position of the two types of dummy valves can be seen in Figure 1.

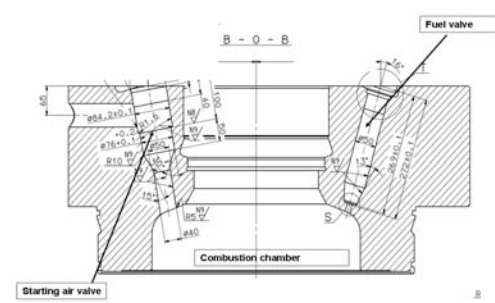

Figure 1: *Sketch of the positions of the two original valves in the engine cylinder. The two optical accesses are based on equipping dummy valves with a sapphire window in the bottom, thereby giving visual access to the inside of the cylinder during combustion.*

It should be noted that the test engine has a total of 4 fuel injection valves (three which cannot be seen in Figure 1), but only uses to or three when running under normal conditions. This means that a variety of different viewing positions are possible, without modifying the combustion conditions.

Results and discussion

With the objectives of the project in mind, the results of the project also include the entire development of the optical accesses to the test engine.

The mounting of the sapphire window in the dummy valve has taken some effort. Tests of several different designs have clearly revealed that the sapphire window is exposed directly to the Diesel flames, and the extend of the influence from this on the materials.

It has proven significantly troublesome to be able to mount the sapphire windows in a way, which fulfils all demands for views into the combustion chamber without cracking the sapphire. Sapphire is a very brittle material, but still regarded the most suitable for the application, as it has a very high resistance against thermal and chemical attacks, and, most important, is one of the world's hardest materials, thus making it tolerant to the very high pressures in the combustion chamber.

When the sapphire is mounted too loose, it will be blown out by the massive pressure in the combustion chamber. Oppositely, a too fierce mounting will cause internal stresses in the material, eventually leading to cracks. This was especially observed in connection with large temperature gradients across the window thickness. Unfortunately, large temperature variations are unavoidable, both because internal cooling is needed for protection of equipment inside the valve, but also because the entire tip of the valve is subject to uneven heating from the Diesel combustion.

Through tests of a number of prototypes, a method with a mechanical fastening of the window has been developed an proved functional.

In the following, the two different optical accesses developed so far will be presented, along with some of the initial experiences gained from these.

Fuel dummy valve

One of the developed optical accesses use a dummy fuel valve (a fuel atomizer) with a small sapphire window and one or more optical fibres connected to a photo multiplier.

The advantage of this equipment is its simplicity, along with the fact that the test engine has four different positions for fuel atomisers, thereby potentially giving view to several different parts of the combustion chamber.

The draw backs include the limitations in both the view of the optical fibre and the quality of data obtainable with a single optical fibre. Further, the positions of the fuel valves is the test engines causes the sapphire window to be rather exposed to both fuel spray and the diffusion flame, thereby inducing need for a robust mounting of the sapphire window in order to avoid cracks.

Soot luminosity tests with fuel dummy valve

The developed fuel dummy has initially been used for ignition delay measurements and cycle-to-cycle variations in the soot luminosity.

Soot particles at the temperatures encountered during the Diesel combustion will emit light at wavelengths from the UV through the visible regime, and it is reported that soot is formed almost immediately after onset of the combustion [1]. Registration of light from the combustion chamber has therefore been assumed reliable as a qualitative representation of the combustion ignition, and especially for comparing cycle-to-cycle behaviour of the emitted light of for example 100 cycles, sees Figure 2.

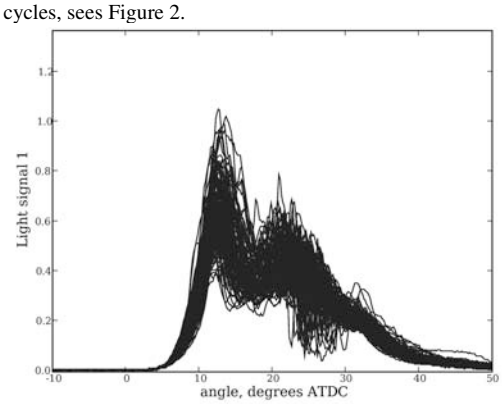

Figure 2 : Example of light signal from soot emission, recorded with an optical fiber through a dummy fuel injection valve equipped with a sapphire window. The light signal is given in arbitrary units as a function of number of crank angles after top dead centre (ATDC).

Signals were collected over 100 combustion cycles with the test engine running at maximum load.

The data have been collected over 100 combustion cycles with a 1 mm diameter quartz fibre. The head of the fibre has been polished to collect light from as large an angle of view as possible (approx. 30° around the centre line of sight). Before entering the photo multiplier, the light is filtered with a UV-filter, in order to both protect the equipment from the very intense radiation and to focus on the wavelengths dominating the ignition of the fuel, i.e. emission from for example OH-radicals.
It can be noted that the initiation of the light signal is rather constant, and good overall qualitative agreement between the light emission behaviour in each cycle can be observed.

Future aspects includes IR-fibre optic investigations and usage of special filters to separate few wave lengths characteristic for given components, or possibly applying a spectrometer.

Air dummy valve
The second optical access is through the larger air valve, also with a sapphire window mounted. The design of the larger optical access is based on the experiences gained from the smaller fuel dummy, and is at the final development stages.
As the engine can be started with starting air valves in just three of the four cylinders, using this for optical access will mean a minimum of modification of the engine and thus provide data of very realistic character.
A model of the dummy starting air valve can be seen in Figure 3.

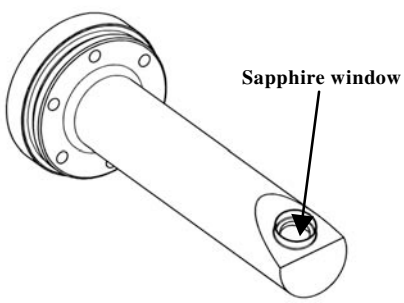

Figure 3: Sketch of the dummy valve to be used in stead of the starting air valve shown in Figure 1. The lower part of the dummy valve will be sticking into the combustion chamber, with the sapphire wondow directed toward the cylinder centre.

The two dummy valves mainly differ in size, as the air dummy valve has room for more equipment, like an endoscope. Having more room also allows for a larger window, thereby enabling detection of less intense light sources. Finally, having an opening large enough for endoscopy and usage of a camera naturally also gives the opportunity for 2-dimensional imaging of the combustion scenario. Future possible applications also includes 2D-IR-imaging with a high speed infra red camera. Natural IR-emissions of components like CO, CO_2 and H_2O can give valuable information on the extend of combustion and efficiency of the scavenging processes.
As can be seen, the window is positioned on the side of the valve, which will allow for views into the centre of the combustion chamber. This differs from the 0° directionality often applied in other optical accessible engines, simply providing a view of the top of the piston. The 70° directionality integrated in this dummy valve is meant to give important observations on for example the nature of the Diesel auto ignition and the flame spread.
The inside of the dummy air valve have been carefully designed to allow room for an endoscope with a corresponding 70° directionality, along with filters, means of mounting both endoscope and camera securely and finally cooling air.
Initial functionality tests are planned to be undertaken in December 2007.

Acknowledgements
This project is funded by MAN Diesel A/S and The Danish Ministry of Science, Technology and Innovation.

References

1. J.E. Dec, C. Esprey, SAE Technical Paper Series 982685 (1998) 1-25.
2. C. Antoni, N. Peters, SAE Technical Paper Series 972917 (1997) 145-155.
3. M. Costa, B.M. Vaglieco, F.E, Corcione, Experiments in Fluids 39 (2005) 512-524.
4. S. Singh, R.D. Reitz, M.P.B. Musculus, T. Lachaux, Combust. Sci. and Tech. 179 (2007) 2381-2414 .

Rudi Pankratz Nielsen
Phone: +45 2210 2522
Fax: +45 8830 3211
E-mail: rpn@scf-technologies.com
WWW:
Supervisors: Kaj Thomsen
Nicolas von Solms
Steen B. Iversen, SCF Technologies A/S
Erik G. Søgaard, Aalborg University

Industrial Ph.D. Study
Started: May 2006
To be completed: April 2009

Analysis of the Physical Chemistry of the CatLiq® Process

Abstract
With increased focus on CO_2 emissions from fossil fuels the interest in biofuels has increased in the last decade. The CatLiq® process is a method for catalytic conversion of biomass to biofuel such as biodiesel. It is intended to optimize the process to achieve a standard conforming bio-crude oil product, but also modeling of the process is a main focus. To model the process both thermodynamics as well as experimental work is required to achieve a thorough understanding of the process and effect of parameters.

Introduction
There are several methods for conversion of biomass today, the most notable being hydrothermal upgrading, supercritical water gasification and transesterfication [1] [2]. The CatLiq® technology is an alternative to these types of biomass conversion and the focus of this industrial Ph.D. project.

The CatLiq® technology is a 2nd generation technology for production of biofuels from a biomass feedstock. The process can basically be described with 2 steps, one is a catalytic conversion of the biomass feedstock, and the second a separation step where the various components of the product stream are separated into several groups. This is illustrated in figure 1.

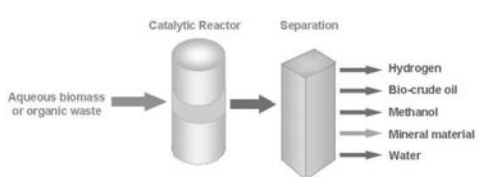

Fig. 1. Principle of the CatLiq® process.

The process operates at near-critical conditions in aqueous solution. During processing both heterogeneous and homogeneous catalysts are utilized to achieve conversion.

Specific Objectives
The specific objectives of the Ph.D. study may be summarized as the following points.

Development of thermodynamic models
Analysis of experimental results
Fitting of parameters to the models
Development of statistical models for the process

There will be made two thermodynamic models, one focusing on determining whether or not salts will precipitate at process conditions, while the other will be a multiphase flash routine to determine phase separations and composition. Due to the complex nature of the feedstock as well as product stream these will be modeled using a lumping method. This means that instead of the individual components groups of components will be modeled by use of a pseudo-component.

The model for precipitation of salts will be based on the extended Debye-Hückel equation which is given as equation 1.

$$\ln \gamma_i^m = \ln x_w - Z_i^2 \frac{AI^{0.5}}{1 + BaI^{0.5}}$$

With

γ_i^m: molal activity coefficient of species i,
x_w: mole fraction of water
Z_i: charge of species i
A: temperature and pressure dependent factor
I: ionic strength
Ba: factor normally set to 1.5 in most cases.

The multiphase flash routine will be based on cubic equations of state such as Soave-Redlich-Kwong or Peng-Robinson. The reason to use a cubic equation of state and not more advanced equations of state such as Statistical Associating Fluid Theory, which has been shown by Feng et. al. [3][4] to work for high temperature and high pressure conversion processes, is that the complexity of the feed and product streams will require very extensive parameter estimation from experimental data. The objective of this model is to give an estimate of the number of phases and the composition of these phases to use in process control/design.

The parameters has to be fitted to experimental data, which will be collected from a pilot scale plant to ensure that the data are as consistent with actual process conditions as possible. To use data from a pilot scale plant compared to doing experimental work on a laboratory scale is that the issues of scaling are removed as there would most likely be some differences between a laboratory setup and the actual process plant.

Besides the thermodynamic models statistical models will be developed to describe the effect of process parameters on the product. These models will form a basis for optimization tools to be used for process control.

Results and Discussion

Currently the thermodynamic models are being developed and the model for precipitation to be evaluated against data from literature in the coming period. To acquire experimental VLE data from the pilot scale plant some modifications are necessary which means that the models will not be tested against this type of data until such modifications have been made.

Still as the plant is operational the product streams can be analyzed to determine the major components of the streams, which is to be used when determining the pseudo-components to be used in the multiphase flash routine.

Conclusions

The CatLiq® technology is a 2nd generation technology for conversion of biomass into biofuels. This Ph.D. project is focused on modeling the process to obtain tools for process design and control.

Currently models are being developed for determination of precipitation of salts during processing as well as a multiphase flash routine to determine the number of and composition of phases during processing. The routines are based on the extended Debye-Hückel and cubic equations of state respectively.

Once completed the models will be fitted with to data obtained from a pilot scale process plant. The feed and product streams analyzed to be used for lumping the streams into a composition of pseudo-components.

Acknowledgements

The author would like to acknowledge the Danish Ministry of Science, Technology and Innovation for funding this industrial Ph.D. project.

References

1. M. Mittelbach, C. Remschmidt, Biodiesel - The Comprehensive Handbook. Martin Mittelbach, Graz, Austria, 2003, p. 4.
2. E.v. Thujil et. al., An overview of biofuel technologies, markets and policies in Europe, ECN report ECN-C-03-008, 2003.
3. W. Feng, et. al., Phase Equilibria for Biomass Conversion Processes in Subcritical and Supercritical Water, Chemical Engineering Journal, 98 (2004) 105
4. W. Feng et. al., Biomass Conversions in Subcritical and Supercritical Water: Driving Force, Phase Equilibria, and Thermodynamic Analysis, Chemical Engineering and Processing 43 (2004) 1459

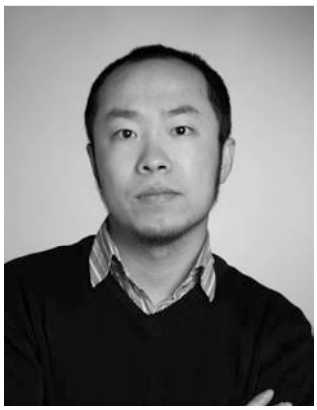

Ben Niu

Phone: +45 4525 2895
Fax: +45 4525 2258
e-mail: beni@kt.dtu.dk
www: www.ivc-sep.kt.dtu.dk
Supervisors: Alexander Shapiro
Erling H. Stenby
Wei Yan

Ph.D. Study
Started: 09 2006
To be completed: 09 2009

Carbon Dioxide Injection in the Carbonate Reservoir

Abstract

Carbon dioxide injection is a widely used EOR (Enhanced Oil Recovery) method. During the injection of carbon dioxide into reservoir at the MMP (Minimum Miscible Pressure), it will be become miscible with original oil. The compositional simulation including the reaction between carbon dioxide and carbonate matrix will also be investigated. The experiments will be conducted with CT scanner and ROP flooding rig under high temperature and high pressure conditions.

Introduction

Today's largest global challenges are climate changes and security of energy supply. With its efficient power plants located near the coast and the North Sea Denmark has a unique position to enable the development of methods to combine the utilization of CO_2 with enhanced oil recovery (EOR). This project is a part of the main project, "Enhanced Oil Recovery through CO_2 utilization" which is to ensure the build-up of knowledge within EOR in Denmark.

During laboratory and field studies, several problems become significantly important. The thermodynamic equilibrium under the circumstance of chemical reaction and the appearance of different ions in the saline water has a direct relationship with the prediction of various parameters in the oil production. The relative permeability between different phases could influence the breakthrough time of different zones, and further the longevity and cost of the whole project. The reaction between carbon dioxide and carbonate matrix will change the porosity and permeability of rock matrix, and further influence the injectivity, and finally limit the longevity of the whole project. The numerical method and algorithm varies with the different dimensions and the complexity of the model, which has significant influence on the robustness, efficiency and accuracy of the model.

The aim of this project is to investigate problems induced by carbon dioxide injection. The current research is focused on the experimental and modeling work.

Process description

The injection of CO_2 into a petroleum reservoir will result in either a miscible or immiscible displacement. If under the prevailing reservoir temperature and pressure, the injected gas is miscible with the reservoir fluid in all proportions, this type of displacement is called first – contact miscible (FCM)[1]. If the injected gas is enriched enough to be completely miscible with reservoir fluid at the front, this kind of displacement is referred as multicontact miscible flood (MCM)[1]. The last type of displacement is in which phases at the gas-oil front can not be miscible. Because the first two kinds of displacement finally achieve similar high recovery efficiency, the MMP has become an important optimization parameter in CO_2 injection.

Experimental Work

The experimental work is mainly conducted with CT scanner (figure 1) and ROP rig (figure 3) in IVC-SEP. In the oil industry, x-ray computed tomography (CT) has been accepted as a routine core analysis tool and mainly used to fundamental studies and recovery mechanisms, like desaturation studies, improved recovery, hydrated studies, recovery of viscous oil, formation damage studies, acid treatment and stimulation[2].The saturation distribution of different phases during or after the flooding can be calculated based on the images from CT scanning.

Figure 1 CT scanner

In the recent experiment, three phases flooding in chalk sample is conducted by using CO_2, doped isopar-L and doped water under medium pressure, 6.5Mpa and room temperature 37C. In figure 2, core is initially saturated with oil and water, and then the water flooding begins to replace oil. The CT images at the same position gradually become lighter as time passes by, which indicates the water saturation is increasing. With proper analysis of those images, water front and its distribution can be captured.

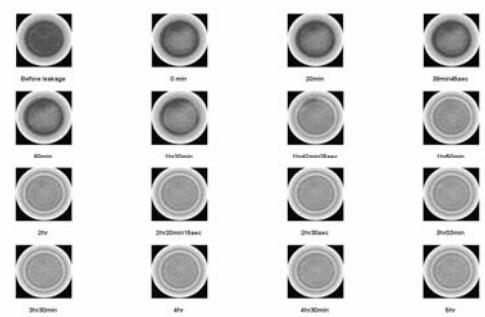

Figure 2 CT images at then same position with different time

With the analysis of CT images and mass conservation calculation, the experimental results indicate that the three phase experiments with two doped phases are difficult and complex and need further attentions.

ROP flooding rig is an effective tool for the measurement of multiphase permeability. As in figure 3, the most important and sensitive part of the equipment is the three phase optical separator, which can separate three phases under medium pressure up to 11.5Mpa.

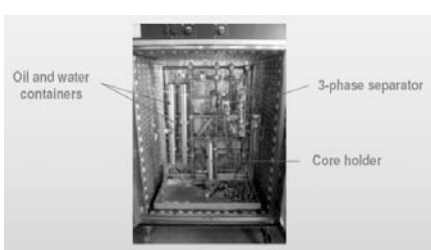

Figure 3 ROP flooding rig

The test experiment with ROP rig reveals that the regulation of gas/oil interface and oil/water interface in the separator is crucial to the success of experiments.

Modeling work

The chemical reactions and multiphase flow in CO_2 flooding are considered in the model, which will be updated step by step.

For a carbonate system the kinetically controlled reactions is[3]:

$$H_2O + CO_2 + CaCO_3 \quad Ca(HCO_3)_2$$

The reaction can change the porosity and permeability at the same time, and correspondingly the mechanical properties of the whole reservoir. The change is complex due to its dependence on rock type and the injection scheme. Suitable amount of icons and reactions will be chosen based on the time scale of the whole process and their individual importance.

Multiphase flow in CO_2 flooding could contain four phases, gas, two liquid hydrocarbon phases, and water. The importance of the second liquid hydrocarbon phase is still not fully clear, as mentioned many literatures[4, 5, 6]. This mechanism will be considered in the model.

At current stage, one dimension model has been proposed and in updating.

Future Work

Future research will be focused on multiphase flow and chemical reaction in carbonate reservoir. Flooding experiment will be mainly conducted under high pressure and high temperature conditions with CT scanner. Numerical simulation will mainly focus on the chemical reaction and the multiphase flow below and above MMP.

References

1. S. Haynes Jr. and R.B. Alston, SPE/DOE 20190 presented at SPE/DOE Seventh Symposium on Enhanced Oil Recovery, Tulsa, Oklahoma, 1990
2. E.M. Withjack, C. Devier, and G. Michael, SPE 83467 presented at SPE Western Regional/AAPG Pacific Section Joint Meeting, Long Beach, California, 19-24 May 2003
3. O. Izgec, B. Demiral, H. Bertin and S. Akin, SPE 100809 presented at the SPE Annual Technical Conference and Exhibition, San Antonio, Texas, USA, 2006
4. Nghiem, L.X., and Li, Y.K., SPE Reservoir Engineering, Volume 1, Number 4, 414-422, July 1986
5. Fanchi, J.R., SPE Annual Technical Conference and Exhibition, Dallas, Texas, 27-30 September 1987
6. K.K. Mohanty, W.H. Masino Jr., T.D. Ma, and L.J. Nash, SPE Reservoir Engineering, Volume 10, Number 3, 214-221, August 1995

Stefan Møller Olsem
Phone: +45 4527 3835
Fax: +45 4527 3700
E-mail: sto@kt.dtu.dk
WWW: http://chec.kt.dtu.dk
Supervisors: Søren Kiil, Kemiteknik, DTU
Kim Dam-Johansen, Kemiteknik, DTU
Lars Thorslund Pedersen, Hempel A/S
Merete Hoegh Laursen, Hempel A/S
Industrial PhD Study
Started: November 2005
To be completed: October 2008

Test of Starch-types for Enzyme-Mediated Controlled Release of Hydrogen Peroxide for Antifouling Purposes in Marine Coatings

Abstract
Enzyme-mediated antifouling based on the in-situ conversion of precursor compounds may be restricted by the applicability of the precursor compounds in the antifouling coatings. This paper evaluates several different starch types originating from corn, rice and tapioca. The evaluation is aimed at identifying the best compatible starch-type for indirect antifouling coatings. The evaluation is based on measures of oil-absorption, content of water soluble material, particle size distribution and coating characteristics of starch containing coatings. Corn and tapioca type starches are shown to be the most promising for antifouling purposes. This is due to a lower content of water soluble material, a higher potential of starch loading in the coating, and better coating performance of corn and tapioca starch-containing coatings.

Introduction
The accumulation of polymers and living species (i.e. fouling) on seawater-immersed constructions causes several problems for the structures. On ship hulls, increased fuel consumption due to higher drag resistance is the major concern. Compensating fuel consumption means a higher emission of greenhouse gasses, and an increase in expenditure for shipping.
Ship hull fouling has been fought for thousands of years, and the means, with which antifouling has been undertaken, have been plentiful and diverse [1]. Recently environmental considerations forced paint manufacturers to discard the more toxic of the compounds utilized. The primary substitute, cuprous oxide has a long residence time in seawater, and is therefore prone to bioaccumulation. In the near future, antifouling coatings based on controlled release of short-lived antifouling agents are likely to be introduced [3].
Enzymes are, in general, easily degradable proteins; they can therefore, presumably, be added to antifouling paints without harmful environmental consequences. Generally enzymes can be applied as antifouling agents in two differing ways. They can be used directly, meaning that the enzymes are used as a substitute to biocides; or they can be applied indirectly, which covers the use of enzymes for biocide generation in-situ in the coating [3].
Hydrogen peroxide is reported to have inhibiting effect on fouling organisms [**Error! Reference source not found.**]. Its lifetime in seawater is however short, as it decompose to water and oxygen. The instability and high seawater solubility makes it virtually inapplicable in antifouling coatings as a common biocide. However, several enzymatic reactions produce hydrogen peroxide, and a controlled release of hydrogen peroxide from antifouling coatings can therefore be controlled by enzymes catalyzing the reactions of a precursor compound into the peroxide. An enzyme system releasing hydrogen peroxide from starch has been described [2].
The system contains two enzymes that turn starch via glucose into hydrogen peroxide and gluconolactone, as shown in Figure 1. The enzymes and substrates may be enclosed in the same capsules as illustrated in Figure 1, or they may be separately acting on their substrates as they pass by on the way from the water insoluble starch through the water containing part of the coating and into seawater.

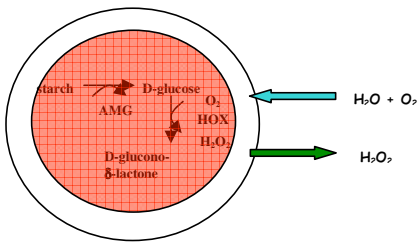

Figure 1: Illustration of the enzyme reactions involved in the release of hydrogen peroxide from within the marine coatings.

The precursor compound cannot be glucose due to too high water solubility [5]. Instead the water insoluble starch is applied. In order to ensure a high release of active ingredient throughout the life time of the coating, starch must constitute a fair percentage of the coating. It is therefore very important that the starch is compatible with the other paint constituents.
Starch is a well-known biochemical compound that can be harvested from several sources [6]. Starches differ in grain size and degree of branching as well as content of crystalline and amorphous starch according to origin [7]. This paper describes the investigations carried out in order to determinate the applicability of 13 different starch types as precursor-compounds in an antifouling coating.

Starch-types
13 different starch types were gathered from different producers. The starch types and some of their characteristics are provided in Table 1. The main difference between the starches is believed to be the origin. Starch from rice, corn and tapioca is considered in this paper.

Table 1: The origin and modification of the starch types tested in this paper. Waxy refer to amylopectin-based starch. Some of the starch-types have been cross-linked or stabilized by additives. This can be seen in the last column of the table.

Abbreviation	Source	cross-link/ stabilization
R1	Rice	
R2	Rice	
R3	Rice	x-link/ acetate
R4	Rice	
R5	Waxy rice	
C1	Corn	
C2	Corn	Adipate/ -
C3	Corn	Adipate/ acetate
C4	Waxy corn	Phosphate/ -
C5	Waxy corn	Phosphate/ -
C6	Waxy corn	Adipate/ acetate
C7	Waxy corn	(cationic)
T1	Tapioca	Phosphate/ acetate

Measurements and results
In total 4 different parameters were used to evaluate paint compatibility of the starches. These were particle size distribution (PSD), content of soluble material, oil absorption/critical pigment volume concentration and water uptake of formulated coatings.

Particle size distribution
Figure 2 shows the particle size distribution of the different starch-types applied in this evaluation. It can be seen, that the particle size is generally dependent on the starch-source. Whereas rice starch granules are considerably smaller than corn-type starches (when disregarding agglomerates), the tested tapioca-type starch resembles corn-type starches greatly in terms of particle size distribution.

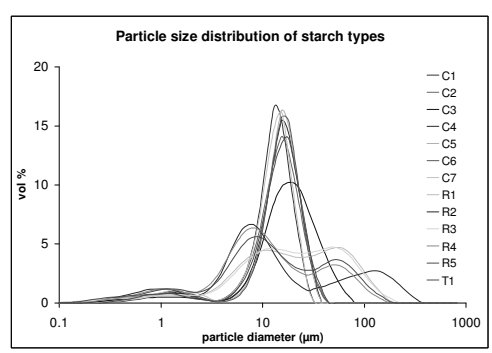

Figure 2: Particle size distributions of the different starch types suspended in water. Corn-type starches are kept in blue colors, rice-type starches are brown and reddish, and tapioca starch is green.

In the paint industry, pigment-particle size should be as small as possible. The larger particles of the rice starch can be assigned to agglomeration; the tendency to agglomerate depends on the propellant of the slurry. Agglomeration does therefore not necessarily occur in solvent based paints. However, prepared coatings containing the different starch types showed a distinctly different topography, which can be seen from Figure 3.

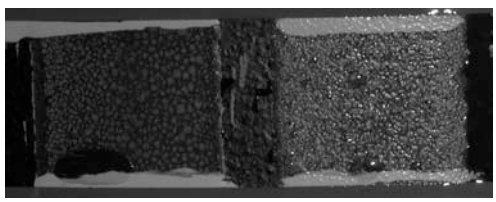

Figure 3: Comparison of roughness of tapioca-based starch (left) and rice based starch (right) in formulated coatings.

Though the agglomerates may be broken during paint production by increasing the shear during grinding, this procedure may be time consuming and reversible.

Soluble fraction of starch

The content of soluble material of the starches was estimated gravimetrically. A slurry of the starches and demineralised water was made, and then centrifuged for five minutes at 150,000 rpm, and the dry matter content of a few milliliters of supernatant was established gravimetrically. Figure 4 shows the results of the measurements.

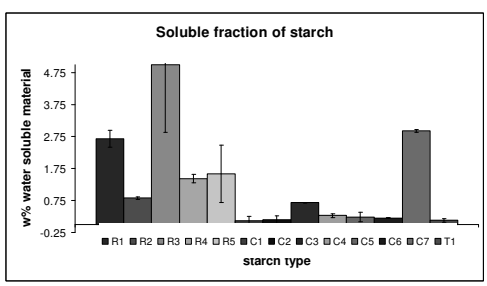

Figure 4: The content of water soluble material in the starch types. The bars indicate the 95% significance interval.

The results provided in Figure 4 are not necessarily the soluble fraction of the starch. The term non-centrifugable content is regarded as more suitable, however, it is believed that the difference in this case is as well little, as of little significance. From Figure 4 it can be seen that all the "small-grained" rice types and the cationic corn-type starch have a considerable amount of water-soluble material.

Oil absorption

Oil absorption is a measure of the compatibility of a given pigment in a paint system. The oil absorption is measured by adding oil to a known amount of substrate. The amount of oil required to achieve a pasty material can be converted to the volume of voids between the pigments and thus the maximum of pigment contained in a coating of normal characteristics. Figure 5 shows the critical pigment volume concentration (cPVC) of the starch-types tested. The cPVC is calculated from oil absorption measurements.

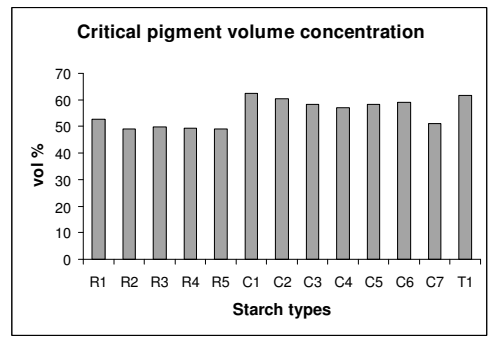

Figure 5: The critical pigment volume concentration of the starch-types tested. The values have been determined based on measurements of oil absorption.

Water uptake of starch coatings

Structural integrity and stability of a formulated antifouling coating immersed in seawater can be estimated by establishing the water uptake of the starch containing coating in the laboratory. If the coating takes up a high amount of water, the general coating properties of the coating may be limiting. The (artificial) sea water uptake of several starch-containing coatings has been monitored gravimetrically over several weeks. The results are presented in Figure 6.

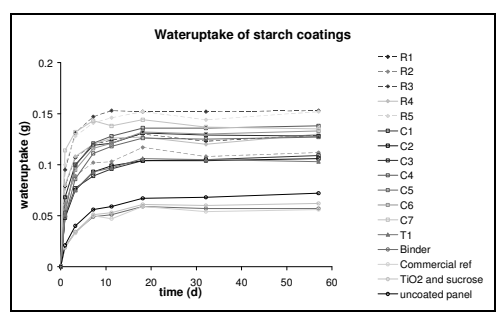

Figure 6: Gravimetrically determined water uptake of starch containing coatings during two months immersion in artificial seawater at room temperature.

In Figure 6, four regimes can be identified. The bottom regime with the lowest water uptake covers the reference coatings and the uncoated panel. The lowest intermediate regime covers the starch types C1, C2, R2 and T1. The two regimes taking up the most water contain the remaining starch types, which is primarily rice-type starches.

Discussion

Based on the tests presented above, the best starch-type for enzyme-mediated release of hydrogen peroxide may be identified.

The particle size distribution should preferably be as low as possible. However, the tendency to agglomerate is another concern that must be taken. The agglomerates may be dispersed during paint production, but high shear force may be needed, and the process is reversible. Therefore, the mono-disperse distribution of corn and tapioca - type starches is preferred.

Considering the measurements of oil absorption, the higher critical PVC the more starch can be loaded into the paint and the higher release rate of hydrogen peroxide or the longer service life of the coating can be achieved, without loss of strength and other general film properties. Looking at Figure 5, we can see that the corn starches C1, C2 and the Tapioca starch have critical PVC values that are more than 10 volume percent above the rice-type starches. However, measurements of oil absorption are concerned with a fair degree of uncertainty, and to calculate the critical PVC, one must extrapolate from linoleic oil to the binder system. Therefore, the results provided in Figure 5 should only be used to identify a slight tendency that corn starch has a higher critical PVC value. The values should be considered uncertain.

It is not surprising the starch-types containing stabilizing agents that contains the most water soluble material. However, there is a clear tendency towards the smaller rice granules also containing oligo-saccharides short enough to contribute to the non-centrifugable content of the starch.

Furthermore, it should come as no surprise, that there is a strong correspondence between the starch-types of high water-soluble content and the coatings taking up the most water.

Formulated coating of the starches take up a considerable amount of water compared to the commercial reference coating. This can be ascribed to the hydrophilic nature of the pigment. However, the starches, C1, C2, R2 and T1 take up considerably less water than the remaining starch-types. Corn-type starches are therefore also preferred based on the water uptake of formulated coatings.

Conclusion

When comparing the performance of the starch-types tested, the best performing are originating from corn or tapioca. More specifically the corn type starches C1 and C2 and the Tapioca starch T1 are believed to be most compatible with antifouling coatings, based on the four measurements provided in this paper.

References

1. D.M. Yebra, S. Kiil, K. Dam-Johansen, C. Weinell. Progress in organic coatings 50 (2003). 75-104.
2. C.H. Poulsen, K.M. Kragh. US patent application. US2002/0106361A1.
3. S.M. Olsen, S. Kiil, L.T. Pedersen, M.H. Laursen, K. Dam-Johansen. Biofouling 23 (5) (2007) 369-383.
4. K. Nishimura, T. Yasunaga, S. Ichikawa, Y. Wakao. Marine biology. 1988. vol 99. p 145-150.
5. S. Kiil, K. Dam-Johansen, C.E. Weinell, M.S. Pedersen. Progress in Organic Coatings 45 (2002) 423-434.
6. Starch. (2007). Encyclopædia Britannica Online. 26 Nov. 2007 <http://www.search.eb.com.globalproxy.cvt.dk/eb/article-9069451>
7. Cereal processing (2007). Encyclopædia Britannica Online. 26 Nov 2007 <http://www.search.eb.com.globalproxy.cvt.dk/eb/article-50131>

Brian Richard Pauw
Phone: +45 4525 6864
Fax: +45 4588 2161
e-mail: brian@stack.nl
www:
Supervisors: Martin E. Vigild, DTU
Kell Mortensen, KU
Jens W. Andreasen, Risø Forskningscenter
Enno A. Klop, Teijin Twaron, Netherlands

Started: October 2006
To be completed: September 2009

On the Microstructure of High-Performance Polymer Materials

Abstract
This research aims to provide an uncompromising and authoritative methodology to the determination of the nanostructure of high-performance polymer materials. Much of this research is based upon methods derived in the era before computational power was readily available, and thus aims to concatenate the most valid relationships and update them where required. This methodology will be utilized to characterize high-performance aramid yarns, whilst varying many environmental conditions.

Introduction
High performance polymers, such as the aramid yarn used for example in bulletproof vests, competition sails and as asbestos replacement, are by definition unparalleled in their physical characteristics. These yarns, as the main focus of this research, have been investigated in detail since their appearance in the marketplace approximately 30 years ago. The crystal structure of the polymer material has been characterized, as well as a great number of physical properties such as tensile strength and phase diagrams. However, only a few attempts have been made with respect to the determination of the microstructure of the yarn, i.e. structural elements with sizes bigger than what can be observed by crystallography, but smaller than the optical limit. Especially the micropore structure, with structural elements (micropores) in the range of 1-100 nanometers, is a less well known area [1].

The main technique to investigate such microscale structures, is Small-Angle X-ray Scattering (SAXS). This is the only technique that can determine such structural elements (henceforth referred to as *contrasting objects* when associated with SAXS) without destructive sample preparation, and above all, resulting in average parameters, valid over the entire irradiated area [2]. These values are much more representative for the entire yarn, when compared to techniques of the microscopic kind, for microscopic techniques can only scrutinize small cross-sections of material at once. Naturally, techniques such as Transmission Electron Microscopy (TEM) and Scanning Probe Microscopy (SPM) will nevertheless be employed to provide visual cues to data measured with techniques such as SAXS. Furthermore Wide-Angle X-ray Scattering (WAXS) and absorption studies can be used to provide additional data [3].

The trouble with SAXS
The advantages with SAXS are offset by the complexity of the data analysis procedure. The obtained data (scattering pattern) is, mathematically speaking, a (auto-convoluted) Fourier transform of the electron density. Not only that, but due to physical limitations, only a slice of the actual 3D transform is obtained, and due to detector limitations, only a subset of the data in that slice is available.
The result of all this is that the obtained data no longer has a unique solution in the real-space world (as opposed to the Fourier transformed world), and back-transformation of the data results in non-unique solutions.
Therefore, the most common means to obtain meaningful data is to fit the data to a model function describing the Fourier transform of an idealized structure. This raises the question of how to validate said methods and whether the models on which they are based are a good representation of the contrasting objects they purport to portray.

Designing a new fitting model
In order to obtain more physically meaningful parameters from the obtained SAXS patterns, a scattering function (for data fitting purposes) was developed that is in line with our initial guess as to the structure of the contrasting objects. Our initial guess assumes a system of cylindrical scattering elements. The

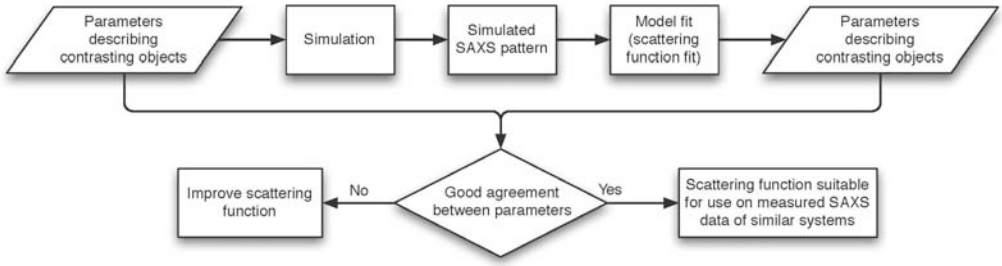

Figure 1: Method for validating model fitting functions using simulated scattering patterns of known physical structure

cylinders are shaped by radius according to a certain radial distribution (e.g. lognormal) and (mis-)aligned along the fibre axis according to another distribution. The cylinders are of finite length. A scattering function was made that describes this system.

For testing the validity of said scattering function (see also Figure 1), simulation software was developed that can generate a system of cylinders bound by a certain volume. From this set of simulated cylinders, a simulated scattering pattern can be generated.

The thus obtained scattering pattern can be fit using our previously developed scattering function. In this manner, the scattering function can be tested against a system for which it was designed. Parameters obtained from the data fit can then be compared to the parameters that went into the simulation. Agreement between those two indicate that the scattering function can be used to fit similar systems.

The current state of affairs

Today, the scattering function has been developed, and programmed into MATLAB. Since it contains a few numerical integrations, one iteration step lasts about ten seconds on a standard desktop.

The simulation software has been written and tested to produce scattering patterns of systems of cylindrical contrasting objects. Computing the average scattering pattern of a system with one set of parameters, takes approximately three to four hours on a standard desktop.

Thus, a range of simulated scattering patterns are now available (e.g. Figure 2), and tests are underway to validate the scattering function. Initial results indicate that adjustments to the scattering function are required before a solid match is obtained between the simulation parameters and the resulting fitting parameters.

Future

In the near future, further focus will be put on the validation of the fitting models, besides which separate data analysis methods will be investigated as well. Synchrotron measurements have provided a wealth of high-intensity measured SAXS patterns to ease the fitting process. All the information together should allow for an authoritative view of the nano-structure to be constructed.

Collaborations

Teijin Twaron, manufacturer of the high-performance materials and co-contributor to the project, will collaborate extensively with this project. Amongst others, they will provide the phenomenological parameters measured at their own research lab, crucial for making the structure-property relationships. Furthermore, the company will supply custom yarns to the project.

Knowledge on the DTU, KU and Risø side, will be combined with the knowledge on the Teijin Twaron side, resulting in unparalleled science.

For introduction of 2D fits to the research community, a collaboration has been initiated with Karsten Joensen of JJ-Xray. The free Matlab program developed as a result of this collaboration shall include a GUI-like approach to 2D data fitting.

Acknowledgments

The author would like to express his sincere gratitude to Steen L. Hansen, for his selfless assistance and contributions to this project.

References

[1] J. Aerts, J. App. Cryst. 24 (1991) 709-711

[2] P. Debye and A. M. Bueche, J. App. Phys. 20 (1949) 518-525

[3] Y. Cohen and E. L. Thomas, Macromolecules 21 (1988) 433-435

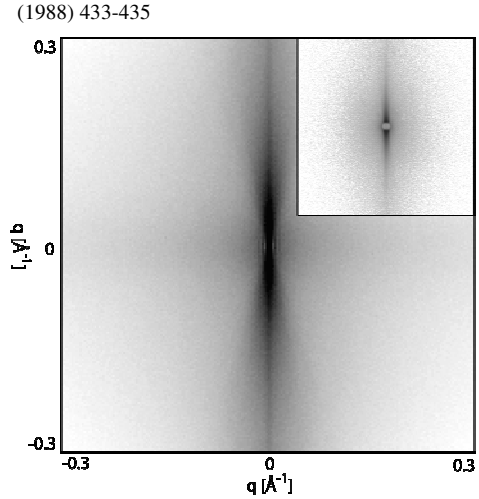

Figure 2: A simulated scattering pattern of a system of cylinders (main) compares well to measured SAXS data of a fibre sample (inset)

Kim Hougaard Pedersen

Phone: (+45) 45 25 28 90
Fax: (+45) 45 88 22 58
e-mail: kvp@kt.dtu.dk
www: www.chec.kt.dtu.dk
Supervisors: Anker Degn Jensen
Kim Dam-Johansen

Ph.D. Study
Started: September 2004
To be completed: May 2008

Application of Fly Ash from Solid Fuel Combustion in Concrete

Abstract
Fly ash, a by-product from pulverized coal combustion, is utilized in the concrete manufacture where it serves as partial replacement of Portland cement. The residual carbon in fly ash is known to interfere with the chemicals added to the concrete to enhance air entrainment. The degree of interference is not only related with the amount of residual carbon, but also the properties of this carbon. The main objective of this project is to obtain knowledge of how the combustion conditions of pulverized coal is related with the amount and properties of the residual carbon in fly ash with emphasis on its utilization in concrete. Part of the work will focus on improvement of fly ash quality by post treatment methods and development of a standardized method to quantify the interactions between fly ash and air-entraining chemicals.

Introduction
About 24 % of the electricity produced worldwide (2002) is generated in coal fired power plants. As a consequence, large amounts of fly ash are produced. The demand for environmentally clean and cost effective power generation has increased the motivation of fly ash recycling.

The pozzolanic property of fly ash, i.e. its capability to react with water and calcium hydroxide to form compounds with cementitous properties at ambient temperature, makes it useful in the concrete industry, where it serves as partial replacement of cement and give rise to increased strength of concrete [1]. However, the fly ash has been reported to interfere with air entrainment in concrete, which is important to obtain high resistance toward freezing and thawing conditions [2]. Special surfactants, called air-entraining admixtures (AEAs), control this air entrainment by stabilizing the air as small bubbles in the concrete paste. They adsorb strongly to the air-water interface, but fly ash present in the concrete paste are capable of adsorbing the AEAs as well. Hereby less AEAs are available to support the air bubbles and the amount of entrained air is lowered. Increasing the dosage of the AEAs may compensate for the adsorption loss, but normal variations in ash properties lead to large and unacceptable variations in the entrained air [3].

Even though modern coal fired power plants have high burnout efficiencies, significant amounts of carbon still exist in the fly ash after combustion. This residual carbon and not the mineral matter of fly ash is responsible for the adsorption of AEAs [3]. A large part of the carbon surface is non-polar compared with the polar surface of the mineral matter. This provides active adsorption sites for the hydrophobic part of the surfactants, thus the carbon competes with the sites at the air/water interface [4] as illustrated in Figure 1.

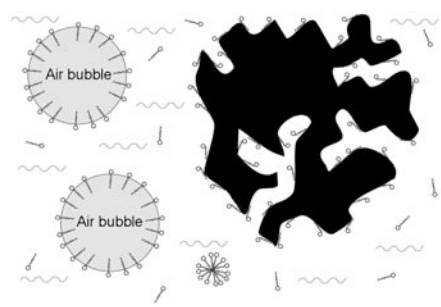

Figure 1: Adsorption sites for AEAs at air/water interface and at carbon surface [4]. The small circles of the AEAs correspond to the polar end and the tail corresponds to the hydrophobic end.

The problem with decreased air entrainment in fly ash concrete has worldwide lead to regulations for its application in concrete taking the presence of carbon in fly ash into account. These regulations are based on a maximum limit of the amount of carbon in fly ash, e.g. according to the Danish Standard DS/EN 450 the carbon content in fly ash are not allowed to exceed 5 wt\%. However, in recent years the carbon content of a fly ash has been found insufficient as a criterion for its application in concrete and problems with air entrainment have been observed with fly ashes having levels of carbon below the limits [3]. These observations have lead to further studies of the interactions between AEA adsorption and properties of carbon in fly ash; factors such as accessible surface area and surface chemistry of the residual carbon are believed to affect the AEA adsorption as well [4].

The combustion conditions under which the fly ash has been produced influences the properties of the residual carbon. The worldwide introduction of improved burner technologies in order to reduce NO_x-emissions has lead to problems with achieving a correct amount of air entrainment in fly ash concrete [5]. These burner technologies work with hot fuel rich zones in order to combust under reducing conditions and these conditions are believed to create fly ash being poor in quality for concrete utilization.

The AEA adsorption capacity of a fly ash is usually determined by the foam index (FI) test, which is a simple laboratory titration procedure involving the use of commercial AEAs and visual observation of foam stability. These parameters reduce the comparability of the test, i.e. commercially available AEAs vary in chemical nature and criterion on foam stability is operator individual. Therefore, it is of interest to develop a reproducible method, which is able to determine the fly ash quality with respect to air entrainment in concrete [6].

Specific Objectives

The aim of this project is to obtain further knowledge of how the combustion conditions of pulverized coal influences the fly ash quality for concrete utilization with emphasis on the air entrainment in concrete. Part of the work will focus on improvement of fly ash quality by post treatment methods. Furthermore, steps will be taken toward the development of a reproducible test method to replace the foam index test.

Combustion Conditions and Fly Ash Quality

Fly ash has been produced from combustion of pulverized coal under various combustion conditions in an entrained flow reactor (EFR) sketched in Figure 2.

The main part of the EFR is an electrically heated ceramic reactor, where the combustion of the fuel takes place. The coal and part of the combustion air is introduced from the top and into the reactor through a water-cooled feed probe. The remaining air is pre-heated before it is mixed with the coal/air mixture. A particle sampling probe is mounted in the bottom of the reactor. The fly ash particles are sampled from the flue gas stream by isokinetic gas sampling and collected on a filter further downstream. The parameters adjusted in the combustion experiments are the total excess air (λ_{total}) and the ratio between feed and total air ($\lambda_{feed}/\lambda_{total}$). The collected fly ashes are analyzed for carbon content (determined by weight loss, LOI) and foam index.

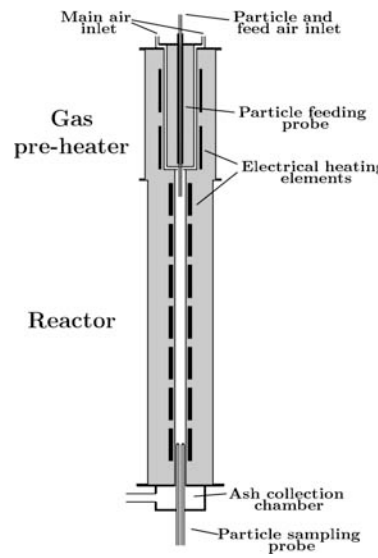

Figure 2: Sketch of EFR. The ceramic reactor is 2 m long and 8 cm in diameter. Conditions used in the EFR: coal feed rate: 0.34-0.46 kg/h, temperature: 1350 °C, feed air: 6-17 Nl/min, total air: 58 Nl/min, gas mean residence time: 1.7 s

Figure 3 shows the residual carbon content of the collected fly ashes produced at different feed/total air ratios and total excess air.

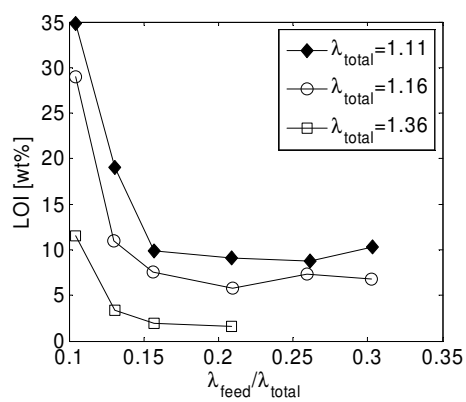

Figure 3: Carbon content (LOI) in fly ashes compared with the feed/total air ratio at different total excess air.

The carbon content of the fly ashes are found to decrease with increasing feed/total air ratio and excess air. The feed/total air ratio is observed to have major impact on the carbon content at lower ratios, but not at ratios above app. 0.16, where the fly ashes are produced with constant carbon content. The initial decline in carbon content with the ratio are presumably due to an improved mixing between coal and air caused by increasing jet velocity at higher feed/total air ratio. This leads to increased oxygen concentrations in the early stage of combustion and thereby a higher conversion of the coal particles. A further rise in feed air reduces the temperature and concentration of coal particles in the air flow, which can result in a delayed ignition [7] and this may explain the constant carbon content found in ashes produced at higher feed/total air ratios. The increase in total excess air raises the oxygen concentrations in the reactor and gives rise to decreased carbon content in the produced ashes as well.

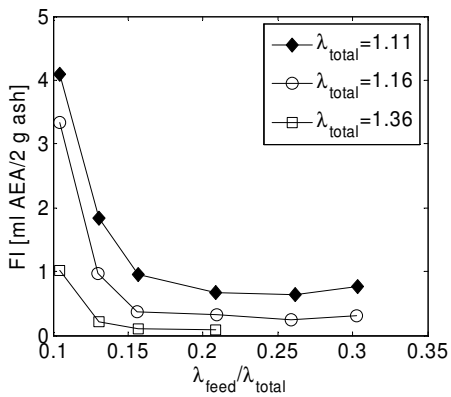

Figure 4: Foam index of fly ashes compared with the feed/total air ratio at different total excess air. The foam index test is performed on two grams of fly ash and the results are reported as ml AEA per two gram of fly ash.

The determined foam index values of the coal ashes (Figure 4) are from a visual comparison observed to follow the tendency of the carbon content; increasing excess and feed/total air ratio results in ashes with lower foam index values and low feed/total air ratios do highly affect the foam index, which on the other hand stays constant at higher ratios. The high foam index found among ashes with elevated carbon content are in agreement with results from others [3], that the residual carbon accounts for the adsorption of AEAs in concrete mixtures.

In order to uncover whether the difference in foam index between the ashes is solely caused by a change in carbon content, or if it may be due to a variation in the AEA adsorption properties of the residual carbon as well, the foam index is normalized to the carbon content of the fly ash, also known as the specific foam index. The results are presented in Figure 5, where the AEA adsorption capacity of the residual carbon (spec. FI) is found to decrease with the feed/total air ratio. Moreover, higher specific foam indexes are found at the lowest overall excess air (λ=1.11). Thus, the variations in AEA adsorption of the produced ashes are apparently caused by changes in both carbon content and AEA adsorption capacity of the residual carbon.

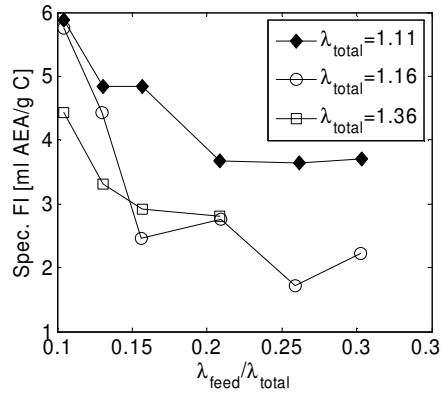

Figure 5: Specific foam index of fly ashes compared with the feed/total air ratio at different total excess air. The specific foam index corresponds to AEA adsorption capacity of the residual carbon.

It is found that more fuel rich conditions (lower excess air or feed/total air ratio) do not only lead to an increased carbon content and thereby a raise in foam index of the produced ashes, but the carbon is also capable to adsorb higher amounts of AEAs, making the consequences of increased carbon content worse.

The present observations support what others have discussed about the mechanism of the AEA adsorption [5]. It has been suggested [5] that a stable film of oxides is formed on the surface of carbon during conversion in an oxidizing environment. The increased polarity of the carbon surface creates less adsorption sites for the hydrophobic part of the AEA and thus, less AEA is adsorbed by carbon as illustrated in Figure 6.

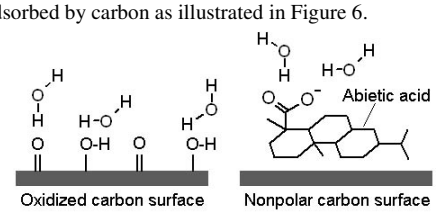

Figure 6: The hydrophobic part of a surfactant molecule (in this case abietic acid) interacts by dispersion forces, with the non–polar carbon surface (right). On the other hand, at the polar carbon surface (left), water molecules interact with the surface oxides by hydrogen bonding. The dispersion forces from the surfactant are not strong enough to displace water and hence, the surfactant is not adsorbed by the carbon.

Opposite to this, fuel-rich combustion conditions will drive off surface oxides, leading to a less polar surface. These fuel rich conditions are usually found near the

burner in low-NO_x environment, where they reduce the formation of NO_x but lead to lower fly ash quality. It is noted that variations in AEA adsorption of the residual carbon may be due to its surface area and particle size as well and this will be subject for further investigation.

A linear relationship was found between NO_x emission and the feed/total air ratio. The foam index of the produced ashes compared with measured NO_x emissions are presented in Figure 7. The foam index is within each series of constant total excess air series found to decrease with the NO_x emission

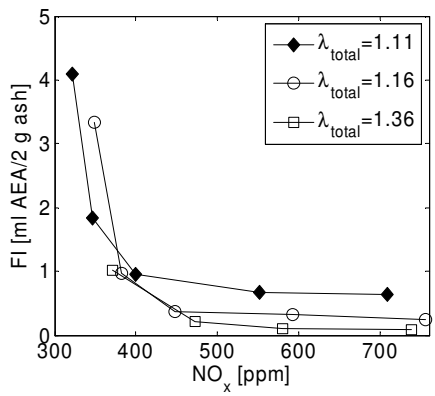

Figure 7: Foam index of the produced fly ashes and NO_x emissions at different total excess air.

until it reaches a constant level at app. 450 ppm NO_x. Therefore, increased fly ash quality in the EFR is achieved when operating at enhanced oxidizing conditions (expressed as higher NO_x emissions), but only until a certain level. It appears as if there exist a trade-off between low NO_x emission and a low foam index of the produced fly ash. Thus, determination of optimal combustion conditions, where high fly ash quality and low NO_x emission are achieved, will be beneficial in operation and future design of combustion technologies.

Conclusion

Pilot scale experiments on an EFR have shown how low-NO_x combustion of pulverized coal generates fly ash with higher carbon content, increased foam index and increased AEA adsorption of the residual carbon, all making the fly ash less suitable as concrete additive. The results indicate that optimal conditions exist between the foam index of the produced fly ashes and NO_x emissions on the present setup. Work will continue on the EFR involving other types of fuel and temperatures.

Acknowledgements

The research activities of CHEC are co-funded by the Technical University of Denmark, Dong Energy A/S, Vattenfall A/S, Energinet.dk, the Danish Council for Production and Technology Sciences, the Danish Energy Research Programme, Nordic Energy Research, EU, and many industrial partners.

References

1. K. Wesche, Fly Ash in Concrete: Properties and Performance, Spoon, London, 1991, p. 5.
2. Y-M. Gao, H-S. Shim, R.H. Hurt, E.M. Suuberg, N.Y.C.Yang, Energy & Fuels 11 (1997) 457-462.
3. E. Freeman, Y-M. Gao, R. Hurt, E. Suuberg, Fuel 76(8) (1997) 761-765.
4. L. Hachmann, A. Burnett, Y-M. Gao, R.H. Hurt, E.M. Suuberg, Proceedings of the Combustion Institute 28 (1998) 2965-2971.
5. Y. Gao, I. Külaots, X Chen, E.M. Suuberg, R.H. Hurt, J.M. Veranth, Proceedings of the Combustion Institute 29 (2002) 475-483.
6. O.E. Manz, Fuel 78 (1999) 133-136.
7. X. Jun, X. Sun, S. Hu, D. Yu Fuel Processing Technology 68 (2) (2000) 139-151.

List of publications

1. K. H. Pedersen, S.I Andersen, A.D. Jensen, K. Dam-Johansen, Replacement of the foam index test with surface tension measurements, Cement & Concrete Research 37 (2007) 996-1004, .
2. K. H. Pedersen, A.D. Jensen, M.S Skjøth-Rasmussen, K. Dam-Johansen, A review of the interference of carbon containing fly ash with air entrainment in concrete, Progress in Energy and Combustion Science (in press).

Mads Pedersen

Phone: +45 4525 2943
Fax: +45 4593 2903
E-mail: map@kt.dtu.dk
WWW: http://www.bioeng.kt.dtu.dk
Supervisors: Anne S. Meyer
Hanne R. Sørensen, Novozymes A/S

PhD Study
Started: April 2007
To be completed: March 2010

Lignocellulose Pretreatment for Maximal Enzymatic (Ligno) Cellulose Degradation

Abstract
Pretreatment of lignocellulose is an important step for the production of second generation bioethanol. Without pretreatment of lignocellulosic biomass the yield of fermentable monosaccharides, and thereby the yield of bioethanol, is too low to make bioethanol production cost-effective. However, the fast and most effective pretreatment methods are energy demanding and thereby expensive in use. Therefore, it is one of the objectives of this project to evaluate the effectiveness of pretreatment and search for the most cost-effective treatment regarding energy consumption and yield.

Introduction
Degradation of lignocellulosic materials to fermentable monosaccharides can with time become an environmental friendly alternative to fossil gas, thereby reducing the dependency of fossil fuel sources and reduce the release of green house gasses [1]. A part of the process is the pretreatment of the plant material which is an important step in making the production of bioethanol economically feasible. The purpose of the pretreatment is to make the cellulose (and hemicelluloses) more susceptible to enzymatic hydrolysis for production of fermentable monosaccharides [2], see Figure 1. Different methods are used for pretreating the plant material, but they often show to be energy, chemical and time consuming, thereby making the process expensive. Among the used methods are steam explosion and wet oxidation which use high pressure and high temperature to make the polymers degradable [4]. Strong acids and bases are also used for pretreating the plant material, but reduce the yield due to production of infermentable sugars and inhibitors. Due to the inhibitors formed and the demand of energy, the use of bioethanol is not economically feasible compared to the use of fossil fuels [5]. To make the use of bioethanol feasible the pretreatment needs more attention regarding reduction of energy demand and reduction of the production of potential inhibitors. Therefore, more research is needed in the field of pretreatment of plant material and understanding the role of each polysaccharide forming the complex matrix of plant cell wall.

Specifik objectives
The purpose of the project is to find possible improvements for the pretreatment of lignocellulose which can make the production of bioethanol feasible. In the beginning of the project attention will be given to the presently used methods and the issues resulting in expensive processes and low yields. Moreover macroscopic and microscopic examinations of the substrates will be used to gain more knowledge on the effect of the pretreatment. Atomic Force Microscopy (AFM) and Scanning Electron Microscopy (SEM) will be used to clarify the physical and chemical changes in the substrate due to fractionation and pretreatment.

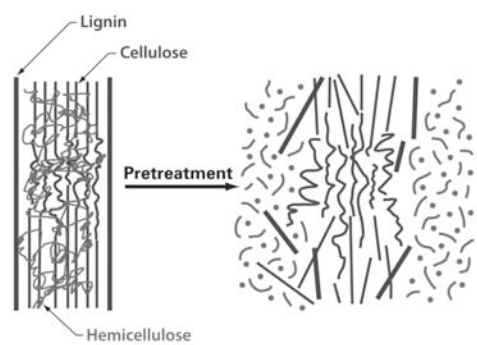

Figure 1: Pretreating the matrix of polysaccharides [3,4].

To increase the yield, factors such as viscosity, size of particles, surface and crystallinity needs to be drawn into consideration.
The project will include theoretically calculations on optimization of the pretreatment and scaling up the process for pilot plant. An important part of the project is to make the process ready for scaling the pretreatment up from a laboratory experiment to larger scale without loss of yield efficiency and still be cost-effective.

Experiments
Experiments have been run at DTU-Risø using their wet oxidation autoclave for pretreating wheat straw. The process is run at 195 °C for 10 minutes with 10 bar initial oxygen pressure [6].
Hydrolyses of the untreated and pretreated wheat straw were made by the commercial enzymes Celluclast 1.5L (Novozymes A/S) and Novozym 188 (Novozymes A/S) to evaluate the pretreatment. The hydrolyses took place in eppendorf tubes at 50 °C in a thermomixer with 2 % dry matter for up to 24 hours [7].
For analyses of the physical alteration of the wheat straw surface a Scanning Electron Microscope (SEM) was used.

Results and discussion
Figure 2 shows the alteration of the wheat straw surface. Before pretreatment the particles show clear line up of the fibers on the outer surface layer. However, when the particles have been pretreated with wet oxidation the line up of the fibers seems disrupted. The disruption of the fiber network leads to a larger surface area which can increase the accessibility for enzymatic hydrolysis.
Figure 3 shows the glucose release from hydrolyses of pretreated and un-pretreated wheat straw. The pretreatment showed a positive effect on the release of glucose. Noticeably, the reduction of the particle size also had an increasing effect on the glucose release, however, only a minor increase was found when the particle size was reduced from 250-500 to 53-149 µm.

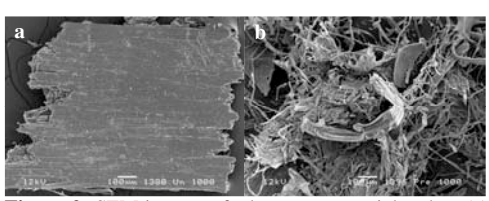

Figure 2: SEM images of wheat straw particle when (a) untreated and (b) pretreated.

Conclusion and future work
So far this project has shown that alongside with the increased release of glucose when pretreating the wheat straw, the reduction of the particle size also has a clear effect on the glucose release. Energy balances are needed to find out whether reduction of the particle size is needed and whether the pretreatment of wheat straw will supply enough monosaccharides for fermentation to reduce the costs of producing bioethanol.

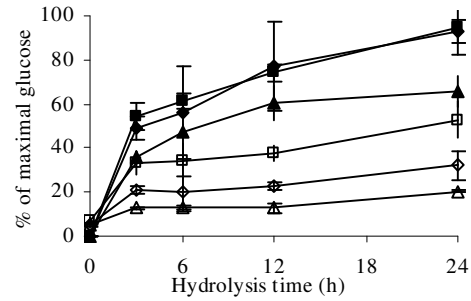

Figure 3: Percentage of maximal glucose release due to enzymatic hydrolysis of pretreated wheat straw (■: 53-149 µm, ♦: 250-500 µm, ▲: 707-1000 µm) and un-pretreated wheat straw (□: 53-149 µm, ◊: 250-500 µm, Δ: 707-1000 µm).

Acknowledgements
We thank Anne Belinda Thomsen and Tomas Fernqvist from DTU-Risø for assistance with wet oxidation and Leila Leth from DTU-IPL for assistance with SEM. At last we thank Jørn Erik Pedersen (Danish Cooperative Farm Supply - DLG) for wheat straw supply.

References

1. M.A. Kabel, G. Bos, J. Zeevalking, A.G.J. Voragen, H.A. Schols, Bioresource Technology 98 (2007) 2034-2042.
2. H.R. Sørensen, S. Pedersen, A. Viksø-Nielsen and A.S. Meyer, Enzyme Microb. Tech. 36 (2005) 773-784.
3. N. Mosier, C. Wyman, B. Dale, R. Elander, Y.Y. Lee, N. Holtzapple, M. Ladisch, Bioresource Technology 96 (2005) 673-686.
4. T.A. Hsu, M.R. Ladisch, G.T. Tsao, Chemical Technology 10 (5) (1980) 315-319.
5. A. Esteghlalian, A.G. Hashimoto, J.J. Fenske, M.H. Penner, Bioresource Technology 59 (1997) 129-136.
6. A.B. Bjerre, A.B. Olesen, T. Fernqvist, A. Plöger, A.S. Schmidt, Biotechnology and Bioengineering 49 (1996) 568-577.
7. L. Rosgaard, S. Pedersen, J.R. Cherry, P. Harris, A.S. Meyer, Biotechnology Progress 22 (2006) 493-498.

List of publications

1. M. Pedersen, H.K. Lauritzen, J.C. Frisvad, A.S. Meyer, Biotechnology Letters 29 (2007) 743-748.
2. M. Pinelo, A.G. Tress, M. Pedersen, A. Arnous, A.S. Meyer, American Journal of Food Technology, In Press.
3. M. Pedersen, M. Hollensted, L. Lange, B. Andersen, Dansk Kemi 29 (5) (2007) 743-748.

Nanna Petersen
Phone: +45 4525 2861
Fax: +45 4593 2906
E-mail: nap@kt.dtu.dk
WWW: http://www.kt.dtu.dk
Supervisors: Krist V. Gernaey
Anna Eliasson Lantz, BioCentrum
Stuart Stocks, Novozymes A/S

PhD Study
Started: October 2006
To be completed: October 2009

Data-Driven Modeling for Monitoring and Control of *Streptomyces* Cultivations

Abstract
Analytical methods utilizing electromagnetic radiation are non-destructive and provide the means of rapidly obtaining important information about fermentation processes. The absorbance in the near infrared region can be used to determine concentrations of relevant chemical constituents while the scattering properties of the broth contain information about the biomass concentration as well as the particle size distribution. The aim of this project is to examine the different methods for modeling these multivariable data sets, estimate reliable models and implement the models in a monitoring and control scheme on a *Streptomyces* cultivation.

Introduction
Measurements of physical, chemical and biological variables are indispensable for monitoring and optimization of fermentation processes. Traditionally, the sensors used for fermentation monitoring measure physical and chemical variables such as temperature, pH and oxygen concentration. Near-infrared spectroscopy can be used to determine the concentration of different biologically important variables such as glucose, ammonia, and biomass on-line in a fermentation process [1].

The morphology of filamentous organisms influences the viscosity of the fermentation broth and thereby also the mass transfer properties of the broth. Furthermore, the metabolism is often closely coupled to the morphology. It is therefore important to monitor and control the morphology of the microorganism. Laser diffraction provides the means of rapidly obtaining robust particle size data. The technique is based on the principle that a particle will scatter light at an angle that is directly related to the size of the particle. It infers a volumetric size distribution, reporting the sizes of spheres with equal volume to the particles actually present. It has the advantage of being much faster than more commonly used microscopy and image analysis. However, it fails to report morphological information such as roughness, compactness, or maximum dimension, which is obtained with image analysis.

The data sets – spectra or size distributions – acquired with NIR spectroscopy and laser particle sizing are very large which makes it difficult to simply visualize the data as well as to interpret them. Therefore, multivariate data analysis techniques are employed in the analysis of these data. Partial Least Squares Regression (PLSR) can be considered the industry standard for the analysis of multivariate data. It is a supervised learning method, which can be used to find correlations between output variables (e.g. biomass and substrate concentration) and a set of input variables (spectral data). PLSR is able to handle correlations in the data by reducing the dimensionality of the data. The data are projected to a subspace spanned by vectors determined to maximize the variance of the input data as well as the correlation with the output variables.

Specific objectives
A first project objective is to establish a data set consisting of a number of batch fermentations with *Streptomyces coelicolor* – a filamentous bacterium producing useful secondary metabolites such as antibiotics – as model organism, and using advanced on-line sensors (NIR) for data collection in addition to standard on-line measurements. The fermentation data set can then serve as a basis for finding and evaluating correlations between sensor data and the course of the submerged bioprocess. A second project objective is to provide a comparison of the performance of several data-driven modeling methods – linear versus non-linear, single model versus multiple local models – on this fermentation data set. A third project objective is to actively use the on-line process variable information obtained from the advanced on-line sensor data in

feedback control loops. Once feedback control using advanced on-line sensors is established, the project focus will shift towards fermentation process optimization.

Concurrently to the work on on-line NIR spectroscopy the multivariate analysis techniques will be used in the analysis of particle size distribution data in filamentous fermentation broths. Common to the work on the different measurement techniques is the focus on increasing the process knowledge, which is an essential part of the PAT initiative published by the FDA in 2004.

Results and discussion

NIR measurements

The first experiments with the NIR sensor have shown that implementing a NIR sensor on-line in a fermenter gives rise to several challenges. The concentrations of the analytes of interest are quite low e.g. for ammonia the range is between 0-0.1 M. This means that the absorbance signal is relatively low. Both air bubbles and biomass particles scatter the light. The scattering depends greatly on the biomass concentration but also on the size distribution of the bubbles and particles. The rapid flow of the air bubbles and particles through the measurement window results in very large variations in the measured light intensity as shown in figure 1.

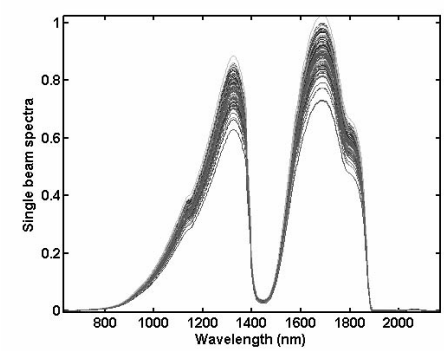

Figure 1. NIR spectra collected for one concentration of biomass, glucose and ammonia in an aerated and agitated fermenter.

The major challenge is to remove all of this unwanted variation while retaining the glucose, ammonia and biomass signal. Pretreatment methods such as multiplicative scatter correction exist which can remove a large part of the scatter effect in the data. The spectra after multiplicative scatter correction are shown in figure 2. The pretreatment has removed a large part of the variations in the data but not entirely. In the coming period different pretreatment methods will be investigated.

The analytes of interest absorb the light in specific wavelength regions. The chemometric modeling methods are developed for handling multivariable collinear data. However, if too many non-informative

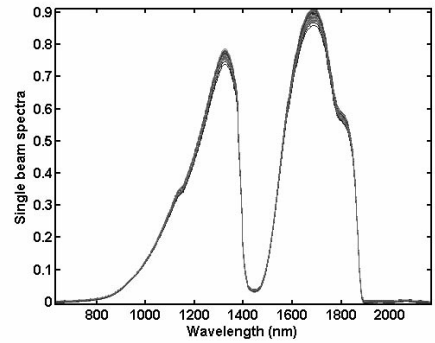

Figure 2. NIR spectra collected for one biomass, ammonia, and glucose concentration in an aerated and agitated fermenter after multiplicative scatter correction.

variables are included in the model this may deteriorate the model quality. Therefore, an important part of modeling the spectral data is to choose which wavelength regions should be included in the model. To support this decision some simple experiments have been carried out in which the NIR absorbance spectra have been collected for different concentrations of ammonia and glucose. The wavelength regions identified for glucose and ammonia are shown in table 1. Interval PLS has also been used for the selection of wavelength regions.

Table 1. Important wavelength regions for glucose and ammonia absorbance.

	Glucose	Ammonia
Wavelength (nm)	1600-1800	1500-1600

When running a fermentation the concentrations of glucose, ammonia and biomass will be correlated due to the specific metabolism of the cell. This may cause problems in the calibration of the chemometric models as it will be uncertain whether the chemometric model is based on the signal of the analyte of interest or some correlation with a signal from another analyte. It will be investigated whether a spiking experiment can break this correlation and thereby improve the robustness of the chemometric models.

Size distribution

Analysis of particle size distribution data was carried out in collaboration with Novozymes A/S [2]. Samples from commercially relevant *Aspergillus oryzae* fermentations conducted in 550 litres pilot scale tanks were characterized with respect to particle size distribution, biomass concentration, and rheological properties. The data set consisted of 99 samples collected from 12 batches.

The size distributions of three different samples from a randomly selected batch are plotted in figure 3.

The multimodal shape of the particle size distribution illustrates that an average size of the particles can be an unsuitable measure of the particle size. There is a clear time dependency in the data. The proportion of larger particles decreases with increasing batch time, while the number of very small particles increases.

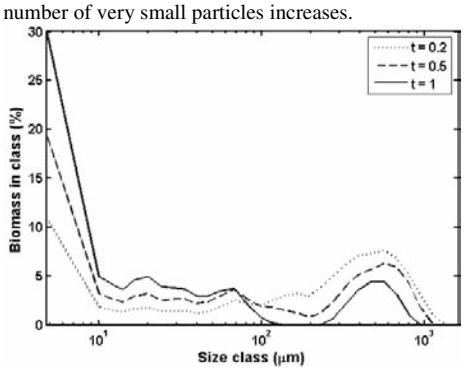

Figure 3. Particle size distributions of three samples taken at three different time points (0.2, 0.5, and 1 normalized batch time) during an *Aspergillus oryzae* fermentation. The graph shows the volume percentage of the particles in each of 31 size classes ranging from 4.75 μm to 1620 μm diameter.

A Principal Component Analysis (PCA) of the data from all 12 batches showed the same overall tendency in all of the batches. The first principal component captured the variation connected to the time development (figure 4) while the second principal component was related to the two different feeding strategies used. From the score plot it was possible to identify batch 5 as an outlier. A look into the process data revealed that a technical malfunction had in fact occurred in batch 5 resulting in a different morphology of the microorganism.

It was possible to correlate the size distribution data to the yield stress, consistency index and the apparent viscosity with PLSR. Validation on an independent test set yielded a root mean square error of 1.20 Nm^{-2} for the yield stress, 0.209 $Nm^{-2}s^{n}$ for the consistency index and 0.0288 $Nm^{-2}s^{-1}$ for the apparent viscosity, corresponding to R^2=0.95, R^2=0.94, and R^2=0.95 respectively.

Conclusion

NIR spectroscopy is a promising technique for monitoring of fermentation processes. However, several challenges must be overcome before the NIR sensor can be used in automatic control of *Streptomyces* fermentations e.g. low signal to noise ratio in on-line applications.

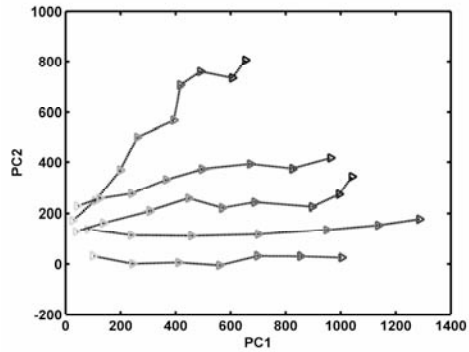

Figure 4. Score plot of the first two principal components in a PCA model of the size distribution data. Scores of the samples from five different batches (batch 5, 11, 9, 2, 1 from top to bottom) colored according to fermentation time from grey to black with increasing batch time. The lines connect samples from the same batch. The other seven batches show the same time development as is seen in the plot but are left out to ease the interpretation.

Chemometric methods can be used to extract valuable information from laser size distribution data. PCA can be used to provide an overview of the multivariate data, explore the data and reveal important correlations. This can be a valuable tool for monitoring purposes but may also help to increase the knowledge of morphology of filamentous organisms.

Acknowledgements

This Ph.D. project is supported by a grant from the Innovative BioProcess Technology Research Consortium financed by the Danish Research Council for Technology and Production Sciences, Chr. Hansen A/S, Danisco A/S, and Novozymes A/S.

References

1. M. Scarff, S. A. Arnold, L. M. Harvey, B. McNeil. Near Infrared Spectroscopy for Bioprocess Monitoring and Control: Current Status and Future Trends. Critical Reviews in Biotechnology 26 (2006) 17-39.
2. N. Petersen, S. Stocks, K. V. Gernaey. Multivariate Models for Prediction of Rheological Characteristics of Filamentous Fermentation Broth from the Size Distribution. Biotechnology and Bioengineering (2007). (In press)

List of Publications

1. N. Petersen, S. Stocks, K. V. Gernaey. Multivariate Models for Prediction of Rheological Characteristics of Filamentous Fermentation Broth from the Size Distribution. Biotechnology and Bioengineering (2007). (In press)

Katja Puder
Phone: +45 4525 2923
Fax: +45 4588 2258
E-mail: pud@kt.dtu.dk
WWW: http://www.chec.kt.dtu.dk
Supervisors: Anker Degn Jensen
Ole Simonsen, Novozymes A/S
Christian Isak Jørgensen, Novozymes A/S

PhD Study
Started: January 2007
To be completed: December 2009

Mechanism of Enzymatic Inactivation in the Animal Feed Pelleting Process

Abstract

Hydrolytic enzymes are applied to animal feed as supplements, attempting to support the breakdown and absorption of poorly accessible nutrients in the diet of animals. For the development of new feed enzymes, enzyme stability is a crucial parameter. But in the animal feed pelleting process, harsh conditions like steam application, and so temperature and moisture impact, stress the enzymes and they become susceptible towards unfolding reactions and inactivation, modifications of the proteins and results in a loss of activity. The aim of this project is to elucidate pathways of enzymatic inactivation in the pelletization by amino acid and structural analysis to get a better understanding of the protein's interaction with their environment. This will provide essential information of new formulations and of protective components which can enhance stability.

Introduction

Enzymes as catalyst are of key importance in the biotechnological sector. After fermentation and recovery, industrial enzymes can be formulated either as liquid or solid product. For practical and stability issues, enzymes are often formulated in solid state (e.g. granulates, lyophilized powder) with the addition of stabilizers.

One of the major enzyme applications is in the animal feed industry presenting a production of 600 mio. Tonnes feed per year. Cereals like maize, wheat, and oats are incorporated in animal feed presenting the major energy source for animals but monogastric animals are not capable of a full digestion [1]; hence the supplement of external enzymes, especially hydrolases, is to degrade and increase bioavailability of grain compounds to enhance nutritional value of animals' diet (e.g. cellulases, phytases) or to supplement animals' own digestive enzyme whenever these enzymes are not fully available (e.g. proteases, amylases) [2].

80% of all animal feed is pelleted, presenting agglomerated compacted feed. Enzyme granulates are directly added to the grinded animal feed compounds within the pelletization process. The feed processing plant encompasses several steps including mixing, conditioning, pelletizing and cooling. In the conditioning step, steam is applied providing heat and moisture to the diet to facilitate hygienization and compaction. The production of pellets is carried out by pelletizing mills but it is getting more and more common to utilize harsher equipment like extruder and expander; finally the pellets are dried and cooled. In that process line, the enzyme granulate is exposed to harsh conditions especially high temperature and moisture but also pressure and friction [3]. Due to the composition of fragile proteins, enzymes are susceptible towards inactivation resulting in a loss of enzyme specificity and reactivity. Therefore enzyme stability, and with it protein stability, is an important parameter which challenge researcher and determines the economic feasibility of animal feed enzymes.

Protein stability is determined by non-covalent forces within the complex protein structure and hereby with the primary structure, the amino acid sequence.

Inactivation can be divided in chemical and physical instability pathways. Physical inactivation indicates non-covalent alterations in the secondary and tertiary structure. The major driving forces are the hydrophobic forces describing the sequestering of non-polar amino acids, strongly conserved by non-covalent forces, into a core. Meanwhile, hydrophilic moieties are situated on the surface [4]. At harsh environmental conditions the interactions are disrupted especially H-bonds, and unbalance the protein leading to unfolding (reversibly or irreversibly), resulting often in denaturation. Also aggregation is a common process; the buried hydrophobic residues tend to become exposed to the solvent and interact with hydrophobic residues from

other unfolding protein molecules to minimize their exposure.
Chemical inactivation means that the amino acids become altered via covalent modifications. Sponteanous non-enzymatic deamidation of glutaminyl (Gln) and asparaginyl (Asn) residues is a common modification process. It results in an unstable succinimide ring which undergoes hydrolysis and racemization. Thus, the possible products are L-, D-aspartyl and L-,D-isoaspartyl (-aspartyl, Asp) peptides. The removal of an amide group introduces a positive charge and might result in a difference in the activity. It is often observed in solid state proteins exposed to moisture and elevated temperatures incorporated in a polymeric system [5, 6]. Oxidation is another major common degradation pathway; especially residues like sulfur containing methionine (Met) and cysteine (Cys) are susceptible sites to experience oxidation. They result in Met sulfoxide while Cys yields in various forms like disulfide, sulfenic, sulfuric, and sulfonic acids, depending upon the conditions [6].
It is essential to understand the interaction of protein with their environment. Various deleterious processes can occur in solid state and reduce the shelf life and value like it is the case during the pelletization.

Specific Objectives

The scientific goal of this project is to get an understanding of the interaction of solid state enzymes with its environment during the pelletization process. Inactivation kinetics of temperature and humidity on the solid state enzyme stability will be investigated. Furthermore, chemical modifications as well as structural analyses of the proteins should provide an insight into the inactivation pathways. In dependence of the obtained results, components improving the stability should be proposed.

Experimental Set up

The set up (figure 1) provides controlled conditions of RH and temperature to 'simulate' pelletization conditions according T and RH. The desired RH is determined by beginning water flow which needs to be evaporated. The generated steam is mixed with a heated dry gas stream. The final gas stream reaches a brass reactor which can be heated or cooled dependent on the desired temperature. The enzyme sample is placed in the brass reactor in an aluminum pan on a metal stick; so the solid state enzyme is in direct contact with the flowing gas.

Future Work

The small scale set up will be used to expose solid state enzyme (lyophilized, granulates) to different environmental conditions; residual activity as well as chemical/ structural alterations will be observed. Several spectroscopic methods like FT-IR and fluorescence are used to determine differences in the secondary and tertiary structures. For detecting chemical modifications peptide mapping via mass spectrometry and amino acid analyzes are carried out.

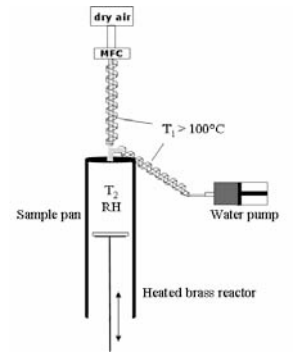

Figure 1 Set up

Acknowledgements

The Novozymes Bioprocess Academy is acknowledged for the financial support of this project.

References

1. Kersten, J., Rohde H.R., Nef, E., 2005, Principle of Mixed Feed Production-Components, Processes, Technology, AGRIMEDIA
2. Bhat, M.K., 2000, Cellulases and related enzymes in biotechnology, Biotechnology Advances, 18, pp. 355-383
3. Froetschner, J.R., 2006, Current Issues in feed manufacturing (II) - Conditioning controls pellet quality, Feed Tech, 10
4. Vielle, C. & Zeikus, G.J., 2001, Hyperthermophilic Enzymes: Sources, Uses and Molecular Mechanism of Thermostability, Microbiology and Molecular Biology Reviews, 65, pp. 1-43
5. Robinson, N.E., 2001, Protein deamidation, Biochemistry, 99, pp. 5283-5288
6. Costanino, H.R., 1995, Stability of solid pharmaceutical proteins, PhD thesis from Massachusetts Institute of Technology

Louise E. Rasmussen
Phone: +45 4525 2935
Fax: +45 4593 2906
E-mail: ler@kt.dtu.dk
WWW: http://www.bioeng.kt.dtu.dk
Supervisors: Anne S. Meyer
Jens F. Sørensen, Danisco

PhD Study
Started: February 2007
To be completed: November 2010

Development of Quantitative Kinetic Models Describing Enzyme Catalyzed Heteropolysaccharide Degradation - Insoluble Arabinoxylan

Abstract
Enzymatic hydrolysis of arabinoxylan is of considerable interest for various biotechnological applications and an efficient exploration of arabinoxylan as carbohydrate source for fermentation to biofuels or novel health promoting food ingredients requires a full understanding of the enzyme systems that effect their conversion. This study focus on selective enzyme biocatalysis and –conversion of water insoluble arabinoxylan and other xylan structure to obtain uniform xylooligosaccharide products and an improved understanding of the enzyme kinetics and quantitative phenomena.

Introduction
Efficient enzymatic modification and degradation of natural plant cell wall polymers have significant implications in food, biofuel and paper processing and may open up for novel biological production platforms in various industries. Arabinoxylan is the main heteropolysaccharide of the hemicellulose fraction of the cell wall of higher plants where it accounts for as much as 35% of the dry weight [1]. Unlike cellulose, arabinoxylan are chemically heterogeneous molecules which consists of a backbone of β-1,4 linked D-xylopyranosyl residues. Depending on the source of the arabinoxylan and the procedure used in its extraction, the xylose units can be substituted at either the C(O)-2 or C(O)-3 or be di-substituted at both the C(O)-2- and the C(O)-3 position with L-arabinofuranose or 4-O-methyl glucuronic acid residues or they can be esterified with acetic acid. Furthermore, the L-arabinofuranosyl side chain residues can be esterified with ferulic and p-coumaric acid [2].

Due to their complex structure, degradation of arabinoxylan requires several enzymes. The major xylanolytic activities are those catalyzed by endo-1,4-β-xylanases, which hydrolyze the β-(1,4) xylosidic linkages in the arabinoxylan backbone, generating a mixture of arabino-xylooligosaccharides (Fig. 1). Other activities are α-L-arabinofuranosidase, α-glucuronidase, acetyl (xylan) esterase, ferulic acid esterases, and β-xylosidases, each having a specific function in the cooperative degradation process [1]. β-Xylosidase cleaves off the terminal xylose unit from the non-reducing end of the xylooligosaccharides arising from endo-1,4-β-xylanase activity [3]. Some of the enzymes acting on the backbone and side chains have been shown to operate synergistically leading to a higher degree of hydrolysis of arabinoxylan [4,5,6].

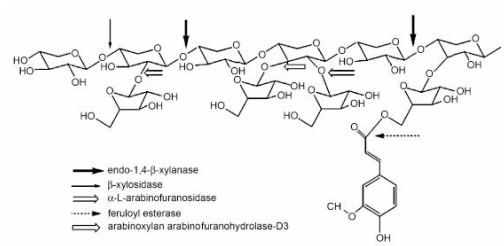

Figure 1: Chemical structure of arabinoxylan and the site of activity of different arabinoxylan degrading enzymes [7].

Xylooligosaccharides (XO) derived from partial hydrolysis of arabinoxylan can be used for several purposes (Fig. 2). One of the most important features of XOs as food ingredients is mainly related to their effect on the gastrointestinal flora where they stimulate growth of intestinal *Bifidobacteria*. Therefore, XOs are considered as prebiotic, which are non-digestible food ingredients that beneficially affect the host by selectively stimulation the growth and/or activity of beneficial bacteria in the colon. Although the health

effects of arabinoxylans are well documented, the effects of the degradation products, XOs, are less studied and therefore, an in-depth study of the prebiotic potential of XOs is warranted [8].

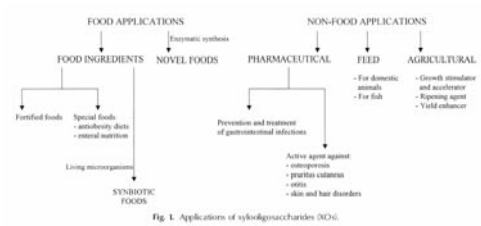

Fig. 1. Applications of xylooligosaccharides (XOs).

Figure 2: Applications of xylooligosaccharides [8].

Specific objectives

This project focuses on enzymatic modification and degradation of water insoluble arabinoxylan and other xylan structure. Experiments will encompass use of selected individual xylanases and intelligently designed combinations of relevant enzymes in statistically designed reactions. In order to obtain uniform xylooligosaccharide products from insoluble arabinoxylan selected enzymes will be used and reaction parameters specified. Evaluation of topochemical equations will provide a better understanding of the enzyme kinetics and quantitative phenomena. Unraveling the quantitative kinetics also encompass consideration of the heterogeneous structure of the substrate matrix and the change occurring during the reaction.

A particular aim is then to study the prebiotic potential of the enzymatically released xylo-oligosaccharides derived from specific modification of the water insoluble arabinoxylan and other xylan structure on intestinal bacteria.

The hypothesis behind the project is that provision of a better quantitative understanding of the modification and degradation of insoluble arabinoxylan is a prerequisite for optimally exploiting enzyme reactions in new food and ingredient processes and for exploiting biomass rationally for production of value added products.

Experimental methods

Assessments of the enzymatic degradation are mainly accomplished by use of state of the art HPLC: High Performance Size Exclusion Chromatography (HPSEC) and High Performance Anion Exchange Chromatography (HPAEC) mainly focusing on the quantification of arabinose and xylo-oligosaccharider.

Current work

The current work encompasses systematic experimental evaluation of the hydrolysis of WUAX by selected pure xylanolytic enzymes, including unraveling degradation products and enzyme kinetics. Pure mono-active enzymes have been obtained from Danisco A/S and Megazyme. The hypothesis is that it is possible to catalyze the solubilization of isolated, insoluble wheat arabinoxylan and bran, by treatment with selected xylanases to obtain at least 65-75% and 50% of hydrolysis respectively.

The future work is directed towards a better understanding of the initial degradation and to optimize reaction parameters in order to obtain a more specific modification and efficient degradation in the initial phase.

Acknowledgements

The project is carried out within the framework of the Research Consortium “Innovative Bioprocess Technology” which is a research platform between Novozymes A/S, Danisco A/S, Chr. Hansen A/S and Center for Biochemical Engineering at The Technical University of Denmark (DTU).

References

1. N.M.E. Peij, J. Brinkmann, M Vrsanská, J. Visser, L.H.D. Graaff, Eur J Biochem 245 (1997) 164-173.
2. E.X.F. Filho, M.G. Tuohy, J. Puls, M.P. Coughlan, Biochem Soc Trans 19 (1991) 25.
3. J.A. Perez-Gonzalez, N.M.E. Van Peij, A. Bezoen, A.P. MacCabe, D. Ramon, L.H.D Graaff, App Env Microbiol 20 (1998) 1412-1419.
4. S.L. Bachmann, A.J. McCarthy, App Env Microbiol 57 (1991) 2121-2130.
5. H.R. Sørensen, A.S. Meyer, S. Pedersen, Biotech Bioeng 81 (2003) 726-731.
6. H.R. Sørensen, S. Pedersen, A. Viksø-Nielsen, A.S. Meyer, Enz Microbiol Tech 36 (2005) 773-784.
7. C. Grootaert, W Verstraete, T. Van der Wiele, Trends in Food Science & Technology 18 (2007) 64-71.
8. M.J. Vázquez, J.L. Alonso, H. Domínguez , J.C. Parajó. Trends in Food Science & Technology 11 (2000) 387-393.

Martin Hagsted Rasmussen

Phone: +45 4525 2923
Fax: +45 4525 2258
E-mail: mhr@kt.dtu.dk
WWW: http://www.chec.dtu.dk
Supervisors: Professor Kim Dam-Johansen
Associated professor Stig Wedel
Kent Thomsen & Jens Peter Hansen, FLSmidth A/S

PhD Study
Started: September 2007
To be completed: September 2010

Reduction of SO_2 Emission from Modern Cement Plants

Abstract

The project concerns the emission of SO_2 from the preheater section of a modern cement plant, with primary focus on the reaction between CaO and SO_2. This reaction is of special interest in connection with the removal of SO_2 from the flue gas because it has been shown to be many times faster than the reaction between $CaCO_3$ and SO_2. The project is in continuation of earlier projects that have been carried out in CHEC in order to understand how SO_2 is formed and removed in modern cement plants and this project will contribute to the basic understanding of the reactions and plant design.

Introduction

The most common way to produce cement today is by the dry process, illustrated in figure 1. In the dry process raw meal, which mainly consist of limestone and clay, is fed to the preheater tower which typically consist of 4-6 cyclones. Through the cyclone tower the raw meal is, step by step and counter-currently, heat exchanged with the hot flue gas from the calciner/kiln.

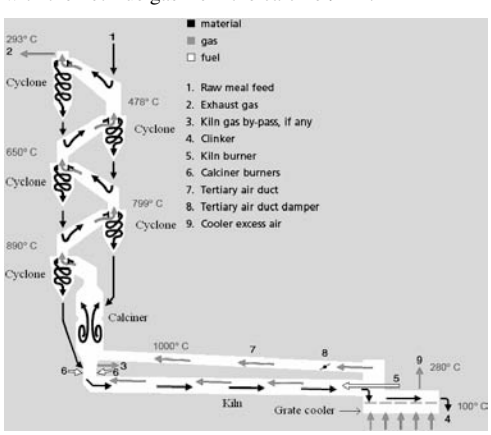

Figure 1: Illustration of the dry process for cement manufacturing.

The raw meal contains small amounts of sulfur, which is mostly found as pyrite (FeS_2). When pyrite is heated in an oxygen containing atmosphere, it will be oxidized to iron oxides and SO_2. This reaction takes place between 400 and 600 ºC [1], which in the plant shown in figure 1 corresponds to cyclone number 2 and 3 from the top. The SO_2 formed can leave the preheater as part of the gas phase or react with the limestone in the raw meal, according to Eq. 1.

$$CaCO_{3(s)} + SO_{2(g)} + \tfrac{1}{2}O_{2(g)} \rightarrow CaSO_{4(s)} + CO_{2(g)} \quad (1)$$

The reaction has been studied by Hu [2] under the conditions (relative low temperatures and short residence times) prevailing in the preheater tower. Hu [2] suggested that the reaction in Eq. 1 could be divided into three steps, consisting of a very fast initial reaction step, followed by a nucleation step in which $CaSO_4$ crystals are formed and finally a slow crystal growing step.

It is also a possibility that the SO_2 formed inside the preheater reacts with CaO, formed in the calciner and transported with the flue gas.

$$CaO_{(s)} + SO_{2(g)} + \tfrac{1}{2}O_{2(g)} \rightarrow CaSO_{4(s)} \quad (2)$$

This reaction has been studied in connection with cement preheaters by Rasmussen [3] using a commercially available CaO source, which turned out not to be representative for the CaO found in cement

plants, because it was heavily sintered. However the results showed that recarbonation of CaO and the surface area of the CaO particles are important.

Specific Objectives

The objectives of this PhD study are:

To obtain kinetic data for the reaction between CaO and SO_2, under condition similar to those in a preheater tower.

To develop a mathematical model that quantitatively can describe the reaction kinetics and transport processes.

To investigate the possibilities for designing new preheaters for cement production with low SO_2 emission.

Experimental Setup

It has been desired to construct a pilot plant setup that can be used for studying the reaction between freshly calcined limestone and SO_2. This has been done by interconnecting two existing setups situated in the CHEC laboratory hall: The Solid Fuel Flow Reactor (SFFR) and the Simulated Preheater (SP). A schematic drawing of the interconnected setup is shown in figure 2.

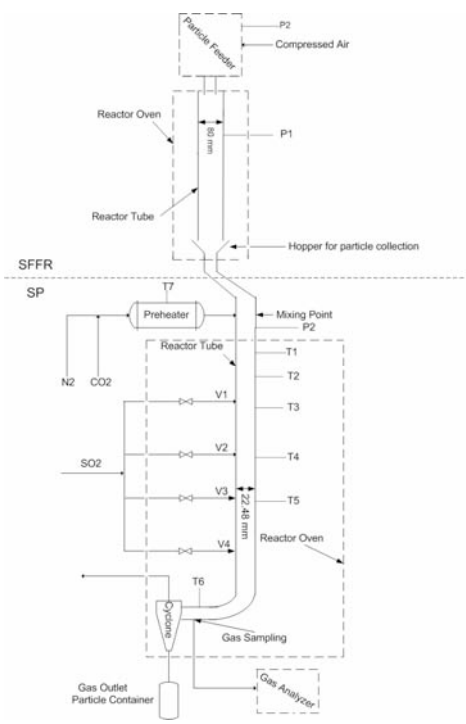

Figure 2: Drawing of the experimental setup that is intended to be used.

When making experiments raw material (limestone) is fed from the particle feeder, along with atmospheric air, through the SFFR where it is calcined at 900 ºC. The CaO formed is fed to the Simulated Preheater where it is mixed with preheated gases from the preheater. After mixing, gas and CaO proceed to the isothermal part of the SP setup, inside which injection of SO_2 is possible. The injection of SO_2 can take place through four different valves, which gives the opportunity to study the reaction at different residence times. Before leaving the setup a part of the gas is sampled for analysis, while the rest is separated from the CaO and discarded.

When operating the setup a high linear gas velocity is used in order to ensure turbulent conditions, avoid particle deposition and minimize the influence of gas film diffusion.

Results

The preliminary experiments have been focusing on the reproducibility of data and the effect of using freshly calcined limestone. The results showed that it was possible to reproduce data with a deviation from the mean that was less than ±10 %. However in order to achieve such a low deviation it was found that the SO_2 adsorption should exceed about 100 ppm.

What regards the use of freshly calcined limestone the results have shown that the reactivity is signifificantly higher compared to the commercial and sintered limestone [3].

Acknowledgements

This project is a part of a Research Platform on Future Cement Technology financed by the High Technology Foundation, FLSmidth A/S and DTU.

References

[1] J.P. Hansen, SO_2 Emissions from Cement Production, Nørhaven Digital, Cph, Denmark, 2003.
[2] G. Hu, Emission of SO_2 from Cement Production, DTU, Lyngby, Denmark, 2007.
[3] M.H. Rasmussen, Optimized Production of Cement, DTU, Lyngby, Denmark, 2007.

Oscar Andrés Prado Rubio
Phone: +45 4525 2801
Fax: +45 4593 2906
E-mail: oap@kt.dtu.dk
www: http://www.kt.dtu.dk
Supervisors: Gunnar Eigil Jonsson
Sten Bay Jørgensen

PhD Study
Started: June 2007
To be completed: May 2010

Modelling and Optimization of Integrated Bioreactor and Membrane Separation Processes

Abstract
The fermentation for lactic acid production suffers from product inhibition. Using the Integrated Reverse Electro-Enhanced Dialysis (REED) process, higher product yield can be achieved through continuous removal of lactic acid from the cultivation broth. The model of the REED module and the lactate profile in the unit are presented. This project is challenging since the design, modelling, optimization and operation of integrated biological reactive systems and membrane separation processes are complex over the space and time domain which leads to a highly nonlinear behavior.

Introduction
In recent years, there has been an increasing interest in fermentations processes since the main raw materials are renewable and products obtained in these processes are widely used in the fine chemical, pharmaceutical and food industry. The main difficulty of obtaining a high productivity in fermentation may be product inhibition of microbial growth.

Lactic acid is an important chemical used in food industry and is considered as a feedstock for the production of the biodegradable Poly-Lactic Acid (PLA). In many cases, PLA can replace hydrocarbon based polymers and therefore reduce the non-biodegradable wastes and the dependence on fossil feedstock. The fermentation of lactic acid by lactic acid bacteria normally does suffer from product inhibition; therefore, continuous removal of lactic acid from the fermenter will result in a higher productivity and product yield.

Recently, the application of membrane techniques has shown promising performance for continuous removal of Lactic Acid during fermentation [1]. The integrated REED process (fig. 1) is composed of a bioreactor, the REED module and an Electro Dialysis Bipolar Membrane (EDBM) unit.

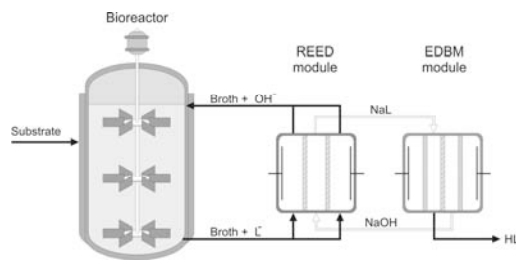

Figure 1: Flowsheet of the fermentation and recovery of lactic acid.

Specific Objectives
The key idea of this project is to reveal the interactions between the fermentation and downstream processing in dependence of primary production objective in order to optimize the integrated process and to aim at a systematic procedure for scale up. Some interesting primary objective functions are: lactate production as potential feedstock for the production of the biodegradable PLA, probiotic culture production (>10 times higher activity) or genetically modified bacteria for protein production.

Modelling the REED unit
One of the most significant obstacles in the separation using electrodialysis is membrane fouling. Previous experiments with REED have demonstrated good

antifouling results in process streams from fermentations [1]. In the REED module only Anion Exchange Membranes (AEM) are used (fig. 2). There, cations are repelled by the fixed positive charges in the membranes while lactate and hydroxide ions are allowed to pass. The direction of the electrical current is changed at regular time intervals to reduce fouling. There is a reduction in the current efficiency when the electrical current is reversed since the concentration profiles in the membranes are also reversed. As a consequence, lactate ions move back to the feed stream. Therefore, optimal operating conditions will be a trade-off between the fouling rate and the reduced current efficiency due to back-flushing of lactate when the current is reversed [2].

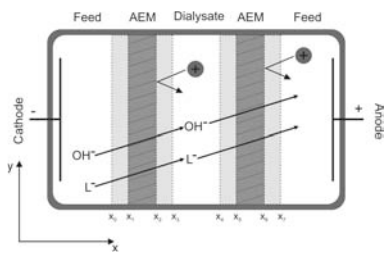

Figure 2: Electro-enhancement of dialysis setup using anion-exchange membranes [2].

The mass balances in the *x* direction can be written in a general way [3]:

$$\frac{\partial C_{k,p}}{\partial t} + \nabla \not{=}_k^p \quad 0 \qquad \begin{matrix} k = L^-, OH^- \text{and } Na^+ \\ p = phase \end{matrix} \tag{1.1}$$

Where the ionic fluxes by diffusion and migration in an ideal solution are estimated using the Nerst-Planck equation [3,4]:

$$J_k^p = -D_k \left[\frac{\partial C_{k,p}}{\partial x} + z_k \frac{F}{RT} \frac{\partial \psi}{\partial x} \right] \tag{1.2}$$

The potential gradient $\partial\psi / \partial x$ can be calculated in electrodialysis from the equation 1.3, since it is assumed that the total current is carried by ions only [3]:

$$I_d = F \sum_k z_k J_k \tag{1.3}$$

Furthermore, the relations between concentrations of the ionic species in the interface solution-membrane are given by the Donnan equilibrium condition [4]:

$$\Delta\psi_{Don} = \frac{RT}{z_k F} \ln \frac{C_k\big|_{x=x_j^-}}{C_k\big|_{x=x_j^+}} \qquad \begin{matrix} j=1,2,5 \text{ and } 6 \\ x_j^-: left;\ x_j^+: right \end{matrix} \tag{1.4}$$

At interfaces two conditions must be fulfilled, the electroneutrality condition and flux conservation [4]:

$$J_k\big|_{x=x_j^-} = J_k\big|_{x=x_j^+} \tag{1.5}$$

$$\sum_k z_k C_k^s = 0 \tag{1.6}$$

$$\sum_k z_k C_k^m + z_{fix} C_{fix}^m = 0 \tag{1.7}$$

Estimation

The model is a system of coupled algebraic and partial differential equations. By application of the method of lines the system of equations is discretized in the spatial domain to obtain a DAE system in time domain. Using this methodology the following lactate concentration profile in the module can be calculated [2].

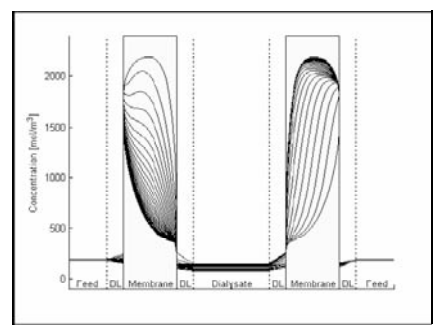

Figure 3: Lactate concentration profiles between two current reversals. The concentration profile is shown at 10 second interval [2].

Conclusions

Modelling can be used to develop a combined knowledge-based and data-driven approach for design, operation, optimization and control of bioprocesses and final production including downstream processing. This methodology will bring new prospects for substantial improvements in production efficiency and product quality.

References

[1] J-U. Rype. Separation and recovery of organic acids using Electrodialysis, Ph. D. Thesis. CAPEC, DTU. (2003).

[2] M. Møllerhøj. Modeling the REED process. MSc. Thesis. CAPEC, DTU. (2006).

[3] R. Taylor, R. Krishna. Multicomponent Mass Transfer. Jhon Wiley & Sons Inc. (1993).

[4] N. Lakshminarayanaiah. Transport Phenomena in Membranes. Academic Press. (1969).

Kavitha Chelakara Satyanarayana
Phone: +45 4525 2981
Fax: +45 4525 2906
E-mail: kac@kt.dtu.dk
WWW: http://capec.kt.dtu.dk
Supervisors: Associate Prof. Jens Abildskov
Prof. Rafiqul Gani

PhD Study
Started: June 2006
To be completed: May 2009

Computer Aided Polymer Design using Group Contribution plus Property Models

Abstract
Selecting the polymer repeat unit structure is an essential step in designing new products involving polymers. Computer aided molecular design (CAMD) is potentially extremely useful in such situations. Any CAMD application requires a set of property models to establish structure-property relationships. These relationships are developed in terms of group contribution plus property models (GC+) for polymers. Two case studies are presented in this paper to highlight to illustrate the application of the developed property models and the CAMD algorithm for polymer design.

Introduction
The search for new polymers satisfying user-specified properties is a common activity in chemical industries as many consumer products use polymers in some form. The traditional experiment based "synthesize-and-test" approach involves protracted and costly series of experiments for synthesizing each product candidate and evaluating their ability to satisfy the demands placed upon them. Computer-aided molecular design (CAMD) methods[1] can partially replace the experiments by forecasting promising (molecular level) polymer structures that meet the required target properties. To extend existing CAMD techniques to polymers, new property models as well as modified CAMD algorithms are necessary. The group contribution plus (GC^+) models[2], which integrate important aspects of previously established state-of-the-art techniques[3,4] based on group and atomic contributions to polymer repeat unit properties, are developed in this work. In order to save development time for the GC^+ models properties of polymer repeat units, OfficeGRID[5], a grid technology based software has been used for parallel development of GC^+ models. In all 20 property models for polymer repeat units were developed at a considerably reduced the time for model development[1].

Methodology
CAMD approach to polymer repeat unit design can be divided into two important stages: stage 1 corresponds to developing property prediction models and stage 2 to developing an algorithm for identifying candidates that match the target properties.

GC^+ Models
GC^+ Models are the combination of Marrero/Gani group contribution models and atom – connectivity index models, where the unavailable GC contributions are predicted from the atom-connectivity contributions, thereby expanding the application range of the "host" GC-model without the need for additional experimental data.

Marrero/Gani group Contribution Method[6]
The Marrero/Gani group contribution model is usually written as,

$$f(x) = \sum_i N_i C_i + w \sum_j M_j D_j + z \sum_k O_k E_k \qquad (1)$$

where C_i is the contribution of the first-order group of type-i that occurs N_i times, D_j and E_k the contributions of the second-order group of type-j and the third-order group of type-k, that occurs M_j and O_k times, respectively. In the first level of estimation, where $w = z = 0$, only first-order groups are employed. In the second level, where $w = 1$ and $z = 0$, only first- and second-order groups are involved. In the third level, both $w= 1$ and $z = 1$, and contributions of groups of all levels are included in the calculation. The left-hand side of Eq. (1) is a simple function, $f(X)$, of the property, X

Atom-Connectivity Index Method
Polymer-repeat unit structures can also be given by an atomic representation for connectivity index-based models, as written by Gani et al. [7]

$$f(X) = \sum_i a_i A_i + b({}^{v}\chi^{0}) + 2c({}^{v}\chi^{1}) + d \qquad (2)$$

X is the polymer property, A_i is the contribution of atom i occurring in the polymer-repeat unit structure ai times. ${}^{v}\chi^{0}$ and ${}^{v}\chi^{1}$ are the zeroth- (atom) and first-order (bond) connectivity indices, b, c, d are adjustable parameters.

Polymer property models for ten properties have been developed so far using the GC+ approach[2], 10 for based on GC, and 10 based on CI to obtain the 10 GC+ models.

CAMD algorithm for polymer design

As a set of polymer property prediction models were developed, the next step was to solve the reverse problem of designing a polymer-repeat unit structure for a given set of target properties. Here, the CAMD algorithm developed by Harper & Gani[1] for molecular design has been adapted for polymer design, where the issue of calculating the missing group contributions, if required, has also been added. The "generate and test" paradigm has been used again for identifying the polymer repeat unit candidates.

Any CAMD problem has two main criteria to be defined. Structural criteria – which gives the details like how the repeat unit structure should be represented. For example, for a representation by groups, how many groups (maximum and minimum) can be present, how many times a particular group can occur in the repeat unit, and rules for combining them. Moreover any chemical structure that is generated should also satisfy certain structural conditions, which for polymer repeat units and molecules are the same except for the two free attachments in the former. The combination rules have been adapted from those of Harper & Gani[1]. Property criteria – these constraints give the information of the target properties that the feasible candidates must have. Mathematically, it can be written as $P_l \leq P(n_i) \leq P_u$, where n_i is the number of times the *i*th group appear in the polymer, $P(n_i)$ is the vector of predicted properties for the polymer, P_l is the vector of lower bounds specified on the various polymer properties and P_u is the vector of upper bounds specified on the various polymer properties.

The Marrero/Gani group contribution method[6] is advantageous with respect to CAMD-based polymer design because it has a large range of groups, classified as either first -, second -, and third – order, and from which, new polymer property models can be developed and used for generation of polymer-repeat unit structures. Nevertheless, all GC-based methods need the entire polymer repeat unit structure to be described by the available groups defined for that method, in order for the relevant property to be predicted. This is where the GC+ models become useful because for any generated structure, if the group contribution is missing, it can be automatically predicted through the available atom-CI contributions.

Figure 1, shows the main steps of the CAMD algorithm adapted for polymer design. Through it, the polymer repeat unit structures, for the given set of structural and property (target) constraints, without having any limitations due to missing group or missing group contributions, can be identified. Given the limitations on the number of reliable data on polymer systems, one cannot expect to have extensive group tables covering all possible structures and properties – these needs to be developed over a period of time. However, as stated above, the GC+ approach has been adopted in the "testing" part of the CAMD algorithm to increase the application range for polymer design.

Case Study

Several case studies reported earlier[8, 9] have been solved to verify the applicability of the developed CAMD algorithm for polymer design and the polymer property models. In all cases, the reported solutions were identified in addition to new ones not reported earlier. In this paper, two new and more realistic polymer design problems are introduced: case study A deals with the design/selection of polymers that has applications as coatings while case study B deals with the design/selection of polymers that can be used as synthetic fibers (to be used as textile products).

Case Study A

Problem formulation: Designing a polymer that has its applications in several areas, such as, coating in cookware, pipes or containers, in insulation cables, bearings, gears, etc., could be very interesting for the modern society. For the polymer to find its applications in the areas mentioned above, several criteria need to be satisfied. To find an application as coating in cookware or pipes or containers, the polymer should be chemically inert, very low friction (which also gives the polymer a non-stick texture) and high heat resistance. The low friction property also allows the polymer to be used in applications where sliding action parts are needed, such as, bearings, brushings, gears, and slide plates. Dielectric constant plays an important role for selecting a polymer to be used as an insulator.

Physical property constraints

Dielectric constant (ε): Normally the dielectric constant of polymers at room temperature is in the range 2 to 10. The lower values of dielectric constant are generally being associated with the lowest electrical loss characteristic[10]. Any material that can be used as an insulator should provide low electrical loss, which implies should have low dielectric constant. Therefore, upper and lower bounds for this property can be written as $2 \leq \varepsilon \leq 2.5$.

High heat resistance: As the desired polymer repeat unit structure should have high heat resistance so as to find its applicability as coating in cookware, it implies that the melting point of the desired candidate should be higher than the cooking temperature. It is therefore desired that the melting point of the polymer should be within 320 to 370 °C. That is $320 \leq T_m \leq 370$. Using the

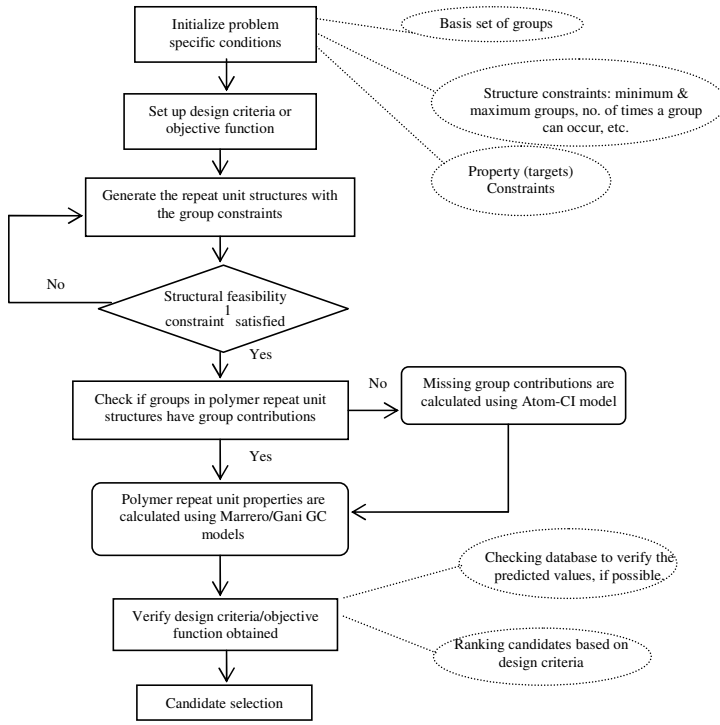

Figure 1: Algorithm for Computer Aided Polymer Design

following relation between melting point and glass transition temperature as given by van Krevelen[3].

'Polymers with T_g/T_m ratios below 0.5 are highly symmetrical and have short repeat units consisting of one or two main-chain atoms each carrying substituents consisting of only a single atom. They are markedly crystalline. ($T_g/T_m \approx 0.5$)'

the lower and upper bounds for T_g can be obtained as $297\ K \leq T_g \leq 322\ K$.

Young's Modulus: Young's Modulus measures how 'stiff' the material is. As the desired polymer is required to coat on the surface of the cookware (our target product) the desired candidate should be flexible enough to be coated in its applications while retaining optimum strength. From the plot of Young's Modulus-density[15], the constraints can be taken as $0.3\ GPa \leq E \leq 0.6\ GPa$. From the same plot[11], for the upper and lower constraints of Young's modulus in the polymer region, density is found to have the lower and upper bounds as, $1.0\ g/cm^3 \leq \rho \leq 2.4\ g/cm^3$. Note that using the density as a property constraint and the plots[15] of Young's modulus against density, we avoid the need for a property model for Young's Modulus for polymers.

Structural feasibility constraints: The basis set of 6 Marrero/Gani groups are taken as shown in table 1. Since, glass transition temperature and melting point relationship is considered, the minimum groups in the generated repeat unit structure is taken as 1 and maximum groups are taken as 3, so as to have a short repeat unit structures.

Final Candidates: Out of the generated candidates, 55 candidates satisfy the structural constraints. The group –CHF-, which was used in the basis set, did not have the Marrero/Gani contributions for glass transition temperature and dielectric constant. Its contributions were determined using atom-CI models for these properties. Out of 55 candidates, 47 satisfied the density criteria; 12 satisfied glass transition criteria and 27 satisfied dielectric constant criteria. But on the whole, only 4 candidates satisfied all the three criteria. Teflon[12], which is commonly used in cookware, insulation material, etc., was one of the 4 final candidates satisfying all the property constraints. From the literature it is found that teflon has very low friction, enabling it to be used in several applications like the ones discussed above in the problem formulation part. The predicted values for teflon match very well with the reported literature[12] values.

Table 1: Final Candidates satisfying the structural & property constraints for case study

Basis Set	CH_2, CH_3, CH, CF2, CHCl, CHF		
Repeat Units	T_g (K)	$\rho(g/cm^3)$	ε
$-[CF_2\text{-}CHF]_n-$	296.8	2.06	2.23
$-[CF_2\text{-}CH(CH_3)]_n-$	310.3	1.49	2.18
$-[CF_2\text{-}CH(CH_3)\text{-}CHF]_n-$	302.8	1.53	2.01
$-[CF_2\text{-}CF_2]_n-$ (Teflon)	317.1	2.4	2.1

Conclusion

The results from the case studies showed that the adapted CAMD algorithm plus the corresponding property models can solve realistic polymer design problems. In this case, the use of the GC+ property models proved to be very useful and efficient. Even though the case studies, which should be regarded as proof of concept studies, have been solved for relatively low number of basis groups, having the corresponding software means that size is not really a factor. The important issue is whether realistic problem can be solved and useful candidates can be identified. The reported results show that the design algorithm and the property models can satisfy this demand. Wider applications mean more groups and contributions for more property models. The design algorithm, however, is generic and can handle any number of groups and/or models. The focus of future work is in the area of new properties as well as higher level of polymer models where the organization of the polymer repeat unit is considered.

References

1. P. M. Harper, R. Gani, Computers & Chemical Engineering, 24 (2000), 2-7, 677-683.
2. K.C. Satyanarayana, R.Gani, J.Abildskov, Fluid Phase Equilibria, 261(2007) 58 – 63.
3. D.W. Van Krevelen, Properties of Polymers, Elsevier (third completely revised edition 1990).
4. J. Bicerano: Prediction of Polymer Properties. Marcel Dekker Inc., 2002.
5. http://www.meshtechnologies.com/products.php?id=OfficeGRID.
6. J. Marrero and R. Gani, Fluid Phase Equilibria, 183-184 (2001) 183 – 208.
7. Gani, R.; Harper, P.M.; Hostrup, M.; *Ind. Eng. Chem. Res.*, 2005, 44, 7262.
8. Derringer, G. C.; Markham, R. L. A Computer-Based Methodology for Matching Polymer Structures with Required Properties. J.Appl. Polym. Sci. 30 (1985), 4609.
9. Venkatasubramanian, V.; Chan, K.; Caruthers, J. M. Computer-Aided Molecular Design using Genetic Algorithms. Computers &.Chemical Engineering, 18 (1994), 9, 833.
10. http://www.ami.ac.uk/courses/topics/0115_cai/index.html
11. http://www-materials.eng.cam.ac.uk/mpsite/interactive_charts/stiffness-density/NS6Chart.html
12. http://en.wikipedia.org/wiki/Polytetrafluoroethylene

Daniel Schäpper
Phone: +45 4525 2960
Fax: +45 4593 2906
e-mail: dsc@kt.dtu.dk
www: www.kt.dtu.dk
Supervisors: Krist V. Gernaey
Anna Eliasson Lantz
Stuart Stocks, Novozymes A/S

Ph.D. Study
Started: May 2006
To be completed: April 2009

Continuous Culture Microbioreactors

Abstract
The current microbioreactors mostly operate as fed-batch or continuous culture with *E. coli* as culture strain. This projects aims to design a microbioreactor running continuous cultures of *S. cerevisiae* in a reactor volume of approximately 100µL. The most important culture parameters can be measured on-line allowing for a high information-per-experiment ratio. Industrial relevance will be proven through comparisons of continuous culture microbioreactor experimental data with bench-scale experiments performed at BioCentrum-DTU.

Introduction
Biotechnology plays an increasingly important role in production processes in the food, the chemical and the pharmaceutical industry. Well-known examples of biotech-based products that have an important function in the life of many people are enzymes used in laundry detergents, pharmaceuticals such as insulin, etc.

However, starting up a new biotechnological production is usually preceded by a tremendous research effort in which for example the productivity of different candidate production strains is compared (=screening). Usually, such screening is done in shake flask cultures. In a later stage of production process development, experiments done in bench scale reactors are performed to investigate the influence of process conditions on productivity.

Experiments done in shake flasks (typically with a volume of 100 mL to 1 L) are easy to set up. However, shake flask cultures only allow batch experiments, and the information gained per experiment is limited: typically only end-point measurements of for example the product quality are performed. If additional measurements are needed, manual sampling is required, which additionally disturbs the culture. Compared to shake flasks, bench scale reactors (typically with a volume of 1 to 10 L) have the advantage that they allow on-line measurements. Moreover, bench scale reactors are flexible since they can be operated in batch or fed-batch, but also as a continuous culture. However, the work effort needed to prepare, operate and subsequently clean bench scale reactors is vast.

Summarizing, biotechnological process development is expensive, for example because both traditional cultivation methods work with substantial volumes that in turn then require preparation of the appropriate amount of expensive nutrient media.

Motivation
Microbioreactors (MBRs) offer the possibility to circumvent many of the above-mentioned problems:

- The production cost of the MBRs is low, since they can be produced from polymers.
- The working volumes are very small (in the µL/mL range), keeping costs for culture media low.
- On-line measurements are possible for the most important culture parameters (optical density (OD), dissolved oxygen (DO), pH).
- Batch, fed-batch and continuous culture conditions can be created in MBRs.
- The reactors are disposable after use and thus require no cleaning effort at all.
- Scaling out MBRs to systems with many parallel reactors allows for high-throughput screening, thus yielding a massive gain in information per experiment with continuously small working volumes.

The above advantages result in more-information-per-experiment (on-line measurements), financial savings (small volumes, less labor intensive) and the possibility to develop production schemes on the resource-saving micro-scale before scaling up a process.

Objectives

Currently, MBRs described in the literature are operated either as fed-batch or as continuous cultures, most often with *E. coli* as the culture strain. This project aims at the development of a continuous culture MBR that can perform experiments with yeast (*S. cerevisiae*). Compared to a batch experiment, the continuous culture has the advantage that steady-state conditions can be achieved. Additionally, it should be possible to induce step changes in the dilution rate, forcing the culture from one steady-state to the other with continuous measurement of the important culture parameters, thus leading to dynamic information on the behavior of the culture under well-controlled experimental conditions.

The planned working volume is in the range of 100µL, which is smaller than most of the current reactors running continuous cultures.

In the first part of the project, a reactor with the above features is to be designed and fabricated, and a complete measurement & control setup is to be installed. The second step will then be to prove the industrial relevance through comparisons of experimental MBR results with larger-scale data from the literature and from *S. cerevisiae* cultivations performed at BioCentrum-DTU.

Naturally, MBR construction also poses some challenges. Proper mixing for example is very essential for good cultivation results, since substrate gradients in the culture might otherwise lead to a varying (location dependent) metabolic state of the culture. In the projected volume range turbulent flow is difficult to achieve due to the small Reynolds numbers. On the other hand the volume is too large to be able to rely on diffusion alone. Therefore one of the challenges in the project is to find a mixing regime which efficiently reduces diffusion distances.

Another challenge is the mechanical integration of the various sensors, a mixing apparatus and the aeration system into the small volume in such a fashion that the device is easy to manufacture.

Microbioreactor Technology

The current reactor is designed to have a working volume of 100 µL which is sufficiently large to allow enough space for the sensors and actuators, but is still small enough to considerably reduce the amount of media needed.

Contrary to conventional reactors which are mostly aerated by means of bubbles, microbioreactors are designed to work bubble-free. Aeration is done through a semi-permeable silicone membrane which allows both the incoming transport of oxygen and the outgoing transport of CO_2.

DO and pH are both measured with fluorescent sensor spots which change both the amplitude and the phase of the emitted light with a change in the sensitive parameter. A lock-in amplifier measures the phase difference and thus quantifies the measured parameter.

Optical density is continuously measured both in the reactor itself and in the outflow channel. Light from a LED is guided into the reactor with optical fibers, sent through the substrate and then guided to a photo detector (Figure 1).

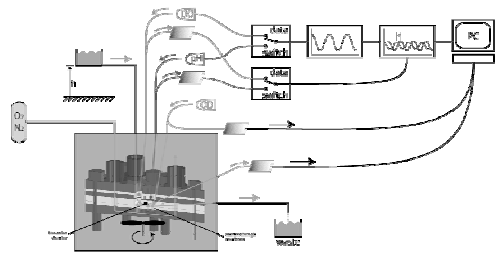

Figure 1: Schematic of a MBR setup

The flow rate is currently adjusted by a syringe drive. Both continuous and step changes in flow rate are possible which allows for various changes in dilution rates.

The reactor is currently fabricated out of the polymers poly(methylmethacrylate) (PMMA) and poly(dimethylsiloxane) (PDMS), which both are cheap materials. Additionally, no clean room fabrication steps are necessary which allows for cheaper manufacturing. Indeed, it means that the final product can be mass-produced, sterilized and pre-packaged similar to syringes.

Work Done

On the one hand a reactor was designed and fabricated, on the other hand the supporting systems were developed. These include tempering & aeration of the broth and measurements of optical density and dissolved oxygen. Also the LabView system that measures and controls the system has been set up. First preliminary cultures with bakers yeast have been run both in batch and in continuous mode proving the basic functionality of the system.

However, mixing still poses a problem and is currently preventing representative cultivations. The challenge here is to provide good mixing (for suspension of the cells, aeration & nutrient provision) without having a complicated setup.

Next Steps

Mixing is the very next problem to solve. Once this is done, cultivations shall be run which first prove the comparability of this system with bench-scale reactors and then pH measurement and control shall be incorporated.

In a next step other measurement principles shall be investigated which might further increase the amount of on-line information per experiment.

Acknowledgements

The Novozymes Bioprocess Academy is acknowledged for the financial support of this project.

Also, I would like to thank all my supervisors for their continuing support.

Ravendra Singh

Phone: +45 4525 2911
Fax: +45 4593 2906
e-mail: rs@kt.dtu.dk
www: http://www.capec.kt.dtu.dk/people/phd
Supervisors: Rafiqul Gani
Krist V. Gernaey

Ph.D. Study
Started: September 2006
To be completed: August 2009

Design of Process Monitoring and Analysis Systems (PAT* Systems)

Abstract

In the manufacturing industry, for example, the pharmaceutical industry, a thorough understanding of the process is necessary in addition to a properly designed monitoring and analysis system (PAT system) to consistently obtain the desired end-product properties. A *model-based computer-aided framework* including the methods and tools through which the design of monitoring and analysis systems for product quality control can be generated, analyzed and/or validated, has been developed. Two important supporting tools within the framework are a knowledge base and a model library. The knowledge base provides the necessary information/data during the design of the PAT system and the model library generates additional or missing data needed for design. Optimization of the PAT system design can be achieved in terms of product data analysis time and/or cost of monitoring equipment subject to the maintenance of the desired product quality.

* PAT: Process Analytical Technology

1. Introduction

Conventional experience and lab-based manufacturing practices provide product of the specified quality but at the expense of time and money. Today a significant opportunity exists to improve the product quality and to optimize the production process through the implementation of innovative system solutions for on-line monitoring, analysis and system control. Application of PAT systems (FDA/CDER, 2005) in manufacturing paves the way for continuous process and product improvements through improved process supervision based on knowledge-based data analysis, 'Quality by design' concepts, and through feedback control (Gnoth et al., 2007). Currently, one of the main difficulties in implementing PAT systems on a manufacturing process is the unavailability of methods and tools through which a PAT system can be designed in a systematic way. In this paper a *model-based computer-aided framework* is presented, including the methods and tools through which the design of monitoring and analysis systems (i.e., the PAT systems) for product quality monitoring and control can be generated, analyzed and/or validated.

2. Specific objectives

The main objective of the project is to develop a model-based computer aided framework for supporting the design, implementation and verification of PAT systems. The model-based framework should be able to perform the following tasks:

- Analyze the manufacturing process in order to identify the critical points and process variables
- Identify the variables that need to be measured and the variables that will need to be manipulated to achieve the desired product quality.
- Select the proper methods and tools for obtaining the measured data
- Connect the measured variables with the manipulated variables (sensor-actuator pairing)

3. Design framework

The *design of a process monitoring and analysis system* is a step-wise procedure involving the selection of critical process variables, followed by the selection and placement of suitable monitoring and analysis equipments, and finally, the coupling of the monitoring and analysis tools to a control system to ensure that the selected critical process variables can be controlled. As shown in fig. 1, the starting point for the design methodology is the problem definition in terms of process specifications and product quality specifications that can be provided either by the manufacturer or the PAT system designer. A model library and a knowledge base have been developed, and act as the supporting tools for the design of a PAT system. The ICAS-MoT modeling tool (Sales-Cruz, 2006) is used for simulation

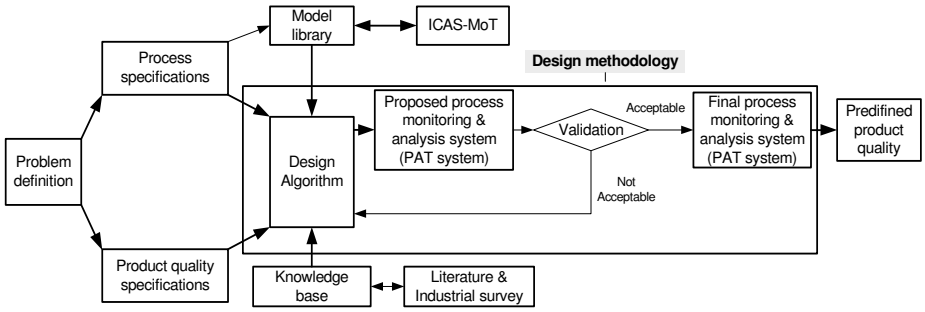

Figure 1. Framework overview

of process operational models and the systematic procedure proposed by Gani (Gani et al., 2006) is used for model analysis. As shown in fig.1, the developed design algorithm relates the available product and process specifications to the available supporting tools, and subsequently generates the PAT system design. If the obtained PAT system satisfies the requirements then it is selected as the designed PAT system. The validation of the obtained PAT system is achieved by comparing the simulated process performance with known process specifications. If the process performance does not comply with the process specifications then the corresponding design steps are repeated until a satisfactory design is obtained.

3.1. Supporting tools

3.1.1. Knowledge base

The knowledge base contains useful information needed for design of PAT systems. It has been built through an extensive literature and industrial survey. It covers a wide range of industrial processes such as fermentation, crystallization and tablet manufacturing. It contains information for typical unit processes in terms of the type of operation they perform, the process variables involved, the corresponding manipulating variables (actuators), the equipments typically used for on-line measurement of data (type of equipment, accuracy, precision, operating range, response time, resolution, drift, cost etc.).

3.1.2. Model library

The model library contains a set of mathematical models for different types of unit processes, sensors and controllers. Similar to the knowledge base, it covers a wide range of industrial processes (fermentation, crystallization, tablet manufacturing). These models support process analysis and help to generate additional or missing data needed to obtain the design of a PAT system. For example, the models can be applied for the prediction of process variables which are not measurable but required for the final design. Simulations with the models can also be used for performing a sensitivity analysis through which the effect of process variables on the final product properties can be analyzed and critical process variables can be identified. The simulation models also provide input for the interdependency analysis, through which the appropriate actuators for each controlled variable can be selected.

3.2. Design methodology

The methodology used for the design of the PAT system is shown in fig. 2 which consists of four analysis steps.

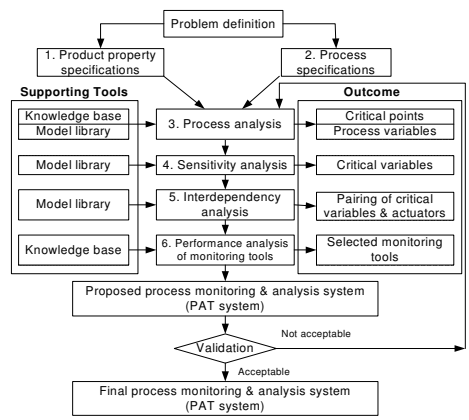

Figure 2. Design methodology

3.2.1. Process analysis

This step is concerned with the listing of the variables involved in the process, and the listing of critical points of the process where monitoring might be required. This can be achieved through a systematic process analysis by using the available product/process specifications and supporting tools (model library and knowledge base).

3.2.2. *Sensitivity analysis*

Through a sensitivity analysis the critical process variables are identified from the selected list of process variables. The model library or process data (if available) are used for this analysis. To perform the sensitivity analysis, the process operational model is simulated through ICAS-MoT. The effect of each process variable on the target product properties is analyzed systematically through open loop simulation. The operational objectives have to be assessed first. If an operational objective is not achieved, then the process variables have to be analyzed. The variables which violate the operational limit and have a major effect on the product quality are considered as the critical process variables. For some of the variables

which can not be modeled the sensitivity analysis has to be performed qualitatively through inference from the knowledge base and/or by the use of process data. All the critical process variables need to be monitored and controlled but for some of the critical variables that can not be measured in real time, some other properties have to be measured that are correlated to them closely enough so that all critical variables can be measured and controlled by using the correlations to the measurable variables (inferential control).

3.2.3. Interdependency analysis

The interdependency analysis is performed to select the appropriate actuators for each selected control variable. In this analysis the effect of process parameters on the individually selected critical process variable is compared. A special feature (Sales-Cruz and Gani, 2006) of ICAS-MoT can be used for this analysis. First, the response variable and the sensitivity parameters are selected. Then these parameters are perturbed and the effect of each parameter on the response variable is analyzed. The process parameter which has the most significant effect on the considered critical process variable (response variable) is selected as the actuator for that variable.

3.2.4. Performance analysis of monitoring tools

The performance analysis of the process monitoring tools is performed to select the appropriate monitoring tools for each measurable critical process variable. The measurement equipment for each measured critical process variable is selected from the knowledge base, where one is able to list all the available sensors included in the knowledge base for that variable. The performance of different types of measurement equipment can be compared. The monitoring tool is then selected on the basis of one or more of the following performance criteria: accuracy, precision and resolution, sensor drift, response time and cost and operating range. The type of performance criterion selected is application specific.

4. Case study: Fermentation process - Design of PAT system

The process flow sheet is adopted from the literature (Petrides et al., 1995) (see fig. 3).

4.1. Product property specifications

The desired product from the fermentation process is *E. coli* cells. At the end of the fermentation process, the assumed *E. coli* cell concentration is 30 g/liter (dry cell weight) in which the protein content is assumed to be 20% of the dry cell mass. The composition (mass basis) of the outlet stream from the fermentor comprises 2.95% biomass, 4.00% glucose, 0.58% salts, and 92.46% water.

4.2. Process specifications

The basic raw materials required include: starting culture (*E. coli* cells), nutrients (glucose and salts), tryptophan, water, ammonia and air. The process equipment includes: fermentor, mixing tank, continuous heat sterilizer, centrifugal compressor, air filter and storage tank.

4.3. Process analysis

The process analysis provides the following list of process variables: temperature in the fermentor, pH in fermentor, dissolved oxygen (DO) in the fermentor, dissolved CO_2 in the fermentor, coolant flow rate, coolant temperature, ammonia flow rate, stirrer speed in the fermentor, stirrer speed and stirring duration in the mixing tank, air flow rate to the fermentor, heat sterilization temperature, steam flow rate in sterilizer, stirrer speed in the mixing tank and stirring duration, cell growth rate, heat of reaction, substrate concentration, biomass concentration in the fermentor, homogeneity in the fermentor, homogeneity in the mixing tank

4.4. Sensitivity analysis

Sensitivity analysis provides the following critical variables: temperature, pH, DO, dissolved CO_2, homogeneity in the fermentor and temperature in sterilizer and homogeneity in the mixing tank.

4.5. Interdependency analysis

Interdependency analysis is performed for each critical process variable to select the actuator. The obtained actuators are as follows: coolant flow rate for temperature, ammonia flow rate for pH, air flow rate for DO and dissolved CO_2, stirrer speed for homogeneity control in the fermentor, steam flow rate for heat sterilization temperature control and stirring duration for homogeneity in the mixing tank.

4.6. Performance analysis of monitoring tools

The performance of available monitoring tools (obtained from the knowledge base) for each measured variable is compared and monitoring tools are selected as follows: Thermocouple for temperature, electrochemical sensor for pH, optical sensor for DO and dissolved CO_2, and NIR for homogeneity.

4.7. Proposed process monitoring and analysis system

A feasible alternative of the process monitoring and analysis system is shown in fig. 3. Within the fermentor, the DO concentration, pH, temperature and homogeneity need to be monitored and controlled. Temperature in the heat sterilizer and homogeneity in the mixing tank also need monitoring and control. The aeration intensity used for DO control also influenced the dissolved CO_2 concentration, and thus it is not needed to control this variable explicitly. The critical process variables, corresponding monitoring tools and actuators are shown in fig. 3. The response time of the selected monitoring tools is also shown in the figure, which illustrates that the selected monitoring tools are robust enough to allow for successful implementation of the control system.

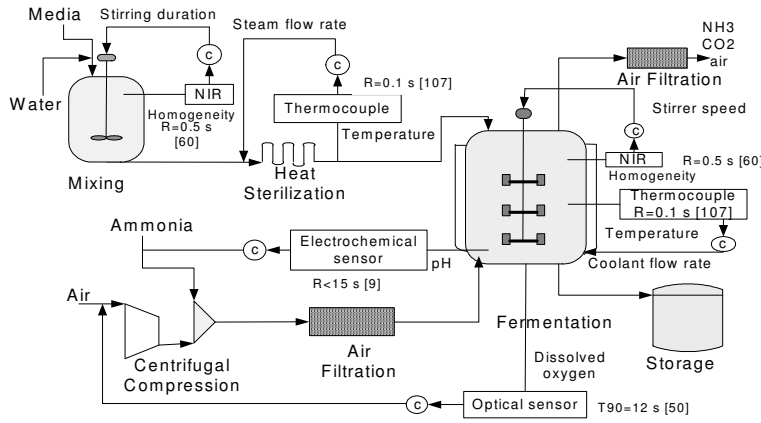

Figure 3. Fermentation process flow sheet with designed PAT system.
c: controller, R: response time, T90: time for 90% response, NIR: near infrared, [ ]: indicates the reference number in the knowledge base

5. Conclusions

A well-designed PAT system is essential to obtain the desired product quality consistently. In this work we proposed a model-based computer aided framework including the methods and tools for systematic design of PAT systems. The application of the developed framework and methodology was demonstrated through a fermentation process case study. The developed framework and methodology are generic: the proposed systematic approach to the design of a PAT system is complimentary to traditional process design, and should thus have a broad application range in chemical and biological processes.

6. Future work

The following case studies are being studied to demonstrate the application of the developed framework and methodology:

- Insulin production process which includes fermentation and downstream processing
- Tablet manufacturing process
- Crystallization process

Acknowledgement

The author acknowledges the financial support of the Technical University of Denmark.

References

1. FDA/CDER, 2005, PAT, Process Analytical Technology (PAT) Initiative, U.S. Food and Drug Administration, Center for Drug Evaluation and Research, http://www.fda.gov/Cder/OPS/PAT.htm
2. Gani, R., Muro-Suñé, N., Sales-Cruz, M., Leibovici, C., & Connell, J. P. O. (2006). Fluid Phase Equilibria, 250, 1-32.
3. Gnoth, S., Jenzsch, M., Simutis, R., & Lübbert, A. (2007). Journal of Biotechnology, 132 (2), 180-186.
4. Petrides, D., Sapidou, E., & Calandranis, J. (1995). Biotechnology and Bioengineering, 48 (5), 529-541.
5. Sales-Cruz, M. (2006). Development of a Computer Aided Modelling System for Bio and Chemical Process and Product Design. PhD. Thesis, CAPEC, Department of Chemical Engineering, Technical University of Denmark.
6. Sales-Cruz, M., & Gani, R. (2006). ChERD, 84 (A7), 583-594.

Publications

1. Singh, R., Gernaey, K. V., Gani, R., "Model-based Computer Aided Framework for Design of Process Monitoring and Analysis Systems", presented at APACT-07 (Advances in Process Analytics and Control Technologies 2007), Edinburgh, UK, April/ May 2007 (oral presentation)
2. Singh, R., Gernaey, K. V., Gani, R., "Design of Process Monitoring and Analysis Systems, using a Model-based Computer Aided Framework", presented at ECCE6 (European Congress of Chemical Engineering-6), Copenhagen, Denmark, September 2007 (oral presentation)
3. Singh, R., Gernaey, K. V., Gani, R., "Design of Process Monitoring and Analysis Systems", presented at AIChE annual meeting 2007, Salt Lake city, Utah, USA, November 2007 (oral presentation)
4. Singh, R., Gernaey, K. V., Gani, R., "Supporting Tools for Design and Validation of PAT system", presented at AIChE annual meeting 2007, Salt Lake city, Utah, USA, November 2007 (poster presentation)
5. Singh, R., Gernaey, K. V., Gani, R., "Off-line design of PAT systems for on-line applications", submitted to ESCAPE-18 proceedings
6. Singh, R., Gernaey, K. V., Gani, R., "Model-based Computer Aided Framework for Design of Process Monitoring and Analysis Systems", to be submitted to Computers and Chemical Engineering Journal

Piotr Szewczykowski
Phone: +45 4525 6814
Fax: +45 4588 2161
E-mail: pps@kt.dtu.dk
WWW: www.polymers.dk
Supervisors: Martin E. Vigild, KT
Sokol Ndoni, Risø

Ph.D. Study
Started: February 2005
To be completed: February 2008

Gyroid Membranes Made from Nanoporous Block Copolymers

Abstract
Among many different potential applications of nanoporous materials from block copolymers we can find ultrafiltration membranes. Gyroid (GYR) morphology of block copolymers is a good candidate for membrane application since it is a bicontinuous structure and it does not need to be aligned to assure the percolation. After crosslinking the majority block and etching of the minority block, the nanoporous material is obtained. The self-supporting membranes of 0.5mm thickness, made by solvent casting technique, was analyzed for the possibility of separation of polyethylene glycol (PEG) molecules of different molecular weight dissolved in methanol/water (80/20) or in water/methanol (80/20) mixture. Permeates and feeds were analyzed by size exclusion chromatography (SEC). The very first results indicate that the cut-off value is between 8000 and 12000[g/mol]. Fluxes of pure solvents and feed solutions were measured. The value was around 1 [l/m^{2}h].

Introduction
Pore size distribution determines the separation properties of porous membranes[1]. Membrane properties depend also on the morphology and on the monodispersity of the pores[2]. Of course the tunability of the pores is desired in order to obtain an efficient membrane. We can use the membrane for separation of the molecules of a small size if we can reduce the pore size diameter. Selectivity of the membrane can be much increased by obtaining the pores in the range of nanometers instead of micrometers. Separation and selectivity depends also on enthalpic interactions with the pore surfaces, therefore on the surface area and surface chemistry.
Potential application as separation media is mentioned in almost any article on nanoporous materials obtained from diblock copolymers[3,4,5]. Till now the effort was to use the hexagonally packed cylinders morphology (HEX) and orient cylindrical cavities perpendicularly to the main surface of the membrane. Orientation of the cylinders in the flow direction and perpendicularly to the main surface is necessary in order to use the material as a membrane. A considerable amount of publications report on the preparation and characterization of thin nanoporous films showing the HEX morphology[6]. Some authors showed that it can be used indeed as an ultrafiltration media, for example to separate viruses[7]. In the case of membranes prepared from diblock copolymers, the gyroid (GYR) morphology is alternative to the hexagonal morphology. The biggest advantage of the cubic GYR structure is, that due to its isotropy it does not need to be oriented in any direction to ensure the percolation from one side of the membrane to the other. The reason for that is that this is a bicontinuous cubic structure of $Ia\bar{3}d$ symmetry. One disadvantage relates to the difficulty of preparation of the gyroid morphology, since it occurs in a narrow range of the diblock copolymer micro phase space, i.e. in a narrow range of composition, chain length and temperature. A strict control of the polymerization process is necessary in order to reduce the composition and chain length composition. This is possible by application of elaborate polymerization techniques such as living anionic polymerization and in lesser degree atom transfer radical polymerization (ATRP). However once the process of synthesis is standardized the samples with GYR morphology can be obtained. The diblock copolymer of 1,2-polybutadiene-*b*-polydimethylsiloxane (1,2-PB-PDMS) with GYR morphology was synthetized by living anionic polymerization. Since both blocks of the copolymer have glass transition temperatures (T_g) below the room temperature it was necessary to crosslink the majority block before etching of the minority block. Otherwise the pores formed during the removal of the minority block would collapse on result of high internal Laplace pressure[8].

The gyroid morphology of diblock copolymers was characterized by many authors[9], but in our knowledge its use as a membrane application has not been reported till now. In our work we try to find out if nanoporous membranes prepared from diblock copolymer with GYR structure can fulfill the demands for the high selectivity and high fluxes? Can we obtain a membrane with very uniform pore size of diameter in the range of nanometers? What selectivity will we get and what kind of solvents can we use?

Nanoporous materials preparation

Block copolymer synthesis. The precursor block copolymer 1,2-polybutadien-*b*-polydimethylsiloxane was synthesized by the living anionic polymerization.

Solvent casting and crosslinking. Dicumyl peroxide (*bis((α,α-dimethylbenzyl) peroxide*) (DCP) (Merck) was used as the crosslinker. 1 mol% of DCP relative to the double bonds in the polybutadiene block was enough to sure pore stability after the etching process.

Etching of PDMS. 1M solution of tetrabutylammonium fluoride (TBAF) in tetrahyfrofurane (THF) (Aldrich) was the compound used for etching PDMS the minority block from the crosslinked copolymer. According to established procedure 5 times molar excess of TBAF relative to the PDMS repeating unit and a reaction time of 36h assure quantitative removal the PDMS block. A nanoporous sample, referred as Sample 1 was obtained after etching.

Membrane performance

Setup

A simple set up (***Figure 1***a) was used for the filtration experiments. Nitrogen was the gas used to create pressure on the feeding side of the membrane. The gas reducer, manometer, security valve, stainless pipes and membrane device were the main parts of setup. The membrane was placed in a home-made device of stainless steel (***Figure 1***b).

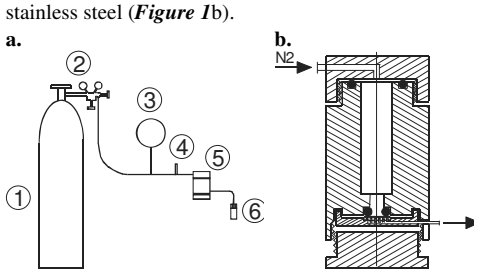

Figure 1 a. Set up overview consists of: 1. nitrogen bottle, 2. gas reducer with valves, 3. manometer, 4.Security valve, 5. Membrane device, 6. Permeate collecting glass b. Details of membrane device.

Size separation

Polyethylene glycols of different molecular weight were codissolved in solutions: 1000 g/mol, 3000 g/mol, 8000 g/mol, 10000 g/mol, 12000 g/mol, 35 000 g/mol and 100 000 g/mol.

Polyethylene glycols were dissolved in a mixture of MeOH and water (80:20 volume ratio). 20% of water was added in order to assure better dissolution of high molecular weight PEG .

Firstly the solution of PEG 1000[g/mol], PEG 10 000[g/mol] and PEG 100 000[g/mol] in MeOH/water (80:20) was prepared. The concentration of each of the components was 0.5mg/ml. This solution is called Feed A. Such a wide range of molecular weights was chosen for the preliminary experiment to give us some idea about the cut off value. After getting the first results it occurred that the molecular weights range can be reduced.

The solution of PEG 1000[g/mol], PEG 3 000[g/mol], PEG 8 000[g/mol], PEG 12 000[g/mol] and PEG 35 000[g/mol] was prepared. Like in the previous case the concentration of each of the components was 0.5mg/ml. This solution is called Feed B.

The third feed solution was prepared in order to see if the same separation results were obtained if dissolve PEGs from Feed B in MeOH/Water (20:80) and use the sample wet in methanol. This solution is referred to as Feed C.

Materials characterization

Electron microscopy.

Each sample for Scanning Electron Microscopy (SEM) was prepared by crushing it in the agat mortar filled with liquid nitrogen. Crushed pieces were than placed on the aluminum speciment mount covered by the Ted Pella double coated carbon tabs. Pieces were additionally stabilized by CCC Carbon Adhesive (Electron Microscopy Science).

Samples were investigated by Scanning Electron Microscopy (SEM): Zeiss 1540 EsB Gemini SEM at the low electron beam accelerating voltage of 2kV. In order to avoid any charging of the samples each of them was sputter-coated with 2-3 nm layer of gold in a Polaron SC7640 instrument. Before the investigation samples were kept for 12-14h in the microscopy chamber.

Chromatography

The separation properties of membrane were quantified by analyzing the feed solution and collected permeates with Size Exclusion Chromatography (SEC). Water was the eluent at a flow rate of 0.6 ml/min. The injection volume was 40µl. The column used was Waters Ultrahydrogel™ Guard Column. Apparatus is made by Waters, consists of Waters™ 717plus Autosampler; Waters™ 600 Controller and Waters™ 410 Refractive Index Detector.

Results and discussion

Electron microscopy.

Investigation of the gyroid morphology with electron microscopy is quite complex, since we observe different surface morphologies depending on the fracture of the sample. Projections along different directions occur as characteristic patterns like: “knitting”, “wishbone” or “wagon wheel”. ***Figure 2***a shows a “knitting” pattern which results from cut along the (211) symmetry plane of unit cell. This result from SEM corresponds very well to the computer graphics which can be found in literature[10,11] (***Figure 2***b). Bright phase corresponds to the 1,2-polybutadiene whereas dark phase corresponds to the pores after etching polydimethylsiloxane block. Pore diameter obtained from SEM pictures was 13±2 nm. The graphical representation of the gyroid network is shown on ***Figure 2***c.

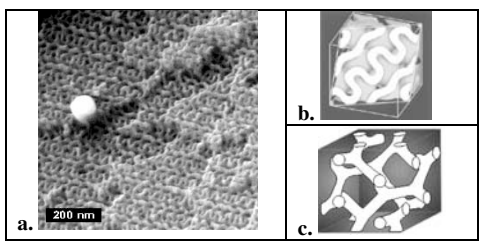

Figure 2 a. SEM picture of “knitting” pattern of nanoporous sample. b. Computer graphic presenting a two dimensional cut along the (211) plane c. Graphical presentation of double gyroid network

Membrane basic characterization.

Size separation of polymers

Size separation

10ml of Feed A and Sample 1 were placed in the filtration device. Permeates were analysed by SEC. By the 1st Permeate we understand the first 0.8ml of permeate collected in the 1ml glass and analysed by SEC. 2nd Permeate and 3rd Permeate were the following 0.8ml and 0.6ml of collected volume respectively. Results are presented on Figure 3a as the detector response in milivolts[mV] vs. retension time in minutes [min]. Values of fluxes (1st; 2nd and 3rd Flux) of the following permeates in liters/m^{2}h at 39.6±3.4 bar are presented in the right down corner of Figure 3a. The flux of MeOH/water (80/20) on the dry disc for comparison was: 1.1 [l/m2h] at 38 bar, which almost does not differ from the flux of PEG dissolved in the same solvent.

After running the SEC the PEG 100 000 [g/mol] appeared as two peaks. That is why it is marked by quotation-marks.

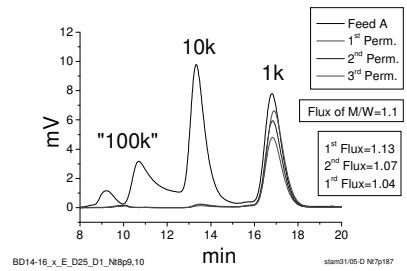

a.

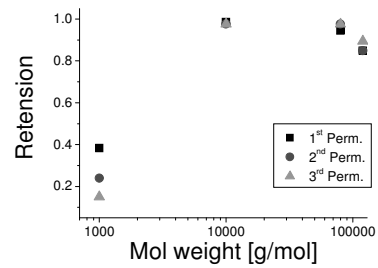

b.

Figure 3 a) Size exclusion chromatography results of filtration Feed A on Sample 1. b) Retension curve based on the analysis of feed and permeates peaks height.

The retension (R) value (Figure 3b) is calculated as:

$$R = 1 - \frac{C_P}{C_F}$$

Where: C_p and C_F are the concentration [mg/ml] of the permeate and the feed respectively. Knowing the concentration of each of PEG in the Feed A (0.5 mg/ml) we find the concentration of the permeate from the ratio of permeate to feed peak height.

From the Figure 3 we can see that the membrane is permeable for PEG 1000 and retension for this molecule decreases with the following collected permeates. The peak for PEG 10000 in all permeates is gone and retension for these molecules reaches value of 1.

The membrane side was swapped after the above experiment so we could obtain the reverse flow through the sample in order to clean the membrane from the separated molecules. 0.8 ml of MeOH/water (80/20) at 38 bar was percolated through the membrane.

The Sample 1 was placed back in the original position in the device filled with 10 ml of Feed B. Permeates were analysed by SEC. The 1st, 2nd and 3rd Permeate mean the first, second and third 0.8ml of permeate collected. Results are presented on Figure 4.

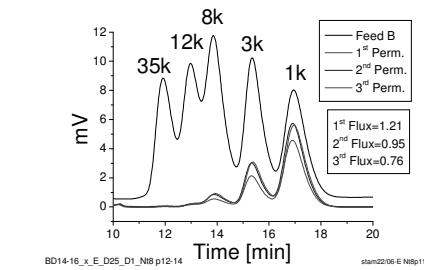

a.

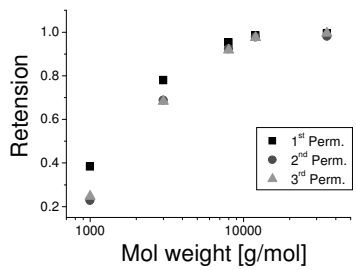

b.

Figure 4 a) Size exclusion chromatography results of filtration Feed B. b) Retension curve based on the analysis of feed and permeates peaks height.

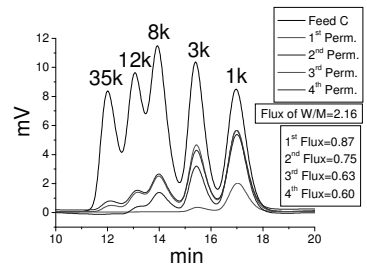

a.

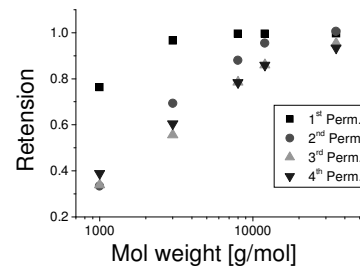

b.

Figure 5 a) SEC results after filtration of Feed C (PEGs in water/MeOH (80/20)) by using Sample 1 with at 38 bar. b) retension curve.

Unexpected result shows quite high retention for PEG 3000 (0.68 for the third permeate). Retensions for PEG 8000, PEG 12000 and 35000 as 0.92; 0.98 and 1 respectively, fits well with the results from the previous experiment (Figure 3).

The Sample 1 was stored in methanol for 99 days and nights. Than it was placed in the device filled with water/methanol 80/20. 1.6 ml of water/methanol 80/20 was percolated and the flux was measured.

The device was filled with 10ml of Feed C after that. Four following permeates (three times 0.8ml and last one 0.6ml) were collected and analysed by SEC. Results are presented on Figure 5.

Conclusions

We managed to obtain a nanoporous material showing the gyroid morphology. Material is characterized with different techniques and the pore size is known. We can see that even with rather primitive, self-supporting kind of membrane of very high thickness, we can get some separation of the polyethylene glycol molecules.

The results of filtrating Feed B on the Sample 2 showed the reproducibility.

References

[1] Liu, G.; Ding, J.; Guo, A.; Herfort, M. Bazett-Jones, D. *Macromolecules* **1997**, *30*, 1851-1853

[2] Liu, G.; Ding, J.; Guo, A.; Stewart, S. *Angew. Chem. Int. Ed.* **1999**, *38*, 835-838

[3] Park, C.; Yoon, J.; Thomas, E.L *Polymer* **2003**, *44*, 6725-6760

[4] Cavicchi, K.A.; Zalusky, A.S.; Hillmyer, M.A.; Lodge, T.P. *Macromol. Rapid Commun.* **2004**, *25*, 704-709

[5] Ndoni, S.; Vigild, M.E.; Berg, B.H. *J. Am. Chem. Soc.* **2003**, *125*, 13366-13367

[6] Russell, T.P. et al. *Advanced Materials* **2004**, *16*, 226-231

[7] Russell, T.P. et al. *Advanced Materials* **2006**, *18*, 709

[8] Muralidhalan, V.; Hui, C.-Y. *Macromol. Rapid Commun.* **2004**, *25*, 1487-1490

[9] Vigild, M.E.; Almdal, K.; Mortensen, K. *Macromolecules* **1998**, *31*, 5702-5716

[10] Hashimoto, T.; Tsutsumi, K.; Funaki, Y. *Langmuir* **1997**, *13*, 6869-6872

[11] Hashimoto, T.; Nishikawa, Y.; Tsutsumi, K. *Macromolecules* **2007**, *40*, 1066-1072

Per Aggerholm Sørensen
Phone: +45 4525 2927
Fax: +45 4525 2258
E-mail: pas@kt.dtu.dk
WWW: http://www.kt.dtu.dk
Supervisors: Søren Kiil
Kim Dam-Johansen
Claus Weinell, Hempel A/S

PhD Study
Started: February 2007
To be completed: January 2010

High Performance Anti-Corrosive Coatings

Abstract
A very important mechanism of organic coating deterioration is the cathodic delamination, which occur on defect coatings immersed in a neutral electrolyte. Quantification of the most important steps responsible for the degradation of organic coatings in a fundamental mathematical model may be an important tool in development of novel high performance anticorrosive coatings and lifetime predictions.

Introduction
Throughout the last decade, organic coatings have been widely applied for protection of metals against corrosion. Though various kinds of steel corrode at different rates, depending on their composition and the presence of mechanical stresses, the basic corrosion reactions are the same. On a steel surface some areas are anodic relative to other areas that are cathodic [1]. At anodes the following reaction takes place

$$Fe(s) \rightarrow Fe^{2+} + 2e^{-} \quad (1)$$

and the cathode oxygen is reduced to hydroxyl ions

$$2H_2O(l) + O_2(aq) + 4e^{-} \quad 4OH^{-} \quad (2)$$

According to Leidheiser et al. [2], reaction (2) is catalyzed by oxidized metals and does not occur to a significant degree in the absence of a solid.
The overall reaction can be written as

$$2Fe(s) + 2H_2O(l) + O_2(aq) \rightarrow 2Fe^{2+} \quad 4OH^{-} \quad (3)$$

In the presence of dissolved oxygen, oxidation of ferrous hydroxide will lead to formation of hydrated magnetite, $Fe_2O_3 \cdot H_2O(s)$, known as rust.

$$Fe(OH)_2 + O_2(aq) \rightarrow 2Fe_2O_3 \cdot H_2O(s) + 2H_2O(l) \quad (4)$$

Despite significant improvement in existing coating technologies, problems continue to exist in the long-term protection of metal from aggressive environments. One of the main reasons for the lack of high performance anticorrosive coatings is the complexity of the coating-substrate system and the number of factors affecting the performance and durability of anticorrosive coating systems. Besides the composition of the coating, which consists of binder, pigments, solvents, extenders and additives, the performance and service life of anticorrosive coatings depend on several different parameters such as type of substrate, pretreatment of substrate, curing, coating thickness, adhesion between the coating and substrate as well as several external environmental parameters [3]. To perform its duty effectively, an anticorrosive coating must possess intrinsic durability, adhesion to the substrate, adequate flexibility and toughness to withstand impacts and cracking as well as maintain its appearance, when subjected to stress, swell, mechanical abuse or weathering.

Specific Objectives
If an anticorrosive coating containing a defect (e.g. a scratch or a scribe) is exposed to the environment, corrosion may initiate much more rapidly than for a defect-free coating. The cathodic delamination is one of the more important processes promoting the degradation of a defect protective organic coating immersed in neutral electrolyte solutions [3]. Cathodic delamination is the result of disruption of the bondings between coating and metal surface. Hence the bare metal is exposed to the surrounding environment, promoting corrosion and further degradation of the anticorrosive coating.

An schematic illustration of the main degradation mechanism of submerged organic coatings (e.g. blistering and cathodic delamination) is given in figure 1.

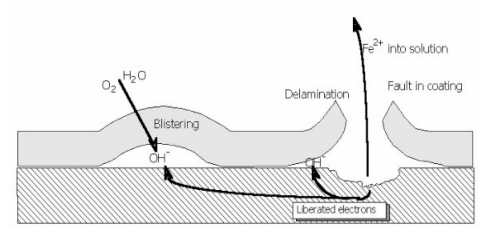

Figure 1: Schematic cross-section view of the blistering and delaminating processes that may occur in a damaged anticorrosive coating. After [3].

Figure 2 shows a top view of a test panel, which has been exposed to artificial sea water. Corrosion is clearly visible, but the degradation of the coatings is not visible (requires removal of the coating).

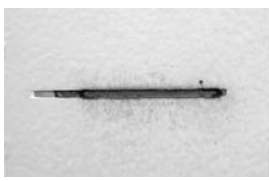

Figure 2: Top view of corrosion on test panel containing an artificial defect (scribe). Corrosion is clearly visible, but the degradation of the coatings is not visible.

The reason for the cathodic delamination is proposed to be so-called polarization [4]. The cathodic polarization of the steel arises when the anodic and cathodic reactions take place at a defect in the coating. The process moves forward under coatings due to continuous migration of water and oxygen (necessary for the cathodic reaction) and positive ions, necessary in order to locally balance the electric charge [5].

Premature coating failure may decrease structural reliability and extreme expenses are associated with corrective repair. Hence it is important to be able to estimate the lifetime and performance of an anticorrosive coating system in a reliable fashion.

The key to lifetime estimations and design of novel or improved formulations of anticorrosive coatings lies in the potential failure mechanisms. It is essential that the controlling mechanisms are identified and quantified through laboratory experiments

The purpose of this project is to obtain detailed knowledge on the mechanism of cathodic delamination and quantify the most important physical and chemical mechanisms in a fundamental mathematical of coating behaviour.

Discussion

Typical organic coatings are so permeable to oxygen and water that the transport of oxygen or water cannot control the rate of cathodic delamination [5]. Hence another mechanism must control the rate of degradation. Feser and Stratman [6] have suggested that interfacial transport of sodium ions from a defect in the coating to the delamination front controls the rate of cathodic delamination. This hypothesis is supported by the fact that Wapner et al. [7] have reported that the interfacial transport of water and sodium ions is several orders of magnitude greater than the transport of the corresponding species through the bulk polymer. Experimental results, which show a linear relationship between the disbonded area and $t^{1/2}$ provide experimental evidence for the fact that interfacial transport may control the rate of cathodic delamination [8].

Conclusions

Cathodic delamination is an interfacial phenomena, which may be controlled by diffusion of reactants and ions from a defect in the coating to the delamination front. Future work will focus on revealing the detailed mechanism of cathodic delamination.

Acknowledgements

The project is funded by Technical University of Denmark and carried out in corporation with Hempel A/S.

References

1. D. A. Jones, Principles and Prevention of Corrosion, Prentice Hall, U.S. 1996
2. H. Leidheiser, W. Wang, L. Igetoft, Prog. Org. Coat. 11 (1) (1983) 19-40.
3. T. Nguyen, J. B. Hubbard, J. M. Pommersheim, J. Coat. Tech.68 (855) (1996) 45-56.
4. W. Funke, J. Coat. Tech. 55 (705) (1983) 31-38.
5. J. E. O. Mayne, Anticorrosion Methods and Materials 20 (10) (1973) 3-8.
6. R. Feser, M. Stratman, Werkstoffe und Korrosion – Materials and Corrosion 42 (4) (1991) 187-195.
7. K. Wapner, M. Stratmann, G. Grundmeier, Electrochemica Acta 51 (16) (2006) 3003-3015.
8. F. Deflorian, S. Rossi, Electrochemica Acta 51 (8-9) (2006) 1736-1744.

Anders Egede Daugaard
Phone: +45 4525 6819
Fax: +45 4588 2161
E-mail: adt@kt.dtu.dk
WWW: www.dtu.dk/Centre/DPC.aspx
Supervisor: Søren Hvilsted

Ph.D. Study
Started: March 2006
To be completed: February 2009

Micro-Sensor Based on Click Chemistry

Abstract

During the last couple of years micro-sensors have received increased attention and the fabrication of micro devices shows a great promise for future applications. Recently a number of highly efficient reactions termed click chemistry have found many applications within macromolecular chemistry. Here the preparation of a new azide functional conductive polymer based on poly(3,4-ethylenedioxythiophene) and its functionalization by click chemistry is presented. This polymer is thought as a precursor for future micro-sensor devices.

Introduction

A micro sensor would normally be based on at least two elements, a receptor element that would bond or interact with the desired target and a responding element that could deliver a response upon detection. This type of system could be based on a conductive polymer as the responding element. If that polymer could be functionalized with different receptors it would be possible to use changes in conductivity upon interaction with a desired target molecule as detection mechanism.

Conducting polymers have been extensively studied during the last few decades for many different applications among others, electrochemical sensors e.g. a biosensor[1]. For the preparation of functional conductive polymers one of the challenges is to produce a functional monomer that would be able to withstand the polymerization conditions. Different functional groups affect the polymerization conditions differently, and thus a standard method to apply different functionalities would be desired. In this respect the recently developed click chemistry[2],[3] is a very good candidate for post polymerization functionalization. By performing the functionalization after polymerization it is only demanded that one monomer can withstand polymerization independent of the desired receptors that can be introduced afterwards.

In the work presented here we have applied a click chemistry approach, where a new functional monomer has been prepared. The monomer, 3,4-(1-azidomethyl-ethylene)dioxythiophene, can withstand the polymerization conditions and have been applied in post polymerization functionalization to obtain new conductive polymers. With the application in micro sensor devices in mind this system is ideal for different receptors, where the standardized method could be applied for all systems.

Specific Objectives

This PhD project is focused towards the application of click chemistry in the preparation of micro sensor systems. Here the preparation of a new conductive polymer and its functionalization through click chemistry is presented. Presently we are working on the preparation of micro sensors by this approach.

Results and Discussion

In order to prepare a PEDOT for use in the click approach it was necessary to synthesize either an alkyne or an azide monomer based on 3,4-ethylenedioxythiophene (EDOT). It was decided to prepare the azide monomer, since that would not have to be protected during polymerization[4] in contrast to the alkyne[5]. The new monomer was synthesized as shown in Scheme 1. A transetherification using 3-bromo-1,2-propanediol gives the bromine functional monomer, **1**, and this is subsequently substituted using NaN_3 to give the product monomer EDOT- N_3, **2**. The reactivity of the monomer was checked in a model reaction using standard click conditions and gave the expected product, **13**.

Scheme 1. Monomer synthesis.

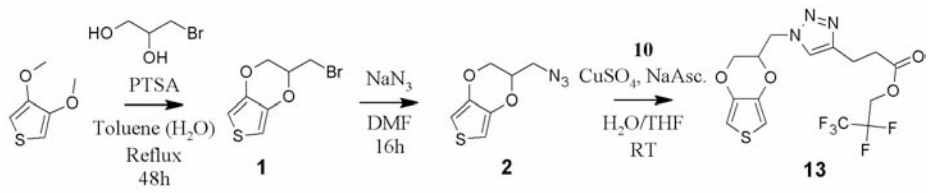

The polymerization method published earlier[6] was not efficient with this new monomer, it appears to have a lower reactivity compared to ordinary EDOT. The polymerization rate under standard conditions is limited by pyridine, however, by omitting pyridine from the mixture the polymerization of EDOT-N_3 occured under otherwise similar conditions.

To monitor the reaction on the surface it was decided to produce a fluorescent alkyne and detect this by fluorescence microscopy/spectroscopy. Fluorescein was chosen as precursor since it is an inexpensive fluorophore and has a sufficiently high quantum yield, even after modification of the phenol and the acid group. It was expected that only a surface layer would be functionalized and this would be difficult to detect with other techniques. In addition to this the UV/VIS spectra of fluorescein could also be used to estimate the degree of reaction at higher concentrations.

The alkyne functional fluorophore was synthesized as shown in Scheme 2. First the methyl ester of fluorescein was prepared through an ester synthesis in accordance to the method by Moore et al.[7]. In the second step the alkyne was introduced using a Mitsunobu ether synthesis in moderate yields, 48%.

Scheme 2. Fluorophore synthesis.

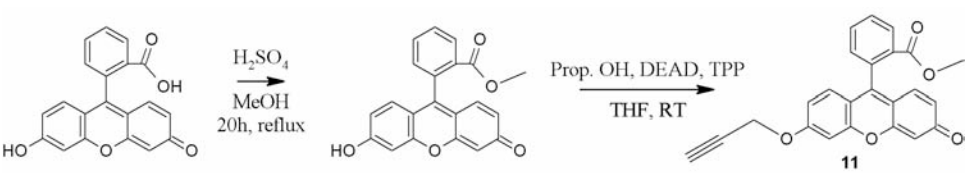

At first the click reactions were performed on the polymer surface in H_2O with a catalyst system of $CuSO_4$ and sodium ascorbate. To make the fluorophore water soluble **11** was deprotected under acidic conditions. Click reactions performed in an alkaline environment (to dissolve the fluorescein alkyne) were ineffective and the approach was dropped. The solvent was replaced by DMF and the catalyst system of $CuSO_4$/sodium ascorbate was applied together with **11**, which was much more efficient. A reference reaction was performed without the catalyst $CuSO_4$ but with otherwise equivalent conditions. Fluorescent microscopy images of the clicked polymer (**14**) and the reference sample are presented in Figure 1.

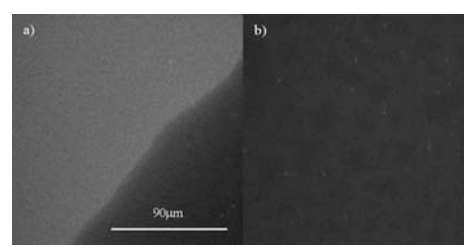

Figure 1. Fluorescence microscopy of the clicked surface, a (**14**); and the reference prepared without $CuSO_4$ under otherwise equivalent conditions, b.

The distinct fluorescence in a) clearly shows that the reaction has proceeded and with the nonfluorescent reference sample in b) absorbed reagent can be disregarded. The image in Figure 1 a) shows the boundary of the exposed area, hence film in the bottom right corner has not been exposed to "click" solution. That the reaction did not work in H_2O was attributed to solubility issues. Earlier results in our group show that free acids are compatible with the cycloaddition[8].

The thickness of the clicked film and the reference film was measured with a mechanical profilometer before and after the reaction. The thickness of the clicked film increased from 240 nm to 420 nm (+/- 10 nm) corresponding to an increase of 75%. The reference film showed a decrease from 235nm to 220 nm. The significant volume expansion of the clicked film shows that the reaction is not only limited to the surface layer, but is also occurring in the bulk phase. Fluorescent microscopy was performed on the pristine **11** spin coated on a glass slide (not shown) and compared with the clicked sample. The detected

fluorescence from **11** was significantly stronger than the clicked sample. This can however be explained by quenching from the conducting polymer backbone. Ramanaviciene et al.[9] reports that the conducting polymer polypyrrole quenches fluorescein and rhodamine B with almost 100%. A similar behavior could be expected from PEDOT.

X-ray photoelectron spectroscopy (XPS) was additionally used to investigate the clicked surfaces. The high resolution peak of nitrogen shown in Figure 2 can be used to check for remaining azides on the surface due to the difference in binding energies of nitrogen in the triazole and the azide. As the azide nitrogens exist in two different states they will give two peaks in XPS, one at 400eV and one at 405eV in a ratio 2:1. The XPS results clearly show the difference in binding energies from PEDOT-N_3 to the product triazole and no residual azide is detected. Since XPS has a penetration dept of approximately 10nm this confirms that the reaction has taken place on the surface. In combination with the data from the model reaction, fluorescense spectroscopy, thickness measurements and UV/VIS data (examples given in Figures 3 and 4) this clearly shows that the click reaction has been performed on the polymer substrate.

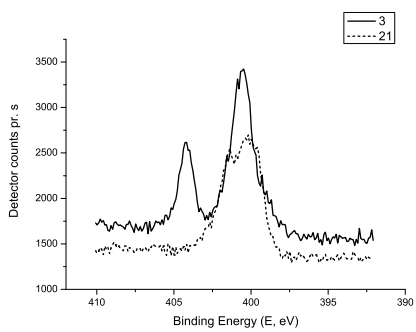

Figure 2. N (1s) high resolution peak for PEDOT-N_3 (3) and the product triazole (21).

Mechanical stirring is not possible in the reaction mixture on the polymer surface and all mixing of the reagents is thus dependent on diffusion. Therefore the necessary catalyst concentration within reasonable time frames was investigated. UV/VIS spectroscopy of the films produced with a catalyst amount of 5, 20 and 100% catalyst based on the alkyne is presented in Figure 3 and compared to a thin layer of **11** spincoated on a glass slide. The UV/VIS spectrum shows that the 20% and 100% samples have the same three characteristic peaks as **11**, although they are shifted 5-10 nm downwards. The strong absorption peaks supports the assumption that more than a surface layer of fluorescein is present after the reaction.

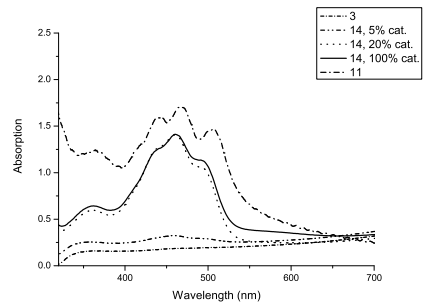

Figure 3. Fluorophore (11) loading on PEDOT-N_3 (**3**) as effect of catalyst concentration in 20h of reaction yielding the functionalized polymer, **14**.

The UV/VIS absorption of the three fluorescein peaks reaches a maximum already at 20% catalyst and conducting the reaction with 100% catalyst made no significant difference. Two explanations for this result seem feasible. Either 20% is sufficient, given the diffusion, to make the reaction proceed to completion within reasonable time or the azide groups on the surface are saturated at 20% loading. The concentration of azides on the surface is based on a very rough assumption that 1mg of azide functional polymer is reacted, and that all azide groups are accessible.

Based on 20% catalyst loading the reaction time was monitored using UV/VIS as shown in Figure 4.

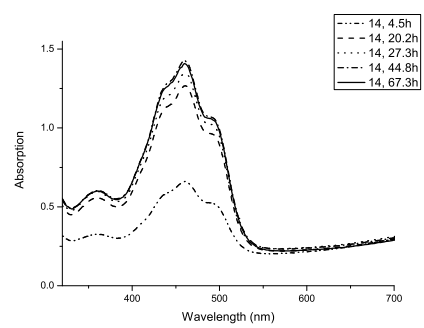

Figure 4. Fluorophore (11) loading on PEDOT-N_3 (3) as a function of reaction time with a constant catalyst concentration of 20%, yielding **14**.

The reaction proceeds mainly during the first 20 hours and then the increase in intensity gradually decreases over time. This decrease in the rate is believed to be due to steric hindrance in the bulk of the polymer film as the loading increases and less free sites are available for reaction. It would demand unreasonable long reaction times to obtain complete

reaction of all azides, and thus the loading obtained after 20h has been found sufficiently high.

The conductivity of the film is not surprisingly affected by the treatment. Before reaction the conductivity of the films are around 60 S/cm. During the reaction the film is reduced by the sodium ascorbate, causing a dramatic drop in conductivity to around 0.2-0.3 S/cm. Most of the conductivity is however regained by reoxidation in an aqueous solution of Fe(III)tosylate ending at approximately 15 S/cm. The loss in conductivity is not as significant as it appears; a considerable decrease is expected due to the increase in volume.

Conclusion

We have developed the synthesis of a new azide monomer, EDOT-N_3, and demonstrated that it can be polymerized to PEDOT-N_3, which can be used as a precursor to obtain conductive polymers with different functionalities. A click reaction with a fluorescein derivative has been performed on the surface, and the reaction conditions have been optimized for other applications. Reoxidation of the samples after functionalization reestablished the conductivity to a reasonable level. We believe that this method can be applied for other systems with different functional groups. The approach is well suited for new sensor devices and we are currently working on the development of different systems.

Acknowledgements

Thomas Steen Hansen and Niels Bent Larsen from Risø national laboratory are acknowledged for their contributions to the work presented here. DTU and the Danish Research Council for Technology and Production Sciences are acknowledged for funding (framework programme ‘‘Design and Processing of Polymers for Microfluidic Applications’’, grant 26-04-0074).

References

1. L. M. Dai, P. Soundarrajan, T. Kim 74 (9) (2002) 1753-1772.
2. H. C. Kolb, M. G. Finn, K. B. Sharpless 40 (11) (2001) 2004-2021.
3. W. H. Binder and R. Sachsenhofer 28 (1) (2007) 15-54.
4. B. S. Sumerlin, N. V. Tsarevsky, G. Louche, R. Y. Lee, K. Matyjaszewski 38 (18) (2005) 7540-7545.
5. M. Malkoch, R. J. Thibault, E. Drockenmuller, M. Messerschmidt, B. Voit, T. P. Russell, C. J. Hawker 127 (42) (2005) 14942-14949.
6. B. Winther-Jensen, D. W. Breiby, K. West 152 (1-3) (2005) 1-4.
7. M. Adamczyk, J. Grote, J. A. Moore 10 (3) (1999) 544-547.
8. A. D. Thomsen, E. Malmstrom, S. Hvilsted 44 (21) (2006) 6360-6377.
9. A. Ramanavicius, N. Kurilcik, S. Jursenas, A. Finkelsteinas, A. Ramanaviciene 23 (4) (2007) 499-505.

List of Publications.

1. A. D. Thomsen, E. Malmström, S. Hvilsted, Carboxylic Acid Functional Polymers and Copolymers, Nordic Polymer Days, Copenhagen, DK, May 2006.
2. S. Hvilsted, E. Malmström, A. D. Thomsen, Novel Polymers with High Carboxylic Acid Loading, Macro 2006, Rio de Janeiro, BR, July 2006.
3. A. D. Thomsen, E. Malmström, S. Hvilsted, Novel Polymers with a High Carboxylic Acid Loading, J. Pol. Sci. Part A. Pol. Chem., 44 (2006) 6360-6377.

Amra Tihic
Phone: (+45) 4525 2863
Fax: (+45) 4525 2800
E-mail: amt@kt.dtu.dk
WWW: http://www.ivc-sep.kt.dtu.dk/staff/amt
Supervisors: Georgios M. Kontogeorgis
Nicolas von Solms
Michael L. Michelsen

Ph.D. Study
Started: May 2005
To be completed: June 2008

Advanced Thermodynamic Tools for Computer-Aided Product Design

Abstract
A Group Contribution (GC) method is coupled with the Perturbed-Chain Statistical Associating Fluid Theory (PC-SAFT) Equation of State (EoS) to predict its characteristic pure compound parameters. The estimation of group contributions for the parameters is based on a parameter database with 400 low-weight compounds estimated by fitting experimental vapour pressures and liquid densities. The method is successfully used to estimate the PC-SAFT parameters for commonly used compounds. Using the new parameters as calculated from the proposed GC scheme, simplified PC-SAFT gives promising modelling results of various binary mixtures exhibiting both vapour-liquid and liquid-liquid phase equilibria. In summary, the data required for calculating phase equilibria with the proposed method are the molecular structure of the compound of interest in terms of functional groups and a single binary interaction parameter for accurate mixture calculations.

Introduction
The prediction or correlation of the thermodynamic properties and phase equilibria with equations of state still remains an important goal in chemical and related industries.

In the early 1980's the theory of Wertheim emerged from statistical thermodynamics. This method has been implemented into a new generation of engineering Equations of State (EoS) called Statistical Associating Fluid Theory (SAFT). Three comprehensive reviews of the development and applications of the various types of SAFT are available for further information [1-2].

Simplified PC-SAFT [3-4] is as a non-cubic, segment-based EoS designed specifically to deal with systems containing polymers and associating fluids and has been successfully applied to a number of complex systems over wide ranges of conditions. The model development of the PC-SAFT EoS is described in detail by Gross and Sadowski [3], while the main equations of the simplified PC-SAFT are given by von Solms *et al.* [4].

Our work aims in developing a theoretically based engineering tool that can be used for complex mixtures of importance to polymer and pharmaceutical industries. Common characteristics of these applications are a high complexity of molecules involved, the presence of various types of intermolecular forces (polarity, hydrogen bonding, etc.), and the frequent coexistence of many phases at equilibrium e.g. vapour-liquid-liquid or solid-liquid-liquid. The thermodynamic model developed in this work is a group-contribution version of the simplified PC-SAFT [4] equation of state where the parameters of the model are estimated via group contributions based on the "conjugation principle" [5].

Specific Objectives
Most SAFT-type models require three parameters for each pure non-associating compound: the segment number (m), the interaction energy (ε/k in K), and the hard-core segment radius (σ in Å) that are typically estimated from vapour pressure and liquid density data over extended temperature ranges. This has been possible for small complex compounds for which such data are readily available. However, for more complex compounds such as polymers, pharmaceuticals and pesticides, vapour pressures and liquid densities are not available and in many cases they cannot even be measured. As mentioned, this limits the applicability of the models.

The suggested solution to this problem is to develop a group contribution scheme for estimating the parameters of these equations of state from low molecular weight compounds for which data is available and then extrapolate to complex molecules.

Theory and Background

Simplified PC-SAFT

The following section summarizes the main equations of simplified PC-SAFT.

The reduced Helmholtz energy for mixtures of associating molecules is given as follows:

$$\tilde{a} = \frac{A}{kTN} = \tilde{a}^{id} + \tilde{a}^{hc} + \tilde{a}^{disp} + \tilde{a}^{assoc} \quad (1)$$

where the first term is the ideal gas contribution, the second term is the contribution of the hard-sphere chain reference systems, the third term is the dispersion contribution arising from the square-well attractive potential, and the last term is the contribution due to association. The expressions for the contributions from the ideal gas and dispersion are identical to those of Gross and Sadowski [3]. The contribution to the hard-chain term is made up of two contributions: the hard-sphere term and the chain term,

$$\tilde{a}^{hc} = \tilde{m}\tilde{a}^{hs} - \sum_i x_i (m_i - 1) \ln g_{ii}^{hs}\left(d_{ii}^{+}\right) \quad (2)$$

where x_i is the mole fraction of component i and $\tilde{m}$ is a mean segment length defined as $\tilde{m} = \sum_i x_i m_i$ and the hard-sphere term is given by

$$\tilde{a}^{hs} = \frac{4\eta - 3\eta^2}{(1-\eta)^2} \quad (3)$$

The radial distribution function at contact is

$$g^{hs}\left(d^{+}\right) = \frac{1 - \eta/2}{(1-\eta)^3} \quad (4)$$

The volume fractions $\eta = \pi\rho\tilde{m}d^3/6$ are based on an average diameter given as following:

$$d = \left(\frac{\sum_i x_i m_i d_i^3}{\sum_i x_i m_i} \right)^{1/3} \quad (5)$$

where the individual d_i are temperature-dependent segment diameters

$$d_i = \sigma_i \left[1 - 0.12 \exp\left(-3\frac{\varepsilon_i}{kT} \right) \right] \quad (6)$$

Thus, it is assumed that all the segments in the mixture have a mean diameter d, which gives a mixture volume fraction identical to that of the actual mixture.

Extension to mixtures requires combining rules for the segment energy and diameter. The following Lorentz-Berthelot rules

$$\varepsilon_{ij} = \sqrt{\varepsilon_{ii}\varepsilon_{jj}}(1 - k_{ij}) \quad \text{and} \quad \sigma_{ij} = \frac{\sigma_{ii} + \sigma_{jj}}{2} \quad (7)$$

are employed for the calculations. For mixtures where experimental data are available, a binary interaction parameter, k_{ij}, can be used as a correction to the geometric mean rule.

Group-Contribution approach

Unlike other group contribution (GC) approaches found in the literature, this GC methodology includes two levels of contributions, both first-order groups (FOG) and second-order groups (SOG) that can, to some extent, capture the proximity effects and distinguish among structural isomers. The basic level includes contributions from first-order functional groups such as those currently applied for the estimation of mixture properties. The next level considers a set of simple and small SOG, which uses the FOG as building blocks. The definition and identification of SOG are theoretically based on the concept of conjugation operators according to the ABC theory of molecular structures [6], whose basic property is the standard enthalpy of formation at 298K. Every molecule has definitely FOG, but it may or may not have SOG.

At the present, a group contribution scheme including 45 FOG and 26 SOG contributions is developed. Assuming that a given molecule contains n*i* groups of type *i*, the following relations are applied:

$$m_{molecule} = \sum_i (n_i m_i)_{FOG} + \sum_j (n_j m_j)_{SOG} \quad (8)$$

$$(m\sigma^3)_{molecule} = \sum_i (n_i m_i \sigma_i^3)_{FOG} + \sum_j (n_j m_j \sigma_j^3)_{SOG} \quad (9)$$

$$(m\varepsilon/k)_{molecule} = \sum_i (n_i m_i \varepsilon_i/k)_{FOG} + \sum_j (n_j m_j \varepsilon_j/k)_{SOG} \quad (10)$$

where m_i, σ_i, and ε_i/k are the contributions of the FOG of type *i* that appears n_i times, and m_j, σ_j, and ε_j/k are the contributions of the SOG of type *j* that appears n_j times.

Using the above approximations, the pure parameters of simplified PC-SAFT EoS for each investigated compound can then be calculated where the only input needed is the molecular structure in terms of present functional groups and the molecular weight for the case of polymer calculations.

Example: Poly (iso-propyl methacrylate) (PIPMA)

Using the values of the present FOG and SOG contributions, the following results are obtained:

FOG(i)	Occurrences n_i	m_i	$m_i\sigma_i^3$	$m_i\varepsilon_i/k$
CH_3	3	1.93309	102.5086	388.1598
CH_2	1	0.384329	24.33981	102.3238
CH	1	0.043834	13.95391	68.20842
C	1	-0.49208	2.325415	-10.983
COO	1	1.43911	32.51328	351.1344
		$\sum n_i \cdot m_i =$	$\sum n_i \cdot m_i\sigma_i^3 =$	$\sum n_i \cdot m_i\varepsilon_i/k =$
		3.30828	**175.64107**	**898.8434**

SOG(j)	Occurrences n_j	m_j	$m_j\sigma_j^3$	$m_j\varepsilon_j/k$
$(CH_3)_2CH$	1	0.01626	0.28087	-9.83615
		$\sum n_j \cdot m_j =$	$\sum n_j \cdot m_j\sigma_j^3 =$	$\sum n_j \cdot m_j\varepsilon_j/k =$
		0.01626	**0.28087**	**-9.83615**

The molecular weight of the repeating unit for PIPMA is 128.17 g/mol. From those values, the following PC-SAFT parameters are calculated:

$$m/Mw = (3.30828 + 0.01626)/128.17 = \underline{0.02594}$$

$$\sigma = \sqrt[3]{(m\sigma^3)/m} = \sqrt[3]{(175922/3.3245} = \underline{3.7543\text{Å}}$$

$$\varepsilon/k = (m\varepsilon/k)/m = 889.0073/3.3245 = \underline{267.41\text{K}}$$

Results and discussion

A few modelling results of phase equilibria of binary systems obtained with the simplified PC-SAFT are presented in the following.

Non-polymer systems

LIGHT GASES: The expanded liquid region in **Figure 1** shows that neon is moderately soluble in liquid argon in the range of temperatures and pressures studied. Those liquid lines show a small but unmistakable decrease in slope with increasing temperature, indicating an increase in solubility with temperature at a constant partial pressure of neon.

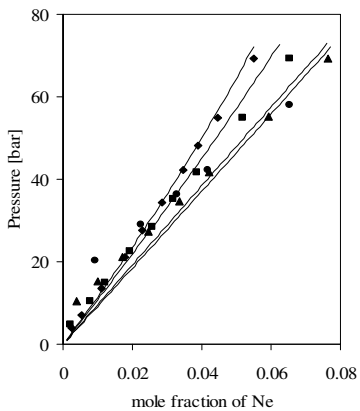

Figure 1. Isothermal P-x diagram of argon-neon mixture at 84.42K (diamantes), 95.82K (squares), 110.78K (triangles), and 121.36K (circles), where the solid lines are the correlations with simplified PC-SAFT (k_{ij}=0.14).

BENZENE MIXTURES: Benzene being one of the most important feedstock's for the chemical industry is used for the manufacture of a wide range of everyday items. As shown in **Figure 2**, after calculating model parameters for both compounds, the benzene-squalane mixture is reasonably well predicted with the simplified PC-SAFT model.

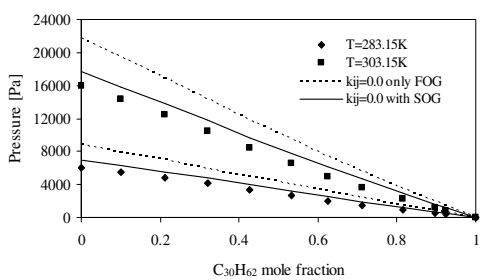

Figure 2. VLE of benzene+squalane. Experimental data (points) and simplified PC-SAFT predictions with FOG (dotted lines) and with SOG included (solid lines).

POLYNUCLEAR AROMATIC HYDROCARBONS (PAHS): This group of more than 100 different chemical compounds that results from the incomplete combustion of organic materials such as coal, oil, wood, etc., have a wide-range of potential commercial applications.

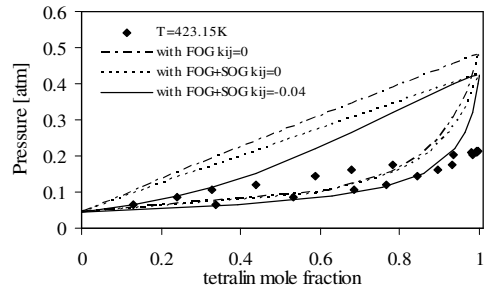

Figure 3. VLE for the system tetralin-biphenyl.

The results in **Figure 3** show that for this particular system, the model cannot accurately calculate saturated vapour pressures of tetralin, and therefore the correlated results still deviate from the experimental data. This is an example where the approach needs some improvements in order to model this type of compounds more accurately. The issue calls for further evaluation.

POLAR COMPOUNDS: Phase behaviour of some polar compounds has been analysed as well. Dipole interactions have a significant effect on the phase behaviour of systems of industrial importance such as mixtures containing ketones, esters, ethers, and aldehydes, as well as many polar polymers, copolymers, and different biochemicals.

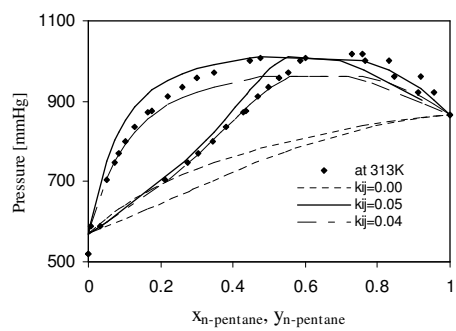

Figure 4. VLE for the system pentane-propanal. Experimental data at 313K (points) and simplified PC-SAFT predictions (dotted lines) and correlations (solid lines).

Although the methodology of this work is primarily targeted at non-associating solutions, **Figure 4** shows that for this particular system, the model gives rather good correlations without including additional polar terms.

Polymer systems

The presented GC method is able to reproduce the experimental densities of polymers over a wide range of temperatures and pressures with an average error of 2.24%. **Figure 5** reports predictions of densities of some investigated polymers at the pressure of 1 bar. For a purely predictive method the accuracy of the density predictions is considered to be reasonably good.

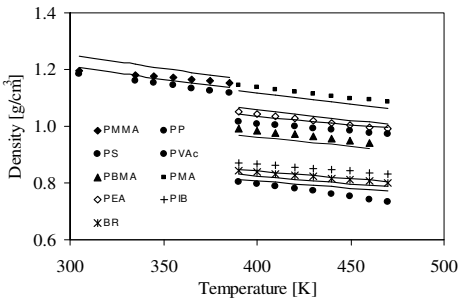

Figure 6. Polymer density predictions (lines) with simplified PC-SAFT using group-contribution estimated parameters as a function of temperature at P=1 bar. Experimental data are indicated with points.

Presented in **Figure 7** is the VLE phase diagram of poly(vinyl acetate)(PVAc)-methyl acetate system. This system is rather well predicted at all three temperatures and excellent correlations are achieved using a small negative temperature-independent binary interaction parameter (k_{ij}=-0.005).

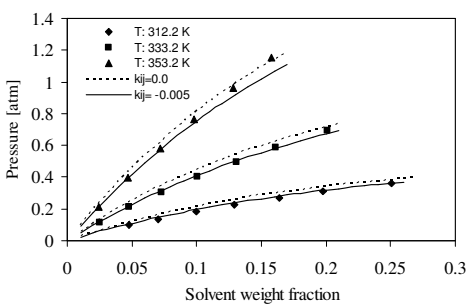

Figure 7. VLE for the system PVAc-methyl acetate.

Comparisons of modelled results with experimental LLE data provide a much more rigorous test and challenge for a model and its parameters than comparison with experimental VLE data. This test is shown in **Figure 8**.

The results presented in Figures 6-8 demonstrate that properly calculated pure predictive group-contribution-estimated polymer parameter values can result in quite accurate modelling of mixture phase equilibria. For many other systems investigated in this work, a small k_{ij} value is needed so that the model can accurately correlate experimental data [6-7].

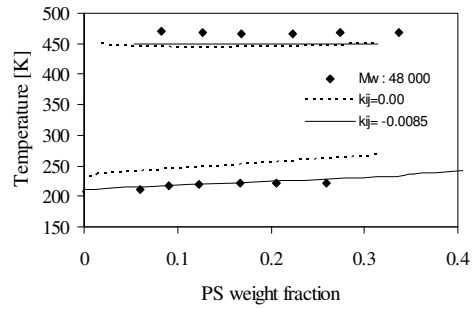

Figure8. LLE for the system polystyrene (PS)-acetone.

Conclusions

A GC method is developed for predicting the simplified PC-SAFT parameters and it is applied to both low and high molecular weight compounds. The proposed technique requires only information in terms of structural properties, presence of FOG and SOG of the compounds of interest and, if necessary, the molecular weight.

Our newly developed group-contribution scheme used to calculate the parameters for complex compounds can make the simplified PC-SAFT model a relevant and useful tool in the design and development of complex products, e.g. detergents or food ingredients, pharmaceuticals, and some other specialty chemicals, where predictions of various thermodynamic and phase equilibrium properties are required.

Acknowledgments

The author and the supervisors wish to thank the Danish Technical Research Council (STVF) for financial support of this work as part of a grant entitled "Advanced Thermodynamic Tools for Computer-Aided Product Design".

The author wishes furthermore to thank Georgios Kontogeorgis, Michael Michelsen and Nicolas von Solms for their supervision, as well as Dr. Leonidas Constantinou.

References

1. E.A. Müller, K.E. Gubbins, Ind. Eng. Chem. Res. 40 (2001) 2193
2. I.G. Economou, Ind. Eng. Chem. Res. 41 (2002) 953
3. J. Gross, and G. Sadowski, Ind. Eng. Chem. Res. 40 (2001) 1244
4. N. von Solms, M.L. Michelsen, and G.M. Kontogeorgis, Ind. Eng. Chem. Res. 42 (2003) 1098
5. L. Constantinou, R. Gani, AIChE J., 40 (1994) 1697
6. A. Tihic, G.M. Kontogeorgis, N. von Solms, M.L. Michelsen, Fluid Phase Equilibria, 248 (2006) 29
7. A. Tihic, G.M. Kontogeorgis, N. von Solms, M.L. Michelsen, L. Constantinou, Ind. Eng. Chem. Res. (2007) accepted

Stuart R Tindal

Phone: +45 4525 2950
Fax: +45 4525 2906
E-mail: st@kt.dtu.dk
WWW: www.bioeng.kt.dtu.dk
Supervisors: John M Woodley
Suzanne Farid, UCL
Helen C Hailes, UCL
Ian Archer, Ingenza Ltd

PhD Study
Started: September 2006
To be completed: August 2010

Improved Amino acid Oxidase Stability for Reactor Scale-Up

Abstract

Biocatalysis is an expanding area of BioProcess Engineering that offers novel and alternative synthetic strategies to a range of useful chemical products. In particular chiral intermediates represent a huge potential market for biocatalysis-based products. However, enzyme stability has hindered the implementation of many enzymes. Using an amino acid oxidase (AAO) based deracemisation platform as a test conversion, stability has been assessed. Modelling the factors that are at the root of the activity loss gives a foundation to further improve the reaction conditions or enzyme formulation.

Introduction

Biocatalysis contributes to just over 2% of the total $27 billion market for basic, intermediate, fine and specialty chemicals and polymers[1]. The potential for this to grow is enormous, especially given the current pressures to reduce waste and increase process sustainability, atom efficiency and product quality. A key area in which biocatalysis can complement chemical catalysis is in the production of chiral molecule building blocks for use in the chemical development of new and existing pharmaceuticals[2]. One such example is the deracemisation of chemically produced amino acid racemates into their corresponding optically pure forms. The chiral raw materials and synthetic intermediates market currently stands at $15 billion and is growing at 9.4% annually. The high enantio- and regioselectivity of biocatalysis is well suited to chiral organic synthesis and the progress of techniques in bioinformatics and microbial genomics are broadening the capacity and availability of new biocatalysts. A promising prospect is the synthesis of optically pure amino acids in a process that incorporates a hybrid chemoenzymatic reaction to convert a racemate into an enantio-pure material.

Specific Objectives

The principle reaction in this project is the conversion of one enantiomer in a racemate producing an enantiomerically pure solution[3]. Further, to improve the yield beyond 50% a non-selective chemical reducing agent to produce the desired enantiomer in excess of 99% as shown in Figure 1[4]. The production of these key building blocks is essential in many important pharmaceutical products. Currently, the reaction is being scaled up to an industrial level and has the potential to become a valuable biocatalytic synthetic process[5]. The process is shown schematically in Figure 2.

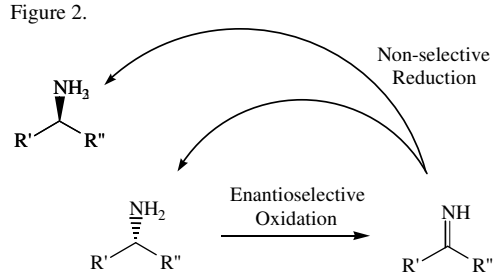

Figure 1: Generic deracemisation process using AAO. The AAO reacts much faster with one of the enantiomers oxidising it to the imine which is reduced by the chemical reducing agent to produce an equal amount of both enantiomers. Hence the unreactive enantiomer accumulates resulting in an enantiomeric excess above 99%[6].

The focus of this project is to quantify and model the factors impacting on the stability of the various mutants of AAO using Design of Experiments (DoE) and reaction progress kinetic (RPK) analysis.[7] The detrimental variables uncovered will become the focus of a stability improvement study, using process conditions, reactor design and biocatalyst modification.

Results

An early study into the variables which affect the stability of the AAO was done with DoE using pH, temperature and agitation (to vary gas-liquid mass

transfer, K_La) as the variables. The simple model created (Figure 3) displays the three temperature lines defining the boundary conditions where the enzyme loses 95% of its original activity. These results indicate that the enzyme rapidly loses activity under these reactor conditions.

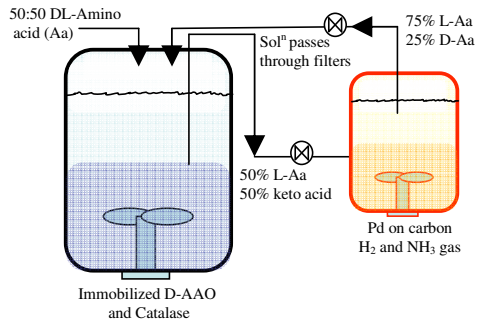

Figure 2: Deracemisation process concept. This two vessel system with conditions optimised for the oxidation (left vessel) and reduction (right vessel) could be run as a cyclic batch process to produce pure enantiomer.

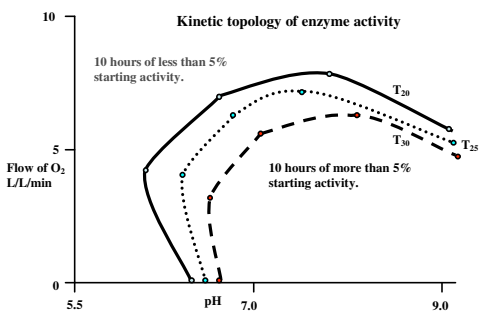

Figure 3: The effects of pH, temperature and gas-liquid mass transfer on activity.

The factors that affect the stability of an enzyme are numerous and their relative impacts can vary tremendously. The AAO example chosen for this study may at first glance seem a simple reaction but as Figure 4 demonstrates this is not the case. The AAO uses molecular oxygen as a substrate and produces hydrogen peroxide, both of which are extremely oxidizing to the protein[8]. Evaporation of ammonia will alter pH as the oxidation progresses; this introduces time dependent variables which will increase the complexity of the model. The mass transfer of oxygen can become limiting at the higher concentrations of enzyme and substrate, giving the maximum volumetric productivity of the oxidation.

Conclusions

Modelling the stability of AAO under process conditions is a challenging venture. Taking extremes of the conditions observed in the oxidation reaction, the sets of activity profiles with respect to time will be plotted to indicate the enzymes stability. These variables

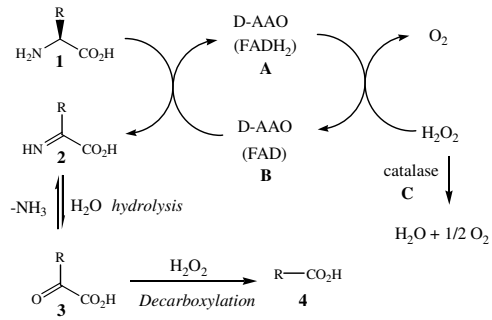

Figure 4: Reaction scheme including material circulation within the oxidation reaction. **1**. R-amino acid **2.** imino-acid **3.** keto acid **4.** (n-1) carboxylic acid **A.** Flavin adenine dinucleotide **B**. Flavin adenine dinucleotide reduced **C**. undefined catalase.

will not be compiled using an empirical method but using a statistical design that will highlight co-dependent variables. With that model it is possible to implement improvements to the process conditions or the biocatalyst formulation. The model will improve the understanding of each physical, chemical and design principle that governs the deactivation of the biocatalyst. The AAO based deracemisation platform reaction can be applied to a vast number of different substrates and related enzymes, for example monoamine oxidases (for the deracemisation of amines). The tools developed here can be applied to modelling other biocatalytic processes.

Acknowledgements

I would like to thank the EPSRC and Ingenza Ltd for the funding of this project and UCL and DTU for hosting my laboratory studies.

References

[1]. Schmid A, Hollmann F, Park JB, Buhler B. 2002. *Current Opinion in Biotechnology* **13**:359-368.

[2]. Pollard DJ, Woodley JM. *Trends in Biotechnology.* 2007. **25**(2):66-73

[3]. Fotheringham I. 2006. *Biocatlysis* (November): 38-39.

[4]. Alexandre F-R, Pantaleone DP, Taylor PP, Fotheringham IG, Anger DJ, Turner NJ. *Tetrahedron Letters* 2002. **43**:707-710.

[5]. Taylor IN, Brown RC, Bycroft M, King G, Littlechild JA, Lloyd MC, Praquin C, Toogood HS, Taylor SJC. *Biochemical Society Transaction*s 2004. **32**:290-292.

[6]. Fotheringham I, Archer I, Carr R, Speight R, Turner NJ. *Biocatalysis Biochemical Society Focused Meeting.* 2006: 287-291.

[7]. Blackmond DG. *Angew. Chem. Int. Ed.* 2005. **44**:4302–4320.

[8]. Tishkov VI, Khoronenkova SV. *Biochem (Moscow).* 2005. **70**(1):40-54

Maja Bøg Toftegaard
Phone: +45 3094 9991
Fax: +45 4588 2258
E-mail: mbt@kt.dtu.dk
WWW: http://www.kt.dtu.dk
Supervisors: Anker Degn Jensen
Peter Glarborg, Peter Arendt Jensen
Bo Sander, DONG Energy

Industrial PhD Study
Started: April 2007
To be completed: March 2010

OxyFuel Combustion of Coal and Biomass

Abstract
A drastic decrease of the CO_2 emission from power production is necessary to prevent global warming. One of the promising technologies which will enable an almost complete capture of CO_2 from thermal power plants burning fossil fuels is OxyFuel combustion. There lacks a more in-depth insight in the fundamental aspects of the effects of OxyFuel combustion regarding combustion chemistry and the effects on e.g. ash quality. The current PhD study includes an experimental and theoretical investigation of these aspects.

Introduction
The increased focus on the effect of CO_2 emission on global warming has a major impact on the application of fossil fuels in both industry, transport, and for power production. Even though our demand for energy is increasingly satisfied by renewable sources the need for fossil fuels in the energy sector will remain for several years to come. The dominant fuel in power plants is coal. This is due to its relatively higher availability and lower price when compared to oil and natural gas. The draw-back of coal is though that the relative CO_2 emission per unit electricity produced is higher than for the other fossil fuels. The development of a cost-efficient method for reducing this emission is thus necessary if coal should continue to be an available fuel for the power plants.

Principally, there are three possible ways of reducing the CO_2 emission from power production:

1. Increase the efficiency of the power plant
2. Change to a fuel with a lower content of fossil carbon, e.g. biomass
3. Capture and store the CO_2 produced from conventional coal firing

Means 1 and 2 are very important and are continually implemented in the Danish power plants. They will, though, only have limited effect on a complete elimination of the CO_2 emission. In order to decrease the emission drastically, the latter method should be applied.

Different technologies have been proposed and are investigated for carbon capture and storage (CCS). Preliminary technical-economical studies have shown great potential for the so-called OxyFuel combustion technology [1]. In OxyFuel combustion the fuel which could be coal, biomass, or others, is burnt in an atmosphere consisting of oxygen (> 95 % pure) and recirculated flue gas (consisting primarily of CO_2 and water). The result is a flue gas with a CO_2 content of up to 95 % on a dry basis from which it is relatively easier to extract a pure CO_2 stream which can be stored, than from the flue gas of a conventionally fired power plant which has a CO_2 content of about 14 %. Figure 1 shows the principle in OxyFuel combustion and CO_2 capture in a power plant.

OxyFuel combustion will potentially induce a considerable altering of the operational mode of the power plant compared to conventional operation. Generally, there exists an insufficient knowledge on many fundamental and practical aspects related to the change from the conventional to the OxyFuel combustion process. This concerns among others the emission levels of CO, NO_x, and SO_2, the quality of the ash fractions, the risk of increased corrosion due to a change in the chemical composition of deposits, and the temperature and radiation in the boiler which is affected by the changed gas phase composition, i.e. the increased level of CO_2.

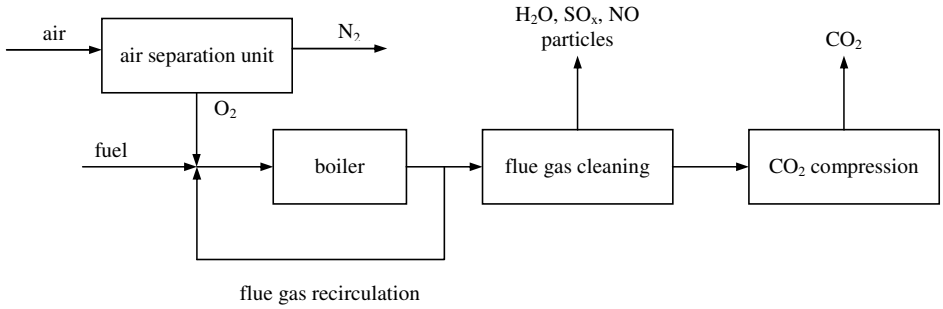

Figure 1: General flow diagram for OxyFuel combustion and CO_2 capture.

Another issue of great importance for the Danish power plant companies is the possibility of co-firing coal or other fossil fuels with biomass such as straw or wood under OxyFuel conditions. OxyFuel combustion of biomass has not been addressed in the literature, but it is not necessarily the case that results obtained on coal can be directly transferred to biomass.

Specific Objectives

The aim of the PhD study is to strengthen the scientific basis for the development and application of the OxyFuel combustion technology to thermal power plants. Both experimental and theoretical investigations of the fundamental aspects of the combustion chemistry obtained when burning coal and biomass will be performed. Specific topics which will be addressed are:

- Ash composition and quality, especially related to sulphur chemistry – because of the application of fly ash in cement and concrete production this is a very important area of investigation.
- Deposits composition – are indicative of the risk of corrosion in the system
- Emissions of CO, NO_x, and SO_2 from the boiler – the recirculation of flue gas will play a role in the obtained levels of the emissive gas phase components together with the chosen strategy for flue gas cleaning
- The effect of co-firing coal with biomass (wheat straw)

The results obtained in the experimental investigations will be applied in a validation of a Computational Fluid Dynamics (CFD) model for OxyFuel combustion. The CFD model will be built as part of the PhD study and should be applicable for design and process optimization in full scale boliers.

Experimental setup

An existing experimental setup is applied in the investigations, see Figure 2. The setup consists of a cylindrical reactor (inner diameter 39 cm) with a swirl burner. The setup is equipped with a solid fuel feeder, a fly ash sample system (not shown), and several measuring ports for temperature and gas phase composition measurements. The setup can run at an effect of approximately 30 kW.

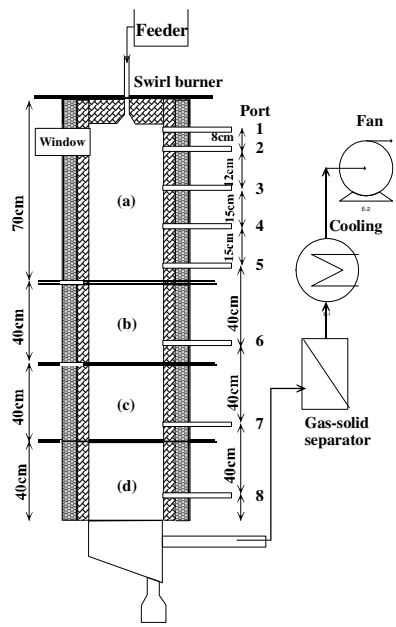

Figure 2: Sketch of the experimental setup – a 30 kW swirlburner.

Acknowledgements

The PhD study is part of PSO project 7171 (Oxy-fuel Combustion for below zero CO_2 emissions) which is carried out in collaboration between DONG Energy, Vattenfall A/S, the Combustion and Harmful Emission Control (CHEC) group at the Chemical Engineering department (KT), and department of Manufacturing Engineering and Mangement (IPL).

The PhD study is financially supported by PSO, DONG Energy, and the Ministry of Science Technology and Innovation (VTU).

References

1. B.J.P. Buhre, L.K. Elliott, C.D. Sheng,, R.P. Gupta, and T.F. Wall. Progress in Energy and Combustion Science 31 (4) (2005) 283-307.

Yanwei Wang

Phone: +45 4525 6809
Fax: +45 4588 2161
E-mail: wyw@kt.dtu.dk
WWW: http://www.dtu.dk/Centre/DPC.aspx
Supervisors: Ole Hassager
Flemming Y. Hansen (DTU Kemi)
Günther H. Peters (DTU Kemi)

PhD Study
Started: August 2005
To be completed: August 2008

On the Universal Behavior of Equilibrium Partitioning of Macromolecules between Bulk Solution and a Slit Confining Geometry

Abstract
Equilibrium partitioning of macromolecules between bulk solution and a slit confining geometry with inert surfaces is investigated under a framework that we have developed for the description of macromolecules subject to spatial confinement. Two new molecular functions are introduced for the description of structure properties of macromolecules, and a general relation is pointed out between the confinement size and the equilibrium partition coefficient in the dilute solution limit. We show that this relation is universal to all macromolecules.

Introduction
Comprehensive understanding of the configurational and statistical thermodynamic behavior of macromolecules subject to confining geometries is necessary in providing a fundamental account of such phenomena as polymer aid colloidal stabilization, oil recovery, surface lubrication and size exclusion chromatography (SEC) [1-3]. Many of these practical applications involve restrictions of polymer configurations due to the presence of spatial confinement, and have been studied through different approaches including equilibrium partitioning of macromolecules between bulk and confined solutions, concentration depletion effect in micro-/nano-fluidics and conformation anisotropy of confined macromolecules [4-6]. For example, the partitioning of polymers between bulk and confined solutions underlines various polymer separation techniques such as SEC. It is general accepted that the separation process in SEC relies on a differential penetration of polymers into the pores of the column packing material and it is clear on theoretical background that this partial penetration is determined by the loss of configurational entropy when a polymer chain enters a confining geometry [7].

The partition phenomenon is described by the partition coefficient, $K = c_I/c_E$, where c_I and c_E are the concentrations of macromolecules inside the confining geometry and in bulk solution, respectively, as illustrated in Fig. 1. In the case of purely steric exclusion where enthalpic effect is neglected, the equilibrium partition coefficient K_0 is determined only by the change in configurational entropy ΔS as the molecule is brought into the confining geometry from bulk solution and is given by $K_0 = \exp(\Delta S/k_B)$ [3], where k_B is the Boltzmann constant.

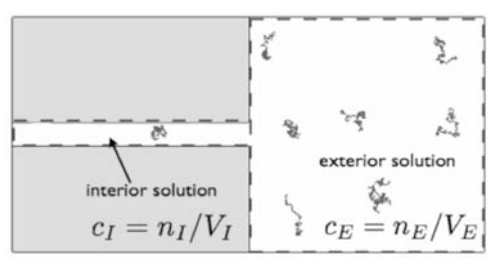

Figure 1: Sketch of solutions of polymer chains in bulk (exterior) and in a confining geometry (interior). c_I and c_E are the concentrations of macromolecules inside the confining geometry and in bulk solution, respectively. n_I and n_E are the average number of macromolecules in the interior and exterior solutions, respectively. V_I and V_E are the volumes of the interior and exterior solutions, respectively.

Different theoretical approaches have been employed to determine K_0 as a function of molecule-to-pore size ratio [3, 8]. It is understood from the equilibrium partitioning theory that polymers in SEC are separated according to their equilibrium partition coefficients, and therefore effort has been put to find the

most relevant molecular size parameters that characterizes the equilibrium partitioning behavior. It was found by Casassa and Tagami [9] that plots of K_C as a function of R_g/d do not follow a common curve for ideal polymers of linear and star architectures. In an effort to bring these plots into a universal relationship, they proposed using $R_g g^{-1/3}/d$, where g is the Zimm-Stockmayer branching parameter [10]. More recently, Radke [11] and Teroka [12] proposed the use of the hydrodynamic radius R_h instead of R_g and $R_g g^{-1/3}$. Both the use of $R_g g^{-1/3}/d$ and R_h are capable of providing a better universality than the use of R_g. However, the success is limited, and a fundamental understanding of the universal partitioning behavior is still lacking.

We have developed a new framework for the description of macromolecules subject to confining geometries [8]. The two main ingredients in this framework are a new computation method and a new molecular size parameter. The computational method, called the Confinement Analysis from Bulk Structures (CABS), allows the computation of K_C for slits, channels and box confining geometries as a function of confinement size on the basis of only one sampling of the configuration space of a macromolecule. A simple analysis of our CABS method for the calculation of K_C for a slit confining geometry leads to the definition of a new geometric size measure of macromolecules. We suggest that this molecular size parameter, called the steric exclusion radius, R_s, is the relevant molecular length scale for characterization of spatial confinement effect on macromolecules. As shown in Fig, 2, results for K_C as a function of R_s/d show a unique curve for $R_s/d < 0.2$. In particular, results for a linear self-avoiding-walk (SAW) polymer, a linear random walk (RW) polymer and a symmetric RW star polymer are nearly indistinguishable in Fig. 2, which indicates that the separation of polymers in SEC is based on their steric exclusion radius.

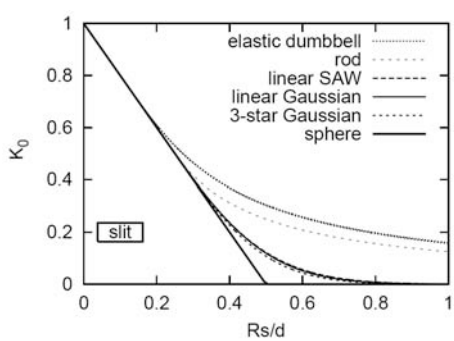

Figure 2: K_C as a function of R_s/d for (from top to bottom) an elastic dumbbell, a rigid rod, a linear SAW polymer, a linear RW polymer, a symmetric 3-arm RW star polymer and a sphere.

Specific Objectives

It is clear from Fig. 2 that when K_C is shown as a function of R_s/d, we see a unique curve as $R_s/d \to 0$, while as R_s/d increases, deviations appear. This naturally gives rise to a clarification of the weak and high confinement regimes [8]. In the weak confinement regime, K_C depends only on R_s/d regardless of the molecular details, while in the high confinement regime, such a relation between K_C and R_s/d breaks down. The objective of this work is therefore to find out a general relation between the confinement size and the equilibrium partition coefficient that is valid for both the weak and high confinement regimes.

Results and Discussions

Our CABS method for the calculation of the equilibrium partition coefficient for a slit confining geometry gives [8]

$$K_0(d) = \left\langle \left(1 - \frac{\sigma}{d}\right) \mathrm{H}\left(1 - \frac{\sigma}{d}\right) \right\rangle \qquad (1)$$

where $\langle ... \rangle$ denotes an ensemble average over the orientational and configurational freedom of a macromolecule; $\mathrm{H}(x)$ is the Heaviside function; as shown in Fig. 3, d is the width of a confining slit, and σ is the maximum distance covered by a certain molecular configuration in the direction normal to the slit plane which is denoted by a unit vector $\vec{e}_k$ in Fig. 3. Mathematically, σ may be expressed as

$$\sigma = \max(\{\vec{r}\}_i \cdot \vec{e}_k) - \min(\{\vec{r}\}_i \cdot \vec{e}_k) \qquad (2)$$

Where $\{\vec{r}\}_i \equiv \{\vec{r}_1, \vec{r}_2, ..., \vec{r}_N\}_i$ denotes the collection of monomer position vectors of the i-th molecular configuration. It is clear from Eq. 1 that the equilibrium partition coefficients can be obtained for all confinement sizes by our CABS method, and we note here that the extension of Eq. 1 to channels and box confining geometries is straightforward. Besides the superior property in efficiency compared to previous Monte Carlo studies, CABS also facilitates the identification of possible universal behavior.

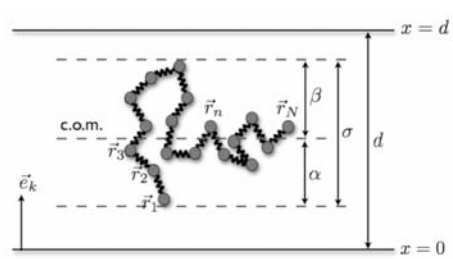

Figure 3: Illustration of a polymer configuration $\{\vec{r}\}_i$ and a slit confining geometry of width d. A unit vector $\vec{e}_k$ normal to the slit plane is drawn to define the orientation of the confinement slit relative to the polymer configuration. σ is obtained as the maximum distance covered by $\{\vec{r}\}_i$ in $\vec{e}_k$ direction.

Let us denote by $f(\sigma)$ the probability density function found for σ. By introducing $f(\sigma)$, we replace the ensemble average in Eq. 1 by an integral and obtain

$$K_0(d) = \int_0^d \left(1 - \frac{\sigma}{d}\right) f(\sigma) d\sigma \qquad (3)$$

As $d \to \infty$, Eq. 3 reduces to

$$K_0(d) = 1 - 2R_s/d \qquad (4)$$

where R_s, called the steric exclusion radius, is given by

$$2R_s = \langle \sigma \rangle = \int_0^\infty \sigma f(\sigma) d\sigma \qquad (5)$$

We note here that for some simple shaped rigid macromolecules and ideal polymers, it is possible to obtain algebraic expressions of $f(\sigma)$. Besides, with the rapid advances in computing facilitates and molecular simulation techniques, a numerical determination of $f(\sigma)$ is rather simple by sampling the configuration space of a macromolecule. Fig. 4 shows the distribution functions of σ/R_s for a rigid rod, an elastic dumbbell and a long chain linear RW polymer obtained both from our Monte Carlo simulations by a simple histogram analysis and from our theoretical predictions, where simulations and theory agree with each other very well.

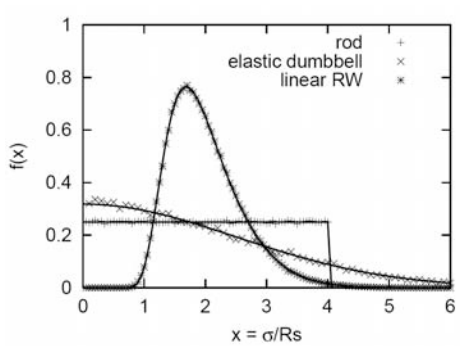

Figure 4: The distribution function of σ/R_s calculated for a rigid rod, an elastic dumbbell and a long chain linear RW polymer. Points: our Monte Carlo simulations. Lines: our theoretical predictions.

The universal partitioning behavior in Eq. 4 is essentially the partitioning behavior of a sphere of radius $R = R_s$, which accounts for the unique curve shown in Fig. 2. It is clear both from Fig. 2 and Eq. 4 that as $R_s/d \to 0$, the equilibrium partition coefficient K_0 depends only on the ratio of R_s to the confinement size d regardless of molecular details. However, as R_s/d increases, Eq. 4 will eventually deviate from the exact solution of K_0, i.e. Eq. 3. In order to obtain a general relation between K_0 and d that is also valid in the high confinement regime, we introduce two molecular functions as

$$F(d) = \int_0^d f(\sigma) d\sigma \equiv \left\langle \mathrm{H}\left(1 - \frac{\sigma}{d}\right) \right\rangle \qquad (6)$$

$$2R_{s,d}(d) = \int_0^d \sigma \frac{f(\sigma)}{F(d)} d\sigma \equiv \frac{\langle \sigma \mathrm{H}\left(1 - \frac{\sigma}{d}\right) \rangle}{\langle \mathrm{H}\left(1 - \frac{\sigma}{d}\right) \rangle} \qquad (7)$$

Function $F(d)$ defined in Eq. 6 is the cumulative distribution function of variable σ, which is the probability that variable σ lies in the interval $[0, d]$. The normalization condition thus tell us that as $d \to \infty$, $F(d) \to 1$. The ratio of $f(\sigma)$ to $F(d)$ can be regarded as a normalized probability density function of variable σ in the range from 0 to d. Function $R_{s,d}(d)$ is thus be regarded as half of the expected value of variable σ that lies in the interval $[0, d]$, and the steric exclusion radius defined in Eq. 5 is therefore a limiting value of $R_{s,d}(d)$ as $d \to \infty$. Substitution of Eq. 6 and Eq. 7 into eq. 3 leads to

$$\frac{K_0(d)}{F(d)} = 1 - 2\frac{R_{s,d}(d)}{d} \qquad (8)$$

A unique curve can therefore be obtained in a plot of $K_0(d)/F(d)$ as a function of $R_{s,d}(d)/d$ as shown in Fig. 5. Since Eq. 8 is obtained without any assumption of the molecular conformation and chain statistics, it is therefore universal to all macromolecules in both weak and high confinement regimes.

The two molecular functions introduced in Eq. 6 and Eq. 7 can be determined from $f(\sigma)$. Results of $F(d)$ and $R_{s,d}$ for a sphere, a linear long chain RW polymer and a rigid rod are shown in Fig. 6 and Fig. 7, respectively. As one may expect, for $d/R_s >> 1$, $F(d) \to 1$, $R_{s,d}(d) \to R_s$, and the universal behavior in the weak confinement regime i.e. Eq. 4 is recovered. It is also interesting to notice that $F(d) = R_{s,d}(d)/R_s$ holds for a sphere and a rigid rod, respectively.

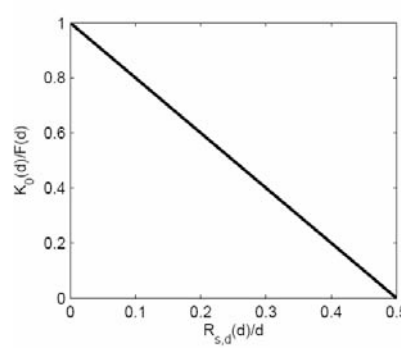

Figure 5: a universal behavior of equilibrium partitioning of macromolecules between bulk solution and a slit confining geometry of width d with inert surfaces in the dilute solution limit.

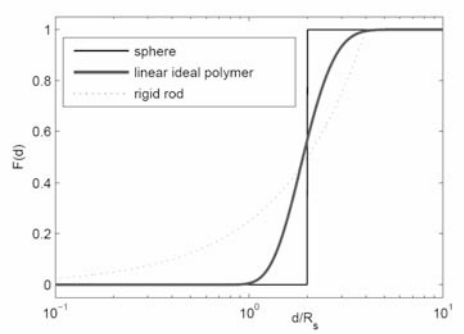

Figure 6: $F(d)$ as a function of d/R_s for a sphere, a linear ideal polymer and a rigid rod.

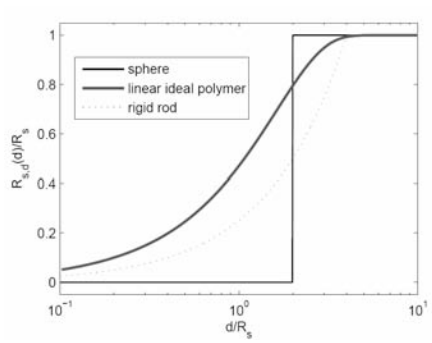

Figure 7: $R_{s,d}/R_s$ as a function of d/R_s for a sphere, a linear ideal polymer and a rigid rod.

Conclusions

Equilibrium partitioning of macromolecules between bulk solution and a slit confining geometry with inert surfaces in the dilute solution limit is investigated under a framework that we have developed for the description of macromolecules subject to spatial confinement. A general relation is obtained between the confinement size and the equilibrium partition coefficient. This relation holds in both weak and high confinement regimes and is also valid to all macromolecules. In order to obtain this relation, two new molecular functions are introduced, and the equilibrium partition coefficient in a slit confining geometry is determined solely by these two molecular functions through a simple relation.

Acknowledgements

This project is funded by DTU and the graduate school of polymer science. Y. W. also acknowledges support by the Danish Research Council for Technology and Production Sciences grant no. 26-04-0074. Simulations were performed at the Danish Center for Scientific Computing at the Technique University of Denmark.

References

1. P. G. de Gennes, Scaling Comcepts in Polymer Physics, Cornell Univ. Press, Ithaca, 1979
2. A. T. Clark and M. Lal, J. Chem. Soc. Faraday Trans. 2 (77) (1981) p. 981.
3. I. Teraoka, Prog. Polym. Sci. 21 (1996) p. 89.
4. E. F. Casassa, J. Polym. Sci. Part B Polym. Lett. 5 (1967) p. 773.
5. D. Stein, E. H. J. van der Heyden, W. J. A. Koopmans and C. Dekker, PNAS, 103 (2006) p. 123101.
6. M. Daoud and P. G. de Gennes, J. Phys. (Paris), 38 (1977) p. 85.
7. J. C. Giddings, E. Kucera, C. P. Russell and M. N. Myers, J. Phys. Chem. 72 (1968) p. 4397.
8. Y. Wang, G. H. Peters, F. Y. Hansen and O. Hassager, in preparation.
9. E. F. Casassa and Y. Tagami, Macromolecules, 2 (1969) p. 14.
10. B. H. Zimm and W. H. Stockmayer, J. Chem. Phys. 17 (1949) p. 1301.
11. W. Radke, J. Chromatohr. A, 1028 (2004) 211.
12. I. Teraoka, Macromolecules, 37 (2004) p. 6632.

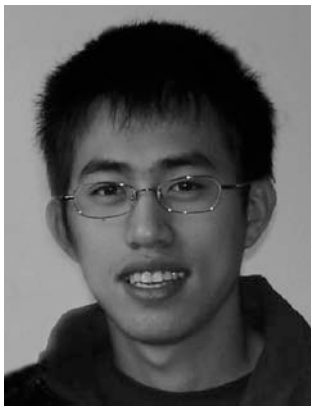

Hao Wu
Phone: +45 4525 2927
Fax: +45 4588 2258
E-mail: haw@kt.dtu.dk
WWW: http://www.chec.dtu.dk
Supervisors: Peter Glarborg
Kim Dam-Johansen
Flemming Frandsen

PhD Study
Started: November 2007
To be completed: October 2010

Co-Combustion of Fossil Fuel and Wastes

Abstract
Co-combustion of coal and wastes is recognized as one of the most promising methods to reduce the CO_2 emissions from fossil fuel combustion. The term wastes used here represent all of the residues from forestry, agriculture, industry and household. Applications of co-combustion of coal and wastes have been conducted actively but not widely in many countries. The major technical concerns related with co-combustion are fuel supply, pretreatment and storage, combustion efficiency and stability, pollutants formation, ash deposition, ash quality, corrosion to the equipments and influences to the SCR process. The current PhD study aims to identify suitable wastes and develop corresponding technologies to co-combust coal and wastes in existing industrial pulverized coal boilers. The pretreatments of the wastes, the influences of co-combustion to the ash quality, the emissions of trace elements and the deactivation effects to the SCR catalyst are mainly focused. The contents of this study include preparation and characterization of waste materials, testing co-combustion in lab scale facility, pilot plant and full scale plant, optimizing the co-combustion process through experiments and modeling.

Introduction
Energy resources in the world have been divided into three categories: fossil fuel, renewable resources, and nuclear resources. Among these categories, Fossil fuel, which consists of coal, oil and natural gas, is the major energy resource supplying nearly 80% of the world primary energy [1]. The application of fossil fuel is mostly achieved through combustion that releases greenhouse gases (e.g. CO_2 and CH_4) and pollution emissions (e.g. NO_x and SO_x, etc) [2]. The greenhouse gases and pollutant emissions accompanied by fossil fuel combustion have received much attention in recent years, particularly the CO_2 emission which has increased by more than one-third over the past 100 years and contributes to approximately 55% of the world's current greenhouse effect [3]. A large number of technologies have been developed to reduce the green gases and pollutant emissions for fossil fuel combustion. Among these technologies, co-combustion of coal and wastes is regarded as a near-term, low-risk, low-cost and sustainable technology that can reduce the net CO_2 emissions as well as the NO_x and SO_x emissions from coal combustion efficiently [4].

The wastes used in this study consist of all of the residues from forestry, agriculture, industry and household. Most of these residues are biogenetic and are considered to be CO_2 neutral due to the short time required for their regeneration [2]. Energy produced from the combustion of these residues can replace part of the energy produced by fossil fuel combustion, thus can reduce the net CO_2 emissions in the world. Furthermore, biogenetic residues not used as fuel usually decay to CO_2 and other more potent greenhouse gases such as CH_4 [4]. It has been reported that between 20 and 70 million metric tons of CH_4 were emitted annually from the anaerobic decomposition of organic waste at landfills worldwide [5]. Moreover, biogenetic wastes usually contain less sulfur and nitrogen contents than coals. Hence, utilization of these wastes in energy production also reduces the NO_x and SO_x emissions in the earth [2].

Non-biogenetic wastes mainly contain plastics and waste tires which are not very feasible to recycle and landfill. Combustion of non-biogenetic wastes provides an effective way to dispose the wastes as well as utilize the high energy contents existing in these wastes. Also, the NO_x emissions from the combustion of these residues are generally lower than those from coal combustion [6, 7].

Wastes can be combusted either directly or together with other fossil fuels such as coal. Compared to direct combustion of wastes, co-combustion of coal and wastes in existing coal-fired boilers offers several advantages. First, the capacity cost is much lower for

co-combustion in existing coal-fired boilers than building new dedicated waste combustion plants. Second, the electric efficiency in coal fired boiler is usually higher than that in the dedicated waste plant. Third, the power generation in coal-fired boiler is usually two orders of magnitude larger than that from dedicated waste plants. As a result, the energy produced from wastes can be increased largely and quickly, even if co-combustion is applied in relatively minor coal-fired boilers [8].

Apart from the major advantages mentioned above, there are also other advantages of co-combustion of coal and wastes such as: the high carbon content of coal and the high volatile content of most wastes can compensate each other and generate a better combustion process than for separate fuels, co-combustion is more feasible for the regions where waste can not be produced continuously as the plant can be changed to dedicated co-fired plant flexibly [9], the synergetic effects between coal and wastes may also reduce NO_x and SO_x emissions [8].

Problems and challenges are also associated with co-combustion technology. For most coal-fired boilers, co-combustion with wastes requires pretreatments to the wastes. These pretreatments usually include drying, grinding and sometimes densification that increase the cost of using the technology [9]. Ash deposition and corrosion problems are generally more significant for co-combustion boilers than for dedicated coal-fired boilers, especially for herbaceous wastes which contain high contents of alkaline metals and chloride [3, 4]. The high operation temperature of co-combustion boilers is also preferred by ash deposition, compared to dedicated waste combustion boilers [9]. The deactivation of Selective Catalytic Reduction (SCR) catalyst caused by fly ash with high alkali content may also be an important challenge for co-combustion of coal and wastes [9]. Co-combustion may affect the ash qualities (high alkali metal and chlorine contents), and restrain the application of fly ash in building materials or cement industry [9]. The trace element emission may also become a significant problem when co-combustion coal with wastes (e.g. sewage sludge) which contain high amount of trace elements [10]. Other problems, such as reduction of the boiler efficiency and flame stability, may appear as well when co-combustion coal with certain waste materials [4].

In spite of the problems and challenges mentioned above, co-combustion is still regarded as one of the most promising short-term options for reducing the net CO_2 emissions from coal-fired power plants and disposal the wastes [8]. To promote this technology, problems related with co-combustion must be investigated and solved.

Specific Objectives

The objective of this PhD project is to identify suitable wastes and develop corresponding technologies to co-combust coal and wastes in existing industrial pulverized coal boilers. The major focuses of the project are the pretreatments of the wastes, the influences of co-combustion to the ash quality, the emissions of trace elements and the deactivation effects to the SCR catalyst. The work includes a literature survey on co-combustion of coal and wastes, preparation and characterization of wastes, testing in lab scale facility, pilot plant and full scale plant, and optimizing the co-combustion process through experiments and modeling.

Acknowledgements

The PhD study is sponsored by the Technical University of Denmark.

References

1. UNDP, World energy assessment: overview 2004 update, New York, 2004.
2. M. Sami, K. Annamalai, M. Wooldridge, Prog Energy Combust Sci 21 (2001) 171-214.
3. A. Demirbas, Prog Energy Combust Sci 31 (2005) 171-192.
4. L. Baxter, Fuel 84 (2005) 1295-1302.
5. D.N. Beede, D.E. Bloom, The World Bank Research Observer 10 (2) (1995) 113-150.
6. S. Gupta, V. Sahajwalla, J. Wood, Energy Fuels 20 (2006) 2557-2563.
7. Y.A. Levendis, A. Atal, B. Courtemanche, J.B. Carlson, Combustion Sci Technol 131 (1998) 147-185.
8. A.L. Robinson, H. Junker, S.G. Buckley, G. Sclippa, L.L. Baxter, Proceedings of the Combustion Institute 27 (1998) 1351-1359
9. J. Werther, M. Saenger, E.-. Hartge, T. Ogada, Z. Siagi, Prog Energy Combust Sci 26 (2000) 1-27.
10. R. Cenni, F. Frandsen, T. Gerhardt, H. Spliethoff, K.R.G. Hein, Waste Manage 18 (1998) 433-444.

Cheng Xu

Phone: +45 4525 2935
Fax: +45 4525 2258
E-mail: cxu@kt.dtu.dk
WWW: http://www.kt.dtu.dk
Supervisors: Anne Meyer, DTU
Jens Sørensen, Danisco A/S

PhD Study
Started: March 2007
To be completed: Month 200Y

Kinetic Models Describing Enzyme Catalyzed Degradation of Water Soluble Arabinoxylan

Abstract
The project focuses on modelling of the cooperative and synergistic action of the enzymes during modification, debranching and depolymerisation of differently substituted, water soluble arabino-xylooligosaccharides. The main purposes are to study the kinetics model of degradation with pure enzymes and to design a process in order to obtain a target xylo-oligosaccharide with high prebiotics activity

Introduction
Native arabinoxylans are abundant in cereal plant cell walls and are composed of a backbone of (1,4)-linked-D-xylose residues having α-arabinose substituents. Recent findings indicate that xylooligosaccharides stimulate the growth of probiotic, cecal bifidobacteria in vivo and exert inhibitory effects on precancerous colon lesions in rats. An overall aim of the PhD project is to use specific enzymes to design biofunctional xylooligosaccharides with defined substitution patterns and chain lengths, and in particular to quantify the rates of the different events by developing enzyme kinetic models. Purified microbial enzymes, including α-Larabinofuranosidases, endo-1,4-beta-xylanases, and beta-xylosidase from various microbial sources will be systematically combined to obtain reaction rates for the different enzyme catalyzed reactions, e.g. removal of arabinose from singly versus from doubly substituted xyloses, and different patterns of xylan depolymerisation. The enzymes as well as different types of arabinoxylans have recently become commercially available. Rates of reactions will be determined from HPLC evaluation of arabinose, xylose, and xylo-oligomer release in timed enzyme experiments. In order to find better ways to reuse the enzymes to save costs, the effects and mode of removal of the monosaccharide products to eventually abolish product inhibition will also be assessed. The hypothesis behind the project is that provision of a better quantitative understanding of the events by modelling of the reactions is a prerequisite for optimally exploiting the complex, sequential enzyme reactions in new food and ingredient processes and development. With arabinoxylan, the results are particularly relevant in baking, brewing, prebiotics design, and in non-food cereal based processes.

The enzymatic hydrolysis of arabinoxylan is a complicated process which requires the action of different enzyme activities for complete hydrolysis; These are first and foremost various α-L-arabinofuranosidases, endo-1,4-β-xylanase and β-xylosidase [1]. Arabinoxylan consist of (1,4)-β-linked D-xylopyranosyl residues to which α-L-arabinofuranosyl residues can be single substituted at α-1,3 or α-1,2 and double-substituted at α-1,3 and α-1,2, [2]. The enzymatic degradation of arabinoxylan, can be expected to depend on the degree of arabinose substitution, the position of glycosidic bonds and their distribution along the xylan backbone [3].

Specific Objectives
The purpose of current study is to understand the enzyme kinetics in arabinoxylan degradation. The overall aim is that we can design and control the reaction optimally; a particular purpose of this study is to control the hydrolysis in order to produce specific xylo-oligsacchrides with high prebiotics activity.

Preliminary Result
Special attention is given to the action of α-L-arabinofuranosidases which are represented by the glycoside hydrolase (GH) families: 3, 10, 43, 51, 54 and 62. The enzymes catalyse the hydrolysis of α-1,2, α-1,3 and α-1,5 glycosidic bonds of α-L-arabinofuranosyl residues [4]. Also the action of β-xylosidase is taken into account. β-Xylosidases catalyse the cleavage of xylobiose and attack the non-reducing ends of short xylooligosaccharides to liberate xylose [1][5]. β-

xylosidase activity has been reported to be rate-limiting in arabinoxylan hydrolysis [6]. Enzymes exhibiting β-xylosidase activity are categorised into the following seven different GH families: 3, 30, 39, 43, 51, 52 and 54. The synergistic effect of the enzymes acting on arabinoxylan is analysed with enzyme preparations from *Aspergillus niger*, *Bifidobacterium adolescentis* and the enzyme blend "Celluclast 1.5 L" (Novozymes A/S, Denmark).

Here, we use C+A represent the enzyme combination Celluclast 1.5 L and Arabinofuranosidase from *A.niger* , C+B represent the enzyme combination Celluclast 1.5 L and Arabinofuranosidase from *Bi.Adolescentis,* C represent pure Celluclast 1.5 L. Figure 1 shows the initial rate of xylose release in the arabinoxylan degradation on different substrate concentration.

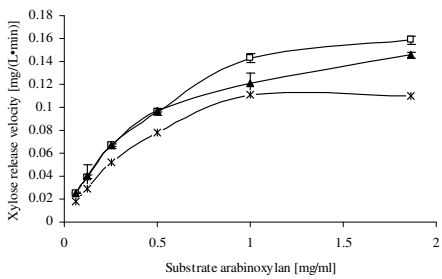

Figure 1: 2 The 20min reaction velocity for the enzymatic release of xylose plotted against substrate concentration treated with different enzyme combinations C+A (□), C+B (▲) and C (*)

The xylose release (beta-xylosidase activity) apparently follows the Michaelis-Menten kinetics curve. The reaction rate increases as substrate concentration increases. As arabinoxylan concentration gets higher, the enzyme becomes saturated with the substrate and the rate reaches the apparent Vmax, the enzyme's maximum rate on this substrate.

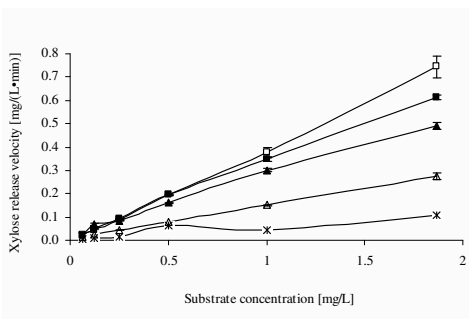

Figure 2: 20min arabinose release velocity plotted against substrate concentration treated with different enzyme combinations C+A (□), C+B (▲), C (*), A (■) and B

In Figure 2, the release of arabinose doesn't give a Michealis-Menten kinetics curve. Since the number of the arabinose residue is comparably low in arabinoxylan, and only a part of them can be released, the reason of this linear curve might be the substrate concentration is not higher enough to obtain the apparent Vmax

Acknowledgement
I would like to thank Danisco A/S for delivering enzymes for the experimental work.

References

1. Rasmussen LE, Sørensen HR, Vind J, Viksø-Nielsen A (2006) Mode of action and properties of the β-xylosidase from Taleromyces emersonii and Trichoderma reesei. Biotechnol Bioeng 94:869-876
2. Izydorezynk MS, Biliaderis CG (1995). Cereal arabinoxylans: advances in structure and physicochemical properties. Carbohyd. Polym. 28: 33-48.
3. Dervilly-Pinel G, Tran V, Saulnier L (2004). Investigation of the distribution of arabinose residues on the xylan backbone of water-soluble arabinoxylans from wheat flour. Carbohyd. Polym. 55: 171-177..
4. De Vries RP, Visser J (2001). Aspergillus enzymes involved in degradation of plant cell wall polysaccharides. Microbiol. Mol. Biol. R. 65: 497-522.
5. Sørensen HR, Meyer AS, Pedersen S (2003) Enzymatic hydrolysis of water-soluble wheat arabinoxylan. 1. synergy between α-L-arabinofuranosidases, endo-1,4-β-xylanases, and β-xylosidase activities. Biotechnol Bioeng 81:726-731
6. Poutanen K and Puls J (1988). Characteristics of Trichoderma reesei β-xylosidase and its use in the hydrolysis of solubilized xylans. Appl Microbiol Biotechnol. 28: 425-432.

AYTEN YILMAZ WAGNER

Phone: +45 4525 2920
Fax: +45 4588 2258
e-mail: ayt@kt.dtu.dk
www: www.kt.dtu.dk
Supervisors: Peter Glarborg
Hans Livbjerg
Per G. Kristensen, DGC

Ph.D. Study
Started: August 2005
To be completed: September 2008

Particle Formation during Natural Gas Combustion at Domestic Appliances

Abstract

Epidemiological associations between illness and nitrogen dioxide may be the consequence of confounding by fine particle numbers. Like many other phenomena in nature, the presence of carbon nano-forms in blue combustion flames went virtually unrecognized because it was essentially unexpected. Observation of carbon nano-forms in relatively efficient burning, mostly blue combustion flames suggests that the proliferation of so-called clean-burning gaseous fuel sources, particularly methane-series gases (CnH2(n+1); n=1,2,3…etc) may, in fact, make a significant contribution of carbon nanocrystal forms to both the indoor and outdoor air environment. In this PhD study, particle formation from gas cookers is investigated.

Introduction

The contribution of the home environment and other life style factors in the pathogenesis of allergic disease has attracted much attention, particularly the role of indoor pollution from gas cooking appliances via nitrogen dioxide (NO_2) and carbon-monoxide (CO) emissions. In particular, natural gas is recognized as one of the most important cooking fuels for domestic gas burners in developed countries (1).

A recent hypothesis (2, 3) is that the epidemiological associations between illness and nitrogen dioxide may be the consequence of confounding by particle numbers. When particles are measured as mass the greatest contribution comes from the largest particles, but the greatest number of particles by far are the submicron ones. These ultrafine particles are generated, as is NO, by the combustion process, and therefore the two pollutants (ultrafine particles and NO_2) are likely to correlate closely.

There are several studies available in literature reporting the effects of cook-top burner design and operation factors (such as cap material, cap size, port shape, port size, port spacing, central secondary aeration, flame inserts, load height, load height to flame length ratio, thermal input, etc) on the gaseous emissions (NOx, CO and hydrocarbon emissions) from the natural gas fired cook-top burners (4, 5, 6). However these studies do not provide any correlations for particulate matter or soot emissions. Gas composition is particularly a vital parameter affecting burner performance. It is known that using the same gas stove to burn natural gas with various heating values other than the intended fuel is inappropriate and hazardous due to the possible occurrence of incomplete combustion (i.e. a increase of CO emissions and/or soot formation) lift-off, flashback and inadequate heat input.

It was communicated that like many other phenomena in nature, the presence of carbon nanotubes in blue combustion flames went virtually unrecognized because it was essentially unexpected (7). Observations of carbon nanotubes and related nano-forms in relatively efficient burning, mostly blue combustion flames such as propane and natural gas suggests that the proliferation of so-called clean- burning gaseous fuel sources, particularly methane-series gases (CnH2(n+1); n=1,2,3…etc) may, in fact, make a significant contribution of carbon nanocrystal forms to both the indoor and outdoor air environment. Murr et al (8) reported aggregated multiwall carbon nanotubes with diameters ranging from 3 to 30 nm and related carbon nanocrystal forms ranging in size from 0.4 to 2 μm (average diameter) in the combustion streams for methane/air, natural gas/air, and propane gas/air flames from domestic (kitchen) stoves.

Specific Objectives

In this PhD study, particle formation during natural gas combustion at domestic appliances will be investigated. The work involves determination of particle size distribution and chemical composition of the particles together with the total amount of particles formed. Once the particles have been identified, mechanism of formation of the particles will be studied and a model for particle formation during gas combustion will be developed.

Methods, Results and Discussion

Preliminary experiments were carried out using the gas cooker in its normal procedure - natural gas supplied from the city line and air supplied from the surroundings. There were no pots placed above the cooker. Samples were collected at ~10cm above the burner using a gas ejector probe developed for particle analysis in a research program instigated to study fine particles (9). Particle concentrations are measured with a Model 3775 Condensation Particle Counter (CPC). Particles are classified with a Model 3080 Electrostatic Classifier with a Model 3081 LDMA (Long Differential Mobility Analyzer), and/or a Model 3085 NDMA (Nano Differential Mobility Analyzer).

Figure 1: Gas cooker and the ejector probe

Since particle concentrations in the ambient air were changing over time and there was no experimental control over the gas quality, the repeatability of experiments was not likely. It has been observed that the –supposed to be blue flame – was sometimes becoming a colour between yellow to orange. This change in the flame could be due to any impurities coming with the gas or just the changes in air flow around the burner.

Despite changing conditions in each experiment, CPC and SMPS measurements show that particle concentrations increase and size distributions change right after turning on the burner. However the elevated particle concentrations do not go beyond sharp peaks observed once in a while, which could indicate a release of high amount of fine particles at some instant during gas combustion. Because of the changing conditions in each experiment, it was not possible to report a trend for the size and frequency of these peaks. Before correlating these peaks directly to the gas combustion, controlled experiments are required.

For this reason, a well-controlled experimental set-up is prepared. Domestic gas cookers usually apply partial-premixed flame. A reactor, made of steel, is built keeping this configuration. The compartment functions as a steady state reactor with no mechanical mixing.

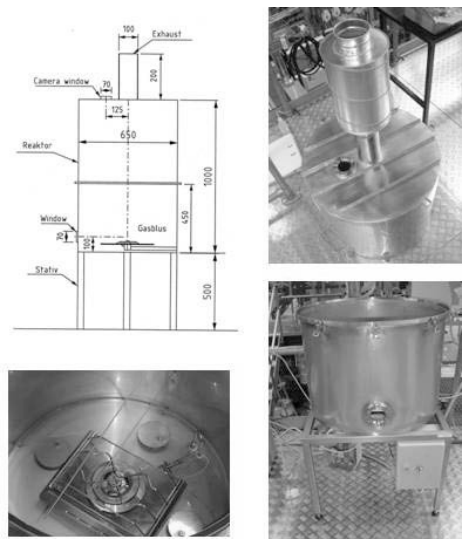

Figure 2: The reactor-technical drawing and the two compartments.

The reactor is composed of two compartments, as presented in Figure 2: 1. The lower compartment where the burner is placed at the bottom with the required gas connections and four ports through which particle free combustion air is supplied to the reactor. The ignition and flow control panel of the burner is kept outside the reactor, leaving the primary air supply nozzle inside the reactor. The reactor bottom allows using different gas rings after the required arrangement of primary air supply nozzle distance. 2. The upper compartment provides extra volume and sampling ports. A silencer is installed at the reactor outlet for preventing noise during experiments.

In order to assure flame stability, flow velocity through the reactor is kept below 10cm/s (10). The excess air ratio of the system is kept above 10. Sampling ports are placed along the reactor to allow sampling at different locations above the flame. The glass windows placed at both compartments allows observation and video recording of the flame through the experiments.

Natural gas from the city line is used as the fuel supply. Experiments are repeated with methane to observe the differences; as well as addition of minor amounts of hydrogen sulphide and acetylene to methane. The studied concentrations of hydrogen sulphide is

<100ppm in the fuel and acetylene <1000 ppm. Excess air ratio is kept above 10. Particle concentrations, size distributions, gas concentrations (CO, CO_2, O_2, NO, NO_x) and temperatures are measured at the reactor outlet.

The present findings of this study concerning the particle concentrations and size distributions are partly in agreement with the ranges reported by Dennekamp et al (3) in that UFP concentrations rise to ~10^5 UFP/cm^3; and with Bang et al (7) and Murr et al (8) that the average diameters of these particles are 3-30 nm. Natural gas resulted in an order of magnitude higher particle concentration than methane. Addition of hydrogen sulphide to methane resulted in an increase in particle concentrations to the levels achieved from natural gas combustion. Acetylene addition did not create an effect in the concentrations studied, but an effect is expected if added in higher amounts.

In order to study the morphology of the particles, transmission electron microscopy (TEM) is used. Initial samples were collected by inserting the grid into the reactor. The particle number density on the TEM grids was too low by this method of sample collection that performing EDX studies on these samples was not possible. In order to improve the sample collection, a thermophoretic sampler, named KAHLAYPET is built. Thermophoresis is a phenomenon in which a temperature gradient in a gas causes suspended particles to migrate in the direction of decreasing temperature. The sampler is composed of three channels: Cold water flows in the innermost channel and leaves the sampler through the middle channel, while the gas flow is driven through the outermost channel by the use of a pump. The grid is placed on the outer surface of the innermost channel, exposed to the gas flow. By providing a temperature difference, particles would be forced to move toward the grid due to a gain of thermophoretic velocity. The recent samples collected by this method are found promising compared to the 'diffusion only' collection of the particles. However there is room for improvement in order to avoid the damage created on the grid.

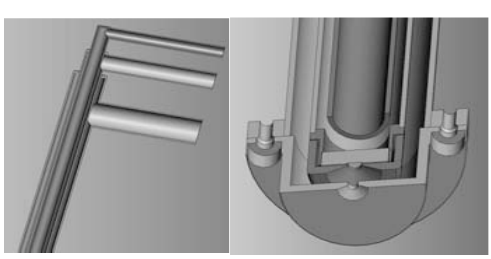

Figure 3: A thermophoretic sampler, KAHLAYPET

Conclusions

The present findings of this study concerning the particle concentrations and size distributions are partly in agreement with the ranges reported by Dennekamp et al (3) in that UFP concentrations rise to ~10^5 UFP/cm^3; and with Bang et al (7) and Murr et al (8) that the average diameters of these particles are 3-30 nm. Addition of hydrogen sulphide to methane resulted in an increase in particle concentrations to the levels achieved from natural gas combustion.

TEM samples collected by KAHLAYPET are found promising compared to the 'diffusion only' collection of the particles. However there is room for improvement in the method.

Acknowledgements

This PhD study is co-founded by The Graduate School in Chemical Engineering, DTU: Molecular Products and Product Technology MP2T, Danish Research Training Council - FUR under the Ministry of Science, Technology & Development and DGC (Dansk Gas - teknisk Center).

References

1. Chauhan, A.J., Clinical and Experimental Allergy, (29) (1999) 1009–1013.
2. Seaton, A., Dennekamp, M., Thorax (58) (2003) 1012-1015.
3. Dennekamp, M., S. Howarth, C.A.J Dick, J.W. Cherrie, K. Donaldson, A. Seaton, Occupational and Environmental Medicine, (58), (2001), 511–516
4. Junus, R., Stubington, J. F., Sergeant, G. D., International Journal of Environmental Studies (45) (1994) 101-121.
5. Stubington, J.F., Beashel, G., Murphy, T.,. Junus, R , Ashman, P.J., Sergeant, G.D., Journal of Institute of Energy (67) (1994) 143-155.
6. Shaddix, C. R., Harrington, J.R., Smyth, K.C., Combustion and Flame (99) (1994) 723-732.
7. Bang, J.J., Guerrero, P.A., Lopez, D.A., Murr, L.E., Esquivel, E.V. Journal of Nanoscience and Nanotechnology (4.7) (2004) 716- 718.
8. Murr, L.E., Bang, J.J., Esquivel, E.V., Guerrero, P.A., Lopez, D.A. Journal of Nanoparticle Research (6) (2004) 241–251.
9. Johannessen, J.T., Pratsinis, S.E., Livbjerg,H., Chemical Engineering Science, 55(1), (2000) 177-191.
10. Matthews, T. G., Thompson, C. V., Wilson, D. L., Hawthorne, A. R., Environment International, (15),(1989) 545-550.

Chemistry at work

Combustion and Harmful Emission Control

Phase Equilibria and Separation Processes

Computer Aided Process Engineering

BioProcess Engineering

Danish Polymer Centre

Aerosol Technology

Department of Chemical
and Biochemical Engineering
DTU Building 229
Søltofts Plads
DK-2800 Kgs. Lyngby
www.kt.dtu.dk